

**FATIGUE LIFE PREDICTION UNDER CONSTANT
AMPLITUDE AND INTERSPERSED MODE-I AND
MIXED-MODE (I AND II) OVERLOAD USING
AN EXPONENTIAL MODEL**

A thesis submitted in partial fulfillment for award of the degree of

Doctor of Philosophy

by

JYOTIRANJAN MOHANTY

under the supervision of

Prof. B. B. Verma

Mettalurgical & Mats. Eng. Dept.

Prof. P. K. Ray

Mechanical Engg. Dept.



National Institute of Technology, Rourkela

(Deemed University)

May 2009

Dedicated
To
My Parents

CERTIFICATE

*This to certify that the thesis entitled “**Fatigue life prediction under constant amplitude and interspersed mode-I and mixed-mode overload using an exponential model**” submitted by **Jyoti Ranjan Mohanty** for the award of the degree of **Doctor of Philosophy** of NIT Rourkela, is a record of bonafide research work carried out by him under our supervision and guidance. Mr. Mohanty has worked for more than three and half years on the above problem and the work reached the standard requirements and the regulation relating to the degree. To the best of our knowledge, the work incorporated in this thesis has not been submitted in full or part, to any other university or institute for the award of any other degree or diploma.*

*(Prof. Bipin Bihari Verma)
Metallurgical & Mats. Eng. Dept.
N.I.T, Rourkela.*

*(Prof. Prabal Kumar Ray)
Mechanical Eng. Dept.
N.I.T,Rourkela.*

ACKNOWLEDGEMENT

*The author would like to express his deepest and most sincere gratitude to his supervisors **Prof. B. B. Verma**, Professor, Department of Metallurgical and Materials Engineering and **Prof. P. K. Ray**, Professor, Department of Mechanical Engineering, N.I.T, Rourkela for his continuous guidance, encouragement and sharing valuable time throughout the process of this research work and in the preparation of this thesis.*

*His sincere thanks are due to **Prof. Sunil Kumar Sarangi**, Director, N.I.T, Rourkela for granting permission to use the facilities available in the institute for this study.*

*The author's special thanks **Prof. D. R. K. Parhi**, Professor, Department of Mechanical Engineering, for his help in soft-computing.*

The author also wishes to thank the staffs of the Department of Metallurgical and Materials Engineering for their sincere co-operation during this research work.

The author feels pleased and privileged to fulfill his parents ambition and greatly indebted to them for bearing the inconvenience of his stay away from them in time of their need.

*The author wishes to extend thanks to his daughters **Guddy** and **Guguli**, son **Supu**, younger brother **Pupu** and his sister-in-law, **Quina** who were a constant and active source of support throughout the endeavor. Very special thanks go to his wife, **Itila**, who has sacrificed time and companionship to complete this work.*

(Jyotiranjana Mohanty)

ABSTRACT

Fatigue performance of structures is greatly affected by the presence of stress raisers such as fastener holes, manufacturing errors, corrosion pits, and maintenance damage which serve as nucleation sites for fatigue cracking. During service, sub-critical cracks nucleate from these sites and grow till catastrophic failure takes place when the crack length reaches a critical dimension. A structure can not be retired from service simply on detecting a fatigue crack. Hence, proper evaluation of fatigue crack propagation and residual life prediction of structures (aircraft, ship, railways, bridges, gas and oil transmission pipelines, etc.) are important to ensure the public safety, environmental protection, and economical consideration.

In this research a new methodology, based on 'exponential model' has been developed to determine the crack growth rate from raw laboratory crack length and number of cycle data. That concept has been subsequently extended to estimate the fatigue life of 7020-T7 and 2024-T3 aluminium alloys under different loading conditions, i.e. constant amplitude loading, and constant amplitude loading interspersed with mode-I and mixed-mode (I and II) spike overload. The exponential index of the proposed model has been correlated with various crack driving forces and material properties such that the differential form of the equation conforms to dimensional analysis concept. It has been observed that the methodology under predicts the fatigue life but, nonetheless, captured the measured life within a $\pm 0.025\%$ error band.

Furthermore, two soft-computing methods, i.e. ANN and ANFIS, have been formulated and applied to predict the fatigue life under the same loading conditions in order to compare the relative performances of all the models. From the evaluation of results, it is seen that the fatigue life predicted from 'exponential model' gives reliable and conservative results in comparison to soft-computing methods which over-predict the life.

CONTENTS

	Page No.	
Certificate	i	
Acknowledgement	ii	
Abstract	iii	
Contents	iv	
List of figures	ix	
List of tables	xvi	
Nomenclature	xviii	
Publications arising from this dissertation	xxii	
CHAPTER I INTRODUCTION		
1.1	Background	1
1.2	Objectives	2
1.3	Thesis structure	3
CHAPTER II LITERATURE REVIEW		
2.1	Introduction	4
2.2	Life prediction models	4
2.2.1	Life prediction models under constant amplitude loading	4
2.2.2	Life prediction models under variable amplitude loading	6
2.2.3	Non-conventional life prediction models	11
2.3	Summary and the justification of the proposed model	13
CHAPTER III EXPERIMENTAL INVESTIGATION		
3.1	Introduction	17
3.2	Test specimens and accessories	17

3.2.1	Material	17
3.2.2	Specimen geometry	19
3.2.3	Mixed-mode attachment	20
3.2.4	Test equipment	21
3.3	Test program	22
3.3.1	Determination of crack coefficient	22
3.3.2	Fatigue crack growth tests	23
3.3.2.1	Constant amplitude load test	23
3.3.2.2	Constant amplitude loading interspersed with mode-I spike overload	24
3.3.2.3	Constant amplitude loading interspersed with mixed mode (I and II) spike overload	25
 CHAPTER IV EVALUATION OF EXPERIMENTAL RESULTS		
4.1	Introduction	26
4.2	Determination of fatigue crack growth rate from experimental data: A new approach	26
4.3	Test results	31
4.3.1	Constant amplitude loading	31
4.3.2	Constant amplitude loading interspersed with mode-I spike overload	36
4.3.3	Constant amplitude loading interspersed with mixed mode (I and II) spike overload	43
 CHAPTER V PREDICTION OF FATIGUE LIFE BY EXPONENTIAL MODEL		
5.1	Introduction	49
5.2	Background and approach	49
5.3	Model formulation	51
5.4	Modeling under constant amplitude loading (CAL)	52

5.4.1	Model design	52
5.4.2	Model validation	54
5.5	Modeling under constant amplitude loading interspersed with spike overload in mode-I	61
5.5.1	Model design	61
5.5.2	Model validation	62
5.6	Modeling under constant amplitude loading interspersed with spike overload in mixed mode (I and II)	69
5.6.1	Model design	69
5.6.2	Model validation	70

**CHAPTER VI PREDICTION OF FATIGUE LIFE BY
ARTIFICIAL NEURAL NETWORK (ANN)**

6.1	Introduction	75
6.2	Background	75
6.3	Model formulation	76
6.4	Modeling under constant amplitude loading (CAL)	78
6.4.1	Application design	79
6.4.2	Model validation	80
6.5	Modeling under constant amplitude loading interspersed with spike overload in mode-I	83
6.5.1	Application design	83
6.5.2	Model validation	84
6.6	Modeling under constant amplitude loading interspersed with spike overload in mixed mode (I and II)	89
6.6.1	Application design	89
6.6.2	Model validation	91

CHAPTER VII	PREDICTION OF FATIGUE LIFE BY ADAPTIVE NEURO-FUZZY INFERENCE SYSTEM (ANFIS)	
7.1	Introduction	96
7.2	Background	96
7.3	Model formulation	99
7.4	Modeling under constant amplitude loading	103
7.4.1	Application design	103
7.4.2	Model validation	104
7.5	Modeling under constant amplitude loading interspersed with spike overload in mode-I	107
7.5.1	Application design	107
7.5.2	Model validation	108
7.6	Modeling under constant amplitude loading interspersed with spike overload in mixed mode (I and II)	113
7.6.1	Application design	113
7.6.2	Model validation	113
CHAPTER VIII	RESULTS AND DISCUSSION	
8.1	Introduction	119
8.2	Comparison of predicted and experimental results	119
8.2.1	Constant amplitude loading	119
8.2.2	Constant amplitude loading interspersed with spike overload in mode-I	126
8.2.3	Constant amplitude loading interspersed with spike overload in mixed mode (I and II)	129
8.3	Discussion	131
CHAPTER IX	CONCLUSIONS AND FUTURE WORK	

9.1	Conclusion	134
9.2	Suggested future work	135
	References	136
	Appendix A	153
	Appendix B	156

LIST OF FIGURES

Figure	Page No.
1.1 Plan of the work	3
3.1 Microstructure of 7020-T7 Al alloy etched by Graff reagent	19
3.2 Microstructure of 2024-T3 Al alloy etched by Keller's reagent	19
3.3 Single Edge Notch (SEN) Specimen geometry (LT orientation)	20
3.4 Mixed-mode Loading Fixture	21
3.5 <i>INSTRON 8502</i> dynamic testing machine	22
4.1 Crack length vs. number of cycle	26
4.2 Specific crack growth rate vs. crack length	30
4.3 Comparison of exponential and polynomial crack growth rate with stress intensity factor range	30
4.4 $a-N$ curve of Al 7020-T7	31
4.5 $a-N$ curve of Al 2024-T3	31
4.6 $\log (da/dN)-\Delta K$ curve of Al 7020-T7	32
4.7 $\log (da/dN)-\Delta K$ curve of Al 2024-T3	32
4.8 Comparison of $a-N$ curve for different load ratios (7020-T7)	33
4.9 Comparison of $a-N$ curve for different load ratios (2024-T3)	33
4.10 Comparison of $da/dN-\Delta K$ curves for different load ratios (7020-T7)	34
4.11 Comparison of $da/dN-\Delta K$ curves for different load ratios (2024-T3)	34
4.12 SEM image of fracture surface of 7020-T7 ($R = 0.1$)	35
4.13 SEM image of fracture surface of 2024-T3 ($R = 0.1$)	36
4.14 SEM image of fracture surface of 7020-T7 ($R = 0.5$)	36
4.15 SEM image of fracture surface of 2024-T3 ($R = 0.5$)	37
4.16 Superimposed $a-N$ curve of Al 7020-T7	37
4.17 Superimposed $a-N$ curve of Al 2024-T3	38
4.18 Superimposed $da/dN-\Delta K$ curve of Al 7020-T7	38
4.19 Superimposed $da/dN-\Delta K$ curve of Al 2024-T3	39
4.20 SEM image of fracture surface showing SZW	

	of 7020-T7 ($R_{ol} = 2.5$)	40
4.21	SEM image of fracture surface showing SZW of 2024-T3 ($R_{ol} = 2.5$)	40
4.22	Fracture surface (SEM) of 7020-T7 before overload at $\Delta K = 10.61MP\sqrt{m}$	41
4.23	Fracture surface (SEM) of 2024-T3 before overload at $\Delta K = 10.25MP\sqrt{m}$	42
4.24	Fracture surface (SEM) of 7020-T7 after overload at $\Delta K = 12.32MP\sqrt{m}$	42
4.25	Fracture surface (SEM) of 2024-T3after overload at $\Delta K = 12.12MP\sqrt{m}$	43
4.26	Superimposed $a-N$ curve of Al 7020-T7	43
4.27	Superimposed $a-N$ curve of Al 2024-T3	44
4.28	Superimposed $da/dN-\Delta K$ curve of Al 7020-T7	44
4.29	Superimposed $da/dN-\Delta K$ curve of Al 2024-T3	45
4.30	SEM image of fracture surface showing SZW of 7020-T7 ($\beta = 54^\circ$)	46
4.31	SEM image of fracture surface showing SZW of 2024-T3 ($\beta = 54^\circ$)	46
4.32	Fracture surface (SEM) of 7020-T7 before overload at $\Delta K = 10.85MP\sqrt{m}$	47
4.33	Fracture surface (SEM) of 2024-T3 before overload at $\Delta K = 11.05MP\sqrt{m}$	47
4.34	Fracture surface (SEM) of 7020-T7 after overload at $\Delta K = 13.02MP\sqrt{m}$	48
4.35	Fracture surface (SEM) of 2024-T3after overload at $\Delta K = 13.56MP\sqrt{m}$	48
5.1	$a-N$ curve of Al-7020-T7	55
5.2	$a-N$ curve of Al-2024-T3	55
5.3	$da/dN-\Delta K$ curve of Al 7020-T7	56
5.4	$da/dN-\Delta K$ curve of Al 2024-T3	56

5.5	Variation of specific growth rate with crack length (7020-T7)	57
5.6	Variation of specific growth rate with crack length (2024-T3)	57
5.7	Variation of specific growth rate with number of cycles (7020-T7)	58
5.8	Variation of specific growth rate with number of cycles (2024-T3)	58
5.9	Crack length vs. number of cycle for load ratio 0.5 (7020-T7)	59
5.10	Crack length vs. number of cycle for load ratio 0.5 (2024-T3)	60
5.11	Crack growth rate vs. stress intensity range for load ratio 0.5 (7020-T7)	60
5.12	Crack growth rate vs. stress intensity range for load ratio 0.5 (2024-T3)	61
5.13	Predicted crack length vs. number of cycle for $R^{ol} = 2.35$ (7020-T7)	63
5.14	Predicted crack length vs. number of cycle for $R^{ol} = 2.10$ (2024-T3)	63
5.15	Predicted crack growth rate vs. stress intensity range for $R^{ol} = 2.35$ (7020-T7)	64
5.16	Predicted crack growth rate vs. stress intensity range for $R^{ol} = 2.10$ (2024-T3)	64
5.17	Plastic zone size definitions used in Wheeler's model	65
5.18	Superimposed $a-N$ curve of 7020-T7 (Wheeler, predicted and experimental)	67
5.19	Superimposed $a-N$ curve of 2024-T3 (Wheeler, predicted and experimental)	67
5.20	$da/dN - \Delta K$ curve of 7020-T7 (Wheeler, predicted and experimental)	68
5.21	$da/dN - \Delta K$ curve of 2024-T3 (Wheeler, predicted and experimental)	68
5.22	Comparison of predicted and experimental $a-N$ curves for 54° (7020-T7)	71
5.23	Comparison of predicted and experimental $a-N$ curves	

	for 54° (2024-T3)	71
5.24	Predicted and experimental crack growth rate for $\beta = 54^\circ$ (7020-T7)	72
5.25	Predicted and experimental crack growth rate for $\beta = 54^\circ$ (2024-T3)	72
5.26	Predicted and experimental retarded crack length for $\beta = 54^\circ$ (7020-T7)	73
5.27	Predicted and experimental retarded crack length for $\beta = 54^\circ$ (2024-T3)	73
5.28	Predicted and experimental delay cycle for $\beta = 54^\circ$ (7020-T7)	74
5.29	Predicted and experimental delay cycle for $\beta = 54^\circ$ (2024-T3)	74
6.1	ANN architecture	77
6.2	MSE curve obtained during training of ANN for AI 7020-T7	79
6.3	MSE curve obtained during training of ANN for AI 2024-T3	80
6.4	Predicted (ANN) and experimental crack growth rate for $R = 0.5$ (7020-T7)	81
6.5	Predicted (ANN) and experimental crack growth rate for $R = 0.5$ (2024-T3)	81
6.6	Predicted (ANN) and experimental number of cycle for $R = 0.5$ (7020 T7)	82
6.7	Predicted (ANN) and experimental number of cycle for $R = 0.5$ (2024-T3)	82
6.8	MSE curve obtained during training of ANN for AI 7020-T7	84
6.9	MSE curve obtained during training of ANN for AI 2024-T3	84
6.10	Predicted (ANN) and experimental crack growth rate for $R_{o1} = 2.35$ (7020-T7)	85
6.11	Predicted (ANN) and experimental crack growth rate for $R_{o1} = 2.10$ (2024-T3)	85
6.12	Predicted (ANN) and experimental number of cycle for $R_{o1} = 2.35$ (7020-T7)	86

6.13	Predicted (ANN) and experimental number of cycle for $R_{ol} = 2.10$ (2024-T3)	86
6.14	Predicted (ANN) and experimental retarded crack length (7020 T7)	87
6.15	Predicted (ANN) and experimental retarded crack length (2024-T3)	87
6.16	Predicted (ANN) and experimental delay cycle (7020-T7)	88
6.17	Predicted (ANN) and experimental delay cycle (2024-T3)	88
6.18	MSE curve obtained during training of ANN for AI 7020 T7	90
6.19	MSE curve obtained during training of ANN for AI 2024 T3	90
6.20	Predicted (ANN) and experimental crack growth rate for $\beta = 54^\circ$ (7020-T7)	91
6.21	Predicted (ANN) and experimental crack growth rate for $\beta = 54^\circ$ (2024-T3)	92
6.22	Predicted (ANN) and experimental number of cycle for $\beta = 54^\circ$ (7020-T7)	92
6.23	Predicted (ANN) and experimental number of cycle for $\beta = 54^\circ$ (2024-T3)	93
6.24	Predicted (ANN) and experimental retarded crack length (7020-T7)	93
6.25	Predicted (ANN) and experimental retarded crack length (2024-T3)	94
6.26	Predicted (ANN) and experimental delay cycle (7020-T7)	94
6.27	Predicted (ANN) and experimental delay cycle (2024-T3)	95
7.1	Fuzzy inference system	97
7.2	ANFIS architecture	99
7.3	Flow chart of ANFIS model	102
7.4	Predicted (ANFIS) and experimental crack growth rate for $R = 0.5$ (7020-T7)	105
7.5	Predicted (ANFIS) and experimental crack growth rate for $R = 0.5$ (2024-T3)	106
7.6	Predicted (ANFIS) and experimental number of cycle for $R = 0.5$ (7020-T7)	106
7.7	Predicted (ANFIS) and experimental number of cycle for $R = 0.5$ (2024-T3)	107

7.8	Predicted (ANFIS) and experimental crack growth rate for $R_{ol} = 2.35$ (7020-T7)	109
7.9	Predicted (ANFIS) and experimental crack growth rate for $R_{ol} = 2.10$ (2024-T3)	109
7.10	Predicted (ANFIS) and experimental number of cycle for $R_{ol} = 2.35$ (7020-T7)	110
7.11	Predicted (ANFIS) and experimental number of cycle for $R_{ol} = 2.10$ (2024-T3)	110
7.12	Predicted (ANFIS) and experimental retarded crack length (7020-T7)	111
7.13	Predicted (ANFIS) and experimental retarded crack length (2024-T3)	111
7.14	Predicted (ANFIS) and experimental delay cycle (7020-T7)	112
7.15	Predicted (ANFIS) and experimental delay cycle (2024-T3)	112
7.16	Predicted (ANFIS) and experimental crack growth rate for $\beta = 54^\circ$ (7020-T7)	114
7.17	Predicted (ANFIS) and experimental crack growth rate for $\beta = 54^\circ$ (2024-T3)	115
7.18	Predicted (ANFIS) and experimental number of cycle for $\beta = 54^\circ$ (7020-T7)	115
7.19	Predicted (ANFIS) and experimental number of cycle for $\beta = 54^\circ$ (2024-T3)	116
7.20	Predicted (ANFIS) and experimental retarded crack length (7020-T7)	116
7.21	Predicted (ANFIS) and experimental retarded crack length (2024-T3)	117
7.22	Predicted (ANFIS) and experimental delay cycle (7020-T7)	117
7.23	Predicted (ANFIS) and experimental delay cycle (2024-T3)	118
8.1	Error band scatter of predicted lives of 7020-T7 under CAL (R -constant)	121
8.2	Error band scatter of predicted lives of 2024-T3 under CAL (R -constant)	121

8.3	Superimposed constant amplitude $a-N$ curves of Al 7020-T7 (R -constant)	122
8.4	Superimposed constant amplitude $a-N$ curves of Al 2024-T3 (R -constant)	122
8.5	Error band scatter of predicted lives of 7020-T7 under CAL (R -varying)	124
8.6	Error band scatter of predicted lives of 2024-T3 under CAL (R -varying)	124
8.7	Superimposed constant amplitude $a-N$ curves of Al 7020-T7 (R -varying)	125
8.8	Superimposed constant amplitude $a-N$ curves of Al 2024-T3 (R -varying)	125
8.9	Error band scatter of predicted lives of 7020-T7 under mode-I overload	127
8.10	Error band scatter of predicted lives of 2024-T3 under mode-I overload	127
8.11	Superimposed mode-I overload $a - N$ curves of Al 7020-T7	128
8.12	Superimposed mode-I overload $a - N$ curves of Al 2024-T3	128
8.13	Error band scatter of predicted lives of 7020-T7 under mixed mode overload	130
8.14	Error band scatter of predicted lives of 2024-T3 under mixed mode overload	130
8.15	Superimposed mixed mode (I and II) overload $a - N$ curves of Al 7020-T7	131
8.16	Superimposed mixed mode (I and II) overload $a - N$ curves of Al 2024-T3	131
A1	Time vs. Temperature plot of set-1	154
A2	Time vs. Temperature plot of set-2	155
A3	Time vs. Temperature plot of set-3	155

LIST OF TABLES

Table	Page No.
3.1 Chemical composition of materials	17
3.2 Mechanical properties of materials	18
3.3 Load scenarios and results of CAL (set-1)	24
3.4 Load scenarios and results of CAL (set-2)	24
3.5 Load scenarios of the tested specimens under mode-I overload	24
3.6 Load scenarios of the tested specimens under mixed mode overload	25
4.1 Comparison of experimental and smoothed sets of fatigue growth data	29
4.2 Width of stretch zone for different overload ratios	39
4.3 Width of stretch zone for different overload angles	45
5.1 Curve fitting constants of Al 7020-T7	52
5.2 Curve fitting constants of Al 2024-T3	52
5.3 Curve fitting constants of 7020-T7 aluminum alloy	53
5.4 Curve fitting constants of 2024-T3 aluminum alloy	54
5.5 Constants of Forman model	54
5.6 Predicted results of CAL (Set-1)	55
5.7 Predicted results of CAL (set-2)	59
5.8 Curve fitting constants of 7020-T7 aluminum alloy	61
5.9 Curve fitting constants of 2024-T3 aluminum alloy	62
5.10 Material parameters of Paris and Wheeler model	66
5.11 Experimental results of the tested specimens	66
5.12 Curve-fitting constants of 7020-T7 alloy	69
5.13 Curve fitting constants of 2024-T3 alloy	69
5.14 Experimental results of the tested specimens	70
6.1 Performance of ANN model during training	80

6.2	Comparison of ANN model results with experimental data	82
6.3	Performance of ANN model during training	83
6.4	Comparison of ANN model results with experimental data	89
6.5	Performance of ANN model during training	91
6.6	Comparison of ANN model results with experimental data	95
7.1	Characteristics of the ANFIS network	104
7.2	Performance of ANFIS model	105
7.3	Comparison of ANFIS model results with experimental data	107
7.4	Performance of ANFIS model	108
7.5	Comparison of ANFIS model results with experimental data	109
7.6	Performance of ANFIS model	114
7.7	Comparison of ANFIS model results with experimental data	114
8.1	Model performances under CAL (<i>R</i> -constant)	120
8.2	Model performances under CAL (<i>R</i> -varying)	123
8.3	Percentage deviations of various retardation Parameters (mode-I overload)	126
8.4	Model performances under interspersed mode-I overload	126
A1	Vicker's Hardness of 7020 T7 Al alloy	154
B1	Results of constant amplitude fatigue test – 1	157
B2	Results of constant amplitude fatigue test – 2	158
B3	Results of constant amplitude fatigue test – 3	158
B4	Results of constant amplitude fatigue validation tests	159

NOMENCLATURE

a	crack length measured from edge of the specimen (mm)
a_i	crack length corresponding to the ' i^{th} ' (initial) step (mm)
a_j	crack length corresponding to the ' j^{th} ' step (mm)
a_d	retarded crack length (mm)
a^{ol}	crack length at overload (mm)
a_d^{A}	retarded (ANN) crack length (mm)
a_d^{P}	retarded (exponential) crack length (mm)
a_d^{AN}	retarded (ANFIS) crack length (mm)
a_d^{W}	retarded (Wheeler) crack length (mm)
a_d^{E}	retarded (experimental) crack length (mm)
A, B, C	fuzzy sets
A', B', C', D'	curve fitting constants in the Exponential Model
A_j, B_k, C_m	linguistic labels
b	magnitude of burger vector
B	plate thickness (mm)
'cgr'	crack growth rate
c_1	constant in the Walker equation
C	constant in the Paris equation
C_a	constant in the Forman equation
C_b	constant in the Walker equation
$(C_p)_i$	retardation parameter
COD	crack opening displacement
da/dN	crack growth rate (mm/cycle)
$(da/dN)_{\text{retarded}}$	retarded crack growth rate (mm/cycle)
E	Young's modulus of elasticity (MPa)
E_{rr}	sum-squared error

f	linear consequent function of TSK model
$f(g)$	geometrical factor
$f(\cdot)$	activation function
F	remotely applied load (N)
ΔF	remotely applied load range (N)
F_{\max}	maximum load of constant amplitude load cycle (N)
$F_{\max(ol)}$	maximum load at overload (N)
F_{\min}	minimum load of constant amplitude load cycle (N)
K	stress intensity factor (MPa \sqrt{m})
ΔK	stress intensity factor range (MPa \sqrt{m})
K_{op}	opening stress intensity factor (MPa \sqrt{m})
K_{th}	threshold stress intensity factor (MPa \sqrt{m})
ΔK_{eff}	maximum stress intensity factor (MPa \sqrt{m})
K^{ol}	stress intensity factor at overload (MPa \sqrt{m})
K_I^{ol}	mode-I stress intensity factor at overload (MPa \sqrt{m})
K_{II}^{ol}	mode-II stress intensity factor at overload (MPa \sqrt{m})
K_C	plane stress fracture toughness (MPa \sqrt{m})
K_{IC}	plane strain fracture toughness (MPa \sqrt{m})
K_{eq}^{ol}	equivalent stress intensity factor (MPa \sqrt{m})
K_{\max}^B	maximum stress intensity factor at base line test (MPa \sqrt{m})
$\frac{K_{II}}{K_I + K_{II}}$	mode-mixity
L	dimensionless factor in the ‘Exponential Model’ formulation
‘lay’	layer number
‘MM’	mode-mixity
‘msif’	maximum stress intensity factor
M	specific growth rate
m_{ij}	specific growth rate in the interval i - j

n	exponent in the Paris equation
n_a	exponent in the Forman equation
n_b	exponent in the Walker equation
N	number of cycles or fatigue life
N_i	number of cycles corresponding to the ' i^{th} ' step
N_j	number of cycles corresponding to the ' j^{th} ' step
N_d^A	number of delay cycle (ANN)
N_d^P	number of delay cycle (exponential)
N_d^E	number of delay cycle (experimental)
N_d^{AN}	number of delay cycle (ANFIS)
N_d^W	number of delay cycle (Wheeler)
N_f^A	final number of cycles (ANN)
N_f^{AN}	final number of cycles (ANFIS)
N_f^F	final number of cycles (Forman)
N_f^P	final number of cycles (exponential)
N_f^E	final number of cycles (experimental)
o, p, q, r	consequent parameters
'olr'	overload ratio
P_r^{AN}	prediction ratio of ANFIS model
P_r^P	prediction ratio of exponential model
P_r^A	prediction ratio of ANN model
P	shaping exponent in the Wheeler model
r	label for r^{th} neuron in hidden layer 'lay-1'
r_{pi}	current plastic zone size corresponding to the ' i^{th} ' cycle (mm)
r_{po}	overload plastic zone size (mm)
R	load ratio
R^{ol}	overload ratio

S_1, S_2, S_3	universe of discourse of three input variables
s	label for s^{th} neuron in the hidden layer ‘lay’
‘sifr’	stress intensity factor range
t	iteration number
w	plate width (mm)
w_i	firing strength
$W_{sr}^{\{\text{lay}\}}$	weight of the connection from neuron r in layer ‘lay-1’ to neuron s in layer ‘lay’
x_1, x_2, x_3	input variables of ANFIS
$X_1 \dots X_4, Y_1 \dots Y_4$ and $Z_1 \dots Z_4$	curve fitting constants in the ‘Exponential Model’
y_1, y_2, y_3	inputs to the ANN
ω	exponent in the Frost and Dugdale law
α	momentum coefficient
α_1	ratio of mode-I and mode-II plane stress fracture toughness
β	loading angle
θ_{actual}	neural network output
θ_{desired}	desired output
η	learning rate
$\delta_s^{\{\text{lay}\}}$	local error gradient
γ	retardation correction factor
λ	plastic zone correction factor
ν	Poisson’s ratio
$\mu_{A_j}(x_1), \mu_{B_k}(x_2), \mu_{C_m}(x_3)$	membership grade functions
β_{IC}	fracture toughness correlation factor
σ_{ys}	yield point stress (MPa)
σ_{ut}	ultimate stress (MPa)

PUBLICATIONS (IN PEER REVIEWED JOURNALS) ARISING FROM THIS DISSERTATION

Papers published/accepted

- [i] J. R. Mohanty, B. B. Verma, and P. K. Ray, "Determination of fatigue crack growth rate from experimental data: A new approach," *Int. J. of Micro-struct. and Mats. Prop.*, Inderscience, Accepted, Ref. No. IJMMP-119/08.
- [ii] J. R. Mohanty, B. B. Verma, and P. K. Ray, "Prediction of fatigue crack growth and residual life using an exponential model: Part I (constant amplitude loading)," *Int. J. of Fat.*, Elsevier, vol. 31, pp. 418-424, 2009.
- [iii] J. R. Mohanty, B. B. Verma, and P. K. Ray, "Prediction of fatigue crack growth and residual life using an exponential model: Part II (mode-I overload induced retardation)," *Int. J. of Fat.*, Elsevier, vol. 31, pp. 425-432, 2009.
- [iv] J. R. Mohanty, B. B. Verma, and P. K. Ray, "Prediction of fatigue life with interspersed mode-I and mixed mode (I & II) overloads by an exponential model: Extensions and Improvements," *Engg. Fract. Mech.*, Elsevier, vol. 76, pp. 454-468, 2009.
- [v] J. R. Mohanty, B. B. Verma, and P. K. Ray, "Evaluation of Overload-induced Fatigue Crack Growth Retardation Parameters using an Exponential Model," *Engg. Fract. Mech.*, Elsevier, vol. 75, pp. 3941-3951, 2008.

Papers communicated

- [vi] J. R. Mohanty, B. B. Verma, and P. K. Ray, "Prediction of constant amplitude fatigue life of aluminum alloys under the influence of load ratio effects," *Int. J. of Micro-struct. and Mats. Prop.*, Inderscience, Communicated after complying with reviewers' comments, Ref. No. IJMMP-119/08.

- [vii] J. R. Mohanty, B. B. Verma, P. K. Ray, and D. R. K. Parhi, "Application of artificial neural network for fatigue life prediction under interspersed mode-I spike overload," J. of Test. and Evaluat., ASTM, Communicated after complying with reviewers' comments, Ref. No. JTE101907-08.

- [viii] J. R. Mohanty, B. B. Verma, P. K. Ray, and D. R. K. Parhi, "Application of adaptive neuro-fuzzy inference system in modeling fatigue life under interspersed mode-I overload," Expert System and Applications, Elsevier, Under review, Ref. No. ESWA-D-09-00153.

- [ix] J. R. Mohanty, B. B. Verma, P. K. Ray, and D. R. K. Parhi, "Prediction of residual fatigue life under interspersed mixed mode (I and II) overloads by Artificial Neural Network. Fat. Fract. Engg. Mat. Struct., Blackwell, Under review,

- [x] J. R. Mohanty, B. B. Verma, P. K. Ray, and D. R. K. Parhi, "Application of adaptive neuro-fuzzy inference system in modeling fatigue life under interspersed mixed-mode (I and II) spike overload," Engg. Struct., Elsevier, Under review, Ref. No. ENGSTRUCT-D-08-00872.

- [xi] J. R. Mohanty, B. B. Verma, P. K. Ray, and D. R. K. Parhi, "Prediction of fatigue crack propagation life of aluminum alloys under constant amplitude loading using ANFIS," Int. J. of Comput. Mats. Sci. and Surface Engg., Inderscience, To be communicated.

- [xii] J. R. Mohanty, B. B. Verma, P. K. Ray, and D. R. K. Parhi, "Application of artificial neural network for Predicting fatigue crack propagation life of aluminum alloys," Int. J.of Comput. Mats. Sci. and Surface Engg., Inderscience, Under review.

CHAPTER I

INTRODUCTION

1.1 Background

Realistic fatigue life prediction of engineering structures and components is of prime importance from economic and safety point of view. Conventional life prediction procedures are generally based on the safe-life approach. In this approach, components of a structure are replaced when the probability of failure reaches a prescribed level, even though some of them may have a significant residual life. Hence, it is a highly conservative approach coupled with a penalty on economy. To avoid this, the damage-tolerant approach is often a suitable alternative for life predictions.

Most load bearing structures and components are subjected to variable amplitude loading (VAL) rather than constant amplitude loading (CAL) during their service. The simplest type of VAL is the occurrence of high peak loads interspersed in constant amplitude loading (CAL). An aircraft experiences overload cycles during gust. Ships and offshore structures come under high load cycles during certain period. An overload induces retardation and significantly enhances the fatigue life.

During the growth of a fatigue crack, load excursion in the form of a single tensile overload may occur either in mode I or mixed-mode (mode I and II). Mixed-mode overloads are common in case of aircraft structures, turbine shafts, railroads, angled cracks in pressure vessels, pressure cabins, welds etc. It has been verified [1, 2] that a pure mode-I overload leads to maximum retardation, while mode-II overload has least effect on retardation.

Several interaction and non-interaction life prediction models have been proposed based on different loading conditions. Most of the deterministic crack growth models relate the crack growth rate information with fracture mechanics parameters. Once the model equation is formulated, the next step is to estimate the cyclic life using cycle-by-cycle integration. It complicates the calculation process because of the involvement of a robust numerical integration scheme. The integration approach adopted should be able to accommodate the evaluation of arbitrary crack shape as well as take into account the effects of load interactions. Before formulating any crack growth model, it is necessary to

determine the fatigue crack growth rate (da/dN) from the experimental $a-N$ data, which has large scatter.

Therefore, the first objective of the present work is to evolve a methodology to determine the fatigue crack growth rate from the generated $a-N$ data and subsequently to formulate a model for predicting the remaining fatigue life without any complex integration scheme. This has been achieved by fitting an exponential equation to the raw $a-N$ data which facilitates in determining the fatigue crack growth rate. The second objective has been accomplished by proposing an *exponential model* to estimate the fatigue life under both constant amplitude loading, and constant amplitude loading interspersed with mode-I and mixed-mode (I and II) spike overload. Further, two soft-computing techniques, i.e. Artificial Neural Network (ANN) and Adaptive Neuro-Fuzzy Inference System (ANFIS), have been formulated and their predicted results have been compared quantitatively with that of the proposed exponential model.

1.2 Objectives

The objectives of the present work are:

- To conduct crack growth tests of two aluminum alloys (7020-T7 and 2024-T3) under the following loading conditions:
 - (a) Constant amplitude loading with and without load ratio effect
 - (b) Constant amplitude loading interspersed with spike overload in mode-I
 - (c) Constant amplitude loading interspersed with spike overload in mixed-mode (I and II)
- To evolve a method of smoothening and reducing the scatter of experimental $a-N$ data thereby simplifying the calculation of crack growth rate.
- To propose an *exponential model* (with physical interpretation) to estimate the residual fatigue life under the above mentioned loading conditions.
- To implement two soft-computing techniques (ANN and ANFIS) for fatigue life prediction and compare the predicted life estimates by exponential model with these predicted results.

The overall plan of the work can be visualized from Fig. 1.1.

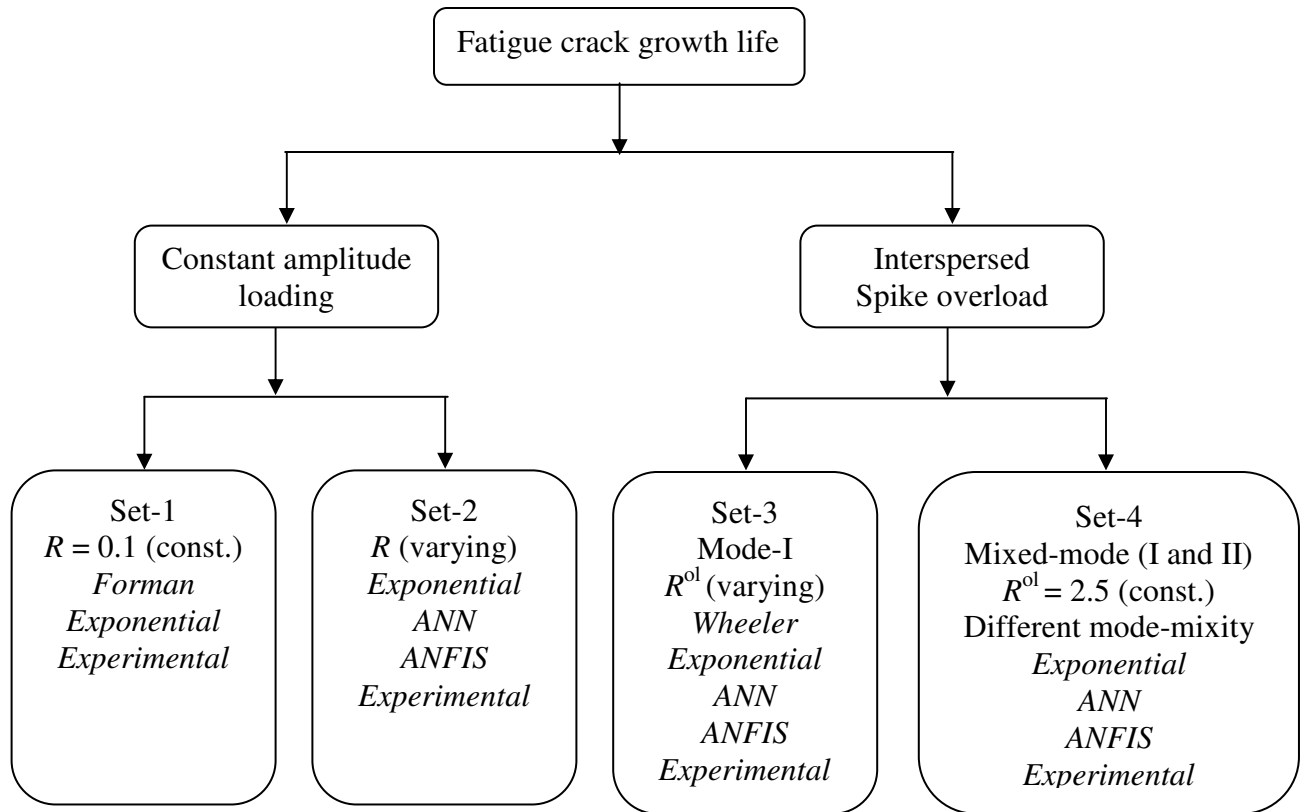


Fig. 1.1– Plan of the work

1.3 Thesis structure

The contents of this investigation are presented through nine chapters whose overall structure has been diagrammatically represented in Fig. 1.2. The first two chapters present an introduction and a brief review of literature. Chapter-3 and 4 describes the details of experimental procedure and their results respectively. Chapter-5 presents the formulation of the proposed *exponential model* along with the model results under different loading conditions. Chapter-6 and 7 are respectively devoted to the formulation of two soft-computing models (i.e. ANN and ANFIS) and the model results. Chapter-8 quantitatively compares the different model results with the experimental data presented in Chapter-3. A general discussion has also been presented in this chapter along with the relative merits and demerits of various models. Finally, concluding remarks and a discussion of possible future work is given in Chapter-9.

CHAPTER II

LITERATURE SURVEY

2.1 Introduction

Several models have been proposed till date in order to predict fatigue crack propagation life under different loading conditions. This chapter briefly reviews the types of conventional and non-conventional life prediction models under three loading conditions: (i) constant amplitude loading with and without load ratio effect, (ii) constant amplitude loading interspersed with spike overload in mode-I and (iii) constant amplitude loading interspersed with spike overload in mixed-mode (I and II). The advantages and limitations of the models have been briefly discussed alongwith a comprehensive summary of the previous work done.

2.2 Life prediction models

Reliable estimation of fatigue crack propagation and residual life prediction are important for designing structures against fatigue. Numerous attempts have been made in developing fatigue crack growth models for constant amplitude loading (CAL) as well as variable amplitude loading (VAL). Every model has its own merits and demerits and applies to specific loading conditions. However, no model has yet been proposed which could fit all the situations. Further, most of the prediction models are based on integration of a crack growth rate equation in order to determine the fatigue life. It limits their applicability because of the involvement of robust and complicated integration scheme. Despite of various shortcomings, the research on fatigue is under constant improvement in developing life prediction models to avoid accidental failures of structures and machine components.

2.2.1 Life prediction models under constant amplitude loading

Many investigators have put forth different life prediction models to predict residual life in case of constant amplitude loading. These models are mainly based on following four approaches [3]:

- a simplified approach that involves one estimate for long life, one for short life, and interpolation between these two
- a simplified approach to low cycle fatigue
- a two stage approach in which the life to the appearance of visible cracks is estimated from local strain considerations and the life from appearance of small cracks to final fracture is estimated from crack growth considerations
- a pre-existing crack, and therefore only crack growth is considered

The existence of a fatigue crack growth threshold was first postulated by McClintock [4]. He mentioned that fatigue crack growth occurs when a critical value of local strain or accumulated damage over certain characteristic distance ahead of the crack-tip reaches a critical value. Frost [5] exhibited experimental evidence supporting the existence of a fatigue threshold when the value of the empirical characterization parameter, $\sigma_a^3 a$ (where, ' σ_a ' is the stress amplitude and ' a ' is the crack length) attained a critical value. With the advent of fracture mechanics and its application to characterize fatigue crack growth, it soon became apparent, particularly with the work of Paris et.al. [6] and Schmidth and Paris [7], that the threshold for the non-propagating long fatigue cracks can be associated with a critical stress intensity factor range, ΔK_{th} . Sadananda and Shahinian [8] proposed that the threshold for crack growth is reached when the shear stress, τ required to nucleate and move a dislocation from the crack-tip reaches a critical value. This criterion led to the result that

$$\Delta K_{th} \propto \tau \sqrt{b} \quad (2.1)$$

where, ' b ' is the magnitude of the burger vector.

The Region-I crack propagation occurs along the plane of maximum shear stress. However, in Region-II it follows along the plane of maximum tensile stress.

Most of the current application of LEFM concepts to describe crack growth behavior is associated with Region-II. In this region the slope of the log (da/dN) versus log (ΔK) curve is approximately linear. The most notable and basic model proposed by Paris in the early 1960's, is

$$\frac{da}{dN} = C(\Delta K)^n \quad (2.2)$$

where C and n are material constants, and ΔK is the stress intensity factor range given by $K_{\max} - K_{\min}$

Several other models are also available in the literature. They can be broadly classified into two categories; (i) geometrical models [9-11] based on the crack-tip displacement, and (ii) damage accumulation models [4, 12] based on strains or plastic work at the crack tip.

In Region-III, unstable crack growth occurs which is sensitive to both microstructures and mean stresses due to the occurrence of static fracture modes such as cleavage, inter-granular fracture etc. In many practical engineering situations this region may be ignored because it does not significantly affect the total crack propagation life. The point of transition from Region-II to Region-III behavior depends on the yield strength of the material. Many semi-empirical and empirical models have been proposed to take into account the load ratio effects and also the growth behavior in the final failure regions. The most widely used models are proposed by Forman et al. [13] and Walker [14]. These two models are expressed as follows:

$$\frac{da}{dN} = \frac{C_a (\Delta K)^{n_a}}{(1-R)K_c - \Delta K} \quad (\text{Forman et al. model}) \quad (2.3)$$

$$\text{and } \frac{da}{dN} = C_b [(1-R)^{c_1} K_{\max}]^{n_b} \quad (\text{Walker model}) \quad (2.4)$$

This stage of crack extension accounts for a small fraction of the fatigue life.

From the above discussion it is evident that Region-II has received the maximum attention as it involves considerable proportion of the life in a cracked body.

2.2.2 Life prediction models under variable amplitude loading

Most load bearing structural components are subjected to variable amplitude loading (VAL) rather than constant amplitude loading (CAL) during their service. The simplest type of VAL is the occurrence of high peak loads interspersed on constant amplitude loading. An aircraft experiences overload cycles during gust. Ships and offshore

structures come under high load cycles during certain period. An overload induces retardation and significantly enhances the life of the structures.

Interspersed mode-I spike overload

Several attempts have been made in developing fatigue crack growth models for variable amplitude loading particularly in case of single spike mode-I overload. These models are mainly divided into two major groups, namely the characteristic methods and the cycle-by-cycle methods.

The models of the first group are based on the similitude concept of the crack-tip field being describable in terms of the root-mean-square value of the stress intensity factor. It assumes that the average crack growth rate in variable amplitude fatigue can be predicted from constant amplitude fatigue data. Barsom's model [15] is an example which is given by the equation:

$$\frac{da}{dN} = C_c (\Delta K)_{\text{rms}}^{n_c} \quad (2.5)$$

$$\text{where, } \Delta K_{\text{rms}} = \left[\frac{1}{n} \sum_{i=1}^n \Delta K_i^2 \right]^{\frac{1}{2}}$$

In the second group of models, consequences of each cycle are added together to predict the overall fatigue life. They may be divided into three main categories namely:

- Yield zone model
- Strip yield model
- Crack closure model

Yield zone model

The basic examples of yield zone models are those proposed by Wheeler and Willenborg. Newman has discussed merits and demerits of some popular yield zone models in his review paper [16]. The retardation model proposed by Wheeler [17] predicts the overload induced crack growth rate by incorporating a factor in the constant amplitude crack growth rate. The Willenborg models [18-22] on the other hand are based on effective stress intensity factor (being reduced by residual compressive stress) without considering any empirical parameters. However, these models do not consider crack growth acceleration due to underloads or immediately following an overload. The yield-zone

models proposed by Chang and Hudson [23], Gallagher [24], Chang et.al. [25] and Johnson [26] took care of both retardation and acceleration. In addition to these, there are other yield zone models which are modifications of original Wheeler and Willenborg models. The details of their merits and limitations have been discussed by Yuen and Taheri [27].

Strip yield model

The strip yield model was initially proposed by Dugdale [28]. The basic assumptions are that for a thin sheet in tension. The plastic region is envisioned as a narrow strip of a non-zero height lying along the crack line and the plastic yielding in the crack-tip together with the residual deformations in the wake influence the crack surface displacements that are used to calculate the closure stresses. The modifications to Dugdale's model include the addition of plastically deformed material in the wake of the crack to account for the crack closure. Strip yield models use discretised elements in order to analyze the effects of individual load and therefore, do require extensive computational capacity for cycle-by-cycle computing. Various strip yield models with their merits and limitations have been discussed by Newman [16].

Crack closure models

The crack closure models are based on closure mechanism proposed by Elber [29]. He suggested that a fatigue crack can only grow if it is fully open. As the crack grows a tensile plastic deformation left in the wake of crack reduces the range of the applied stress for crack propagation. The important task of these models is the determination of crack opening stress required in calculating the effective stress intensity factor (ΔK_{eff}). The accuracy of the models depends on the measurement of crack opening stress, which can be obtained either experimentally [30-32] or by finite element method [33, 34]. There are other crack closure models, where crack opening stress intensity factor (K_{op}) is determined analytically cycle-by-cycle. These models include PREFAS-model [35, 36], the ONERA-model [36, 37] and the CORPUS-model [36, 38].

Although the concept of crack closure was widely used in modeling fatigue life but it was later criticized by several investigators [39, 40] one of the limitations being closure solely depends upon the R-ratio and there is no single equation that could describe closure

in all the three regions. Further, in case of overloads, Sadananda et al. [41] critically examined the closure phenomenon in the context of Unified Approach and suggested that it has negligible contribution behind the crack tip.

Interspersed mixed-mode (I and II) spike overload

Before going further into the content of life prediction models under mixed-mode (I and II) spike overload, it is worth to give some insight to general mixed-mode crack growth both in monotonic as well as cyclic loading. Several structures and components contain randomly located cracks which are in mixed-mode due to their orientation with respect to the loading axis. Sometimes the direction of loading axis may change with respect to the crack geometry leading to mixed-mode condition. A number of mixed-mode situations include aircraft structures, cracked bars in torsion and bending, welds containing defects, pressure vessel nozzles, cracked rotating turbine blades, angled cracks in pressure cabins, rolling contact problem in high speed rotating bearing etc. In mode-I, the direction of crack propagation is perpendicular to the loading axis and it propagates in a self-similar manner due to symmetry, whereas in mixed-mode cases, a fatigue crack tends to grow in a non-self similar manner resulting in changes in the direction of crack propagation during the loading period.

Mixed-mode cracks may be subjected to monotonic or cyclic (fatigue) loading. Qian and Fatemi [42] in their review paper have discussed various criteria and parameters for mixed-mode crack growth directions and rates. The mixed-mode (I and II) fatigue was primarily studied by Iida and Kobayashi [43]. Later Roberts and Kibler [44] proposed the empirical relations for mixed-mode loading. Tanaka [45] put forward an effective stress intensity factor (ΔK_{eff}) to correlate with fatigue crack growth rate (da/dN) in case of mode-I and II loading. Richard [46, 47] has proposed another effective stress intensity factor considering fracture toughness in case of mixed-mode (I and II) loading. Patel and Pandey [48] suggested that the stress intensity factor, the crack-tip opening displacement (CTOD) and the J-integral are not suitable to handle the mixed-mode crack growth problems. They have correlated fatigue crack growth rate with strain energy density factor range for mixed-mode loading. In another development, an equivalent strain energy density factor range has been proposed by Socie [49] to correlate the small crack growth data for SAE 1045 steel

and Inconel 718 under mixed-mode loading. Reddy and Fatemi [50] have suggested another form of effective strain based intensity factor range to correlate the small fatigue crack growth data of same materials under bi-axial loading conditions. Chen and Keer [51] have given an alternative prediction method based on Dugdale's model. The details of different methods have been presented by Tamilselvan et al. [52] and Kim et al. [53].

In addition to the determination of effective stress intensity factor and strain energy density factor to model mixed-mode fatigue crack growth, some other aspects of mixed-mode fatigue have been discussed by different investigators [54-57]. Borrego et al. [54] have analyzed the closure effects on loading angle and K_I/K_{II} ratio experimentally as well as using a finite element method on Al MgSi – T6 Al-alloy. Bemrahou et al. [55] have estimated the size of plastic zone at the crack-tip under mode-I, mode-II and mixed-mode (I & II) both experimentally and analytically in accordance with Von Mises and Tresca criteria. Ma et al. [56] have investigated the effect of loading angle on crack growth rate under mixed-mode loading and developed a numerical model by considering the loading mode and the residual stresses developed during welding. Dahlin and Olsson [57] have observed that there is a reduction of mode-I crack growth rate after a mode-II load cycle mainly due to mode-II induced roughness crack closure.

Srinivas and Vasudevan [58] studied the effect of mixed-mode overload on subsequent mode-I fatigue crack growth of D16AT Al-alloy and concluded that retardation following a mode-I overload was found to be of considerable effect compared to mode-II or mixed-mode (I & II) overloads. Biner [59] in his mixed-mode fatigue crack growth investigation observed that overload crack closure concept was found to be inadequate to fully describe the observed growth behavior under mixed-mode loading. Sander and Rechard [1, 2] have given intensive investigation on the effects of mixed-mode (I & II) overloads on subsequent mode-I fatigue crack growth both experimentally and numerically. They found experimentally that the retardation effect decreased with an increasing amount of mode-II component. Although several investigations have been done in this area, no serious attempt has been made to predict crack growth rate and end life of the components subjected to interspersed mixed-mode (I and II) overload on subsequent mode-I fatigue crack growth.

2.2.3 Non-conventional life prediction models

Problems associated with fatigue are difficult to solve using conventional mathematical models because of non-linearity, noise, cost, time constraint and above all the associated micro-mechanisms. Soft-computing is a good alternative for handling those complex problems as it is tolerant of imprecision, uncertainty and partial truth. The soft-computing methods are always appreciated when the methods based on traditional mathematical models have not produced satisfactory results or their application is too complex and expensive. Soft-computing techniques provide rich knowledge representation, flexible knowledge acquisition, and knowledge processing which enable intelligent process control systems to be constructed at low cost. The application of soft-computing techniques in solving non-linear complex problems, particularly in material diagnosis and life assessment for critical components and nuclear applications has been increasing during the last few years. The main techniques in soft-computing are artificial neural network (ANN), genetic algorithm (GA), fuzzy logic and adaptive neuro-fuzzy inference system (ANFIS).

Prediction of fatigue life by Artificial Neural Network (ANN)

Artificial neural network (ANN) is a class of computational intelligence system, useful to handle various complex problems with a capacity to learn by examples. The first ANN concept was adopted by McCulloch and Pits [60] in 1943, who suggested the cell model. Although some pioneer work was undertaken in 1949 [61] by focusing attention on the learning system of human brain, the actual development on ANN concept started towards 1980 through various studies [62]. It has emerged as a new field of soft-computing to deal with many multivariate complex problems for which an accurate analytical model does not exist [63-65]. Artificial neural networks (ANN) have proved to be a powerful and versatile soft-computing method which is quite efficient in modeling complex linear and non-linear relationships in a number of engineering fields [66-71]. In recent years, ANN finds its application in the field of fatigue for various purposes [72-79].

Genel [80] applied ANN for predicting the strain-life fatigue properties using tensile material data of steels. Satisfactory results with ANN were obtained to estimate $S-N$ curves (constant amplitude loading) for the nominal stress concept [73, 81, 82], which

exceed the quality of the approximation results of conventional methods. Later, it has been applied by Marquardt and Zenner [83] for lifetime calculation under variable amplitude loading on the basis of a linear damage accumulation in accordance to Palmgren and Miner rule. Fotovati and Goswami [84] have used ANN approach to predict fatigue crack growth rate in Ti-6Al-4V alloy at elevated temperature. They reported a least square error of 0.03 with experimental findings. A precise but useful literature survey regarding the application of ANN in the field of fatigue has been made by Jia and Davalos in their research paper [85].

Prediction of fatigue life by adaptive Neuro-Fuzzy Inference System (ANFIS)

Earlier, *crisp mathematical system* was applied in modeling linear time-invariant system into numerous scientific and technical areas. However, many complex non-linear systems remain beyond the reach of the said theory. Zadeh's innovative concept [86] for modeling the mechanism of human thinking with *linguistic fuzzy* values rather than crisp number led to *fuzzy systems*. The *fuzzy logic system* (FLS) achieved much attention in handling both numerical data and linguistic information simultaneously leading to fuzzy system modeling.

Two primary tasks are basically involved in fuzzy system modeling. The first one is structure identification and the second is parameter adjustment. In the early approaches, these were performed by *trial and error*. Since then, gradual research in this recently developed area has been undertaken to search for new hybrid integrated systems. This is done in order to systematize the above two tasks [87]. The best way of applying learning technique for parameter identification of fuzzy models is by hybrid neuro-fuzzy method. Such neuro-fuzzy models are currently a very active area of research [88]. A brief history of the model has been presented by Engin et al [89]. Till date, several neuro-fuzzy models have been reported in the literature [90-96]. Jang [93, 94] used an adaptive neuro-fuzzy inference system (ANFIS) for the adjustment and identification of the parameters of a Takagi-Sugeno-Kang (TSK) [95] fuzzy model. Rahouyi et al [96] presented an application of ANFIS for the modeling of microwave devices.

Different soft-computing techniques are being introduced in the field of fatigue to handle subjective uncertainties in a quantitative way. Fuzzy set theory has been used to

analyze the $S-N$ curves and predict fatigue life [97-99]. Wu et al. [100] applied fuzzy regression analysis to determine the fatigue crack growth rate under constant and random amplitude stress. Jarrah et al. [101] applied ANFIS to model the fatigue behavior of unidirectional glass fiber / epoxy composites under tension-tension and tension-compression loading. Vassilopoulos and Bedi [102] used ANFIS to model fatigue behavior of a multidirectional composite laminate.

2.3 Summary and the justification of the proposed model

The science of fatigue crack growth has been evolved since 1960s by correlating fatigue crack growth rate with stress intensity factor range. Later in the seventies, the concept of crack closure was used successfully and widely in modeling fatigue life. However, in the later stage the popularity of this concept was criticized due to some of its limitations as discussed in section 2.2.2. These shortcomings pave the way to search for an alternative approach to predict fatigue crack growth rate particularly in case of single tensile overload. Subsequently a modern approach was evolved to include load ratio, short cracks, shielding of dislocations, overloads/underloads, surface cracks etc. at a time for fatigue model formulation. This is termed as *the Unified Approach* [41, 103-107], which has proved its potentiality in providing superior quality life prediction methods.

It is generally considered that the most fundamental and widely used fatigue crack growth equation is the Paris-Erdogan relation [108] from which most of the differential form of the fatigue crack growth model proposed so far are based. However, it has some limitations as observed in literature [109, 110]. Spagnoli [109] analyzed the Paris-Erdogan relation on the basis of both similarity methods and fractal concepts and presented some experimental evidence of its breakdown of similitude concept. He observed that the complete self-similarity (corresponding to no crack-size dependence of $da/dN-\Delta K$ relationship) of Paris-Erdogan relation is only possible for larger cracks. In case of small cracks (for micron-sized crack) and in heterogeneous materials like concrete, the crack growth rate depends on crack size leading to incomplete self-similarity (non-self similar). Jones et al. [111] have also questioned the validity of similitude hypothesis in Region I and lower portion of Region II of crack growth. Pearson [112] and Pell et al. [113] also

conformed that fracture mechanics based tools applicable for determination of macroscopic crack growth data had difficulty in predicting crack growth of small micron sized flaws. Further, Maymon [110] observed that a physical inconsistency occurs when the constants of the crack growth rate equation of Paris model are randomized as per dimensional analysis point of view. All these deficiencies may be partially overcome [114] by the log-linear relationship crack growth law proposed by Frost and Dugdale [115] much before the work of Paris. However, the law was able to predict crack growth only for small micron-size flaws on a cycle-by-cycle basis in full-scale aircraft fatigue tests and in an extensive range of coupon tests [116-119]. However, this holds good in Region I and the lower portion of Region II of the crack growth rate curve. One of the fundamental problems concerning the above models is the quantification of the mean stress effect.

The ultimate aim of fatigue crack growth models is to establish a suitable means to predict the residual fatigue life of engineering structures. Usually, the experimental test results in fatigue are noisy and random in nature, although repeated trends are observed. A good prediction of the fatigue crack growth behavior can only be obtained by a stochastic rather than a deterministic differential equation model [120, 121]. However, the very purpose of a scientific model is that it must be simpler and faster to apply with some physical meaning during its solution process. The fatigue life predictions in general, have low accuracy and may vary as much as 10:1 or even more for the same loading condition and material [3]. An error of $\pm 1\%$ in stress intensity factor range can result in an error of -3.5% to +3.7% in fatigue life estimate. The discrepancies may be even more dramatic for initial cracks near the fatigue threshold [122]. The prediction methodology becomes more complex in case of transient load spectra as the micro-mechanisms of fatigue are not yet understood. It has been observed that significant ambiguity and disagreement exist in terms of exact mechanisms involved in estimating the fatigue life. As already mentioned, several life prediction models have been proposed till date considering different load interaction mechanisms. However, each model has its own capabilities and limitations as discussed by Murthy et al. [123]. There is no universal and all encompassing model that has been proposed so far which would incorporate all mechanisms at a time or would be applicable

to all situations. The following conclusions can be drawn regarding the prediction methodology:

1. Each and every crack growth analysis involves the use of fracture mechanics parameters. Once these parameters are estimated precisely, it is to be translated for obtaining crack growth rate. In a closed form method, cycle-by-cycle integration is required to estimate the fatigue life of the components/structures. The integration methods should be able to accommodate the evaluation of an arbitrary/non-planar crack which creates a topological problem for the numerical methods. Further, the residual stresses and load interaction effects create additional problems for which a robust and complex integration scheme is required.
2. The lack of similitude hypothesis in Region-I (i.e. threshold region) underpins most of the current crack growth models. The prediction of fatigue life in case of small micron-sized cracks is difficult by using macroscopic crack growth law.
3. As far as Paris-Erdogan differential equation crack growth model is concerned, there are two significant limitations. Firstly, it shows physical inconsistency while randomizing the constants of the model as per dimensional analysis point view. Secondly, in case of micron-sized cracks and for heterogeneous materials, crack-size dependence of $da/dN-\Delta K$ relationship (incomplete self-similarity) is observed restricting the application of Paris-Erdogan crack growth model.
4. As per the *Unified Approach*, fatigue is fundamentally a two-parameter problem since there are two crack driving forces K_{max} and ΔK required for fatigue crack growth, in contrast to the earlier approach where a single crack driving parameter ΔK was considered sufficient to describe the fatigue crack growth rate.
5. As far as load interaction is concerned, several mechanisms may be responsible for retardation. Based on these facts, a number of investigators have proposed different retardation models but none of them has definitive advantages over the others. It has also been visualized that none of these models has universal acceptance in all transient situations in terms of the dominant mechanisms involved. Therefore, a model should be calibrated by experimental data fitting to encompass all the mechanisms that induce retardation effects [124].

6. During the growth of a fatigue crack, load excursion in the form of a single tensile overload may occur either in mode I or mixed-mode (mode I and II). Most of the available retardation models deal only with mode-I overload situations. No serious attempt has been made to predict crack growth rate and end life of components subjected to interspersed mixed-mode (I and II) overload.

The objective of the present work is to propose a model for the prediction of fatigue life. An attempt has been made to make it universalized by including different loading situations i.e. constant amplitude loading with and without load ratio effect, constant amplitude loading interspersed with spike overload in mode-I and constant amplitude loading interspersed with spike overload in mixed-mode (I and II). The prediction results of the model have been compared with two soft-computing methods i.e. ANN and ANFIS in order to obtain its performance characteristic.

CHAPTER III

EXPERIMENTAL INVESTIGATIONS

3.1 Introduction

The fatigue crack growth tests under different loading conditions (i.e. constant amplitude loading; constant amplitude loading interspersed with mode-I and mixed-mode overload) were conducted on 7020-T7 and 2024-T3 aluminum alloys. All the tests were performed in a servo-hydraulic dynamic testing machine (*INSTRON*-8502) using single edge notch tension (SEN) specimens under load control mode. A mixed-mode holding fixture was fabricated and used to overload the specimens at different loading angles (18°, 36°, 54°, 72° and 90°). Before conducting the tests, crack coefficients were determined for SEN specimens in order to measure the crack length by compliance method with the help of a COD gauge.

3.2 Test specimens and accessories

3.2.1 Material

For this investigation, two aluminum alloys i.e. 7020 and 2024 were selected. 7020 aluminum alloy suitable for ground transport systems was procured in as-fabricated condition whereas, 2024 aluminum alloy, an aircraft structural material was procured in T3 condition. The chemical compositions of aluminum alloys under investigation are presented in Table 3.1.

Table 3.1 – Chemical composition of materials

Materials	Al	Cu	Mg	Mn	Fe	Si	Zn	Cr	Others
(% wt.)									
7020-T7	93.13	0.05	1.20	0.43	0.37	0.22	4.60	-	-
2024-T3	92.78	3.90	1.50	0.32	0.50	0.50	0.25	0.10	0.15

The as-fabricated 7020 Al alloy was subjected to T7 heat treatment. The details of its procedure has been presented in Appendix-A. The tensile properties and plane strain fracture toughness (K_{IC}) were determined as per ASTM E8M-97 [125] using *INSTRON*

1195 static testing machine and are presented in Tables 3.2. The plane stress fracture toughness (K_C) was calculated using following empirical relation proposed by Irwin [126].

$$K_C^2 = K_{IC}^2 (1 + 1.4\beta_{IC}^2) \quad (3.1)$$

$$\text{where, } \beta_{IC} = \frac{1}{B} \left(\frac{K_{IC}}{\sigma_{ys}} \right)$$

Table 3.2 – Mechanical properties of materials

Materials	Tensile strength (σ_{ut}) MPa	Yield strength (σ_{ys}) MPa	Young's modulus (E) MPa	Poisson's ratio (ν)	Plane-Strain Fracture toughness (K_{IC}) MPa \sqrt{m}	Plane-Stress Fracture toughness (K_C) MPa \sqrt{m}	Elongation
7020-T7	352.14	314.70	70,000	0.33	50.12	236.80	21.54 % in 40 mm
2024-T3	469.00	324.00	73,100	0.33	37.00	95.31	19 % in 12.7 mm

Metallography

In order to examine the microstructure, metallographic specimens of the material were prepared in three directions: L-T, L-S, and T-S. The specimens were polymer mounted, polished and etched using *Graff reagent*. Then they were examined in all three directions with the help of an optical microscope using polarized light. The microstructures of all three directions were superimposed to obtain the 3-D view and illustrated in Fig. 3.1 and 3.2.

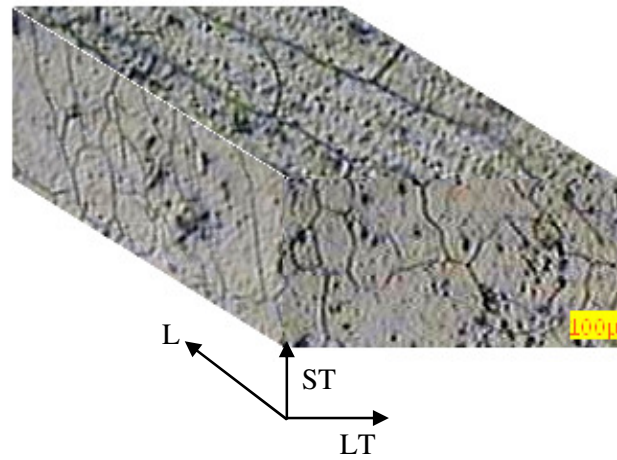


Fig. 3.1 – Microstructure of 7020-T7 Al alloy etched by *Graff reagent*

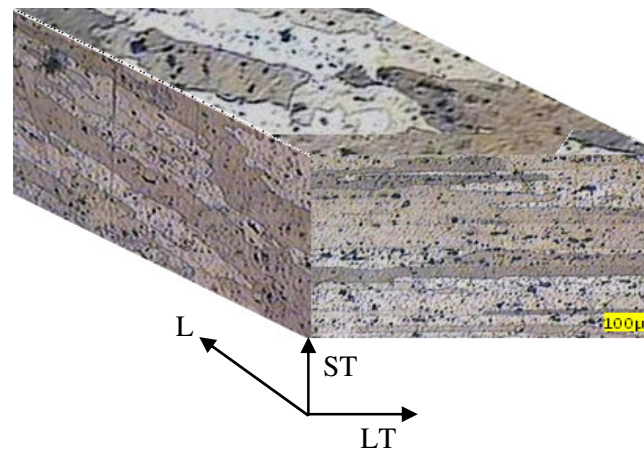


Fig. 3.2 – Microstructure of 2024-T3 Al alloy etched by *Keller's reagent*

3.2.2 Specimen geometry

For conducting the fatigue crack growth tests, single edge notch (SEN) tension specimens were fabricated from supplied 6.5mm thick sheet. The specimens were made in the LT plane, with the loading aligned in the longitudinal direction. The dimensional details of specimen are presented in Fig. 3.3.

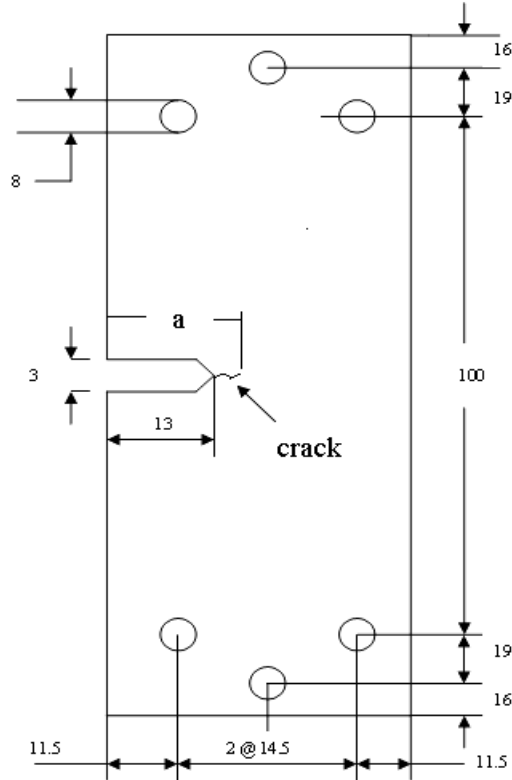


Fig. 3.3 – Single Edge Notch (SEN) Specimen geometry (LT orientation)

3.2.3 Mixed-mode attachment

The mixed mode loading fixture along with pins (to mount-up in machine) was fabricated from a 13.5 mm thick EN24 steel plate. The fixture is designed on the basis of the set-up proposed by Richard [2]. Six holes of 25.5 mm diameter were provided to facilitate loading at an interval of 18° . These holes were used to mount the fixture along with the specimen to the testing machine. Three holes of 8 mm diameters were also made on each set of fixture to attach the test specimen. Holes are made at triangular position due to space limitation and to fix 52 mm width SEN specimen rigidly to avoid tearing failure. Stainless steel bolts were used to attach the specimen with the mixed mode fixture. The test set-up for the present investigation is illustrated in Fig. 3.4.

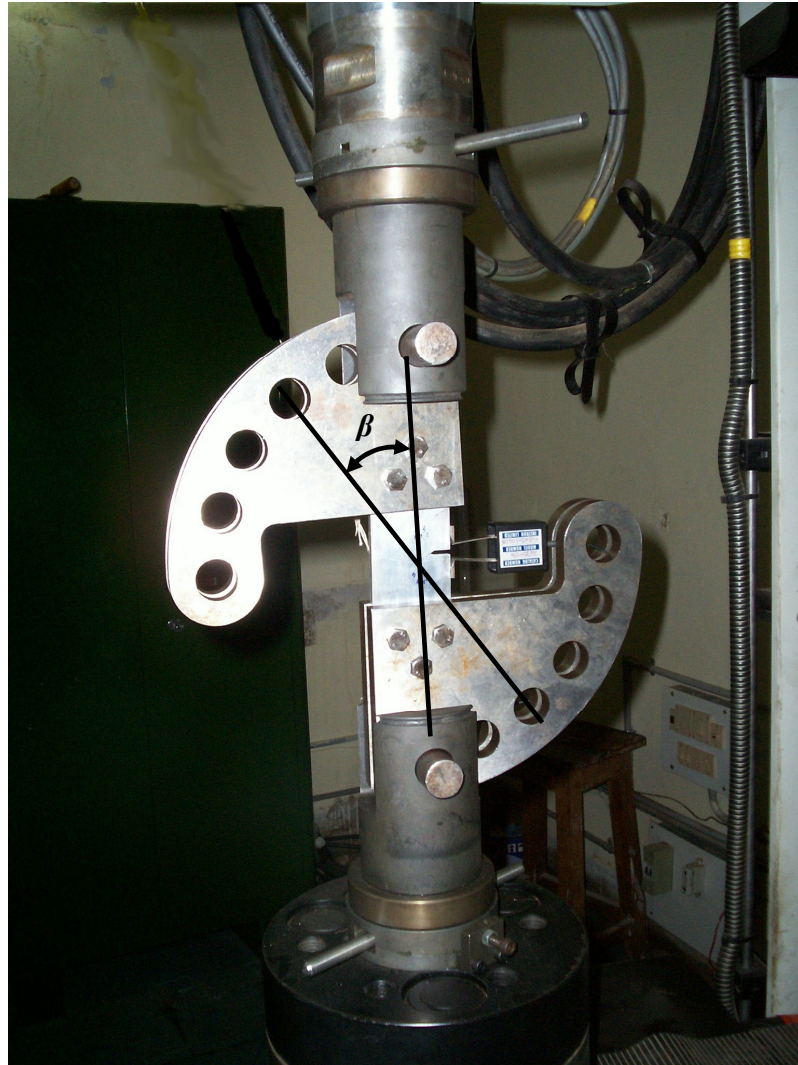


Fig. 3.4 – Mixed-mode Loading Fixture

3.2.4 Test equipment

The machine used for the fatigue tests was a servo-hydraulic dynamic testing machine (*INSTRON 8502 PLUS*) having a load capacity of 250kN interfaced to a computer for machine control and data acquisition. Fig. 3.5 shows the overall arrangement to conduct the test.



Fig. 3.5 – *INSTRON 8502* dynamic testing machine

3.3 Test program

3.3.1 Determination of crack coefficient

INSTRON 8502 PLUS dynamic testing machine uses *INSTRON FAST TRACK da/dN* Fatigue Crack Propagation Program to perform fatigue crack growth studies on standard specimens in accordance with ASTM E647 08 [127]. This test program runs under an environment set up by the LabVIEW programming application from National Instruments. The *da/dN* program has the ability to use the compliance method to measure crack length with the help of a COD gauge which requires various crack coefficients C_0 to C_5 . The values of the coefficients are already incorporated in *da/dN* Fast Track Software for some specimen geometries. Since the crack coefficients for the specimen used in this work was not available in the software, it was necessary to determine the values of the coefficients to be used in the *da/dN* program for computing crack length. Details of the procedures for determination of the crack coefficients are presented in Appendix-B.

3.3.2 Fatigue crack growth tests

Single-edge notched (SEN) tension specimens with a V-starter notch were prepared from 6.5mm thick sheets in the L-T direction. Both sides of the specimen surfaces were given mirror-polish with the help of different grades of emery papers and subsequently by magnesium oxide powder (MgO) suspension. The specimen surfaces were marked at interval of 1 mm to optically monitor the crack extension as well. A pair of knife edges was fixed on the face of the machined V-notch of the specimen. The COD gauge was mounted on the knife edges to monitor crack extension. Fatigue pre-cracking was done under mode-I loading (crack opening mode) at constant ΔK to an a/w ratio of 0.3.

Following four sets (vide Fig. 1.1; Section – 1.2; Chapter - I) of crack growth tests were performed in this investigation: (i) constant amplitude loading with fixed R -ratio, (ii) constant amplitude loading with variable R -ratio, (iii) constant amplitude loading with single tensile overload in mode-I and (iv) constant amplitude loading with single tensile overload in mixed-mode (I and II). The tests were conducted in constant load control mode (i.e. increasing ΔK with crack extension) in accordance with ASTM standard [128] using a servo-hydraulic dynamic testing machine (Section-3.2.4). All the four sets of tests were conducted in ambient condition at a frequency of 6 Hz and load ratio of 0.1. The stress intensity factor K [128] was calculated using following equation:

$$K = f(g) \cdot \frac{F\sqrt{\pi a}}{wB} \quad (3.2)$$

where, $f(g) = 1.12 - 0.231(a/w) + 10.55(a/w)^2 - 21.72(a/w)^3 + 30.39(a/w)^4$

3.3.2.1 Constant amplitude load test

In Set-1, specimens (four from each alloy) were fatigue tested under constant amplitude loading maintaining a fixed load ratio, $R = 0.1$ whereas in second set, specimens (six from each alloy) were tested under same loading conditions with varying load ratios, $R = 0, 0.2, 0.4, 0.5, 0.6$ and 0.8 in order to study their effects on growth rates and also on the fatigue lives. The experimental parameters for both the tests are mentioned in Tables 3.3 and 3.4 respectively for both the materials.

Table 3.3 – Load scenarios and results of CAL (set-1)

Test Specimen	F_{\max} kN	F_{\min} kN	a_i mm	a_f mm
7020-T7	8.89	0.89	18.30	30.24
2024-T3	7.20	0.72	17.75	34.0

Table 3.4 – Load scenarios and results of CAL (set-2)

Test specimen	F_{\max} kN	F_{\min} kN	a_i mm	a_f mm
7020-T7	7.944	3.972	18.3	35.1
2024-T3	7.204	3.602	18.3	35.4

3.3.2.2 Constant amplitude loading interspersed with mode-I spike overload

In case of constant amplitude loading interspersed with mode-I spike overload (Set-3), specimens were tested in order to investigate the effect of a single tensile mode-I overload on the subsequent constant amplitude fatigue crack growth. The crack was allowed to grow up to an a/w ratio of 0.4. This was followed by an overload spike application (at various overload ratios such as 2, 2.25, 2.35, 2.5, 2.6, and 2.75 for 7020-T7 Al-alloy and 1.5, 1.75, 2.0, 2.1, 2.25 and 2.5 for 2024-T3 Al-alloy) in the same crack opening mode at a loading rate of 8 kN/min. The overload ratio is defined as

$$R^{ol} = \frac{K^{ol}}{K_{\max}^B} \quad (3.3)$$

where, K_{\max}^B is the maximum stress intensity factor for base line test. The specimens were subsequently subjected to mode-I constant amplitude load cycles. Table 3.5 shows the experimental details of the tested specimens of both the alloys.

Table 3.5 – Load scenarios of the tested specimens under mode-I overload

Test sample	F_{\max} (kN)	F_{\min} (kN)	F_{\max}^{ol} (kN)	R^{ol}	a_i (mm)	a^{ol} (mm)	a_f (mm)
7020-T7	7.856	0.7856	18.462	2.35	18.30	19.10	29.10
2024-T3	7.305	0.7305	15.341	2.10	17.75	20.40	32.40

3.3.2.3 Constant amplitude loading interspersed with mixed-mode (I & II) spike overload

Similarly in the last set (Set-4) of experiment, specimens were tested under the above loading conditions to study the effect of mixed-mode (I and II) overload spike on crack growth behavior. The overloading was done by using the mixed-mode loading fixture shown in Fig. 3.4. The following equations were used to determine stress intensity factors K_I and K_{II} for different angles of overload application,

$$K_I = f(g) \cdot \frac{F \cos \beta \cdot \sqrt{\pi a}}{wB} \quad (3.4)$$

$$K_{II} = f(g) \cdot \frac{F \sin \beta \cdot \sqrt{\pi a}}{wB} \quad (3.5)$$

All the specimens were subjected to a single tensile overload cycle ($R^{ol} = 2.5$) at various overloading angles, $\beta = 0^\circ, 18^\circ, 36^\circ, 54^\circ, 72^\circ$ and 90° . In this case, overloading ratio is defined as

$$R^{ol} = \frac{K_{eq}^{ol}}{K_{max}^B} \quad (3.6)$$

where K_{max}^B is the maximum stress intensity factor for base line test. The equivalent stress intensity factor (K_{eq}^{ol}) was calculated according to the following equation [2]:

$$K_{eq}^{ol} = 0.5K_I^{ol} + 0.5\sqrt{(K_I^{ol})^2 + 4(\alpha_1 K_{II}^{ol})^2} \quad (3.7)$$

where $\alpha_1 = (K_{IC}/K_{IIC}) = 0.95$ according to strain energy density theory [129] and K_I^{ol} and K_{II}^{ol} are the stress intensity factors of modes I and II during the overload respectively. After the application of overload, the fatigue test was continued in mode-I. Table 3.6 shows the experimental parameters of the tested specimens.

Table 3.6 – Load scenarios of the tested specimens under mixed mode overload

Test Sample	F_{max} (kN)	F_{min} (kN)	R^{ol}	a_i (mm)	a^{ol} (mm)	a_f (mm)
7020-T7	8.429	0.843	2.5	17.75	19.10	31.2
2024-T3	7.197	0.720	2.5	17.75	20.40	32.40

CHAPTER IV

EVALUATION OF EXPERIMENTAL RESULTS

4.1 Introduction

This chapter describes a method for calculating fatigue crack growth rate (FCGR) from the experimental $a-N$ data which are usually scattered. This has been accomplished by fitting an exponential equation to the raw $a-N$ data obtained from each set of tests. Finally, a few fractured samples were selected after each test and were examined under scanning electron microscope (SEM) to study their fracture characteristics.

4.2 Determination of fatigue crack growth rate from experimental data: A new approach [137]

Fatigue crack propagation, a natural physical process of material damage, is characterized by the analysis of the rate of change of crack length (a) with number of cycles (N). It requires a discrete set of crack length vs. number of cycle data generated experimentally. Unlike monotonic test, fatigue test data are usually scattered and is illustrated in a typical $a-N$ plot (Fig. 4.1). The crack growth rates (da/dN) obtained from raw data also exhibit large degree of scatter. Hence, it is necessary to have some means of data smoothening.

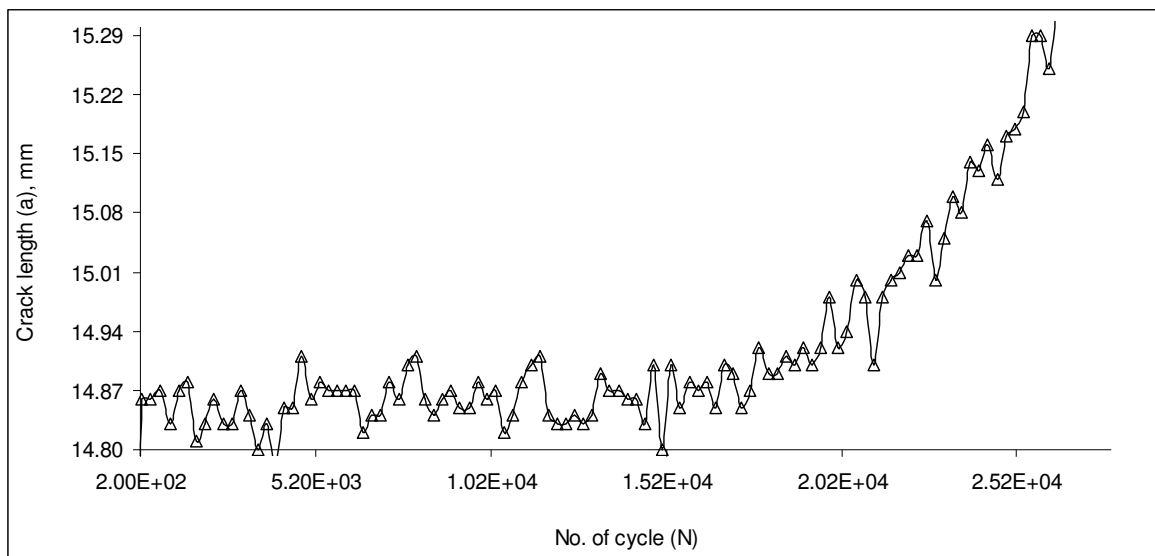


Fig. 4.1 – Crack length vs. number of cycle

In recent years, many crack growth models have been proposed to predict fatigue life under various loading conditions which primarily deal with the relationships between fatigue crack growth rate and different crack driving forces as well as material properties. However, in majority of instances, the method of determination of crack growth rates from $a-N$ data is not explicitly mentioned. The most widely used techniques for crack growth rate determination are:

- a) calculating finite differences between successive data points and making a linear interpolation to estimate the gradient at the mid-point [130];
- b) fitting best smooth curve through $a-N$ data and taking gradients of the slope [131];
- c) fitting an analytical curve (e.g. polynomial) through all or a part of the data [132];
- d) using orthogonal polynomial method for fitting cubic expressions to equidistantly spaced crack length measurements [133];
- e) by spline technique both for interpolation and data smoothing [134];
- f) by incremental polynomial method fitting a second-order polynomial (parabola) to sets of $(2n+1)$ successive data points, where n is usually 1 to 4. [127].

The test results of constant amplitude fatigue crack growth reveal that there is an increase in crack length with number of loading cycles. This increase in crack length is exponential in nature and can be expressed by simple log-linear relationship (Eq. 4.1) as per the observation of Frost and Dugdale [115].

$$\ln(a) = \varpi N + \ln(a_i) \quad \text{or, } a = a_i e^{\varpi N} \quad (4.1)$$

where, N is the fatigue life, ϖ is a parameter that depends on the geometry, material and load scenario, a is the crack length and a_i is the initial flaw size. Other researchers have also observed the apparent exponential rate of crack growth for both micro- and macro-cracks [116-119; 135, 136]. Further, it is known that various types of non-linear functions such as logarithmic, exponential or some other functions can be fitted to the scattered experimental data and then the least squares method can be easily applied to get the smooth curve. Based on the above fact, it is felt that the crack length vs. number of cycle data can be fitted by an exponential equation of the form:

$$a_j = a_i e^{m_{ij}(N_j - N_i)} \quad (4.2)$$

where, a_i and a_j = crack length in i^{th} step and j^{th} step in ‘mm’ respectively,

N_i and N_j = No. of cycles in i^{th} step and j^{th} step respectively,

m_{ij} = specific growth rate in the interval $i-j$,

i = No. of experimental steps,

and $j = i+1$

Procedure for calculation of FCGR

The experimental $a-N$ data of one specimen (Al 7020-T7 under constant amplitude loading condition) is considered to explain the calculation procedure of this new method. The procedures of the method are outlined below with the help of Table 4.1 (since fatigue test data are very large in number, only a small part of the data is presented in the table for the purpose of explaining the procedure of smoothening the $a-N$ curve).

1. The exponent m_{ij} (i.e. specific growth rate) is an important controlling parameter in the proposed exponential equation. The specific growth rate m is not a constant quantity and depends on a number of factors. Its significance and dependence on various crack driving parameters are given by Mohanty et al. [137]. The specific growth rate ' m_{ij} ' is derived by taking logarithm of Eq. 4.2 as follows:

$$m_{ij} = \frac{\ln\left(\frac{a_j}{a_i}\right)}{(N_j - N_i)} \quad (4.3)$$

2. The raw values of specific growth rate from experimental $a-N$ data (columns A and B, Table 4.1) are calculated using equation 4.3 and are given in column C of same table. These are fitted with corresponding crack lengths by a polynomial curve-fit.
3. To get a better result, crack lengths at small increments (0.005 mm in the present case) are tabulated in column D and the corresponding values of m_{ij} are obtained using polynomial equation and presented in column E.
4. The above values of specific crack growth rates are used to get the smoothened values of the number of cycles (column F, Table 4.1) as per the following equation:

$$N_j = \frac{\ln\left(\frac{a_j}{a_i}\right)}{m_{ij}} + N_i \quad (4.4)$$

5. The crack growth rates (da/dN) are calculated directly from the above calculated values of ' N ' as follows:

$$\frac{da}{dN} = \frac{(a_j - a_i)}{(N_j - N_i)} \quad (4.5)$$

The scatter of specific growth rate calculated piecewise and that obtained after data smoothening are shown in Fig. 4.2.

Table 4.1 – Comparison of experimental and smoothed sets of fatigue growth data

A	B	C	D	E	F
No. of cycles (expt)	Crack length (expt) (mm)	Sp. Growth rate (calculated piecewise)	Crack length incremented by 0.055 mm	Sp. Growth rate (calculated from polynomial equation)	No. of cycles (calculated from equation)
66950	20.01	7.7E-06	20.005	8.45E-06	67590
67970	20.2	5.72E-06	20.225	8.6E-06	68871
68980	20.41	1.37E-05	20.445	8.74E-06	70116
70000	20.58	9.73E-06	20.665	8.88E-06	71328
71020	20.77	2.12E-05	20.885	9.03E-06	72508
72040	20.96	9.19E-06	21.105	9.19E-06	73656
73060	21.18	7.27E-06	21.325	9.35E-06	74773
74080	21.4	9E-06	21.545	9.52E-06	75859
75100	21.63	1.07E-05	21.765	9.7E-06	76914
76120	21.79	7.07E-06	21.985	9.89E-06	77939
77140	21.97	7.01E-06	22.205	1.01E-05	78932
78160	22.12	3.48E-06	22.425	1.03E-05	79895
78920	22.27	5.39E-06	22.59	1.05E-05	80596
79940	22.53	1.54E-05	22.81	1.08E-05	81503
80960	22.7	7.05E-06	23.03	1.11E-05	82379
81980	22.95	6.71E-06	23.25	1.14E-05	83223
83000	23.23	9.95E-06	23.47	1.17E-05	84036
84010	23.5	1.36E-05	23.69	1.21E-05	84816
85030	23.79	1.35E-05	23.91	1.25E-05	85565
86050	24.09	9.98E-06	24.13	1.29E-05	86283
87070	24.43	1.31E-05	24.35	1.34E-05	86969
88090	24.77	1.62E-05	24.57	1.39E-05	87624
88600	24.94	1.29E-05	24.68	1.42E-05	87940

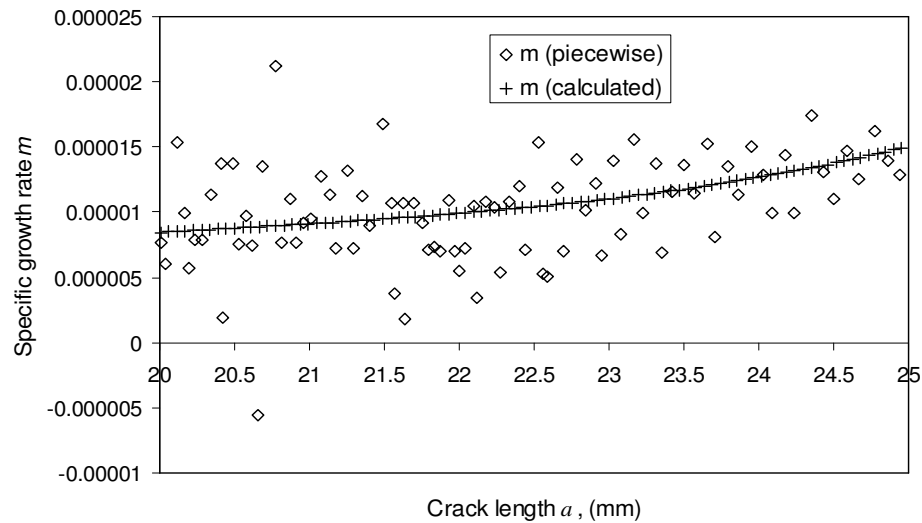


Fig. 4.2 – Specific crack growth rate vs. crack length

Comparison with incremental polynomial method

This method is based on nine point incremental polynomial as per ASTM E647-08 standard [127]. It involves fitting a second-order curve (parabola) to sets of nine successive data points so as to minimize the square of the deviations between observed and fitted values of crack sizes (least squares method). The crack growth rates are obtained from the first derivative of the fitted equation. The calculated crack growth rates for the present case are presented in Fig. 4.3 along with the results of proposed exponential equation method for comparison.

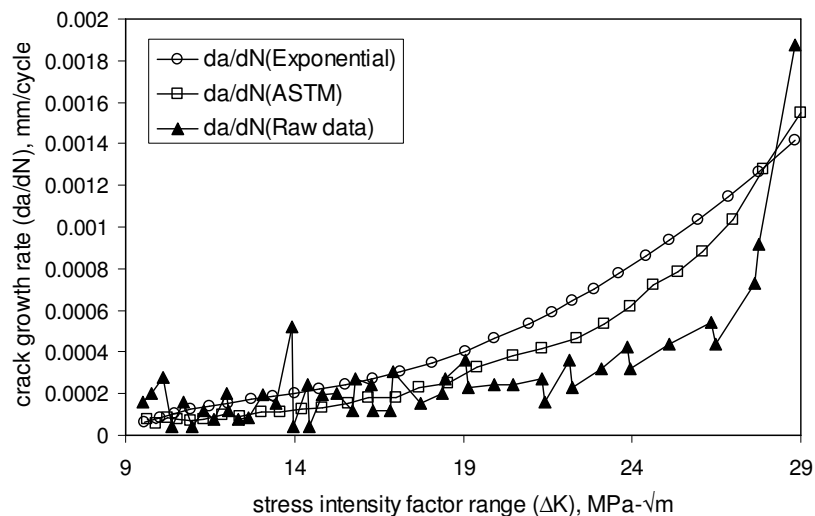


Fig. 4.3 – Comparison of crack growth rate (da/dN) with stress intensity factor range ΔK

4.3 Test results

4.3.1 Constant amplitude loading: *Set - 1*

As mentioned in chapter-III (section-3.3.2), constant amplitude fatigue crack growth tests (set-1) were conducted on four SEN specimens (two from each material) maintaining $R = 0.1$. Crack lengths vs. number of cycles were calculated from the raw experimental $a-N$ data as per the procedures described above in order to get the smoothed values. Figs. 4.4 and 4.5 present the final $a-N$ plots for the alloys under investigation.

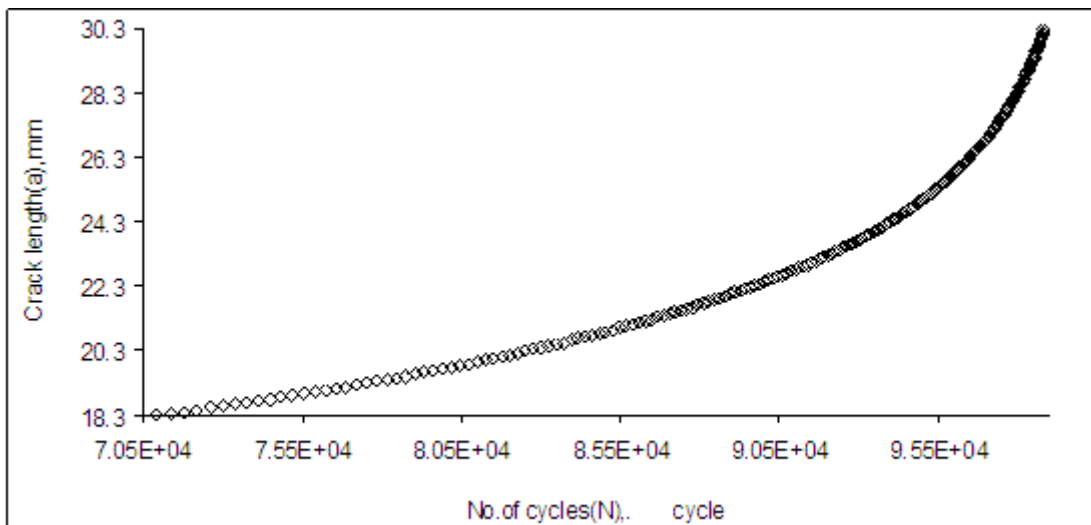


Fig. 4.4 – $a-N$ curve of Al 7020-T7

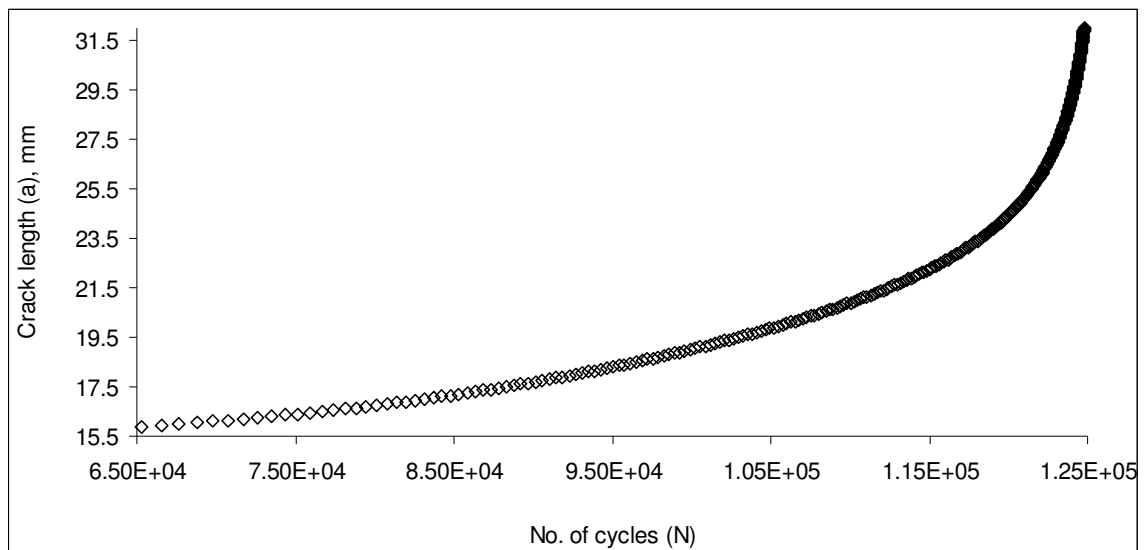


Fig. 4.5 – $a-N$ curve of Al 2024-T3

The corresponding crack growth rates (da/dN) were calculated from the smoothed $a-N$ values as per Eq. 4.5. The corresponding plots of $\log(da/dN)$ vs. $\log(\Delta K)$ are presented in Figs. 4.6 and 4.7.

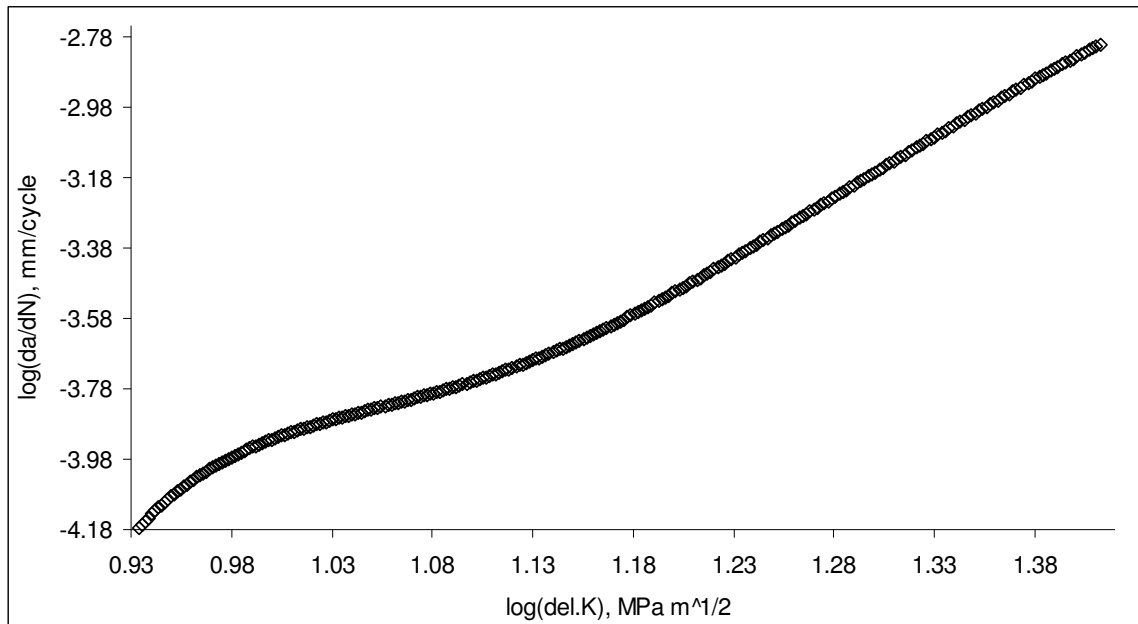


Fig. 4.6 – $\log(da/dN)$ - $\log(\Delta K)$ curve of Al 7020-T7

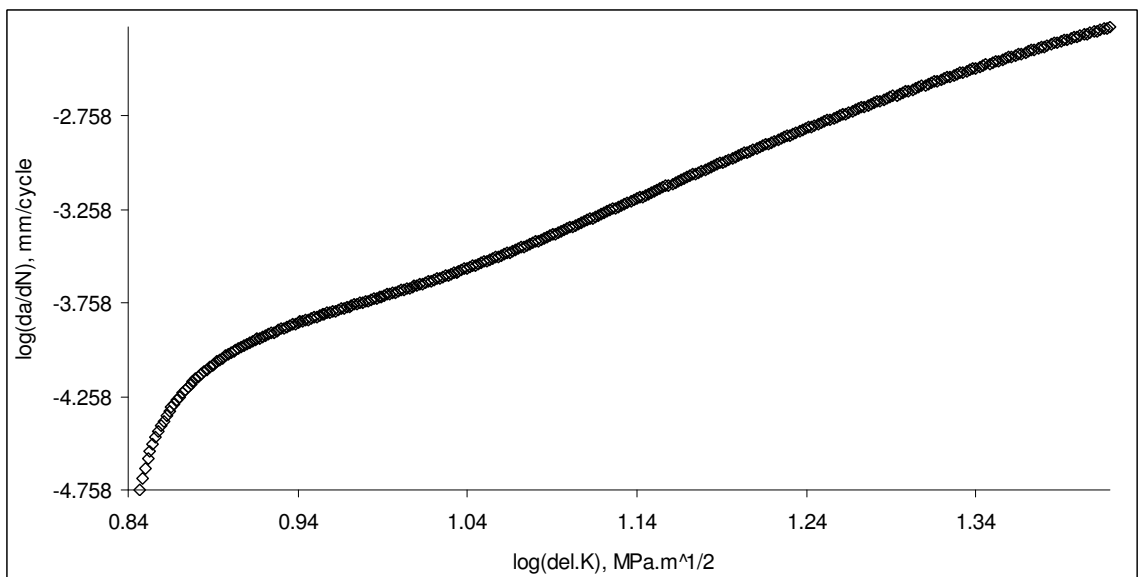


Fig. 4.7 – $\log(da/dN)$ - $\log(\Delta K)$ curve of Al 2024-T3

Set - 2

For set-2 (constant amplitude test series), six different load ratios were maintained for conducting the fatigue crack growth tests. The smoothed $a-N$ plots for all R -values obtained by the proposed method were superimposed and plotted in Figs. 4.8 and 4.9 respectively for 7020-T7 and 2024-T3 alloys. Fatigue crack growth rate values were calculated at regular intervals for all the cases and plotted in Figs. 4.10 and 4.11 along with their ΔK values in linear-linear scale.

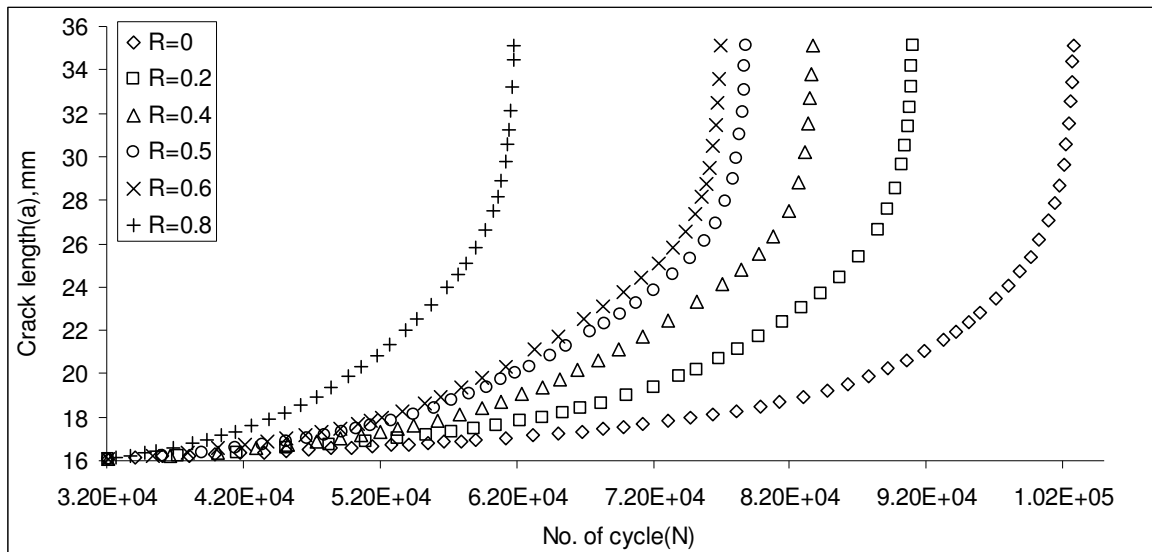


Fig. 4.8 – Comparison of $a-N$ curve for different load ratios (7020-T7)

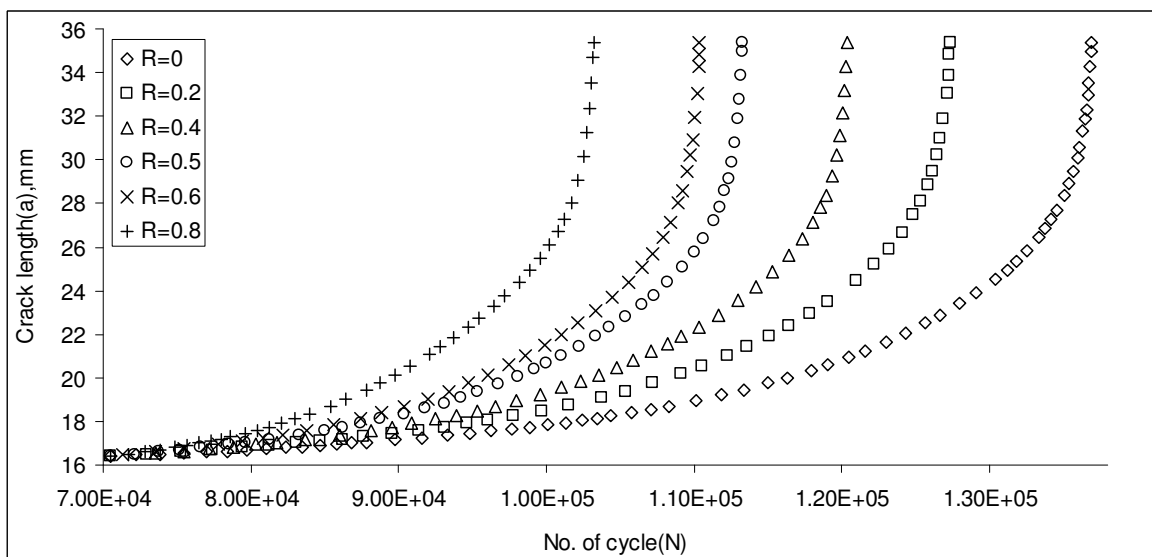


Fig. 4.9 – Comparison of $a-N$ curve for different load ratios (2024-T3)

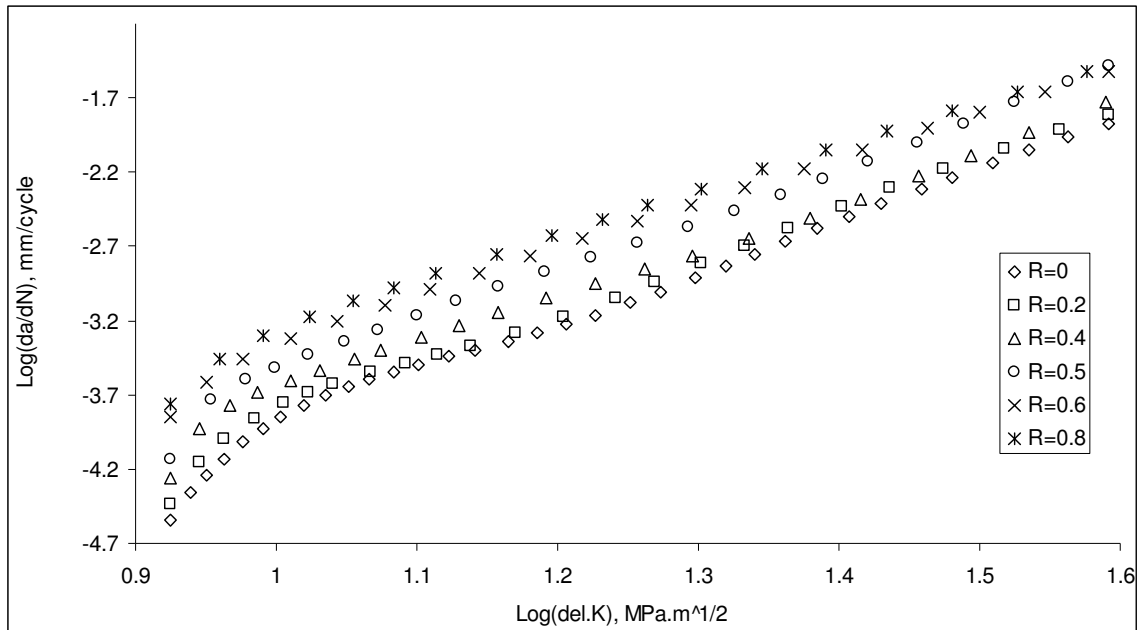


Fig. 4.10 – Comparison of $\log(da/dN)$ - $\log(\Delta K)$ curves for different load ratios (7020-T7)

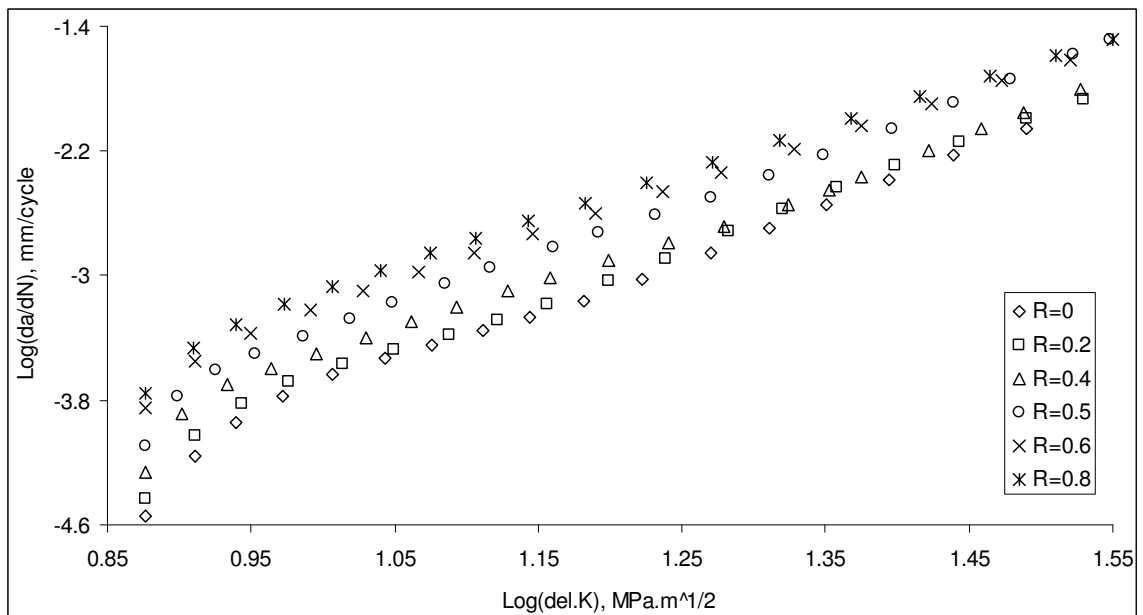


Fig. 4.11 – Comparison of $\log(da/dN)$ - $\log(\Delta K)$ curves for different load ratios (2024-T3)

It is worth to mention that the da/dN - ΔK plots are presented in linear scale instead of log-log scale. This is done since the difference between the crack growth rates under various load ratios are too small to be distinguished in log-log scale.

Fractography

Few representative specimens were examined under Scanning Electron Microscope (SEM) and are presented in Figs. 4.12 to 4.15. Fractographs of 7020-T7 and 2024-T3 Al alloys tested at $R = 0.1$ are presented in Figs. 4.12 and 4.13. In case of higher stress ratios (Fig. 4.14 and 4.15), the difference of fractographic features are not so significant.

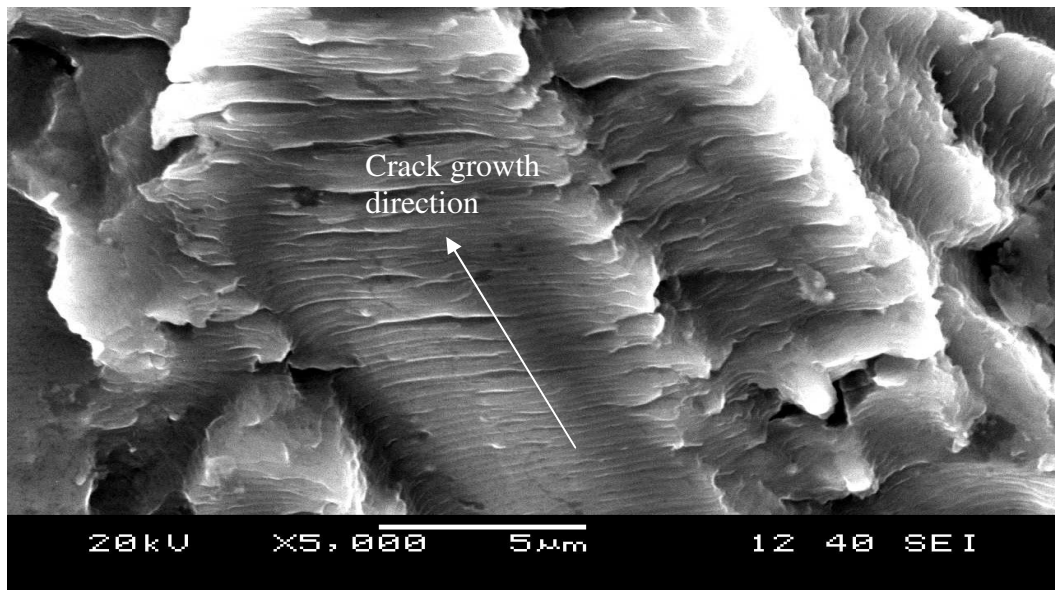


Fig. 4.12 – SEM image of fracture surface of 7020-T7 ($R = 0.1$) at $\Delta K = 10.21MP\sqrt{m}$

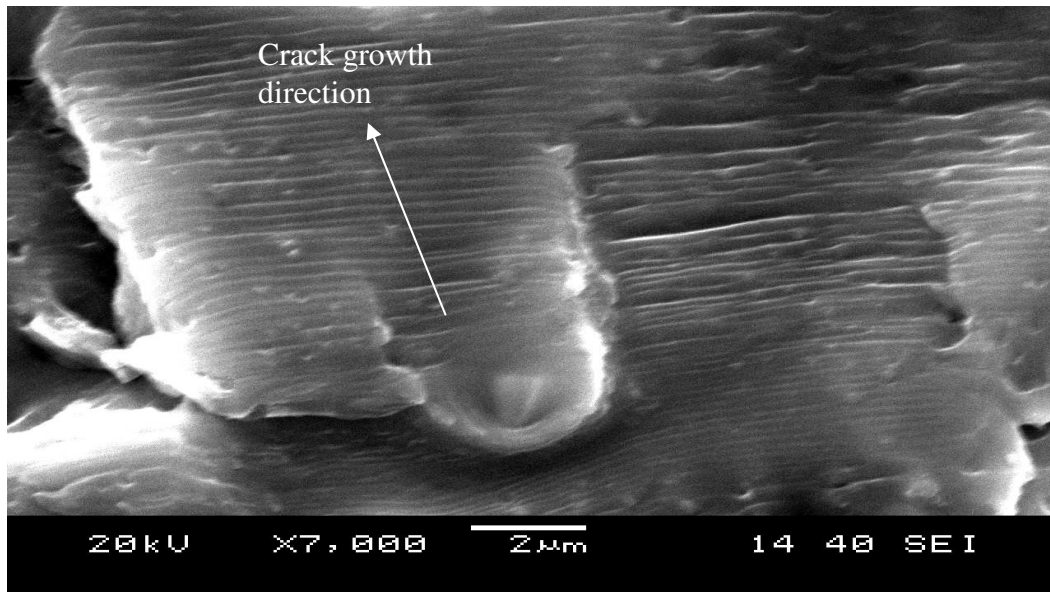


Fig. 4.13 – SEM image of fracture surface of 2024-T3 ($R = 0.1$) at $\Delta K = 10.41MP\sqrt{m}$

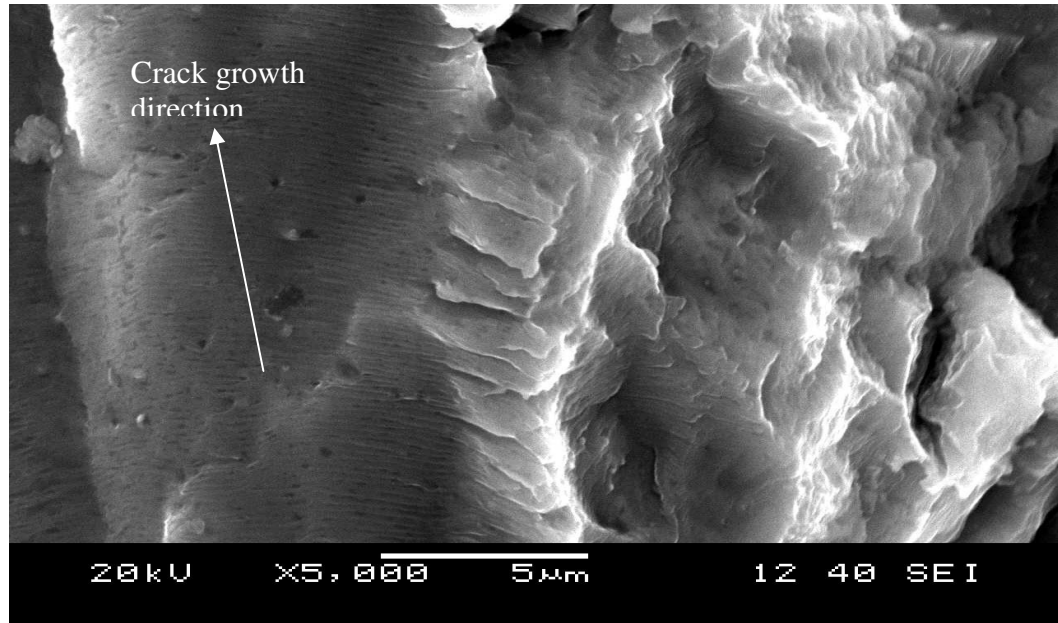


Fig. 4.14 – SEM image of fracture surface of 7020-T7 ($R = 0.5$) at $\Delta K = 10.21MP\sqrt{m}$

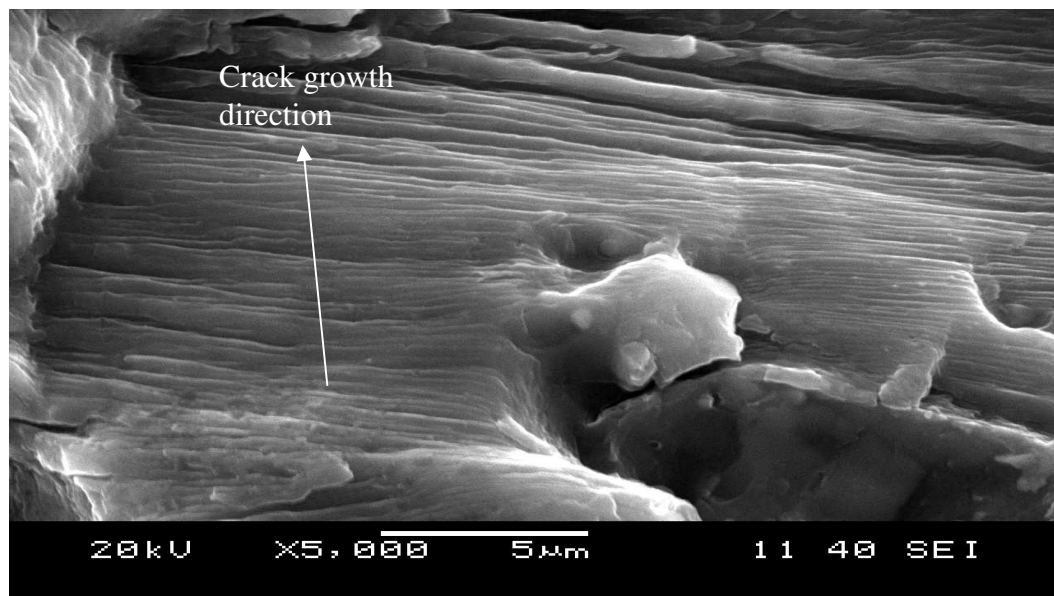


Fig. 4.15 – SEM image of fracture surface of 2024-T3 ($R = 0.5$) at $\Delta K = 10.41MP\sqrt{m}$

4.3.2 Constant amplitude loading interspersed with mode-I spike overload

The crack length vs. number of cycle data obtained from the tests were smoothed by the same procedure and the resulted superimposed curves are plotted along with the

base line data in Figs. 4.16 and 4.17 respectively for both the alloys. Figs. 4.18 and 4.19 show the crack growth rates vs. stress intensity factors curves for different overload ratios.

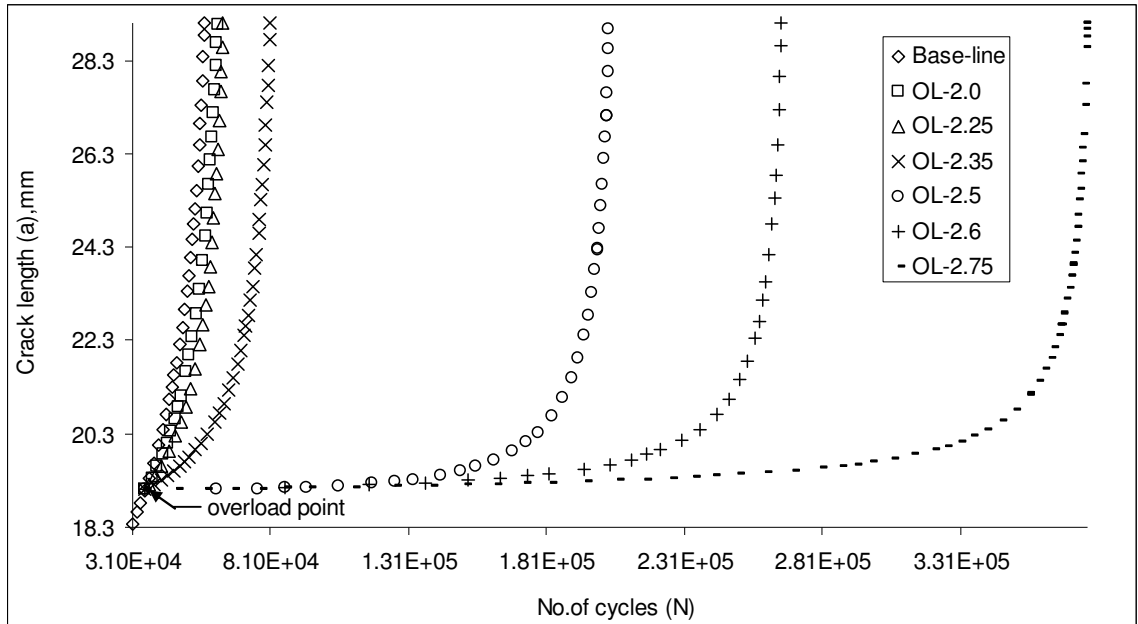


Fig. 4.16 – Superimposed $a-N$ curve of Al 7020-T7

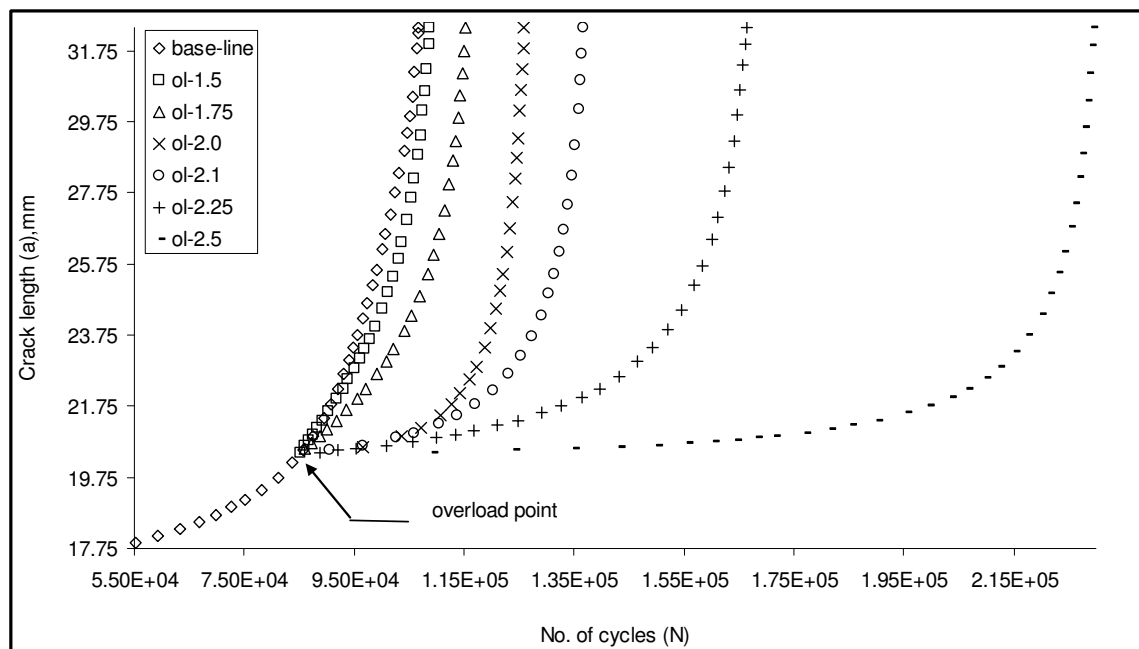


Fig. 4.17 – Superimposed $a-N$ curve of Al 2024-T3

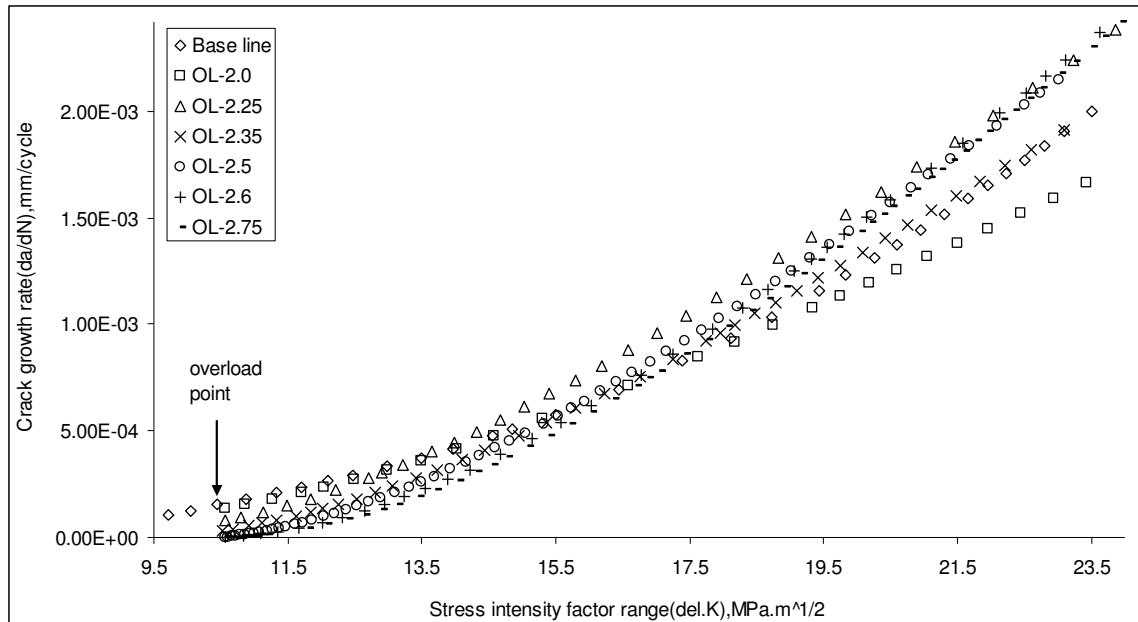


Fig. 4.18 – Superimposed da/dN - ΔK curve of Al 7020-T7

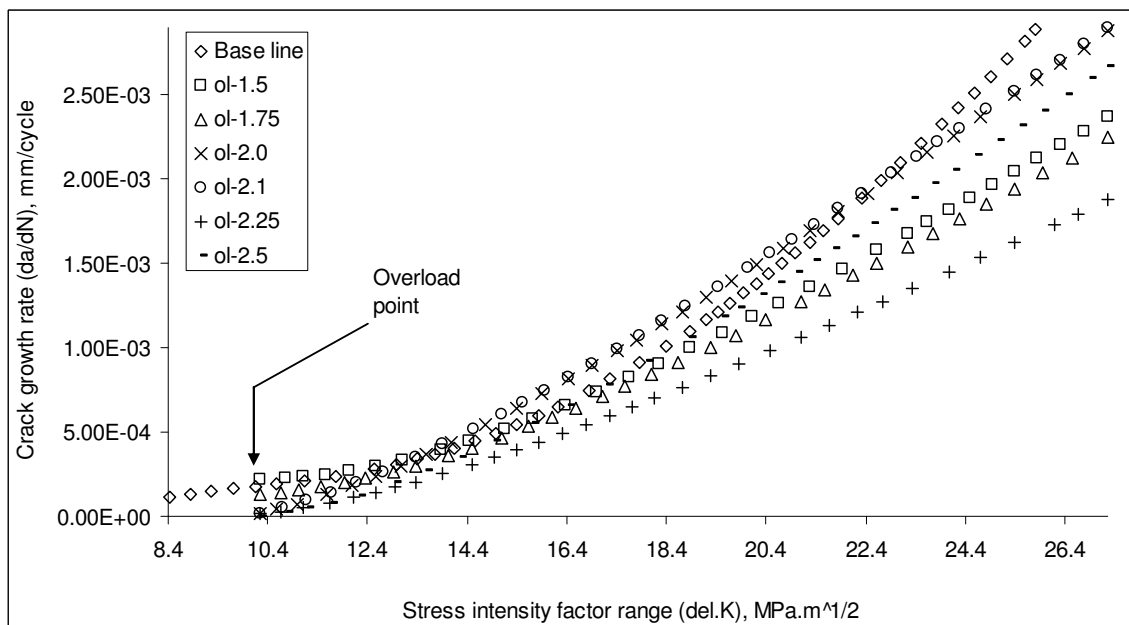


Fig. 4.19 – Superimposed da/dN - ΔK curve of Al 2024-T3

Fractography

Some representative fractographs are presented in Figs. 4.20 to 4.25. Figure 4.20 and 4.21 show a characteristic dark band following the overload in 7020 and 2024 alloys

respectively. The line represents the beginning of overload stretch zone (marked by arrow). As observed in the same figures, the crack front corresponding to the overload cycle is crescent shaped. The width of stretch zone is also visible and marked in the figures for both the cases. For other overload ratios the values of stretch zone width are tabulated in Table 4.2 to show their variations with the magnitude of overloads.

Table 4.2 – Width of stretch zone for different overload ratios

Al 7020-T7		Al 2024-T3	
OLR (R^{ol})	Stretch Zone Width in μm	OLR (R^{ol})	Stretch Zone Width in μm
2.00	115.00	1.50	63.50
2.25	203.35	1.75	79.35
2.35	242.12	2.00	94.12
2.50	295.00	2.10	121.1
2.60	328.85	2.25	179.25
2.75	389.23	2.50	252.00

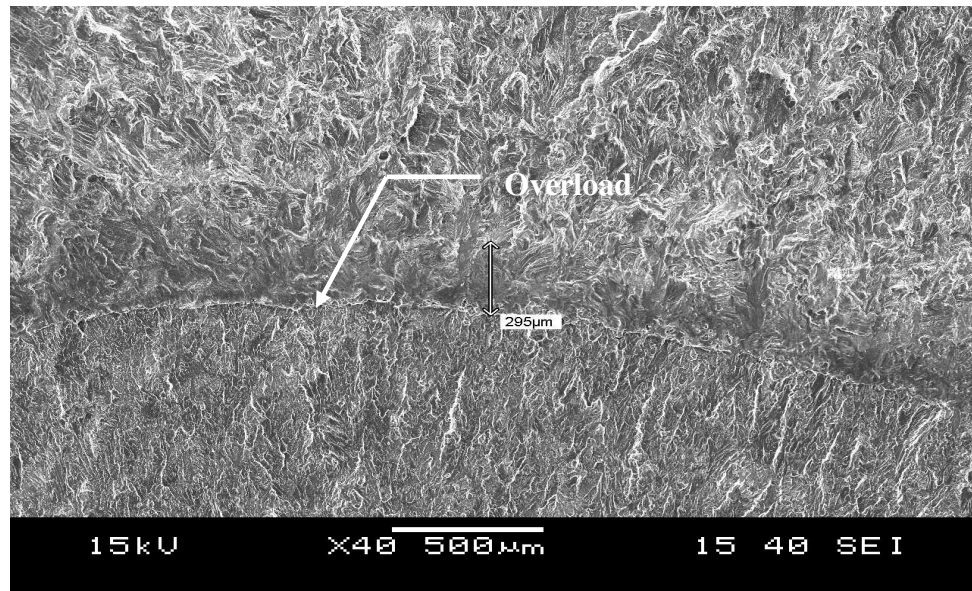


Fig. 4.20 – SEM image of fracture surface showing SZW of 7020-T7 ($R^{ol} = 2.5$)

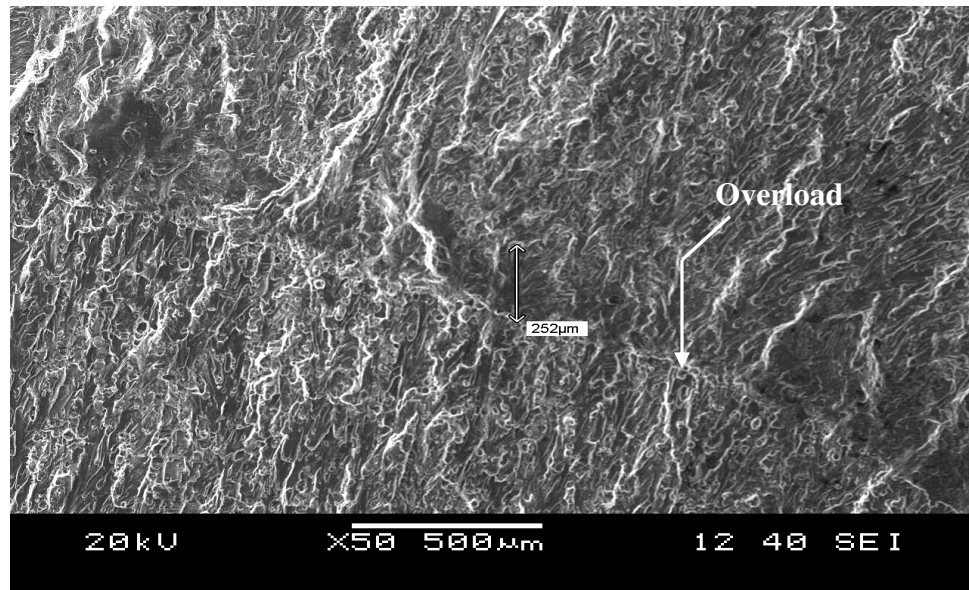


Fig. 4.21 – SEM image of fracture surface showing SZW of 2024-T3 ($R_{ol} = 2.5$)

Figs. 4.22 to 4.25 present fractographs of pre- and post-overload regions of both the alloys ($OLR = 2.5$). Typical fatigue fracture surfaces were having chaotic wavy appearance and the fracture paths did not seem the result from a single mechanism of fracture (Figs. 4.22 and 4.23). Fatigue fractures exhibited relatively smooth areas (labeled A) separated by tear ridges or walls (labeled B). The smooth areas consisted of transgranular fatigue crack propagation containing poorly defined striations with evidence of secondary cracking (Fig. 4.22) and widely dispersed microvoid formation around second-phase particles (labeled C). The occurrence of cleaved particles in voids and the presence of unbroken particles adjacent to some voids (Fig. 4.23) were also observed. Fatigue striations in the direction of crack propagation (marked by arrow) after some distance from the overload point were also observed in both the alloys, but these were more continuous in 2024-T3 (Fig. 4.25) than in 7020-T7 (Fig. 4.24).

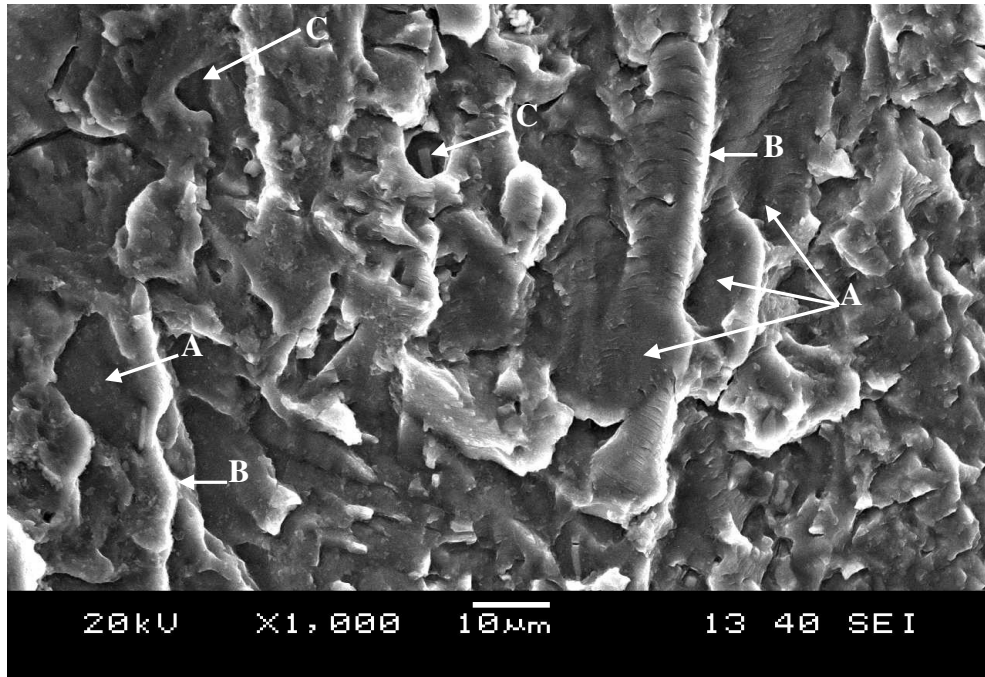


Fig. 4.22 – Fracture surface (SEM) of 7020-T7 before overload at $\Delta K = 10.61MP\sqrt{m}$

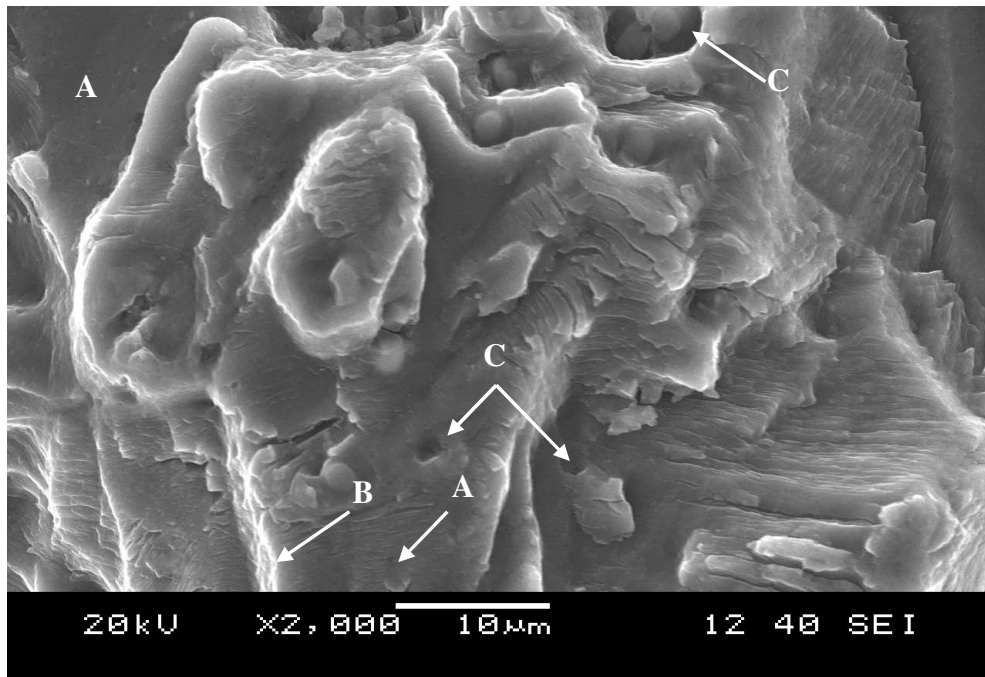


Fig. 4.23 – Fracture surface (SEM) of 2024-T3 before overload at $\Delta K = 10.25MP\sqrt{m}$

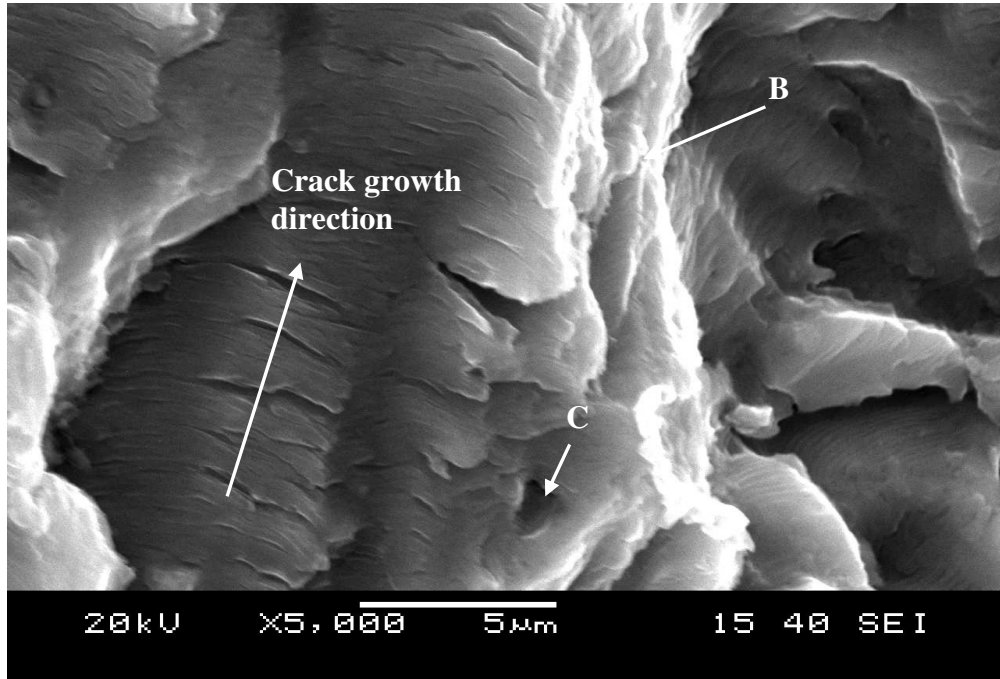


Fig. 4.24 –Fracture surface (SEM) of 7020-T7 after overload at $\Delta K = 12.32MP\sqrt{m}$

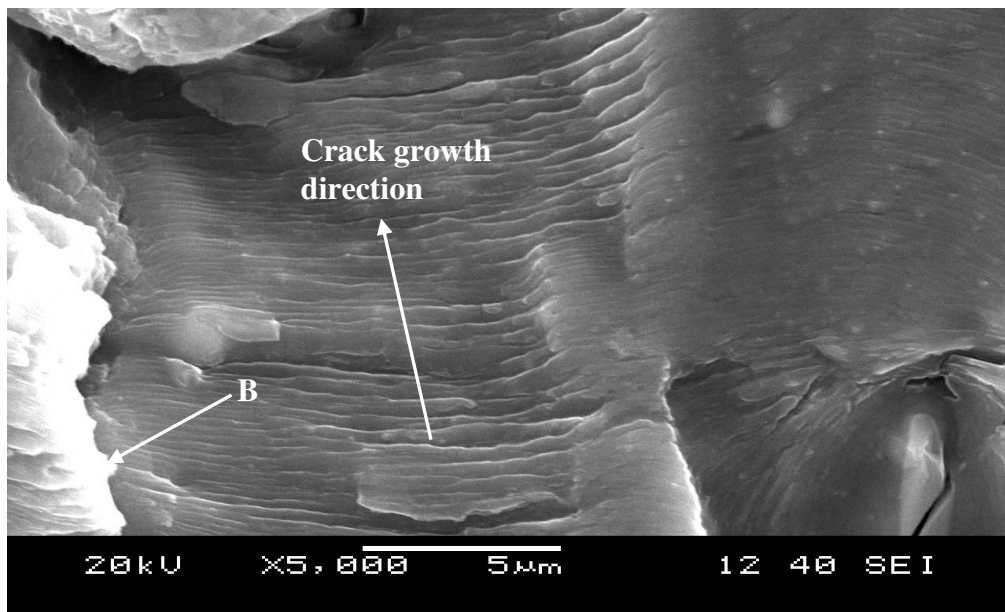


Fig. 4.25 – Fracture surface (SEM) of 2024-T3 after overload at $\Delta K = 12.12MP\sqrt{m}$

4.3.3 Constant amplitude loading interspersed with mixed mode (I and II) spike overload

The crack lengths vs. number of cycle ($a-N$) curves for different overloading angles are obtained from the experimental data by adopting the same procedure and are given in Figs. 4.26 and 4.27. Figs. 4.28 and 4.29 illustrate the superimposed plots of crack growth rates vs. stress intensity factor ranges for the above loading conditions.

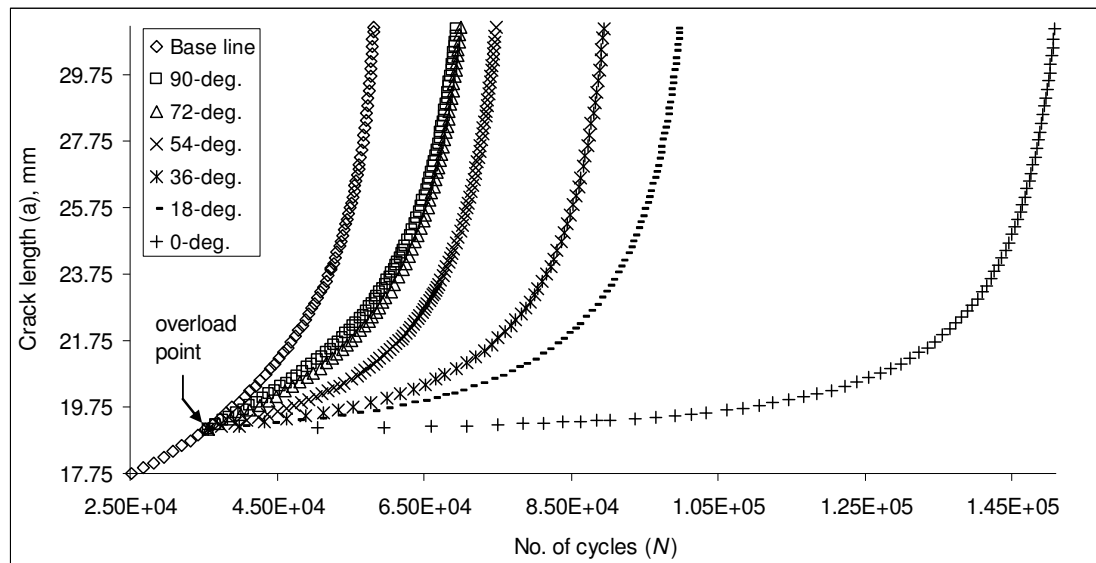


Fig. 4.26 – Superimposed $a-N$ curve of Al 7020-T7

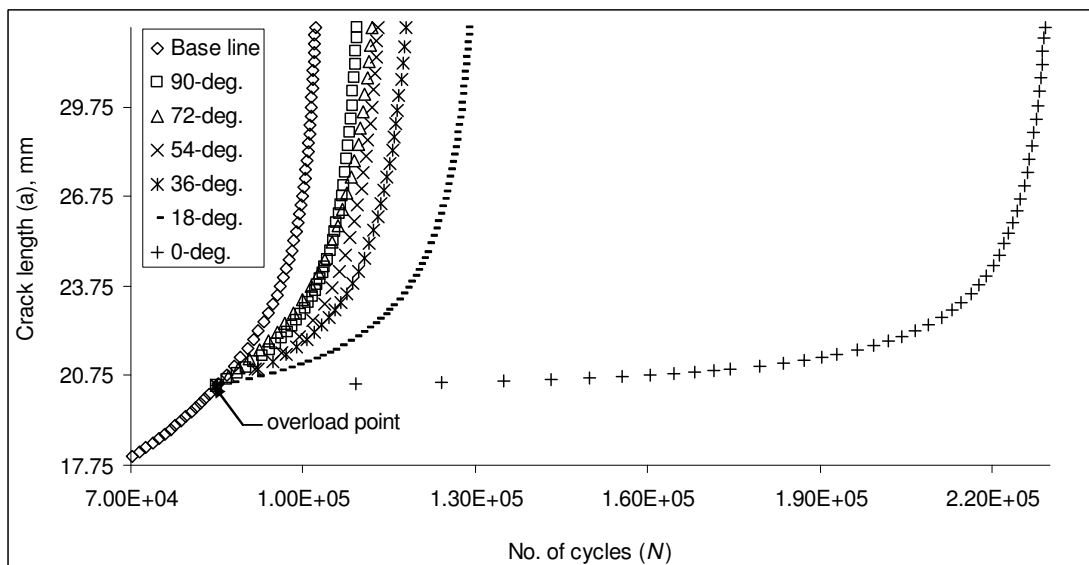


Fig. 4.27 – Superimposed $a-N$ curve of Al 2024-T3

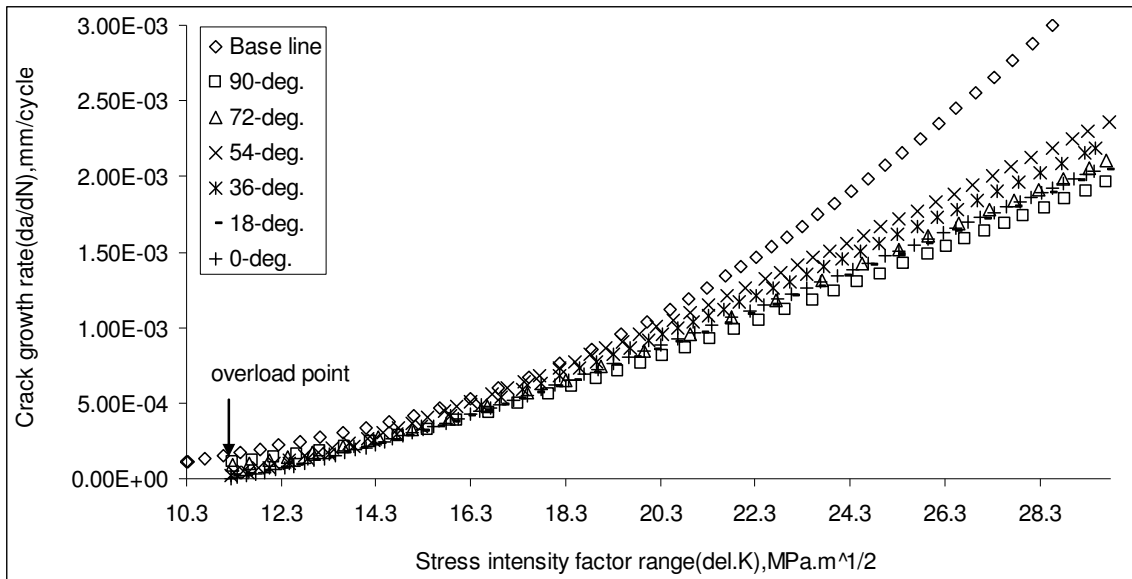


Fig. 4.28 – Superimposed da/dN - ΔK curve of Al 7020-T7

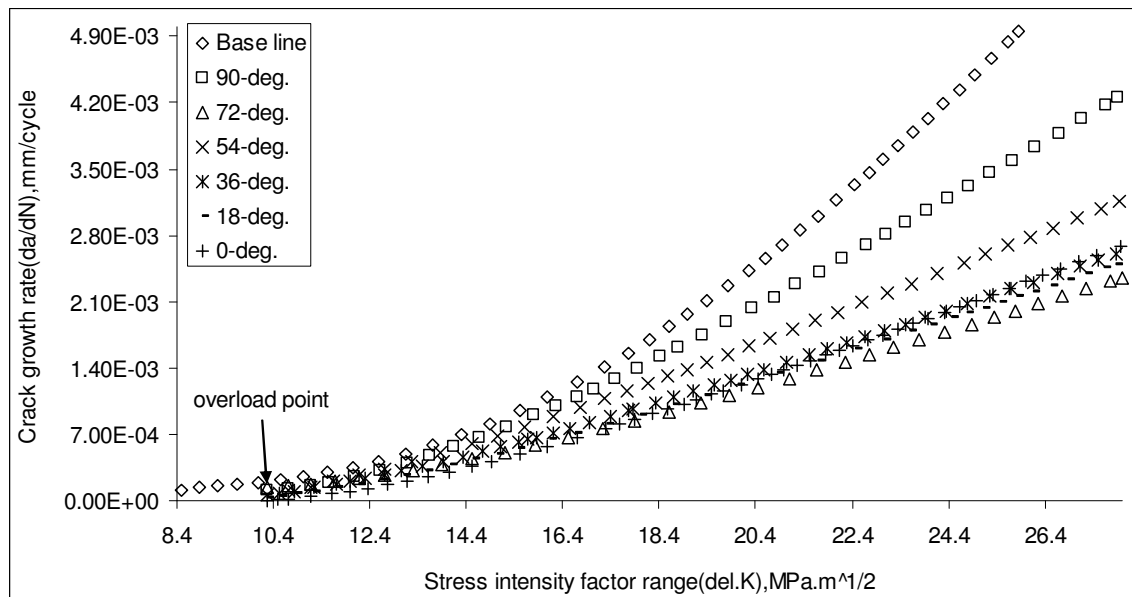


Fig. 4.29 – Superimposed da/dN - ΔK curve of Al 2024-T3

Fractography

After the interspersed mixed mode (I and II) fatigue tests, fractured specimens were examined under SEM. The images of fractured specimens of both the alloys at overloading

angle of 54° are shown in Figs. 4.30 to 4.35. Figs. 4.30 and 4.31 show the typical overload stretch zone at the point of application of overload (marked by arrow) for 54° overloading angle. The values of stretch zone width (SZW) for other overload angles are presented in Table 4.3.

Table 4.3 – Width of stretch zone for different overload angles

Al 7020-T7		Al 2024-T3	
OLR (β)	Stretch Zone Width (SZW) in μm	OLR (β)	Stretch Zone Width (SZW) in μm
90°	101.68	90°	89.25
72°	126.23	72°	92.16
54°	172.00	54°	116.00
36°	194.65	36°	129.02
18°	225.00	18°	205.85
0°	295.00	0°	252.00

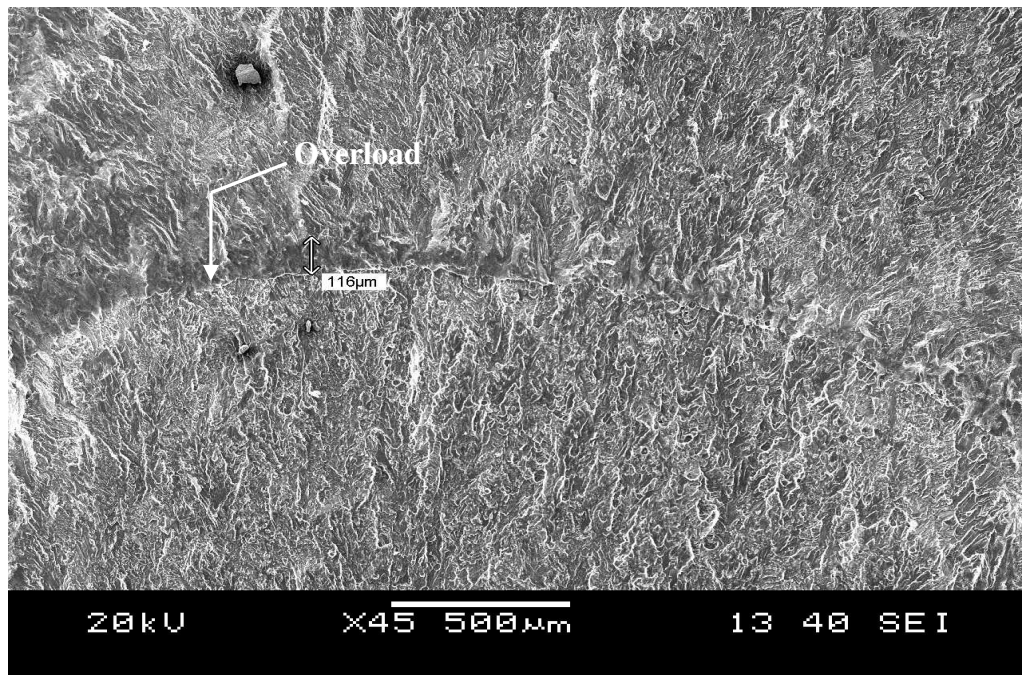


Fig. 4.30 – SEM image of fracture surface showing SZW of 7020-T7 ($\beta = 54^\circ$)

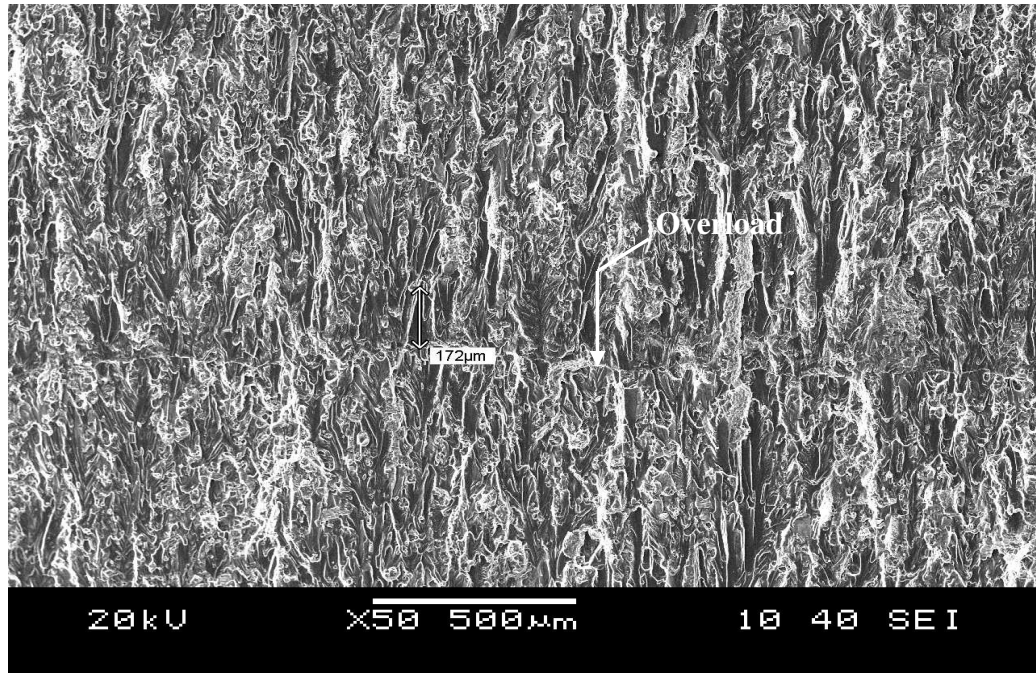


Fig. 4.31 – SEM image of fracture surface showing SZW of 2024-T3 ($\beta = 54^\circ$)

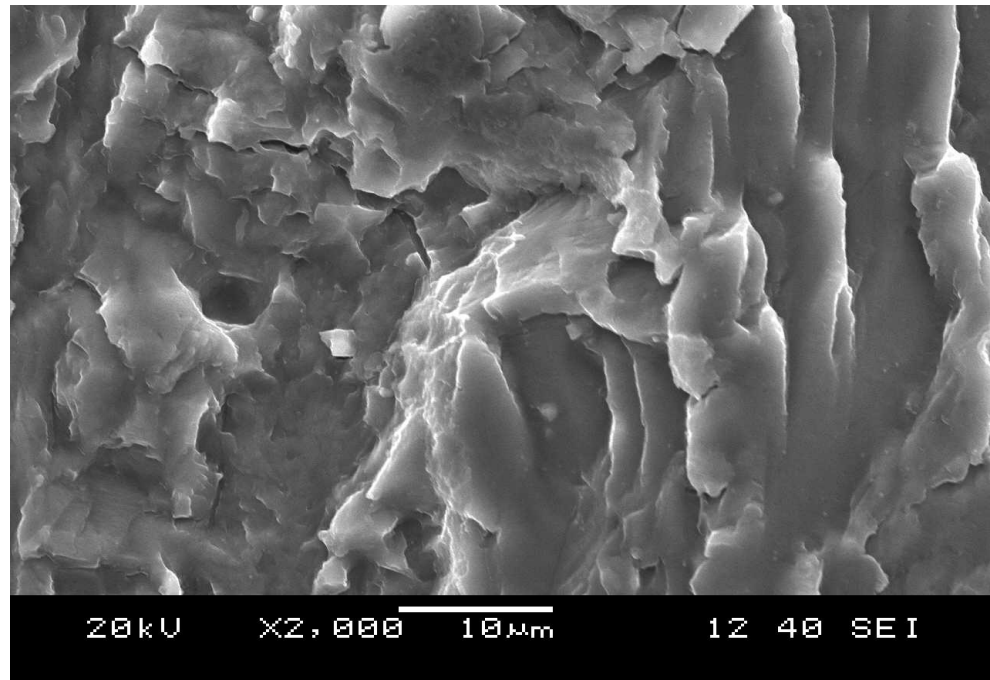


Fig. 4.32 – Fracture surface (SEM) of 7020-T7 before overload at $\Delta K = 10.85 MP\sqrt{m}$

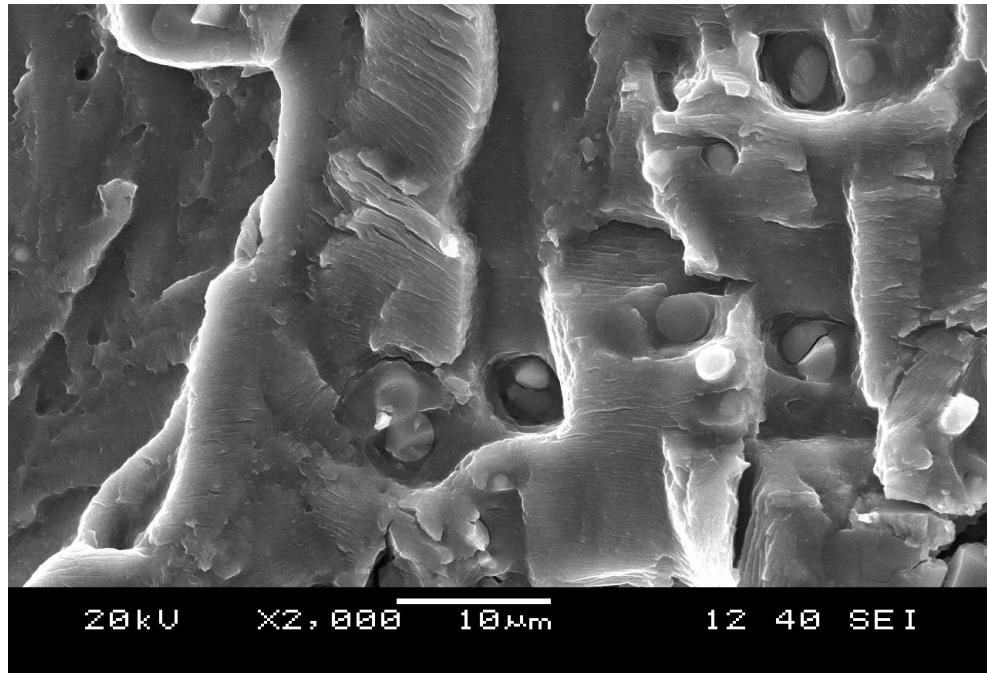


Fig. 4.33 – Fracture surface (SEM) of 2024-T3 before overload at $\Delta K = 11.05 MP\sqrt{m}$

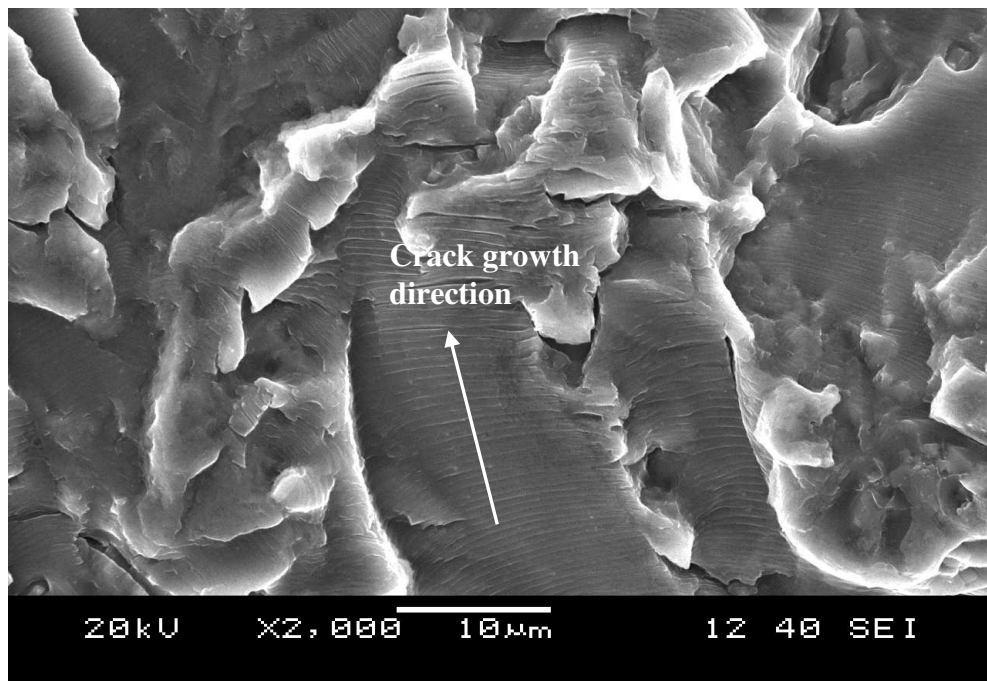


Fig. 4.34 – Fracture surface (SEM) of 7020-T7 after overload at $\Delta K = 13.02 MP\sqrt{m}$

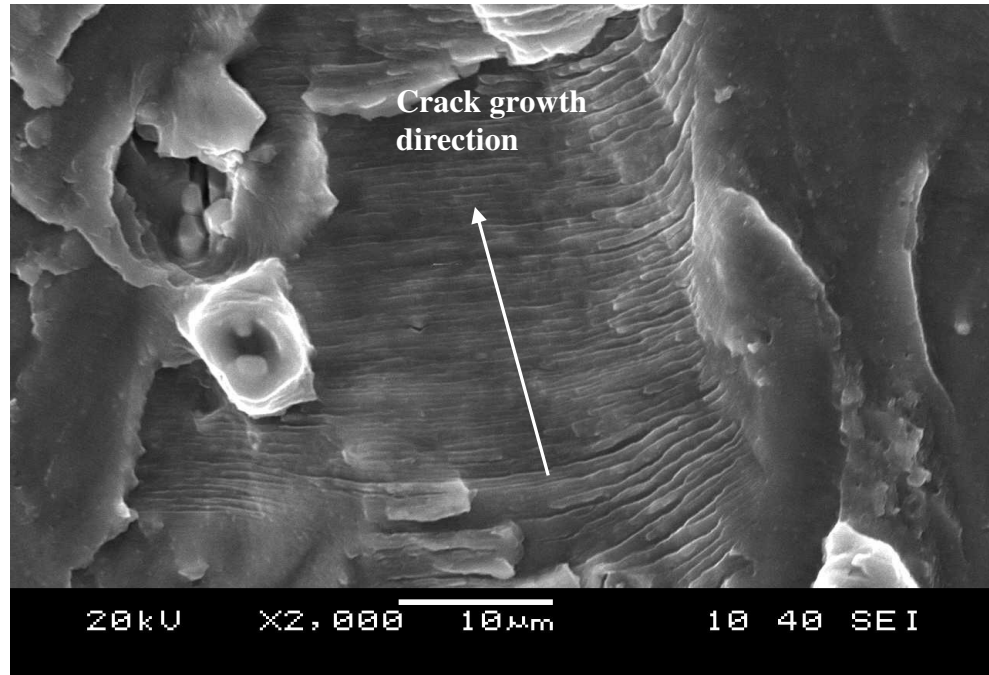


Fig. 4.35 – Fracture surface (SEM) of 2024-T3 after overload at $\Delta K = 13.56 MP\sqrt{m}$

Comparing the fractographic features of mixed-mode overload with that of mode-I, not much qualitative difference has been found.

CHAPTER V

PREDICTION OF FATIGUE LIFE BY EXPONENTIAL MODEL

5.1 Introduction

A new model [138-141] (exponential model) has been formulated to estimate the fatigue life under different loading conditions as described in Chapter-III. The proposed model is based on the exponential nature of growth of fatigue cracks with the number of loading cycles. The main feature of the model is that the exponent (i.e. specific growth rate) of the exponential equation of the model has been judiciously correlated with various physical variables like crack driving parameters and material properties in non-dimensional forms so that the same model can be used for different loading conditions as well as different regimes (II and III) of crack growth. Finally, the validation of the model has been done with the experimental findings in order to compare its accuracy in predicting fatigue life.

5.2 Background and approach

Use of exponential model was first suggested by Thomas Robert Malthus (1766-1834) for the prediction of growth of human population/bacteria. He realized that any species could potentially increase in numbers according to an exponential series. The differential equation describing an exponential growth is

$$\frac{dP}{dt} = rP \quad (5.1)$$

where P is population, t is time and the quantity r in this equation is the Malthusian parameter, also known as specific growth rate.

The solution of the above differential equation is

$$P(t) = P_0 \cdot e^{rt} \quad (5.2)$$

This equation is called the law of growth.

When $t = 0$, $P = P_0$. However, as $t \rightarrow \infty$, P also tends to infinity. But at any point of time the population cannot become infinite due to natural calamities. Hence, some modification is required if this model is to be used for calculation of growth of population.

However, in the present case it was realized that a fatigue crack would grow exponentially and approach to infinity (of course the plate width has to be infinite) as $t \rightarrow \infty$. Although this concept resembles to the earlier work of Frost and Dugdale [115], but the form of exponential equation and its exponent have been treated differently in this work in a sense that the exponent has been correlated with the physical parameters involving fatigue crack growth. The form of exponential equation [138-141] of the proposed Exponential Model is as follows:

$$a_j = a_i e^{m_{ij}(N_j - N_i)} \quad (5.3)$$

The exponent, i.e. specific growth rate (m_{ij}) is calculated by taking the logarithm of the above equation as follows:

$$m_{ij} = \frac{\ln\left(\frac{a_j}{a_i}\right)}{(N_j - N_i)} \quad (5.4)$$

In conventional differential equation model of Paris-Erdogan, there is a physical inconsistency when the constants of the crack growth rate equation are randomized as per dimensional analysis point of view [110]. In case of proposed exponential model, this type of inconsistency does not arise as the specific growth rate m_{ij} is a dimensionless parameter like $\left(\frac{\Delta K}{K_C}\right)$, $\left(\frac{K_{\max}}{K_C}\right)$ and $\left(\frac{\sigma_{ys}}{E}\right)$ as described in the procedure below. Further, Spagnoli [109] analyzed the Paris-Erdogan law on the basis of both similarity methods and fractal concepts and presented some experimental evidence of its breakdown of similitude concept and proposed a crack-size dependent Paris-Erdogan law by strengthening the phenomenon of incomplete self-similarity in the fatigue crack growth process. The differential equation of the proposed model follows the form proposed by Spagnoli for non-self similar growth and for the growth of a fractal crack emphasizing the fact that crack growth rate is crack size dependent as per Frost and Dugdale law.

5.3 Model formulation

Fatigue crack growth behavior is dependent on initial crack length and previous load history. Therefore, while using the exponential model described in Eq. 5.3 each previous crack length is taken as the initial crack length for the present step and the specific growth rate m_{ij} (which is a controlling parameter in the present model) is calculated for each step in incremental manner. Experimental $a-N$ data have been used to determine the values of m_{ij} for each step as per Eq. 5.4. The detail procedure of the model is given below.

General procedure [138]:

1. The specific growth rate m_{ij} is calculated for each step from experimental $a-N$ data according to the Eq. 5.4 and subsequently fitted with corresponding crack lengths by a polynomial curve-fit.
2. To get a better result, crack lengths at small increments (say 0.005mm) are given to the initial crack length, a_i (experimental) so as to reach the final value, a_f and the corresponding (smoothened) values of m_{ij} are obtained using the polynomial equation obtained in step-1.
3. The above smoothened values of m_{ij} are correlated with a parameter l taking into account the two crack driving forces ΔK and K_{\max} as well as material parameters K_C , E and σ_{ys} as follows:

$$l = \left[\left(\frac{\Delta K}{K_C} \right) \left(\frac{K_{\max}}{K_C} \right) \left(\frac{\sigma_{ys}}{E} \right) \right]^{\frac{1}{4}} \quad (5.5)$$

The values of plane stress fracture toughness (K_C) for both the alloys are calculated from plane strain fracture toughness values (K_{IC}) by an empirical relation proposed by Irwin [128] as follows:

$$K_C^2 = K_{IC}^2 (1 + 1.4\beta_{IC}^2) \quad (5.6)$$

$$\text{where, } \beta_{IC} = \frac{1}{B} \left(\frac{K_{IC}}{\sigma_{ys}} \right) \quad (5.7)$$

The different m and l values are fitted by a polynomial equation as follows:

$$m_{ij} = A'l^3 + B'l^2 + C'l + D' \quad (5.8)$$

where, A' , B' , C' and D' are constants of curve fitting.

3. The predicted number of cycles or fatigue life is calculated from the following equation:

$$N_j = \frac{\ln\left(\frac{a_j}{a_i}\right)}{m_{ij}} + N_i \quad (5.9)$$

5.4 Modeling under constant amplitude loading

5.4.1 Model design

Set-1 (Constant R)

As mentioned in Chapter-III, four specimens (from each alloy) were tested in 1st set of experiment under CAL out of which the experimental results of three specimens were taken for model formulation and the 4th one was left for model testing. The values of specific growth rate were calculated from Eq. 5.8 by following the general procedure. The values of the constants A' , B' , C' and D' are tabulated in Tables 5.1 and 5.2 respectively for the two alloys. The predicted values of specific growth rate (m_{ij}) of the tested specimens were calculated by putting the average values of the curve fitting constants in Eq. 5.8. Taking the initial values of a and N from each step of the experimental data, the predicted number of cycles or fatigue life (N_j) were calculated using Eq. 5.9 so as to reach the final crack length a_f (from experiment).

Table 5.1 – Curve fitting constants of Al 7020-T7

Test Specimen	$A' \times 10^{-6}$	$B' \times 10^{-6}$	$C' \times 10^{-6}$	$D' \times 10^{-6}$
1	25226	26640	-5571.7	276.49
2	25035	33750	-7282.8	376.41
3	24353	27263	-5665.7	280.56
Avg.	24871.3	29217.67	-6173.4	311.153

Table 5.2 – Curve fitting constants of Al 2024-T3

Test Specimen	$A' \times 10^{-6}$	$B' \times 10^{-6}$	$C' \times 10^{-6}$	$D' \times 10^{-6}$
1	544055	-46346	838.98	11.84
2	516939	-53301	1277.8	11.249
3	495466	-43411	809.55	10.466
Avg.	518820	-47686	975.443	11.185

Set-2 (Varying R)

Six specimens (from each alloy) were tested under different load ratios out of which five sets (i.e. $R = 0, 0.2, 0.4, 0.6$ and 0.8) of experimental results were used for model formulation. The values of specific growth rate were calculated for each load ratio from Eq. 5.8 in the same manner as that of Set-1. The values of the constants A' , B' , C' and D' for each load ratios for both the alloys are given in Tables 5.3 and 5.4 respectively. Each constant of different load ratios were correlated with the corresponding R by the following sets of equations:

$$A' = X_1R^2 + Y_1R + Z_1 \quad (5.10)$$

$$B' = X_2R^2 + Y_2R + Z_2 \quad (5.11)$$

$$C' = X_3R^2 + Y_3R + Z_3 \quad (5.12)$$

$$D' = X_4R^2 + Y_4R + Z_4 \quad (5.13)$$

where, $X_1, X_2, X_3, X_4, Y_1, Y_2, Y_3, Y_4$ are another set of curve fitting constants relating A' , B' , C' and D' with load ratio, R . The generalized equation for specific growth rate (Eq. 5.8) was:

$$m_{ij} = \{X_1R^2 + Y_1R + Z_1\}^3 + \{X_2R^2 + Y_2R + Z_2\}^2 + \{X_3R^2 + Y_3R + Z_3\} + \{X_4R^2 + Y_4R + Z_4\} \quad (5.14)$$

The predicted values of m_{ij} for the tested specimens ($R = 0.5$) were calculated by putting their respective values of above constants in Eq. 5.14 separately for each material. Subsequently the predicted number of cycles was determined as per Eq. 5.9.

Table 5.3 – Curve fitting constants of 7020-T7 aluminum alloy

load Ratio(R)	$A' \times 10^{-6}$	$B' \times 10^{-6}$	$C' \times 10^{-6}$	$D' \times 10^{-6}$
0.0	300696	-49899	2873.1	-56.178
0.2	361205	-61403	3519.7	-66.708
0.4	431366	-72311	4003.6	-71.464
0.6	433914	-72170	3953.9	-69.641
0.8	403545	-66761	3683.3	-65.589

Table 5.4 – Curve fitting constants of 2024-T3 aluminum alloy

load Ratio(R)	$A' \times 10^{-6}$	$B' \times 10^{-6}$	$C' \times 10^{-6}$	$D' \times 10^{-6}$
0.0	665987	-164037	13843	-390.33
0.2	720615	-181465	15675	-452.43
0.4	870070	-214174	17879	-494.04
0.6	938408	-222270	17717	-459.37
0.8	929936	-221605	17607	-448.1

5.4.2 Model validation

Set-1 (Constant R)

For the first set, the predicted results were compared with the experimental data and the results obtained by using Forman model for a constant load ratio of 0.1 [138]. The values of the constants C_a and n_a of the Forman equation (Eq. 2.3; Section 2.2.1; Chapter-II) were calculated from experimental data by taking the average values of three tested specimens for each material and given in Table 5.5. The predicted a - N curves for both the materials obtained from the proposed exponential model and that of Forman model were compared with the experimental data (Figs. 5.1 and 5.2) and their numerical values are given in Table 5.6. The da/dN - ΔK curves are illustrated in Figs. 5.3 and 5.4 for the tested specimens for comparison.

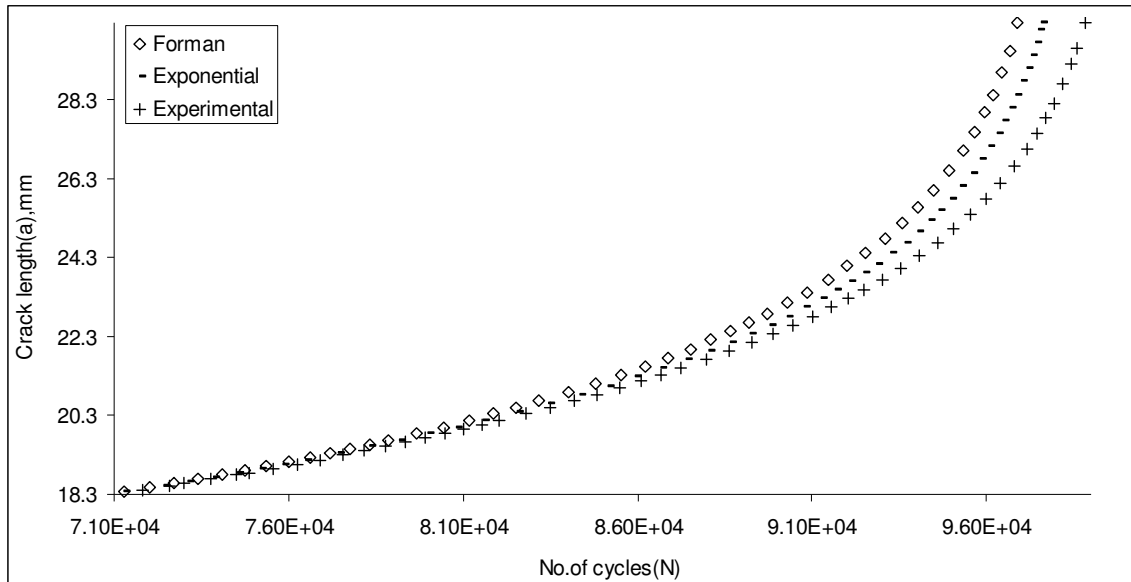
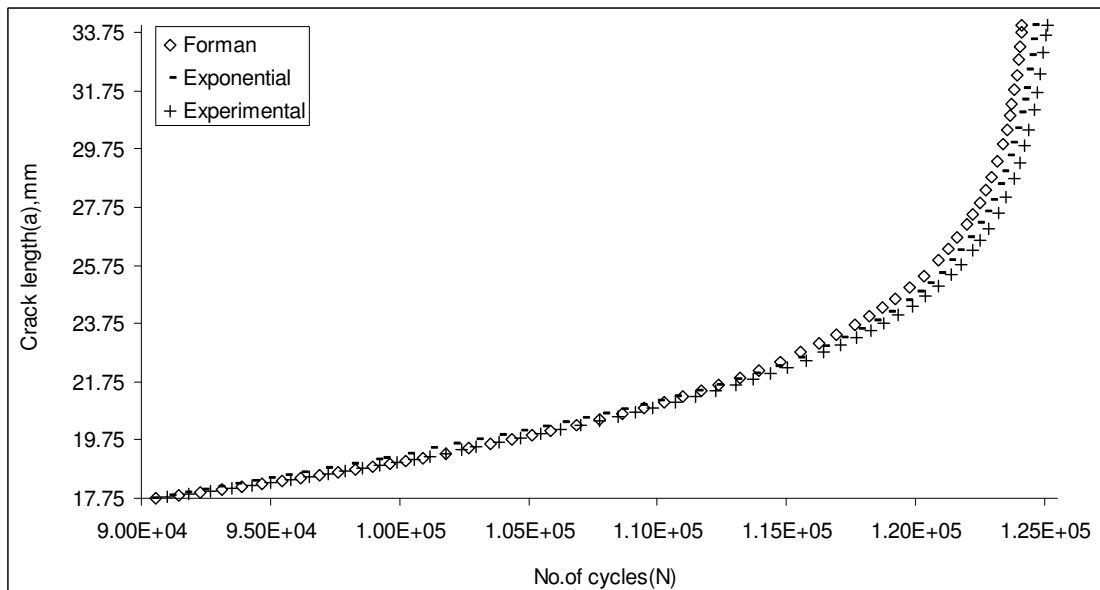
It may be noted that specific growth rate (m_{ij}) is not a constant quantity. It changes with change in loading condition as well as crack length. Since in constant load fatigue test, crack length increases with number of cycles resulting increase in stress intensity factor, the specific growth rate m_{ij} also changes with crack length and number of cycles. The typical variations of m_{ij} with crack length and number of cycles are shown in Fig.5.5 to Fig.5.8 respectively for both the alloys.

Table 5.5 – Constants of Forman model

Forman constants	Specimens (Al 7020-T7)				Specimens (Al 2024-T3)			
	No. 1	No. 2	No. 3	Avg.	No. 1	No. 2	No. 3	Avg.
$C_a \times 10^{-5}$	1.00	2.00	1.00	1.33	2.00	2.00	2.00	2.00
n_a	3.247	3.175	3.164	3.195	2.784	2.786	2.710	2.760

Table 5.6 – Predicted results of CAL (Set-1)

Test Specimen	N_f^F K cycle	N_f^P K cycle	N_f^E K cycle
7020-T7	96.899	97.561	98.829
2024-T3	124.12	124.56	125.09

Fig. 5.1 – $a-N$ curve of Al-7020-T7Fig. 5.2 – $a-N$ curve of Al-2024-T3

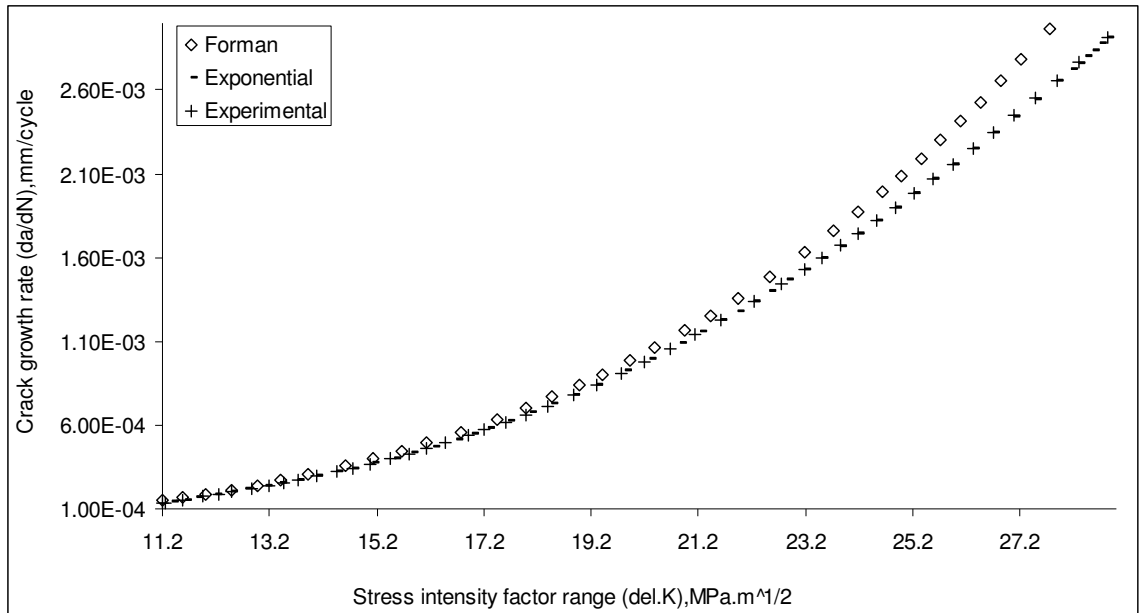


Fig. 5.3 – da/dN – ΔK curve of Al 7020-T7

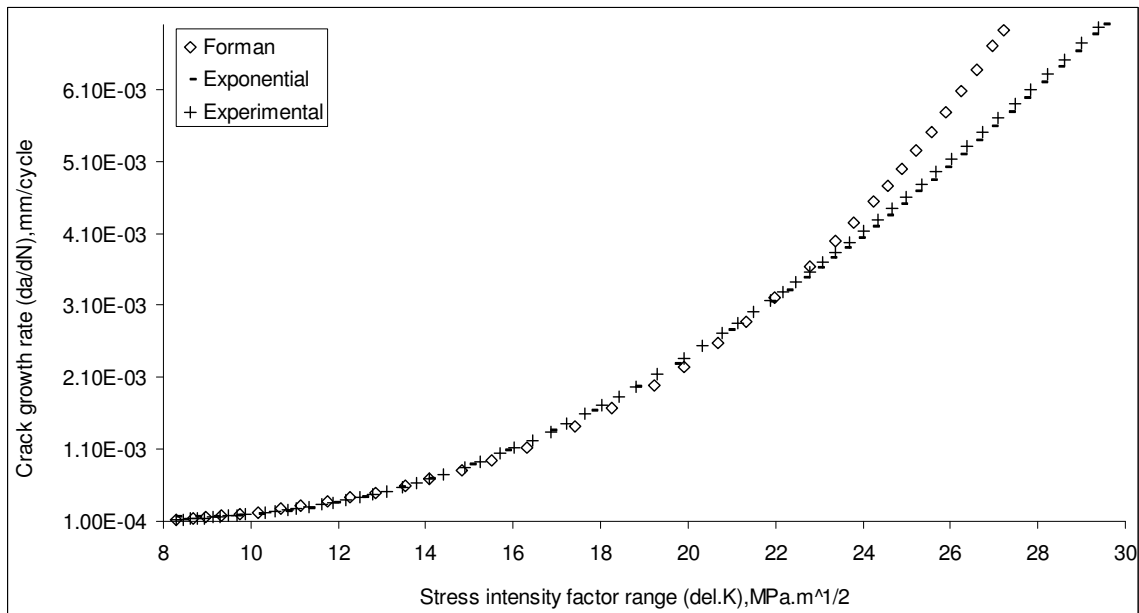


Fig. 5.4 – da/dN – ΔK curve of Al 2024-T3

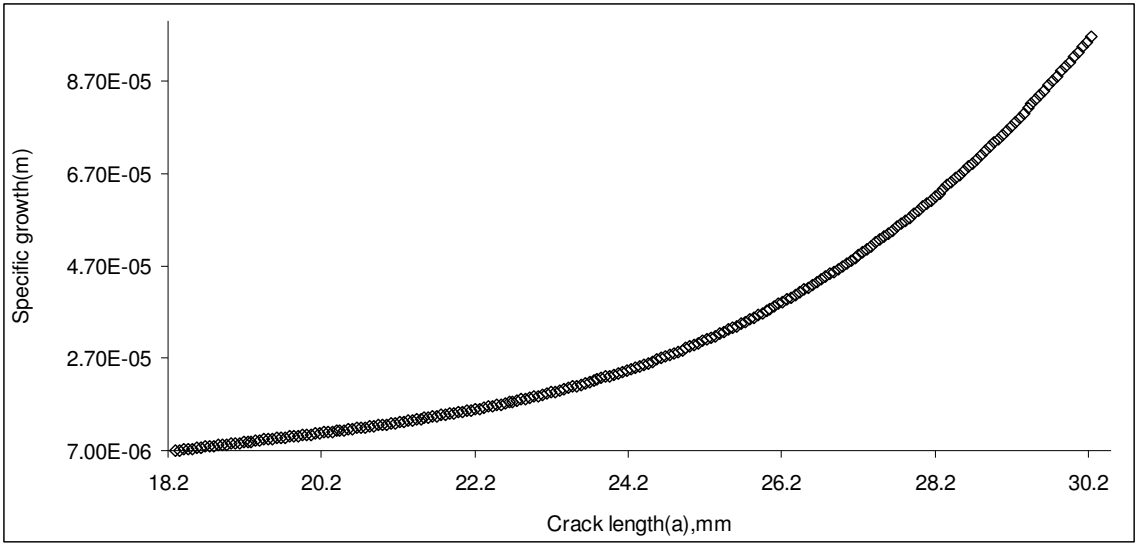


Fig. 5.5 – Variation of specific growth rate with crack length (7020-T7)

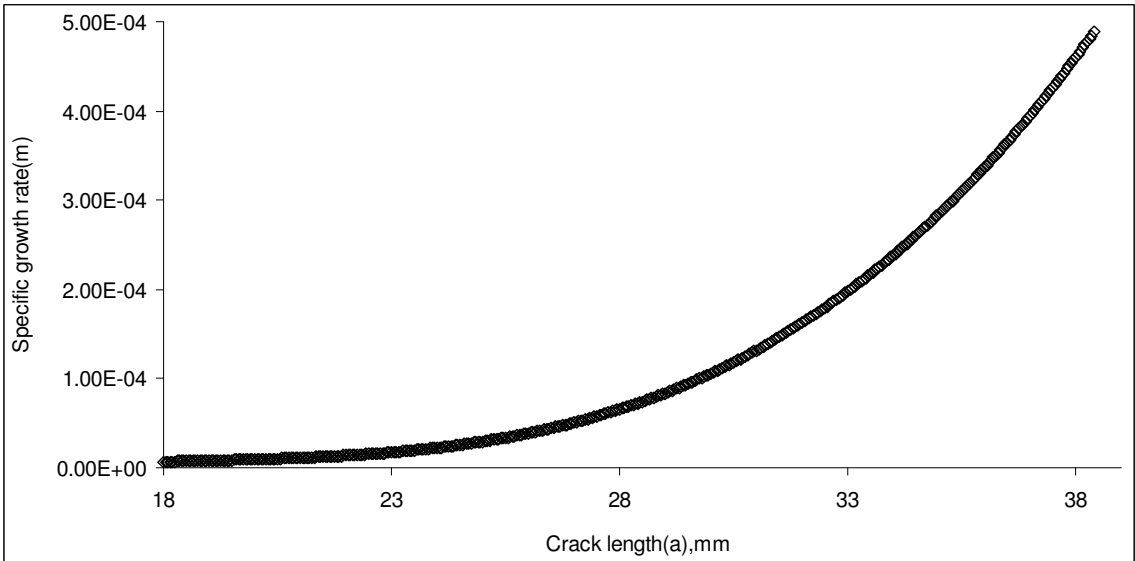


Fig. 5.6 – Variation of specific growth rate with crack length (2024-T3)

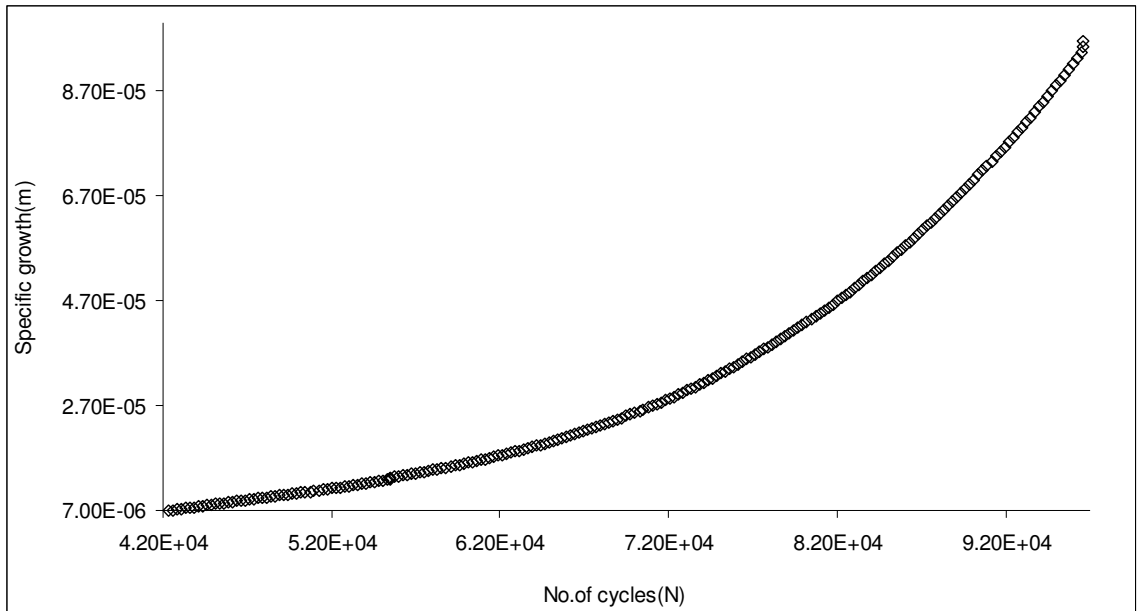


Fig. 5.7 – Variation of specific growth rate with number of cycles (7020-T7)

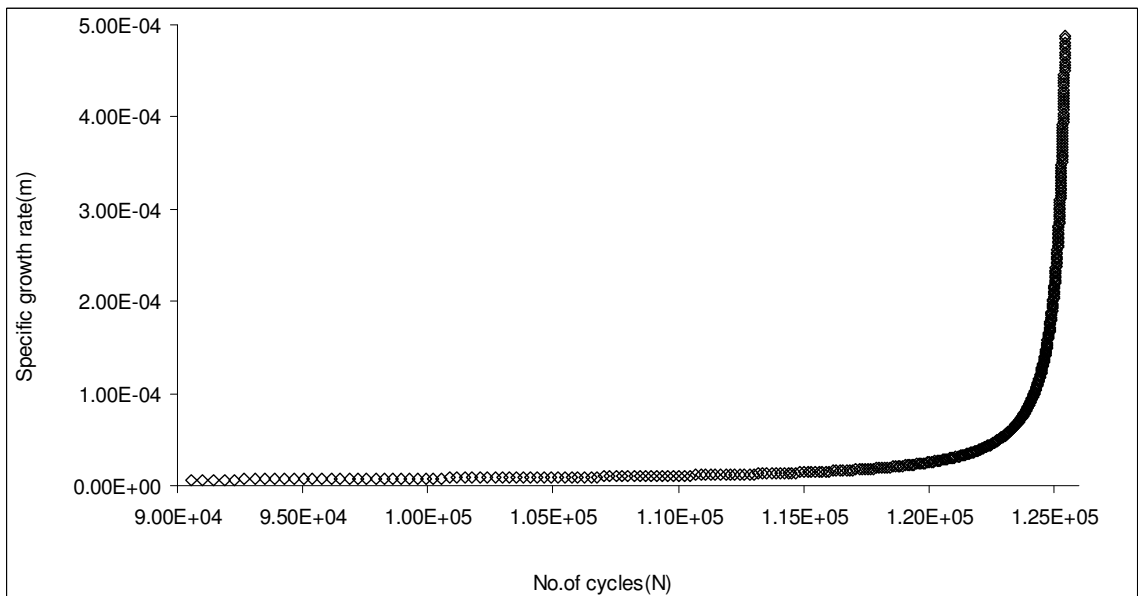


Fig. 5.8 – Variation of specific growth rate with number of cycles (2024-T3)

Set-2 (Varying R)

In the second set, the model result was tested for load ratio of 0.5. Table 5.7 presents the predicted and experimental fatigue lives for both the alloys. The predicted $a-N$ and also $da/dN-\Delta K$ curves are compared with experimental results in Figs. 5.9 to 5.12 respectively.

Table 5.7 – Predicted results of CAL (set-2)

Test specimen	Load ratio R	a_i mm	a_f mm	N_f^P kcycle	N_f^E kcycle
7020-T7	0.5	18.3	35.1	78.265	78.783
2024-T3	0.5	18.3	35.4	112.879	113.298

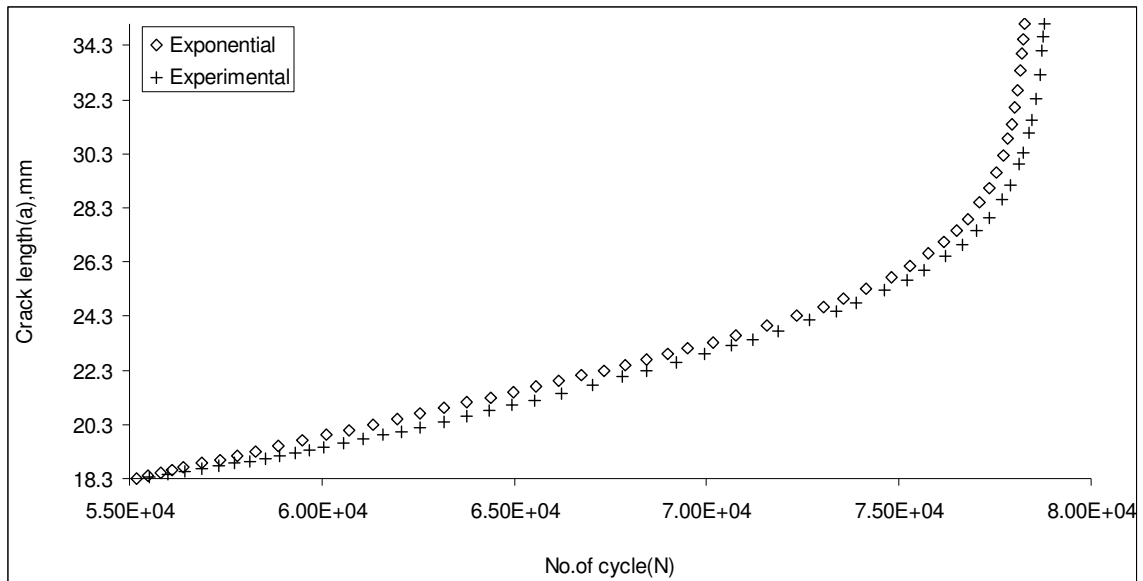


Fig. 5.9 – Crack length vs. number of cycle for load ratio 0.5 (7020-T7)

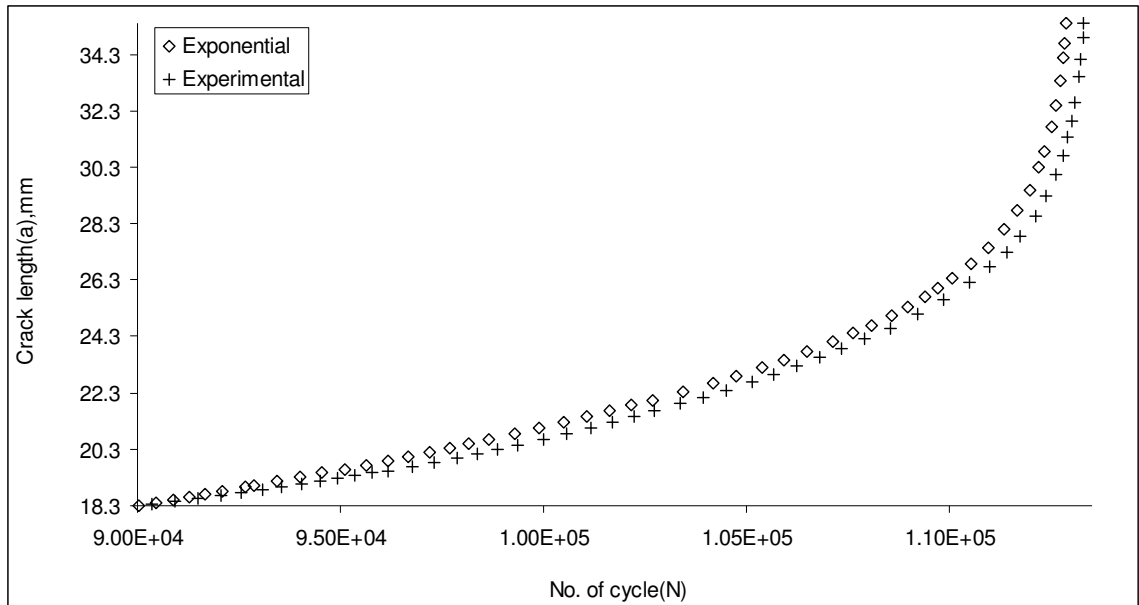


Fig. 5.10 – Crack length vs. number of cycle for load ratio 0.5 (2024-T3)

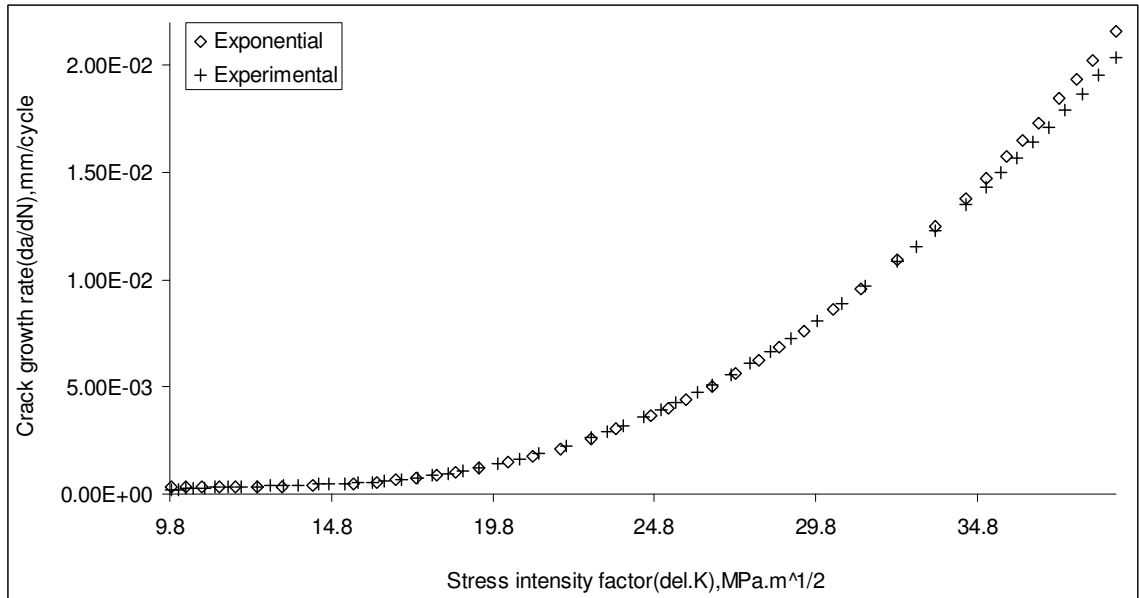


Fig. 5.11 – Crack growth rate vs. stress intensity range for load ratio 0.5 (7020-T7)

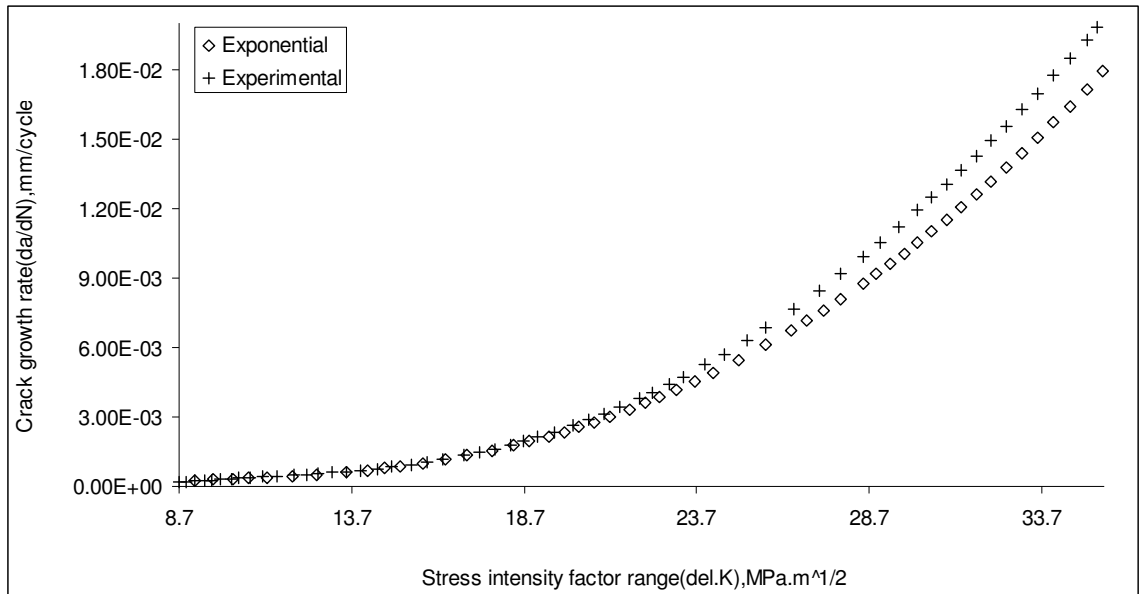


Fig. 5.12 – Crack growth rate vs. stress intensity range for load ratio 0.5 (2024-T3)

5.5 Modeling under Constant amplitude loading interspersed with mode-I spike overload

5.5.1 Model design

As already mentioned in Chapter-III, six specimens (from each alloy) were tested under the above loading condition with different overload ratios out of which five experimental results ($R^{ol} = 2.0, 2.25, 2.50, 2.60$ and 2.75 for 7020-T7 and $R^{ol} = 1.50, 1.75, 2.00, 2.25$ and 2.50 for 2024-T3) were taken for model formulation. The values of the specific growth rate were calculated from Eq. 5.9 as before and the values of the constants A', B', C' and D' for each overload ratios are tabulated in Tables 5.8 and 5.9 respectively for both the alloys.

Table 5.8 – Curve fitting constants of 7020-T7 aluminum alloy

Overload Ratio (R_{ol})	$A' \times 10^{-6}$	$B' \times 10^{-6}$	$C' \times 10^{-6}$	$D' \times 10^{-6}$
2.00	-68004	16721	-1149.9	24.582
2.25	-104212	25796	-1793.1	38.17
2.50	-136870	33690	-2398.5	52.668
2.60	-165538	41857	-3113.5	72.101
2.75	-166698	41801	-3084.1	70.865

Table 5.9 – Curve fitting constants of 2024-T3 aluminum alloy

Overload Ratio (R^{ol})	$A' \times 10^{-6}$	$B' \times 10^{-6}$	$C' \times 10^{-6}$	$D' \times 10^{-6}$
1.50	-22226	9137.4	-1088.20	41.208
1.75	-14173	6054.7	-709.26	25.827
2.00	-15258	5987.1	-545.09	12.189
2.25	-11951	4822.9	-521.37	16.770
2.50	-19774	8027.2	-896.03	30.197

It is observed that the values of the above constants differ according to different overload ratios (R^{ol}) since the amount of retardation depends on R^{ol} . Therefore, the above constants were correlated with R^{ol} by a 2nd degree polynomial through the following sets of equations:

$$A' = X_1(R^{ol})^2 + Y_1R^{ol} + Z_1 \quad (5.15)$$

$$B' = X_2(R^{ol})^2 + Y_2R^{ol} + Z_2 \quad (5.16)$$

$$C' = X_3(R^{ol})^2 + Y_3R^{ol} + Z_3 \quad (5.17)$$

$$D' = X_4(R^{ol})^2 + Y_4R^{ol} + Z_4 \quad (5.18)$$

where, $X_1, X_2, X_3, X_4, Y_1, Y_2, Y_3, Y_4$ are another set of curve fitting constants relating A', B', C' and D' with load ratio, R^{ol} . The generalized equation for specific growth rate (Eq. 5.8) is:

$$m_{ij} = \left\{ X_1(R^{ol})^2 + Y_1R^{ol} + Z_1 \right\}^3 + \left\{ X_2(R^{ol})^2 + Y_2R^{ol} + Z_2 \right\}^2 + \left\{ X_3(R^{ol})^2 + Y_3R^{ol} + Z_3 \right\} + \left\{ X_4(R^{ol})^2 + Y_4R^{ol} + Z_4 \right\} \quad (5.19)$$

The predicted values of m_{ij} for the tested specimens ($R^{ol}=2.35$ for 7020-T7 and 2.1 for 2024-T3) were calculated by putting their respective values of above constants in Eq. 5.19 separately for each material. Subsequently the predicted number of cycles was determined as per Eq. 5.9.

5.5.2 Model validation

The proposed model was tested by comparing experimental result and also the result obtained from Wheeler model with the predicted one for overload ratio of 2.35 for 7020-T7 and 2.1 for 2024-T3 respectively [139].

Comparison with experimental results

The comparison of the model results with the experimental findings is presented in Figs. 5.13 to 5.16 respectively for both the materials. The various values of the retardation parameters and also the number of cycles (i.e. fatigue life) are presented in Table 5.11.

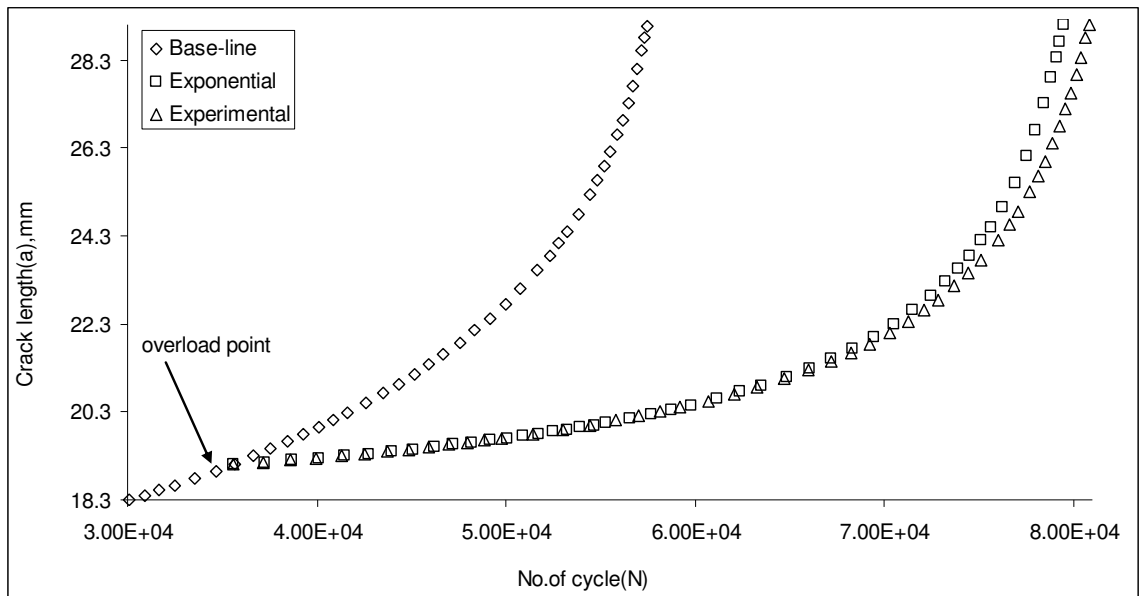


Fig. 5.13 – Predicted crack length vs. number of cycle for $R^{ol} = 2.35$ (7020-T7)

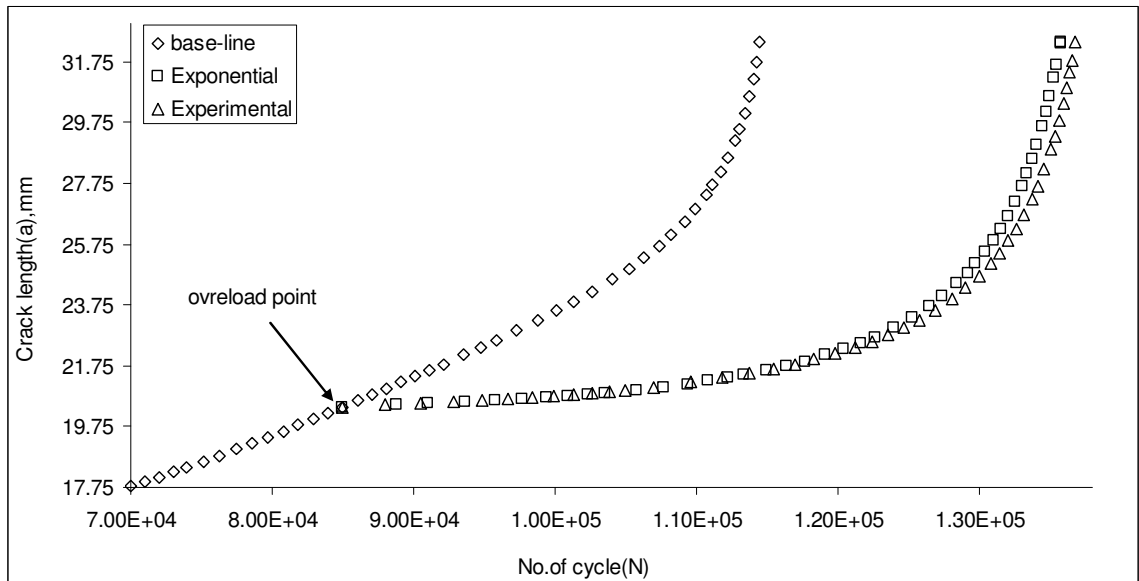


Fig. 5.14 – Predicted crack length vs. number of cycle for $R^{ol} = 2.10$ (2024-T3)

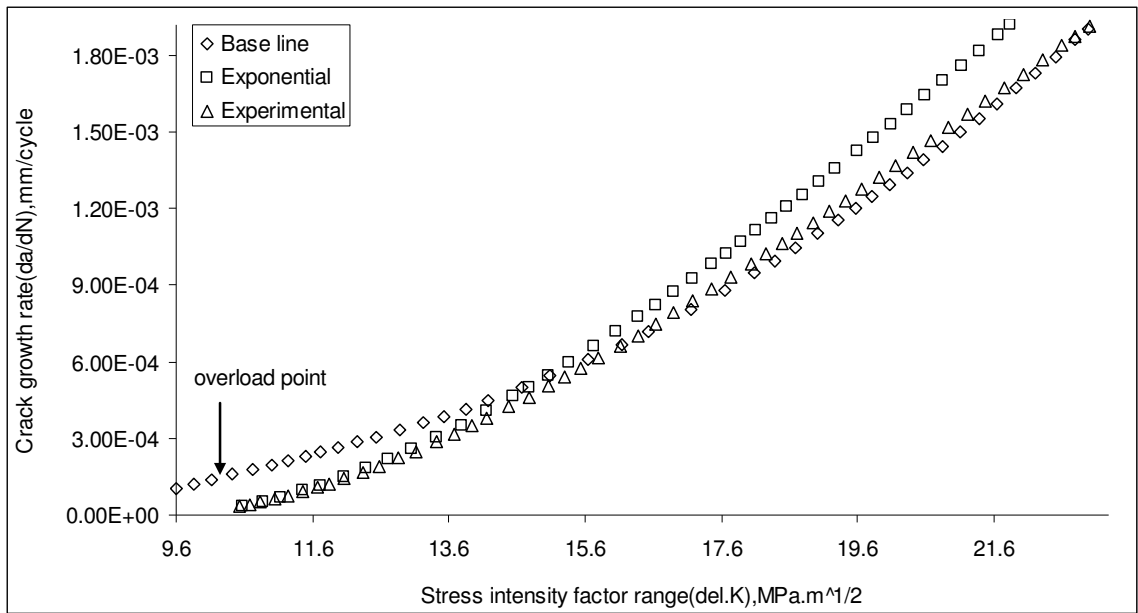


Fig. 5.15 – Predicted crack growth rate vs. stress intensity range for $R^{ol} = 2.35$ (7020-T7)

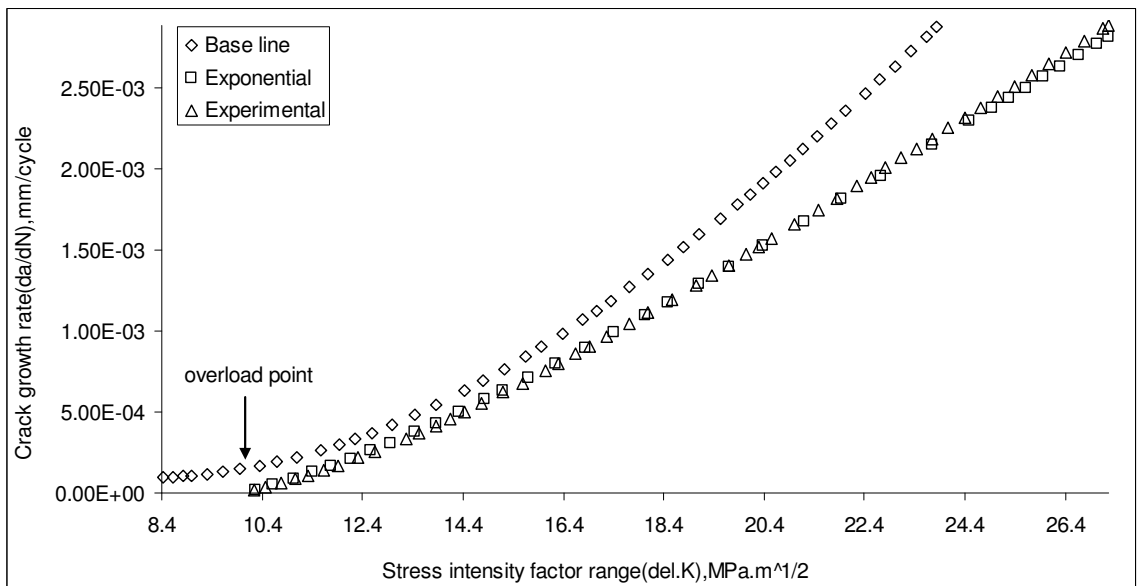


Fig. 5.16 – Predicted crack growth rate vs. stress intensity range for $R^{ol} = 2.10$ (2024-T3)

Comparison with ‘Wheeler Model’:

For determination of the various retardation parameters such as retarded crack length (a_d) and delay cycles (N_d) for Wheeler model, it was necessary to calculate its shaping exponent. The Wheeler model parameters are shown in Fig. 5.17.

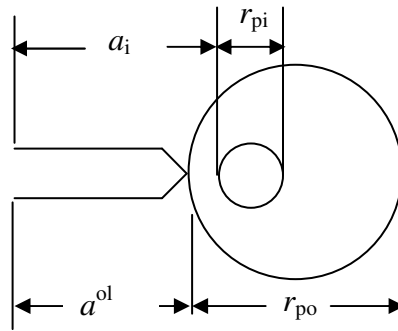


Fig. 5.17 – Plastic zone size definitions used in Wheeler's model

The Wheeler retardation relation for the delay in crack growth due to a single tensile overload is given by:

$$\left(\frac{da}{dN}\right)_{\text{retarded}} = (C_p)_i [C(\Delta K)^n] \quad (5.20)$$

where, $(C_p)_i$ is the retardation parameter and is given by

$$(C_p)_i = \left(\frac{r_{pi}}{[a_{ol} + r_{p0} - a_i]}\right)^p \quad (5.21)$$

where, p = empirically determined shaping parameter

a^{ol} = crack length at overload

and r_{p0} = overload plastic zone size, that was calculated, assuming plane stress loading using the following expression:

$$r_{p0} = \frac{1}{\pi} \left(\frac{K^{ol}}{\sigma_{ys}}\right)^2 \quad (5.22)$$

Assuming plane stress loading conditions, the current cyclic plastic zone r_{pi} was calculated from the expression given below:

$$r_{pi} = \frac{1}{\pi} \left(\frac{\Delta K}{2\sigma_{ys}}\right)^2 \quad (5.23)$$

The presence of a net compressive residual stress field around the crack-tip reduces the usual size of the plane stress cyclic plastic zone size. Therefore, Ray et al. [142] introduced

a plastic zone correction factor λ in the expression of the instantaneous cyclic plane stress plastic zone size in a compressive stress field.

$$r_{pi} = \lambda \left(\frac{1}{\pi} \right) \left(\frac{\Delta K}{2\sigma_{ys}} \right)^2 \quad (5.24)$$

Also from Eq. 5.20

$$C_{pi} = \frac{(da/dN)_{retard}}{C(\Delta K)^n} = \frac{(da/dN)_{retard}}{(da/dN)_{a=a_0}} \quad (5.25)$$

Equation 5.21 is now written as

$$(C_p)_i = \left(\frac{\lambda r_{pi}}{[a_{ol} + r_{po} - a_i]} \right)^p = \gamma \left[\frac{r_{pi}}{(a^{ol} + r_{po} - a_i)} \right]^p \quad (5.26)$$

where, γ is a correction factor which is expressed as $\gamma = \lambda^p$.

The values of γ , λ and p calculated using Eqs. 5.24 and 5.26 are presented in Table 5.10 for tested specimens of both the materials.

Table 5.10 – Material parameters of Paris-Erdogan and modified Wheeler model

Test sample	C	n	λ	p	γ
7020-T7	6×10^{-8}	3.14763	3.5931	0.4246	1.7213
2024-T3	6×10^{-8}	3.270	0.7385	0.3748	0.8926

Table 5.11 – Experimental results of the tested specimens

Test sample	a_d^P mm	a_d^W mm	a_d^E mm	N_d^P k. cycle	N_d^W k. cycle	N_d^E k. cycle	N_f^P k. cycle	N_f^E k. cycle
7020-T7	2.10	2.20	2.13	29.89	29.80	30.51	79.46	80.82
2024-T3	2.06	2.45	2.18	36.65	34.52	37.60	135.75	136.80

Using these values, the crack lengths and the corresponding number of cycles were calculated. The resulting $a-N$ and $da/dN-\Delta K$ curves are presented in Figs. 5.18 to 5.21 respectively along with their experimental and exponential model results for comparison.

The different calculated retardation parameters are given in Table 5.11 for the quantitative comparison of the predicted results.

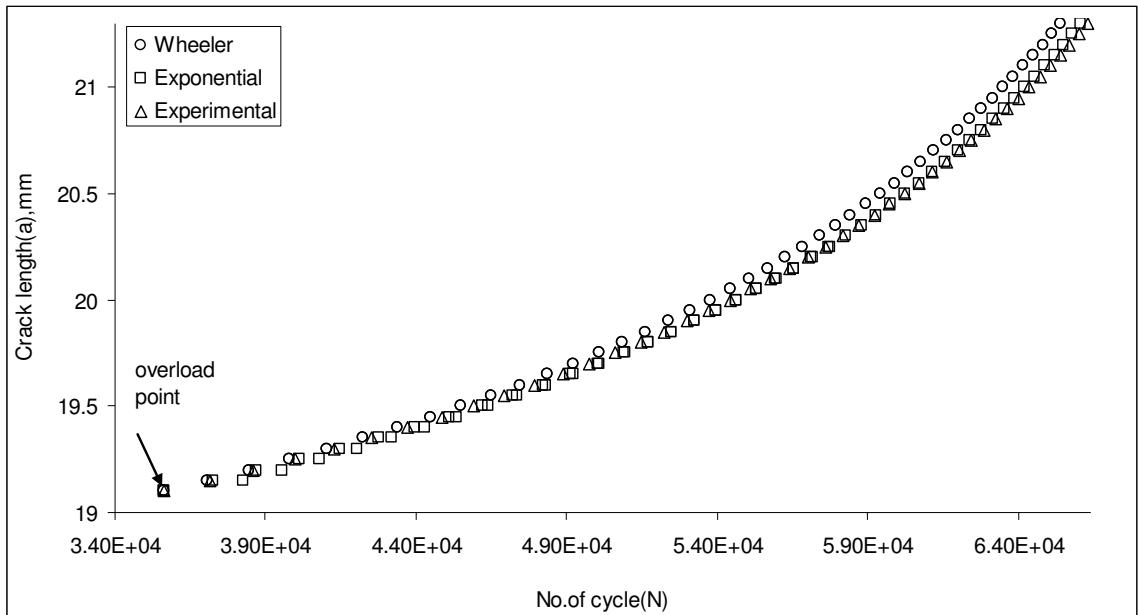


Fig. 5.18 – Superimposed a - N curve of 7020-T7 (Wheeler, predicted and experimental)

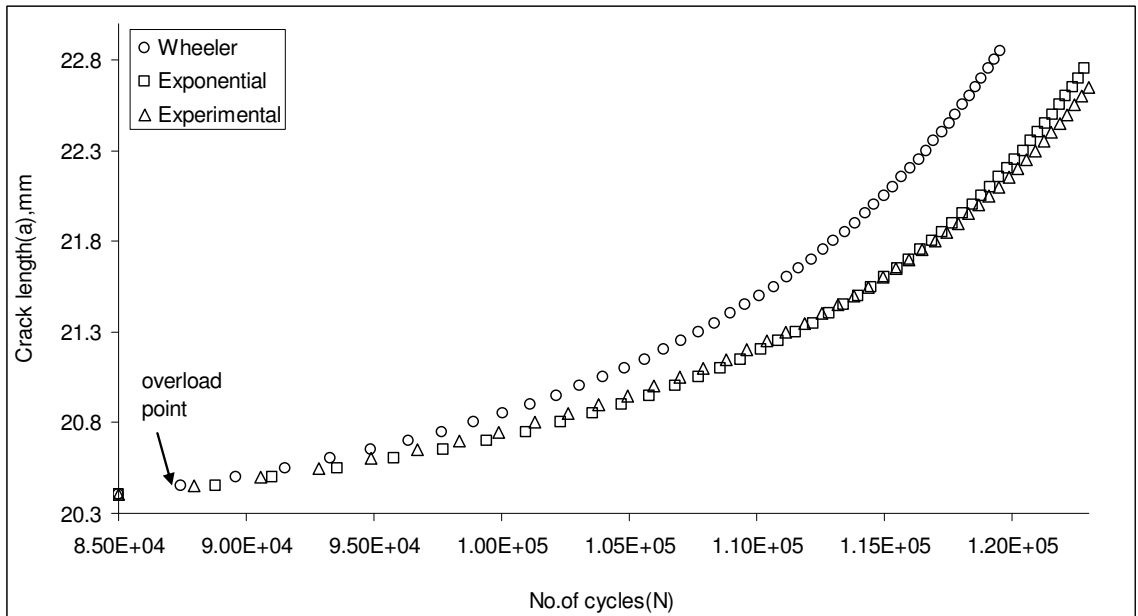


Fig. 5.19 – Superimposed a - N curve of 2024-T3 (Wheeler, predicted and experimental)

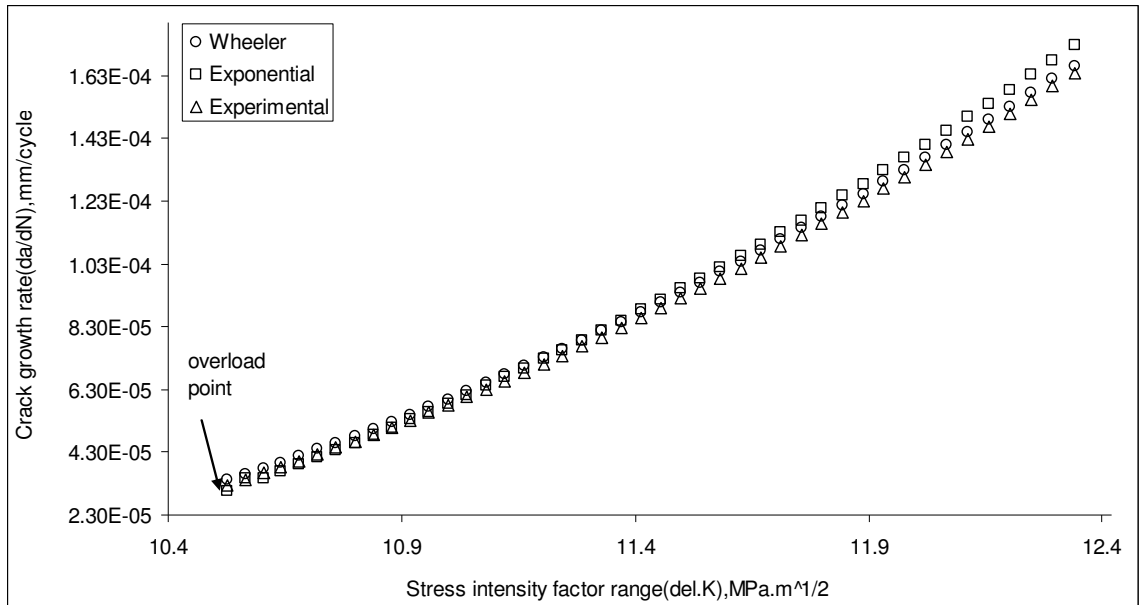


Fig. 5.20- $da/dN - \Delta K$ curve of 7020-T7 (Wheeler, predicted and experimental)

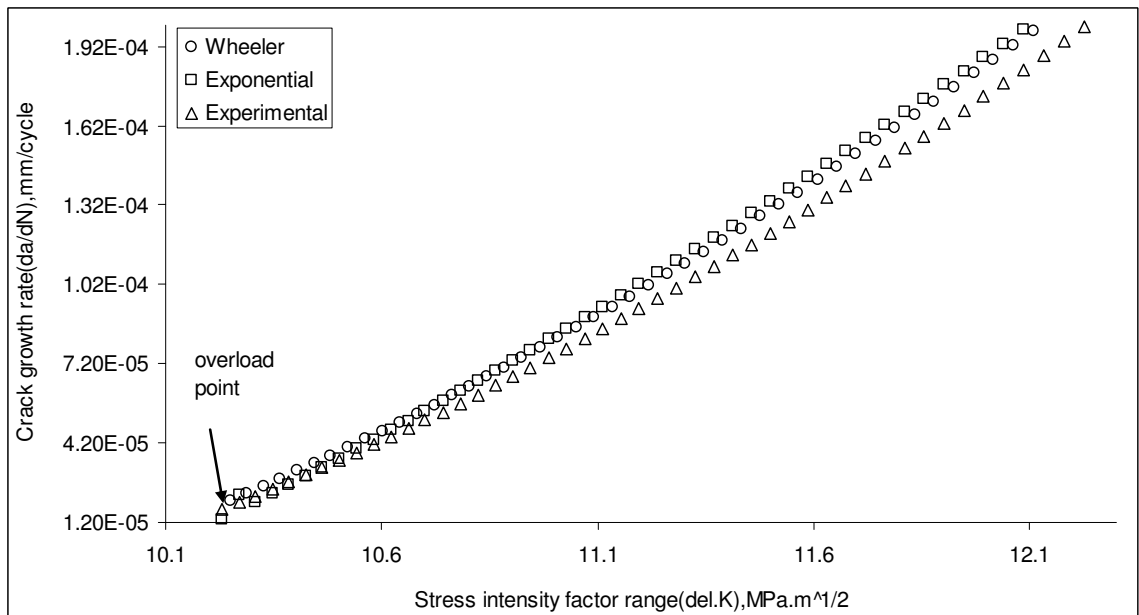


Fig. 5.21- $da/dN - \Delta K$ curve of 2024-T3 (Wheeler, predicted and experimental)

5.6 Modeling under constant amplitude loading interspersed with mixed mode (I and II) spike overload

5.6.1 Model design

In this case, six specimens (from each alloy) were tested under the above loading condition with fixed overload ratio ($R^{ol} = 2.5$) but at different overloading angles (β) out of which five experimental results ($\beta = 0^\circ, 18^\circ, 36^\circ, 72^\circ$ and 90° for both the alloys) were taken for model formulation and the 5th one i.e. $\beta = 54^\circ$ was left for validation. The values of the specific growth rate were calculated from Eq. 5.9 in similar manner as before and the values of the constants A' , B' , C' and D' for each overloading angles are tabulated in Tables 5.12 and 5.13 respectively for both the alloys along with their corresponding mode-mixity.

Table 5.12 – Curve-fitting constants of 7020-T7 alloy

Overload Angle	Mode- mixity	$A' \times 10^{-6}$	$B' \times 10^{-6}$	$C' \times 10^{-6}$	$D' \times 10^{-6}$
90°	1	-539649	145310	-10994.00	259.79
72°	0.755	-502381	134367	-9829.70	220.57
36°	0.421	-398478	104031	-6853.30	126.11
18°	0.245	-375919	98609	-6562.20	122.74
0°	0	-352141	91313	-5839.90	97.56

Table 5.13 – Curve fitting constants of 2024-T3 alloy

Overload Angle	Mode- mixity	$A' \times 10^{-6}$	$B' \times 10^{-6}$	$C' \times 10^{-6}$	$D' \times 10^{-6}$
90°	1	-317743	130554	-14954.0	526.86
72°	0.755	-161221	66285	-7576.1	270.48
36°	0.421	-123760	49826	-5091.6	148.40
18°	0.245	-131140	53025	-5560.5	170.22
0°	0	-184424	75502	-8449.2	284.73

It is observed that the values of the above constants differ according to different mode-mixity $\left(\frac{K_{II}}{K_I + K_{II}}\right)$. Because of such variations the said constants were correlated with mode-mixity, to give the following sets of equations:

$$A' = X_1 \left[\frac{K_{II}}{K_I + K_{II}} \right]^2 + Y_1 \left[\frac{K_{II}}{K_I + K_{II}} \right] + Z_1 \quad (5.27)$$

$$B' = X_2 \left[\frac{K_{II}}{K_I + K_{II}} \right]^2 + Y_2 \left[\frac{K_{II}}{K_I + K_{II}} \right] + Z_2 \quad (5.28)$$

$$C' = X_3 \left[\frac{K_{II}}{K_I + K_{II}} \right]^2 + Y_3 \left[\frac{K_{II}}{K_I + K_{II}} \right] + Z_3 \quad (5.29)$$

$$D' = X_4 \left[\frac{K_{II}}{K_I + K_{II}} \right]^2 + Y_4 \left[\frac{K_{II}}{K_I + K_{II}} \right] + Z_4 \quad (5.30)$$

where, $X_1, X_2, X_3, X_4, Y_1, Y_2, Y_3, Y_4$ are another set of curve fitting constants relating A', B', C' and D' with mode mixity. The generalized equation for specific growth rate (Eq. 5.8) is:

$$m_{ij} = \left\{ X_1 \left[\frac{K_{II}}{K_I + K_{II}} \right]^2 + Y_1 \left[\frac{K_{II}}{K_I + K_{II}} \right] + Z_1 \right\} l^3 + \left\{ X_2 \left[\frac{K_{II}}{K_I + K_{II}} \right]^2 + Y_2 \left[\frac{K_{II}}{K_I + K_{II}} \right] + Z_2 \right\} l^2 + \left\{ X_3 \left[\frac{K_{II}}{K_I + K_{II}} \right]^2 + Y_3 \left[\frac{K_{II}}{K_I + K_{II}} \right] + Z_3 \right\} l + \left\{ X_4 \left[\frac{K_{II}}{K_I + K_{II}} \right]^2 + Y_4 \left[\frac{K_{II}}{K_I + K_{II}} \right] + Z_4 \right\} \quad (5.31)$$

The predicted values of ' m_{ij} ' for the tested specimens ($\beta = 54^\circ$) were calculated by putting the values of different constants in Eq. 5.31 separately for each material. Subsequently the predicted number of cycles was determined using Eq. 5.9.

5.6.2 Model validation

The proposed model was tested for overload angle of 54° for both the materials and the predicted results are compared with the experimental data (Figs. 5.22 to 5.29) [140]. The predicted fatigue life along with the retardation parameters (i.e. a_d and N_d) are tabulated in Table 5.14.

Table 5.14 – Experimental results of the tested specimens

Test sample	a_d^P mm	a_d^E mm	N_d^P kcycle	N_d^E kcycle	N_f^P kcycle	N_f^E kcycle
7020 T7	1.978	1.994	21.49	21.750	74.60	74.78
2024 T3	2.274	2.300	19.564	20.019	118.22	118.48

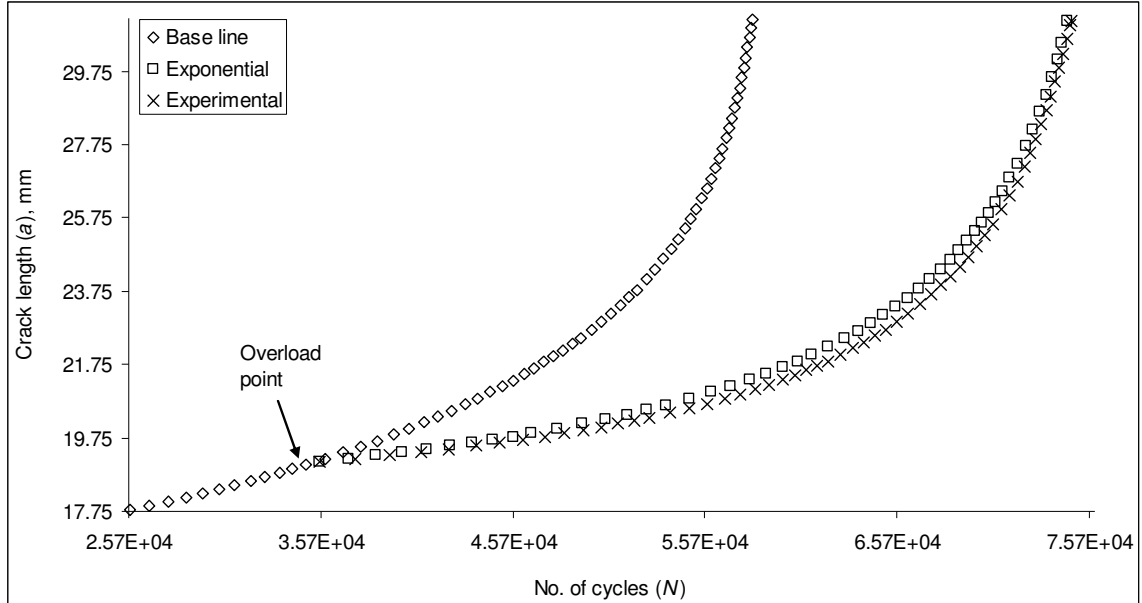


Fig. 5.22 – Comparison of predicted and experimental $a-N$ curves for 54° (7020-T7)

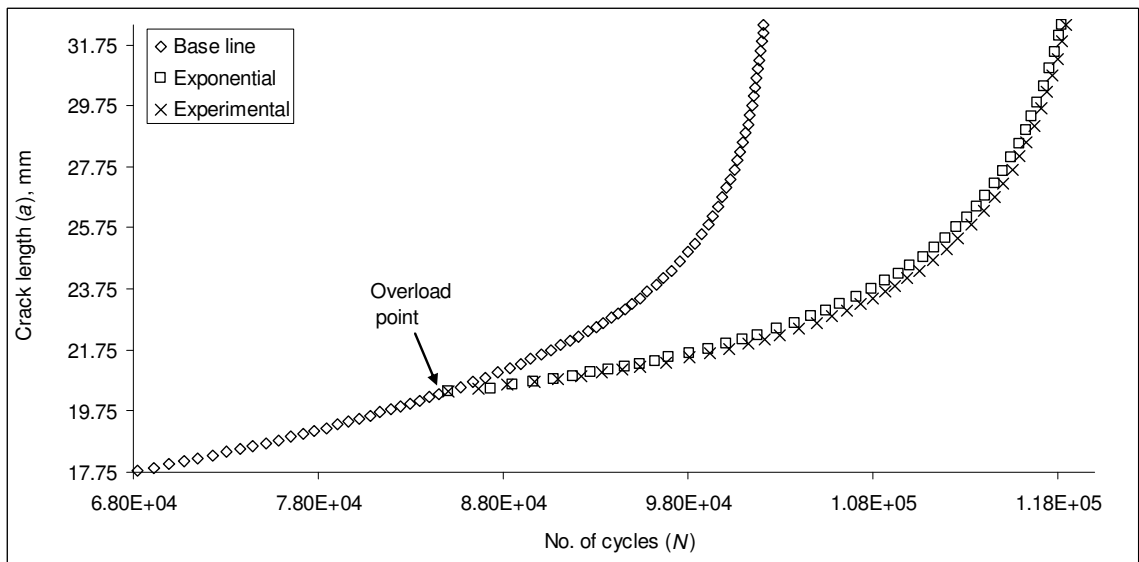


Fig. 5.23 – Comparison of predicted and experimental $a-N$ curves for 54° (2024-T3)

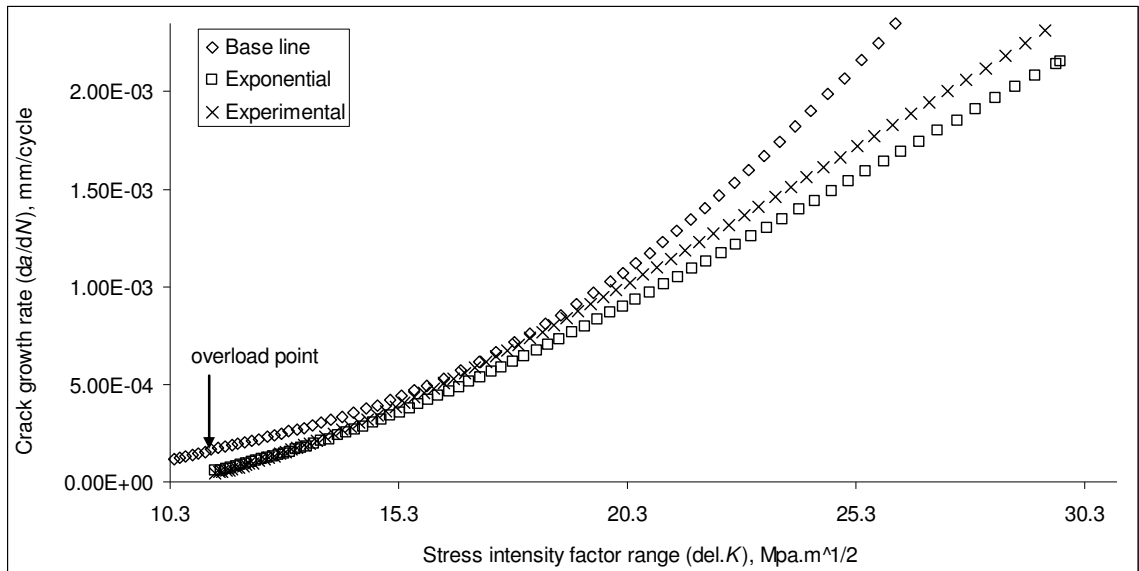


Fig. 5.24 – Predicted and experimental crack growth rate for $\beta = 54^\circ$ (7020-T7)

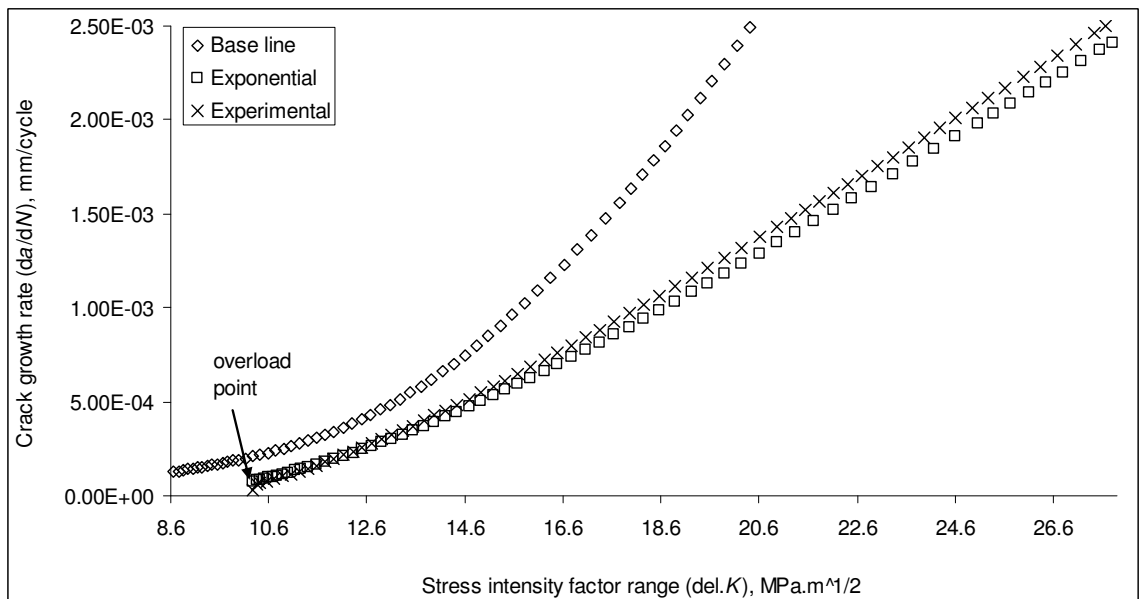


Fig. 5.25 – Predicted and experimental crack growth rate for $\beta = 54^\circ$ (2024-T3)

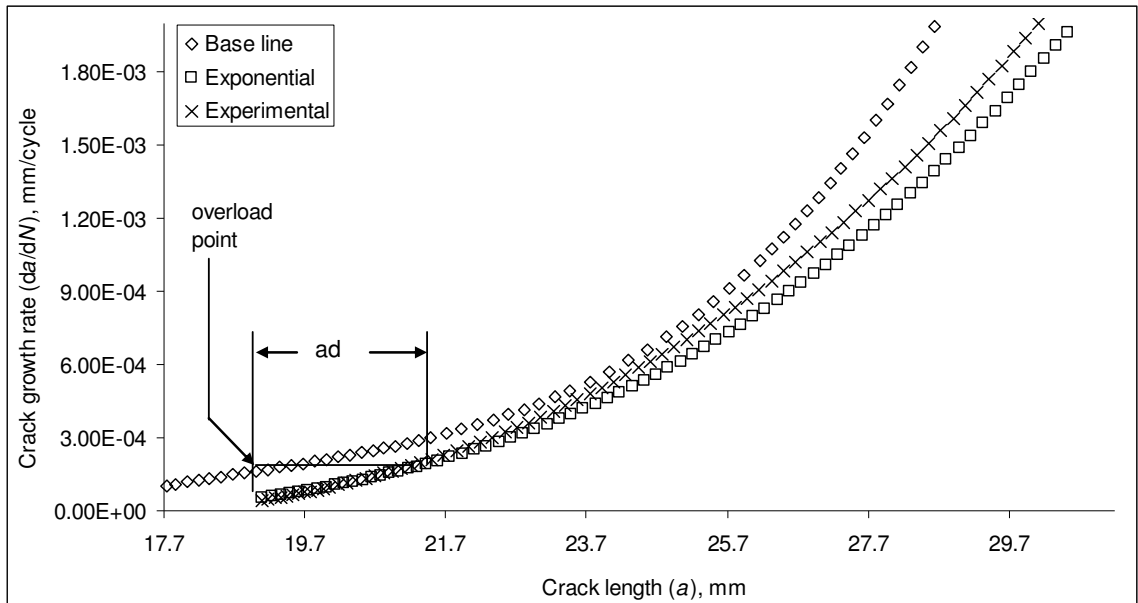


Fig. 5.26 – Predicted and experimental retarded crack length for $\beta = 54^\circ$ (7020-T7)

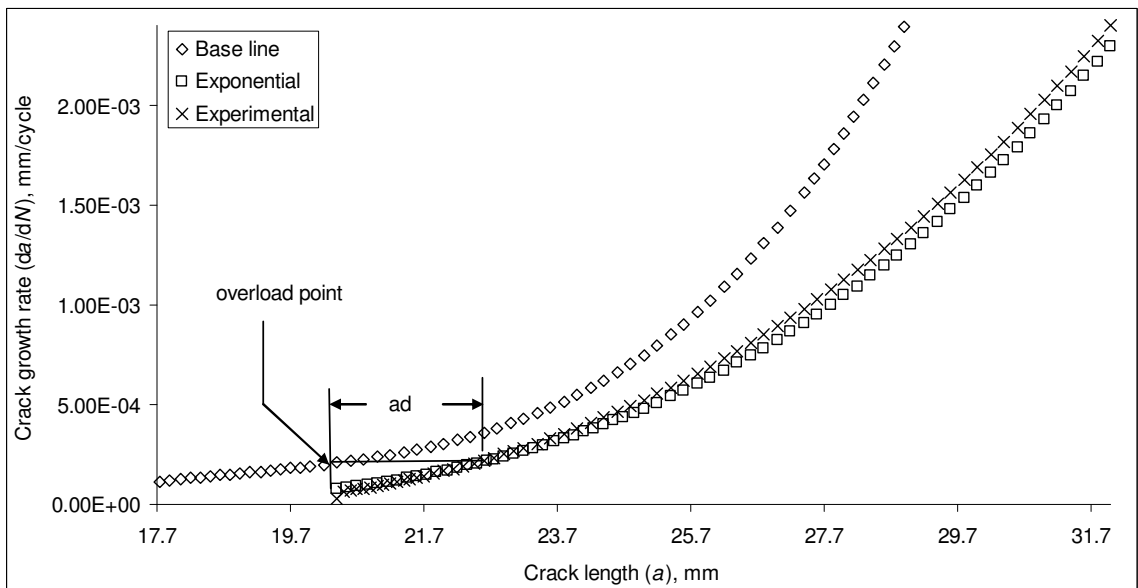


Fig. 5.27 – Predicted and experimental retarded crack length for $\beta = 54^\circ$ (2024-T3)

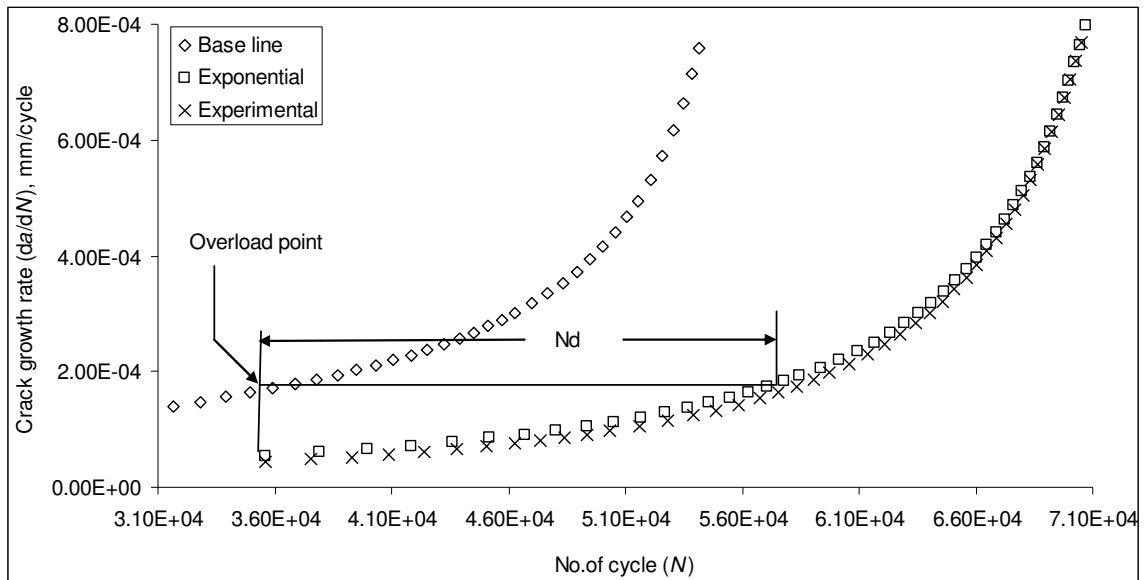


Fig. 5.28 – Predicted and experimental delay cycle for $\beta = 54^\circ$ (7020-T7)

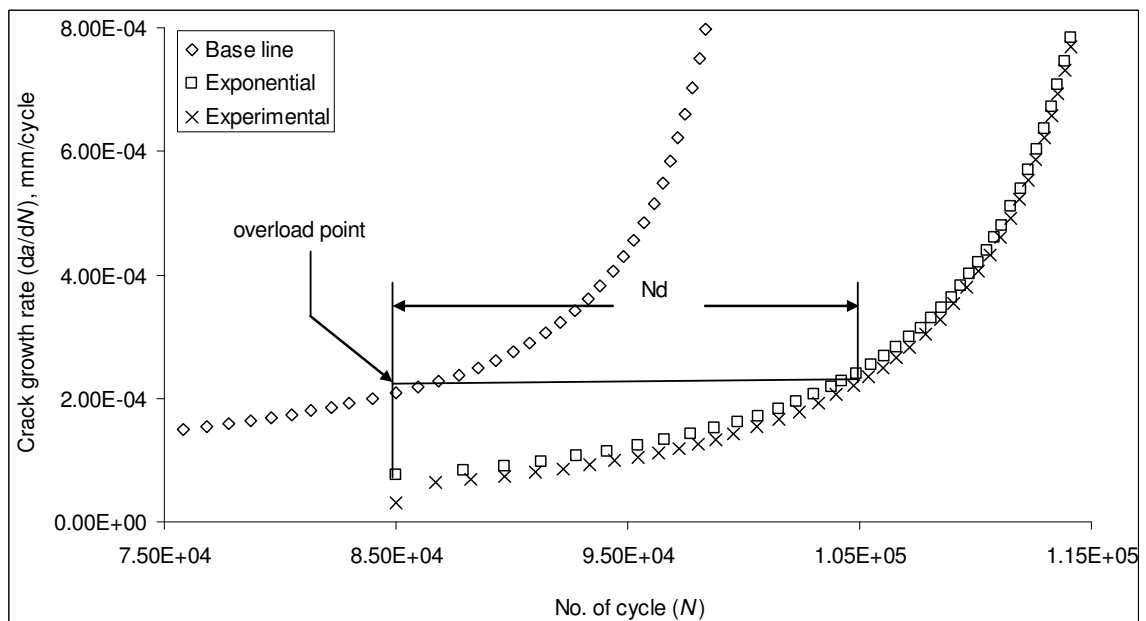


Fig. 5.29 – Predicted and experimental delay cycle for $\beta = 54^\circ$ (2024-T3)

CHAPTER VI

PREDICTION OF FATIGUE LIFE BY ARTIFICIAL NEURAL NETWORK (ANN)

6.1 Introduction

As discussed in chapter II, artificial neural network (ANN) is one of the powerful and versatile soft-computing methods in modeling multivariate complex problems in a number of engineering fields including the field of fatigue. In the present investigation, a multi-layered, feed-forward ANN architecture was developed and implemented for fatigue life prediction under different loading conditions such as constant amplitude loading (variable load ratios) and constant amplitude loading interspersed with mode-I and mixed mode (I and II) spike load. The model results were compared with the experimental data.

6.2 Background

The term “neural network” refers to a collection of neurons, their connections and the connection strengths between them. The knowledge is acquired during the training process by correcting the corresponding weights so as to minimize an error function. There are three types of learning in ANN technology: supervised, unsupervised and reinforcement. In case of supervised learning (learning with a teacher), the network is trained by optimizing corresponding weights in such a way that the significant outputs can be obtained for the inputs not belonging to the training set. The unsupervised training is based on organizing the structure so that similar stimuli activate similar neurons where there is no pre-defined output and the network finds differences and affinities between the inputs. The reinforcement learning, which is a particular form of supervised training attempts to learn input-output vectors by trial and error through maximizing a performance function (named reinforcement signal).

Back propagation networks are in fact the powerful networks which refer to a multi-layered, feed-forward perceptron trained with an error-back propagation algorithm (error minimization technique). The architecture of a simple back propagation ANN is a collection of nodes distributed over a layer of input neurons, one or more layers of hidden neurons and a layer of output neurons. Neurons in each layer are interconnected to

subsequent layer neurons with links, each of which carries a weight that describes the strength of that connection. Various non-linear activation functions, such as sigmoidal, \tanh or radial (Gaussian) are used to model the neuron activity. Inputs are propagated forward through each layer of the network to emerge as outputs. The errors between those outputs and the target (desired output) are then propagated backward through the network and then connection weights are adjusted so as to minimize the error.

6.3 Model formulation

The neural network used in the present investigation is a multi-layer feed forward perceptron [65] trained with the standard back propagation algorithm [143]. It consists of one input layer, one output layer and seven hidden layers. Hence, the total numbers of layers in the network are nine. The chosen numbers of layers have been selected empirically so as to facilitate training. The three input parameters are associated with the input layer whereas the output layer consists of one output parameter. The neurons associated with the input and output layers are three and one respectively. The neurons in seven hidden layers are twelve, twenty four, hundred, thirty five, and eight respectively. These are taken in order to give the neural network a diamond shape as shown in Fig. 6.1.

All the training tests have been performed in MATLAB environment. During training and during validation, the input patterns fed to the neural network comprise the following components;

$$y_1^{\{1\}} = 1^{\text{st}} \text{ input} \quad (6.1)$$

$$y_2^{\{1\}} = 2^{\text{nd}} \text{ input} \quad (6.2)$$

$$y_3^{\{1\}} = 3^{\text{rd}} \text{ input} \quad (6.3)$$

These input values are distributed to the hidden neurons which generate outputs given by:

$$y_s^{\{\text{lay}\}} = f(v_s^{\{\text{lay}\}}) \quad (6.4)$$

$$\text{where, } v_s^{\{\text{lay}\}} = \sum_r W_{sr}^{\{\text{lay}\}} \cdot y_r^{\{\text{lay}-1\}} \quad (6.5)$$

lay = layer number (2 to 8)

s = label for s^{th} neuron in the hidden layer 'lay'

r = label for r^{th} neuron in hidden layer 'lay-1'

$W_{sr}^{\{lay\}}$ = weight of the connection from neuron r in layer 'lay-1' to neuron ' s ' in layer 'lay'

$f(.)$ = activation function, chosen in this work as the hyperbolic tangent function.

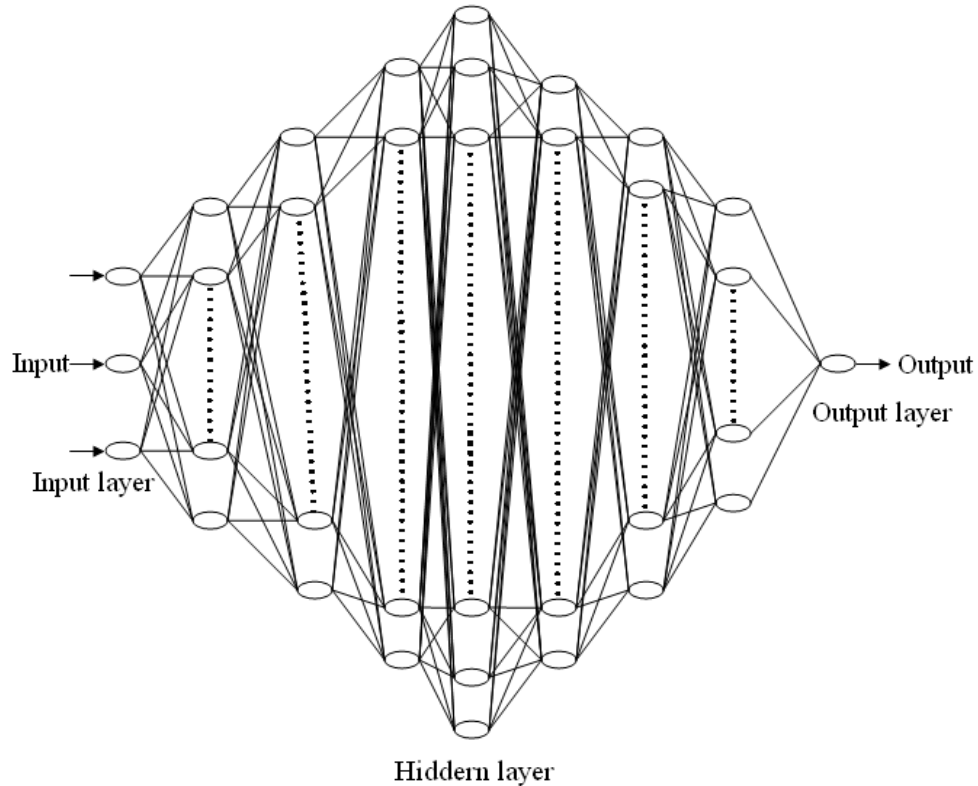


Fig. 6.1 – ANN architecture

During training, the network actual output θ_{actual} , may differ from the desired output $\theta_{desired}$ as specified in the training pattern presented to the network. A measure of the performance of the network is the instantaneous sum-squared difference between $\theta_{desired}$ and θ_{actual} for the set of presented training patterns:

$$E_{tr} = \frac{1}{2} \sum_{\substack{all \\ training \\ patterns}} (\theta_{desired} - \theta_{actual})^2 \quad (6.6)$$

The error back- propagation method is employed to obtain the network [65]. This method requires the computation of local error gradients in order to determine appropriate weight corrections to reduce ' E_{tr} '. For the output layer, the error gradient $\delta^{\{9\}}$ is:

$$\delta^{\{9\}} = f'(V_1^9) (\theta_{desired} - \theta_{actual}) \quad (6.7)$$

The local gradient for neurons in hidden layer {lay} is given by:

$$\delta_s^{\{lay\}} = f' \left(V_s^{\{lay\}} \right) \left(\sum_k \delta_k^{\{lay+1\}} W_{ks}^{\{lay+1\}} \right) \quad (6.8)$$

The synaptic weights are updated according to the following expressions:

$$W_{sr}(t+1) = W_{sr}(t) + \Delta W_{sr}(t+1) \quad (6.9)$$

$$\text{and } \Delta W_{sr}(t+1) = \alpha \Delta W_{sr}(t) + \eta \delta_s^{\{lay\}} y_r^{\{lay-1\}} \quad (6.10)$$

where, α = momentum coefficient (chosen empirically as 0.2 in this work)

η = learning rate (chosen empirically as 0.35 in this work)

t = iteration number, each iteration consisting of the presentation of a training pattern and correction of the weights.

The final output from the neural network is:

$$\theta_{actual} = f \left(V_1^{\{9\}} \right) \quad (6.11)$$

where,

$$V_1^{\{9\}} = \sum_r W_{1r}^{\{9\}} y_r^{\{8\}} \quad (6.12)$$

6.4 Modeling under constant amplitude loading (CAL)

In case of constant amplitude loading, ANN was applied to predict the fatigue life in Set-2 (variable load ratio condition) of fatigue crack growth test (Chapter III). The two crack driving forces: stress intensity factor range (ΔK) and maximum stress intensity factor (K_{max}) were chosen as the two inputs as per 'Unified Approach'. The third input chosen was the load ratio (R) because of its influence on crack growth rate in case of constant amplitude loading (Fig. 4.8 and 4.9). Crack growth rate (da/dN) was selected as the output.

The three input parameters associated with the input layer were as follows;

Stress intensity factor range = "sifr"; Maximum stress intensity factor = "msif"; load ratio = "lr".

The output layer had one output parameter i.e. crack growth rate = "cgr".

6.4.1 Application design

Proper selection of input and output parameters and their normalization are the two primary objectives to design a suitable ANN architecture. The proposed ANN model was developed using back propagation architecture with three inputs and one output. As far as normalization of input and output parameters are concerned, classical normalization, where the range is scaled between 0 and 1, may not be applicable in every ANN model. In order to make the input amenable for successful learning to minimize the overall sum-squared error, the two input parameters ΔK and K_{\max} were normalized between 1 and 4, while the other one, load ratio (R), was normalized between 1 and 3. Similarly the output i.e. crack growth rate was normalized between 0 and 3 for network training and testing. The inputs and outputs of the training sets (TS) were constituted from $50 \times 50 \times 50$ experimental values for each of the load ratios 0, 0.2, 0.4, 0.6 and 0.8 in case of both 7020-T7 and 2024-T3 Al-alloys respectively. Figs. 6.2 and 6.3 illustrate the mean square error (MSE) curves during the training of the model. The performance of the trained ANN model is presented in Table 6.1.

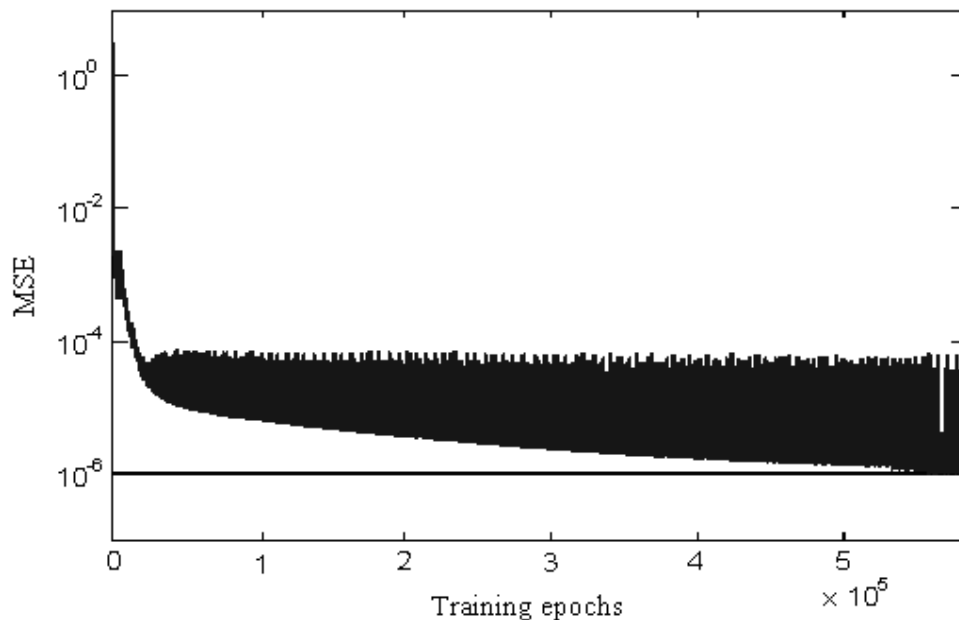


Fig. 6.2 – MSE curve obtained during training of ANN for Al 7020-T7

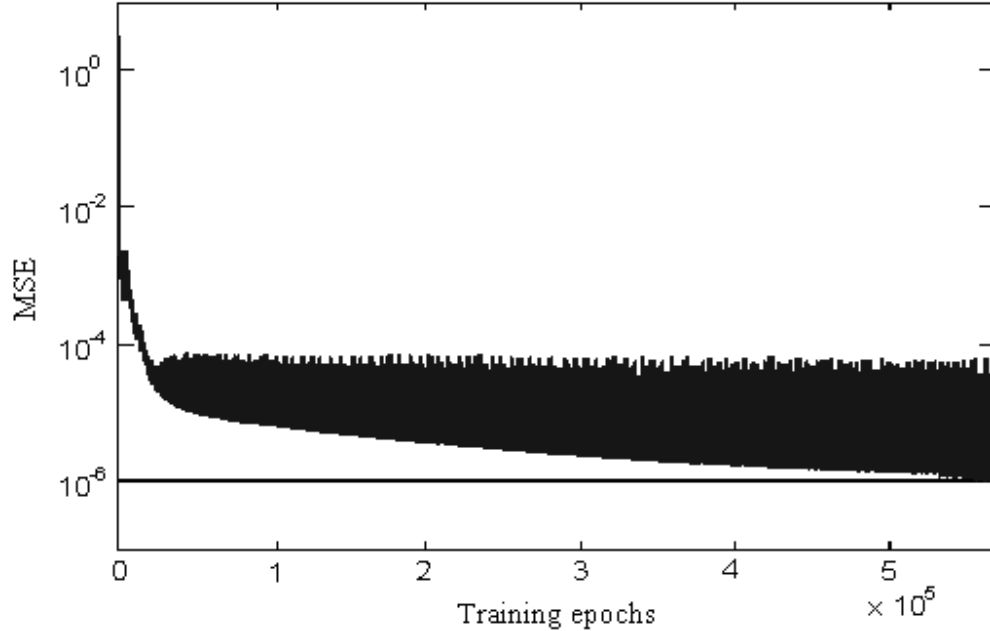


Fig. 6.3 – MSE curve obtained during training of ANN for Al 2024-T3

Table 6.1 – Performance of ANN model during training

Material	Momentum Coefficient	Learning rate	Hidden neurons	MSE	Training epochs	Computational Time (Min.)
7020-T7	0.2	0.35	179	1.278×10^{-6}	5.919×10^5	697
2024-T3	0.2	0.35	179	1.108×10^{-6}	5.627×10^5	626

6.4.2 Model validation

The adopted multi-layer perceptron (MLP) neural network model was applied to simulate the crack growth rate of an unknown set of load ratio ($R = 0.5$) as validation set (VS). The inputs were fed to the trained ANN model in order to predict the corresponding outputs for the validation set. The predicted results are presented in Figs. 6.4 and 6.5 respectively along with the experimental data for comparison. It is observed that the simulated $da/dN-\Delta K$ points follow the experimental ones quite well. The number of cycles was calculated from the simulated crack growth rates by taking the first experimental ‘ a ’ and ‘ N ’ values as the initial values and assuming an incremental crack length of 0.05 mm in steps in excel sheet as per following equation:

$$N_j = \frac{a_j - a_i}{da/dN} + N_i \quad (6.13)$$

The predicted $a-N$ values of the ANN model are compared with the experimental data in Figs. 6.6 and 6.7 respectively for both the materials. The predicted numbers of cycles (fatigue life) along with their percentage deviation from experimental data are presented in Table 6.2.

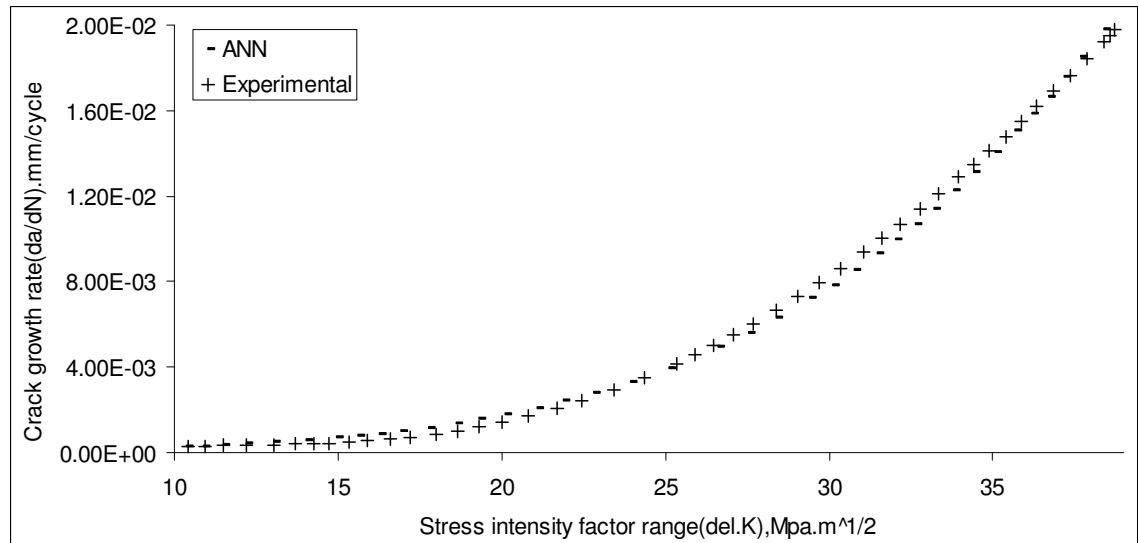


Fig. 6.4 – Predicted (ANN) and experimental crack growth rate for $R = 0.5$ (7020-T7)

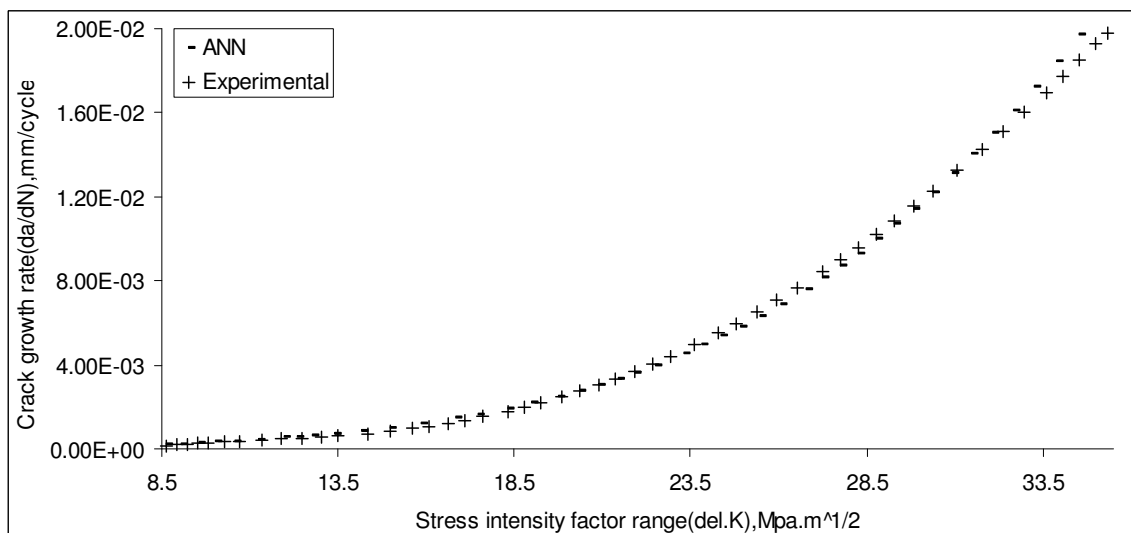


Fig. 6.5 – Predicted (ANN) and experimental crack growth rate for $R = 0.5$ (2024-T3)

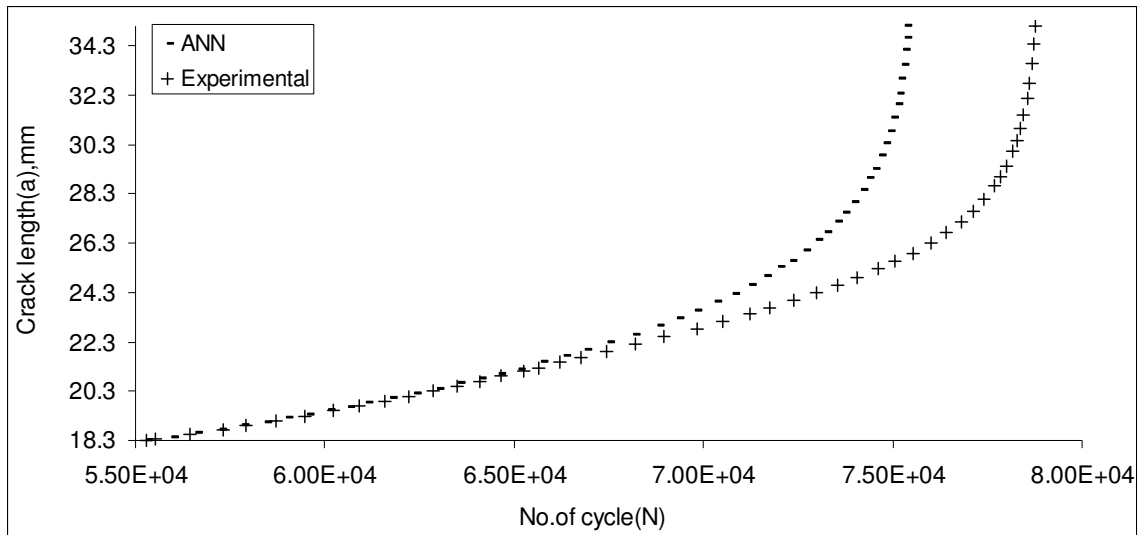


Fig. 6.6 – Predicted (ANN) and experimental number of cycle for $R = 0.5$ (7020 T7)

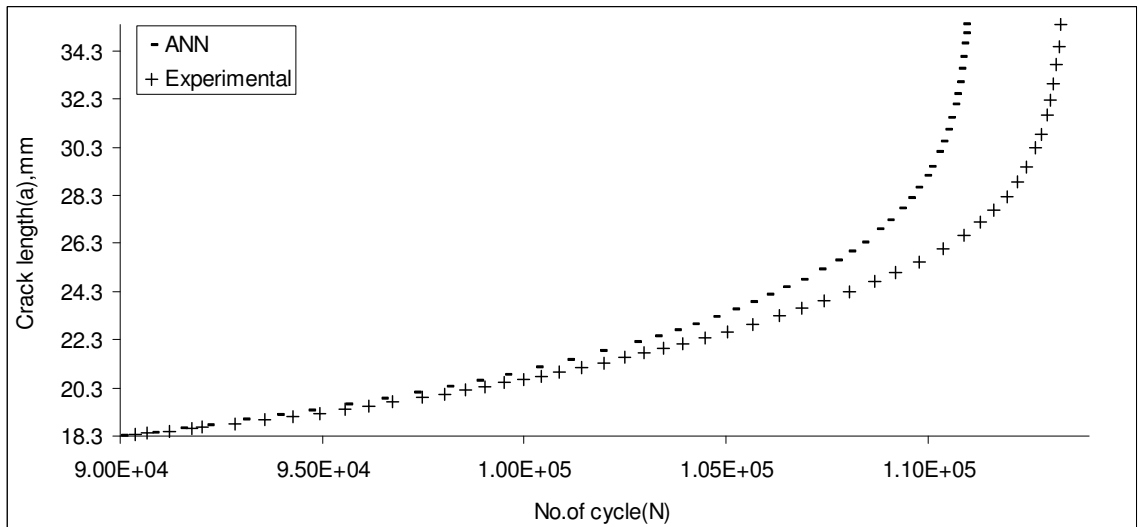


Fig. 6.7 – Predicted (ANN) and experimental number of cycle for $R = 0.5$ (2024-T3)

Table 6.2 – Comparison of ANN model results with experimental data

Test specimens	N_f^A K cycle	N_f^E K cycle
7020-T7	75.343	78.783
2024-T3	110.919	113.298

6.5 Modeling under constant amplitude loading interspersed with spike overload in mode-I

The artificial neural network approach was also applied to predict the fatigue life in case of single tensile overload followed by constant amplitude loading. The fundamental concept of the ANN approach has already been discussed in the previous section.

6.5.1 Application design

In this case, same multi-layer feed forward neural network architecture with back propagation algorithm was selected. But, the only difference was in the selection of 3rd input parameter, which was the overload ratio (“olr”) in contrast to load ratio (“lr”) of previous case. The first two inputs, ΔK and K_{\max} were normalized between 1 and 4, while the 3rd one i.e. overload ratio was normalized between 1 and 3. Similarly the output, da/dN was normalized between 0 and 3 for network training and testing. The inputs and outputs of the training sets (TS) were constituted from $50 \times 50 \times 50$ experimental values for each overload ratios of 2.0, 2.25, 2.5, 2.6, and 2.75 in case of 7020-T7 Al-alloy and that of 1.5, 1.75, 2.0, 2.25 and 2.5 in case of 2024-T3 Al-alloy respectively. The adopted multi-layer perceptron (MLP) neural network model was applied to simulate the crack growth rate of an unknown set of overload ratio ($R^{ol} = 2.35$ for Al 7020-T7 and $R^{ol} = 2.1$ for Al 2024-T3) as validation set (VS). Figs. 6.8 and 6.9 illustrate the mean square error (MSE) curves during the training of the model. The performance of the trained ANN model is presented in Table 6.3.

Table 6.3 – Performance of ANN model during training

Material	Momentum Coefficient	Learning rate	Hidden neurons	MSE	Training epochs	Computational Time (Min.)
7020-T7	0.2	0.35	179	1.056×10^{-6}	6.861×10^5	727
2024-T3	0.2	0.35	179	1.034×10^{-6}	6.559×10^5	694

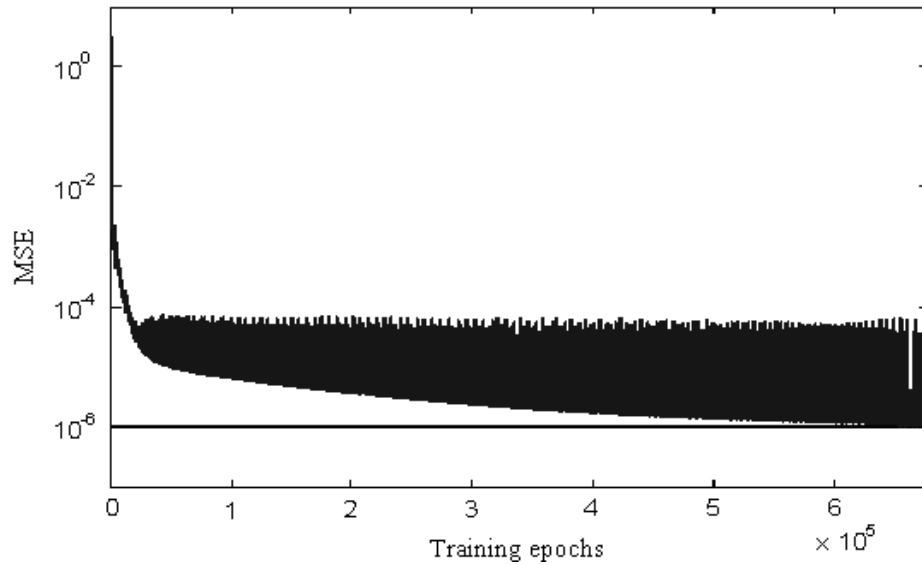


Fig. 6.8 – MSE curve obtained during training of ANN for Al 7020-T7

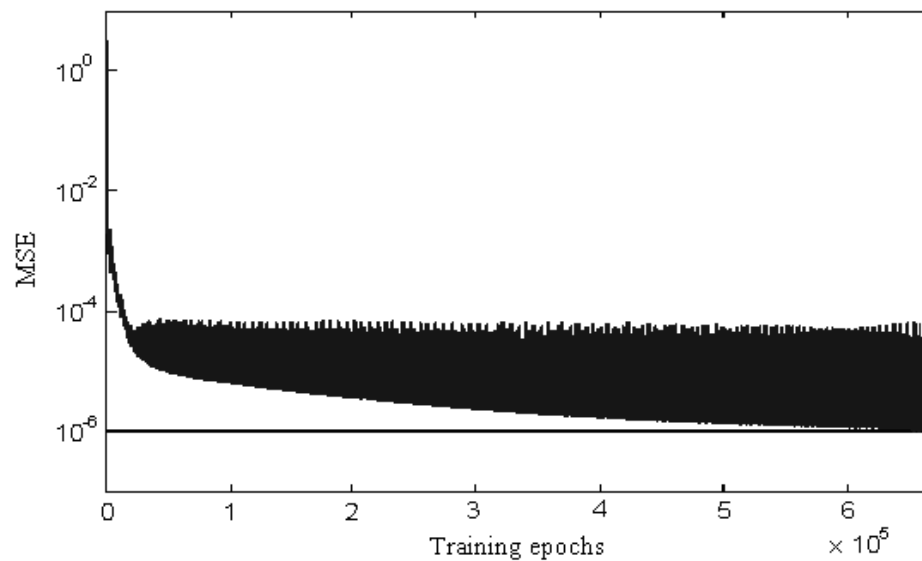


Fig. 6.9 – MSE curve obtained during training of ANN for Al 2024-T3

6.5.2 Model validation

The inputs were fed to the trained ANN to predict the corresponding crack growth rate for the validation set. The predicted results are presented in Figs. 6.10 and 6.11 respectively along with their experimental data for comparison. It was observed that the simulated $da/dN-\Delta K$ points follow the experimental ones quite well. The numbers of cycles were calculated from the simulated da/dN values in similar manner as described

above. Figs. 6.12 and 6.13 show the corresponding predicted $a-N$ curves. The curves of $a-da/dN$ and $N-da/dN$ are plotted in Figs. 6.14 to 6.17 in order to facilitate the calculation of various retardation parameters. Table 6.4 presents the comparison of various predicted results with the experimental data.

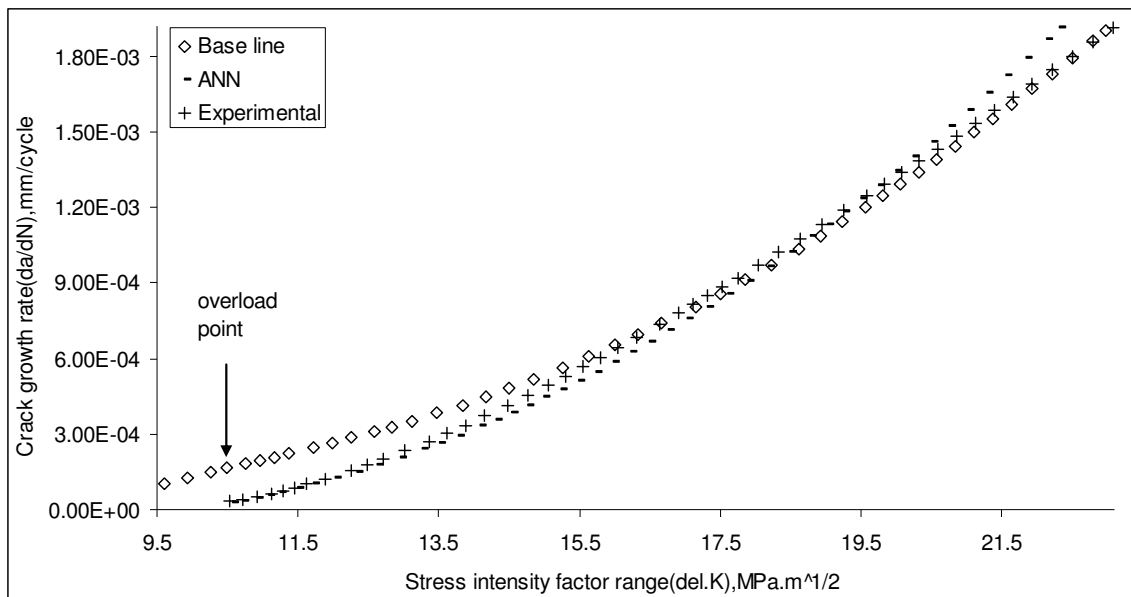


Fig. 6.10 – Predicted (ANN) and experimental crack growth rate for $R_{ol} = 2.35$ (7020-T7)

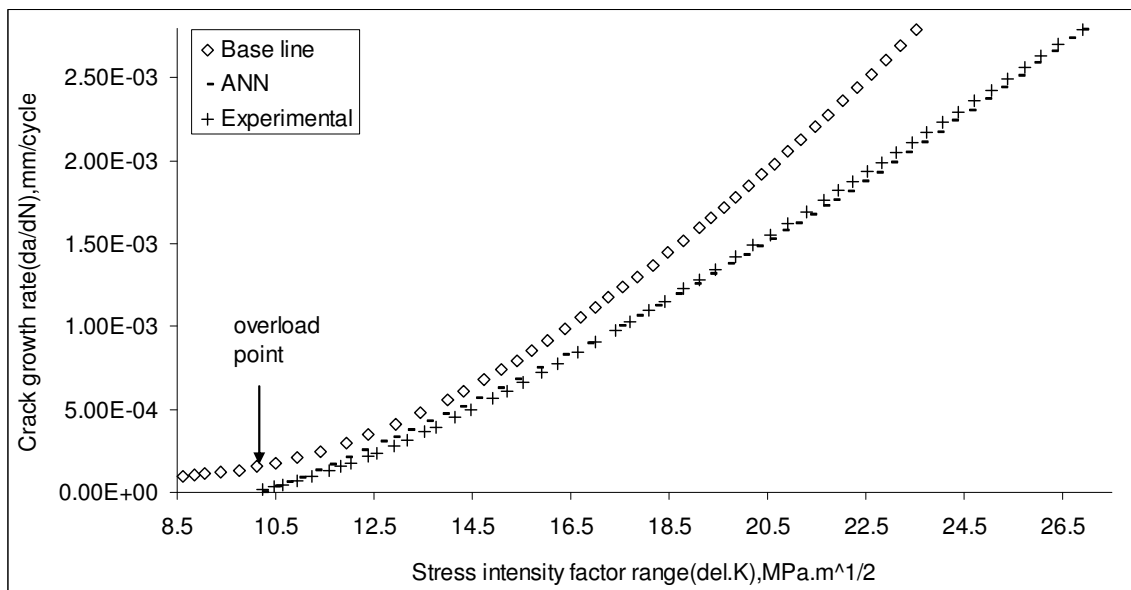


Fig. 6.11 – Predicted (ANN) and experimental crack growth rate for $R_{ol} = 2.10$ (2024-T3)

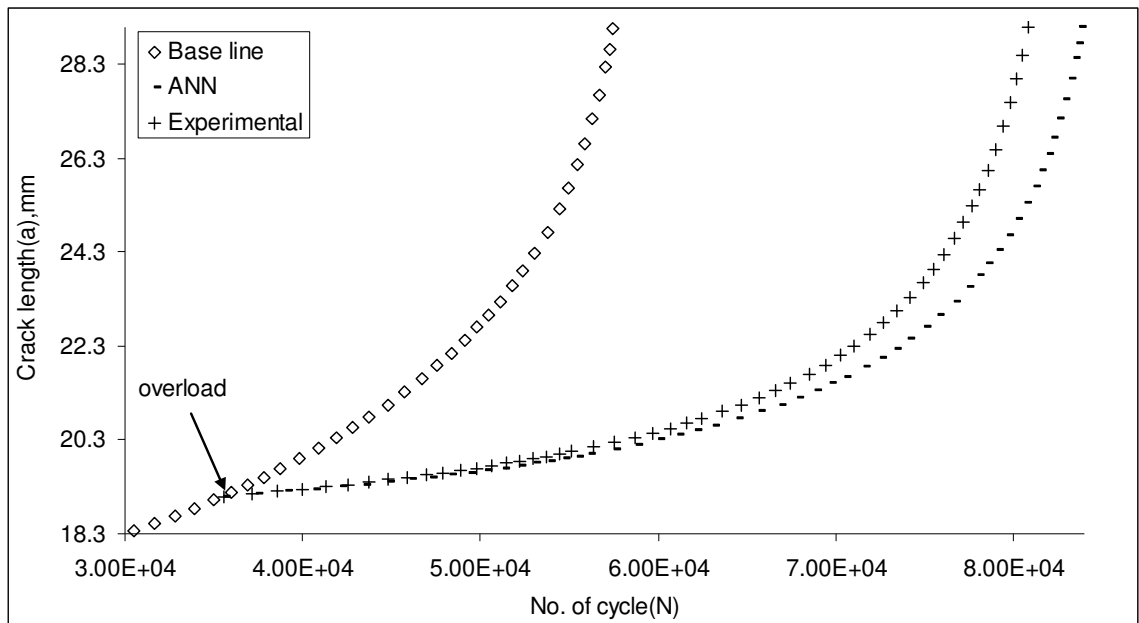


Fig. 6.12 – Predicted (ANN) and experimental number of cycle for $R_{ol} = 2.35$ (7020-T7)

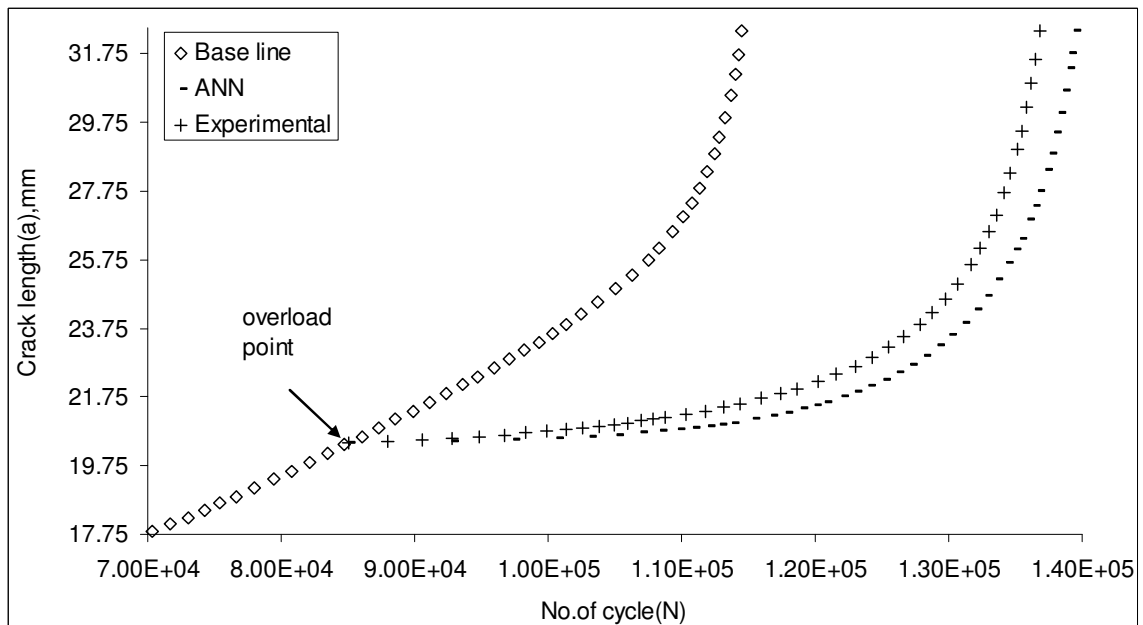


Fig. 6.13 – Predicted (ANN) and experimental number of cycle for $R_{ol} = 2.10$ (2024-T3)

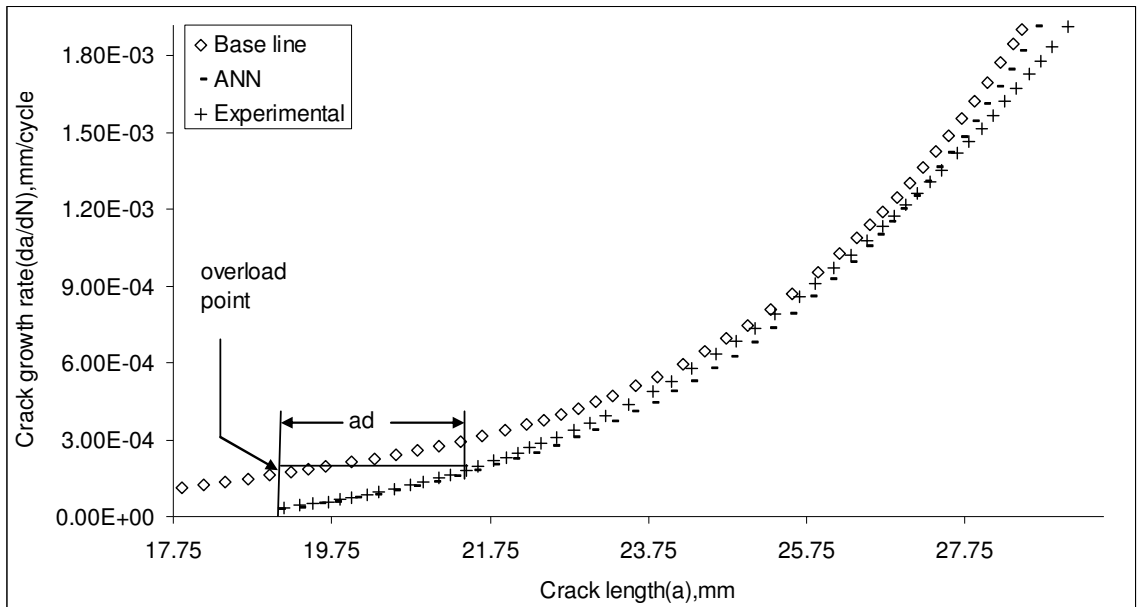


Fig. 6.14 – Predicted (ANN) and experimental retarded crack length (7020 T7)

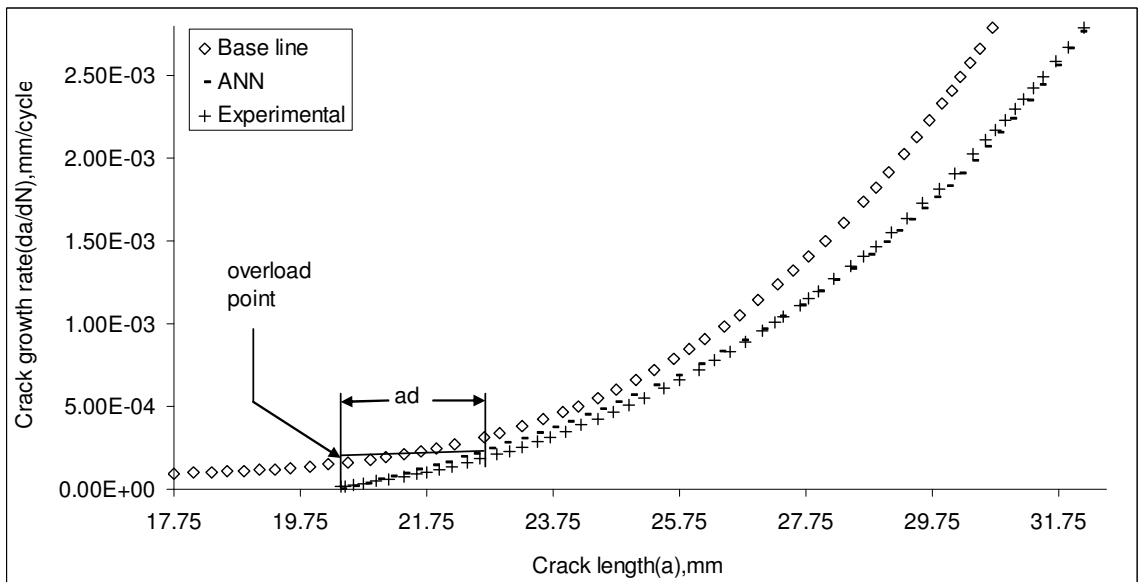


Fig. 6.15 – Predicted (ANN) and experimental retarded crack length (2024-T3)

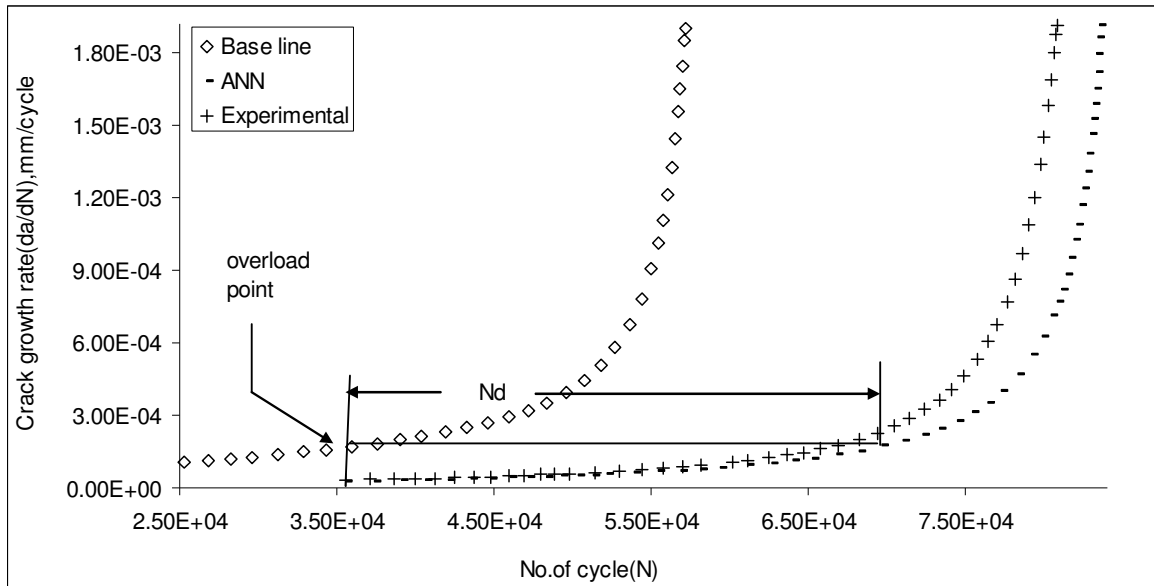


Fig. 6.16 – Predicted (ANN) and experimental delay cycle (7020-T7)

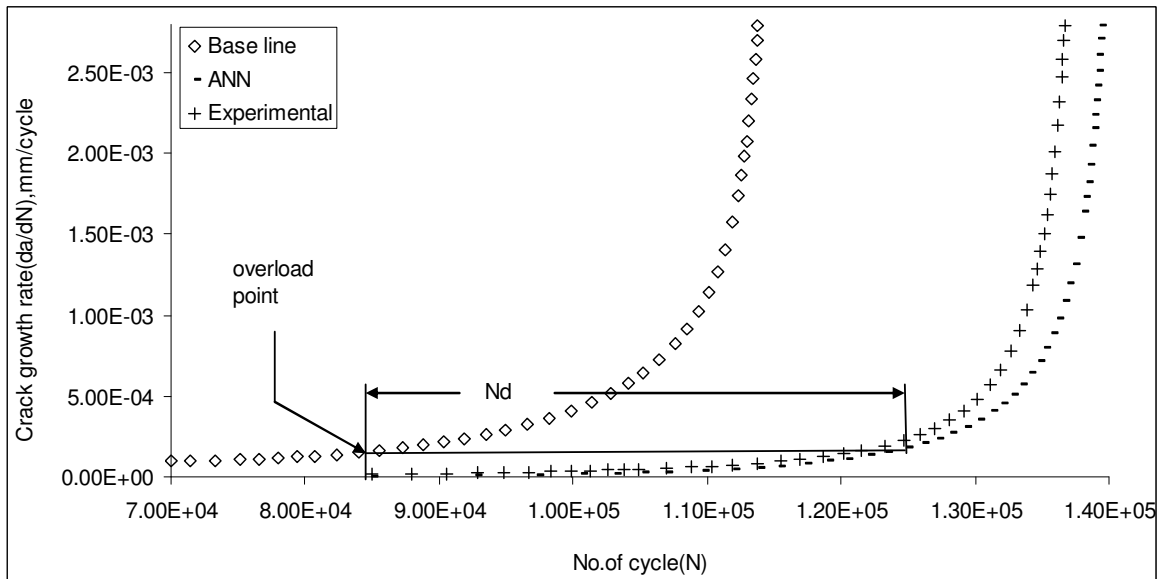


Fig. 6.17 – Predicted (ANN) and experimental delay cycle (2024-T3)

Table 6.4 – Comparison of ANN model results with experimental data

Test sample	a_d^A mm	a_d^E mm	N_d^A kcycle	N_d^E kcycle	N_f^A kcycle	N_f^E kcycle
7020-T7	1.998	2.134	32.673	30.509	83.721	80.815
2024-T3	1.990	2.181	40.716	37.599	139.384	136.80

6.6 Modeling Constant amplitude loading interspersed with spike overload in mixed mode (I and II)

The neural network was also applied in this loading condition in order to predict the end life along with various retardation parameters.

6.6.1 Application design

The same ANN architecture was implemented under the above loading condition. However, the only difference was in the selection of 3rd input parameter. Since the amount of retardation was affected by the overloading angles (Figs. 4.26 and 4.27; Section: 4.3.3), mode-mixity “mm” was considered as the 3rd input for the proposed ANN model. To make the input amenable for successful learning to minimize the overall least normalized mean square error (NMSE), the two inputs ΔK and K_{\max} were normalized between 1 and 4, while the other one, mode-mixity was normalized between 0 and 1. Similarly the output (da/dN) was normalized between 0 and 3 for network training and testing. The inputs and outputs of the training sets (TS) were constituted from $50 \times 50 \times 50$ experimental values for each of the overloading angles 0° , 18° , 36° , 72° and 90° with mode-mixity of 0, 0.245, 0.421, 0.755 and 1.0 in case of both 7020-T7 and 2024-T3 Al-alloys. The multi-layer perceptron (MLP) neural network architecture was applied to simulate the crack growth rate of an unknown set of overload angle, 54° (mode-mixity = 0.579) as validation set (VS) by constructing a training set (TS) with five known sets of overload angles ($\beta = 0^\circ$, 18° , 36° , 72° , 90° and mode-mixity = 0, 0.245, 0.421, 0.755 and 1). Figs. 6.18 and 6.19 illustrate the mean square error (MSE) curves during the training of the model. The performance of the trained ANN model is presented in Table 6.5. The input parameters, stress intensity factor range, maximum stress intensity factor and mode-mixity for the suppressed overload angle 54° have been fed to the trained ANN model in order to predict the corresponding crack growth rate.

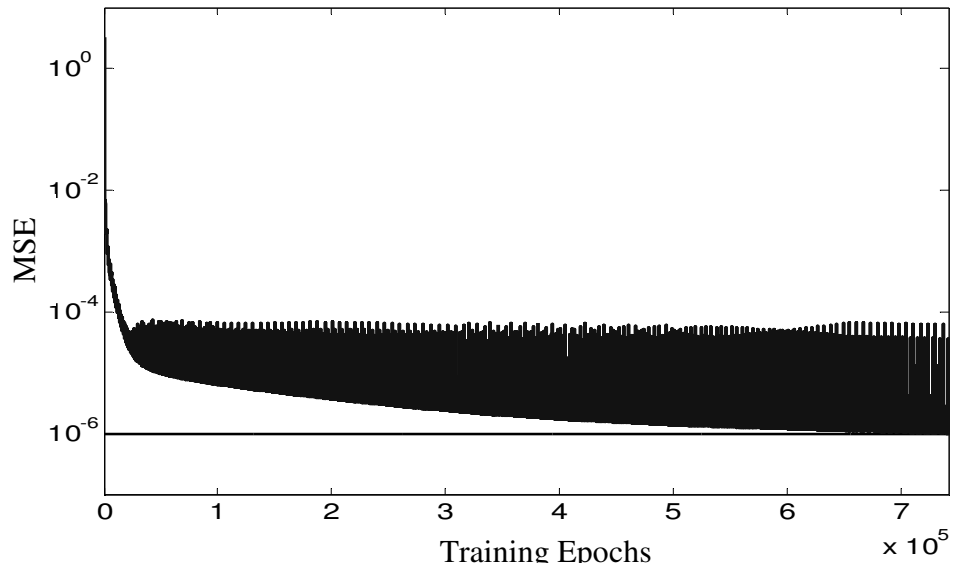


Fig. 6.18 – MSE curve obtained during training of ANN for Al 7020 T7

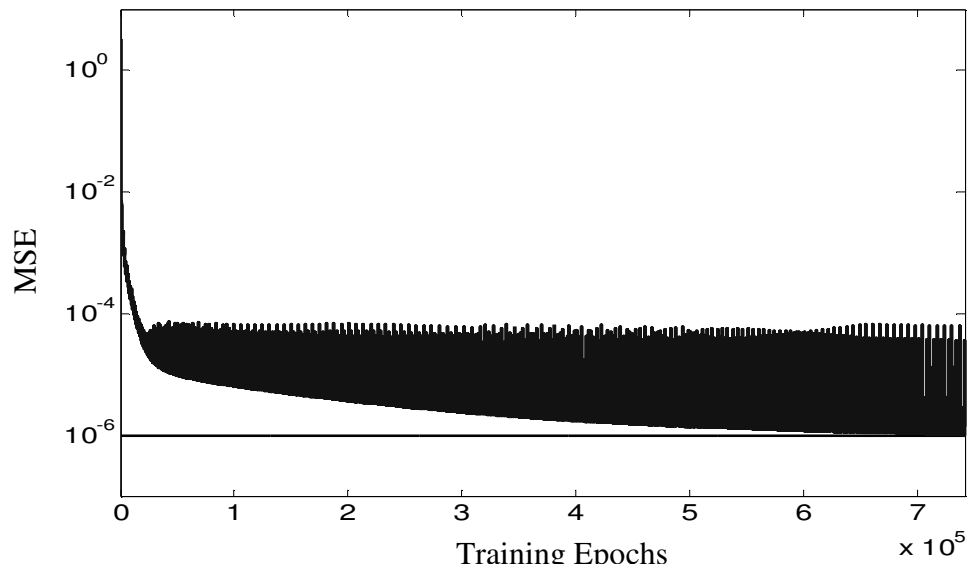


Fig. 6.19 – MSE curve obtained during training of ANN for Al 2024 T3

Table 6.5 – Performance of ANN model during training

Material	Momentum Coefficient	Learning rate	Hidden neurons	MSE	Training epochs	Computational Time (Min.)
7020-T7	0.2	0.35	179	1.688×10^{-6}	7.419×10^5	765
2024-T3	0.2	0.35	179	1.798×10^{-6}	7.789×10^5	686

6.6.2 Model validation

After training, the trained ANN was tested for the validation sets whose predicted results (crack growth rate) are presented in Figs. 6.20 and 6.21 respectively along with the experimental data for comparison. The numbers of cycles were calculated from the simulated da/dN values in similar manner as per previous cases. The predicted $a-N$ values of the ANN model are compared with the experimental data in Figs. 6.22 and 6.23 respectively for both the materials. Table 6.6 shows the predicted fatigue lives of both the materials along with different retardation parameters as calculated from $a-da/dN$ and $N-da/dN$ plots (Figs. 6.24 to 6.27).

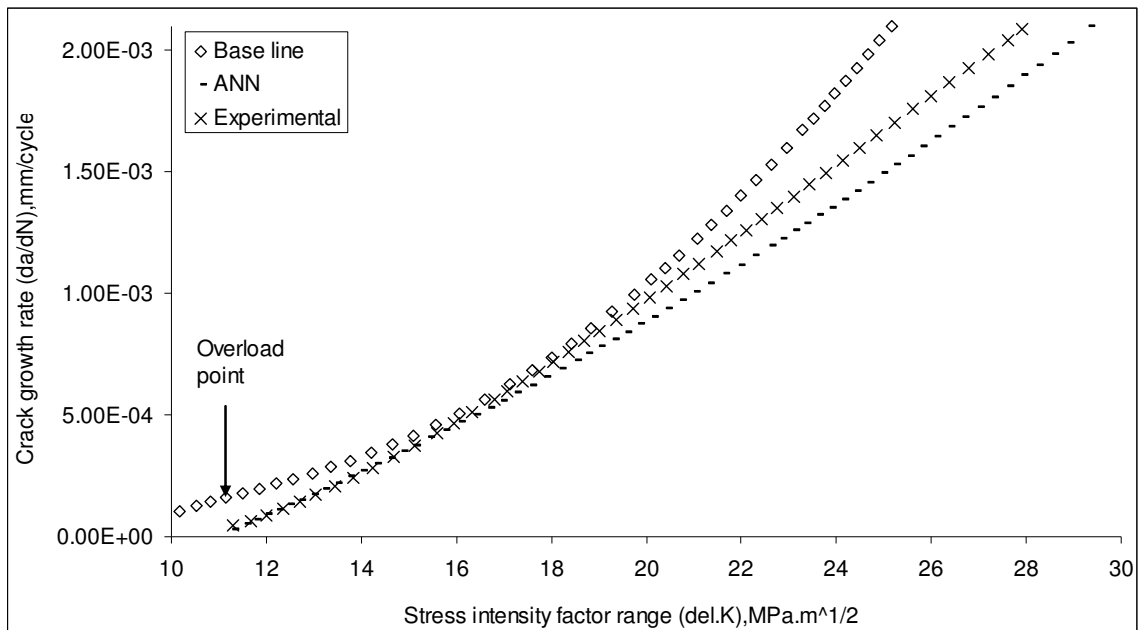


Fig. 6.20 – Predicted (ANN) and experimental crack growth rate for $\beta = 54^\circ$ (7020-T7)

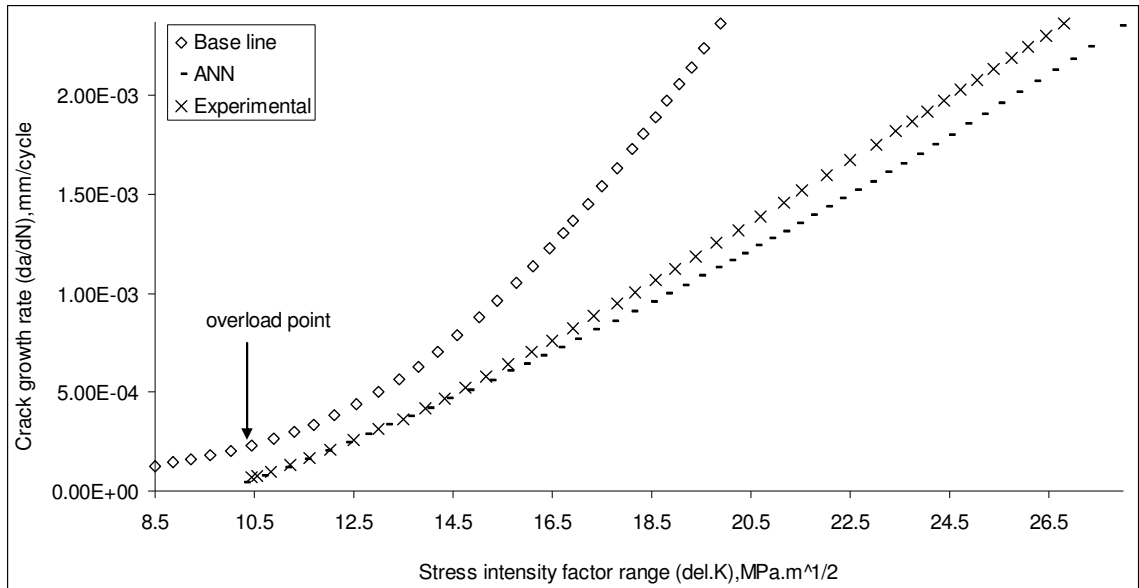


Fig. 6.21 – Predicted (ANN) and experimental crack growth rate for $\beta = 54^\circ$ (2024-T3)

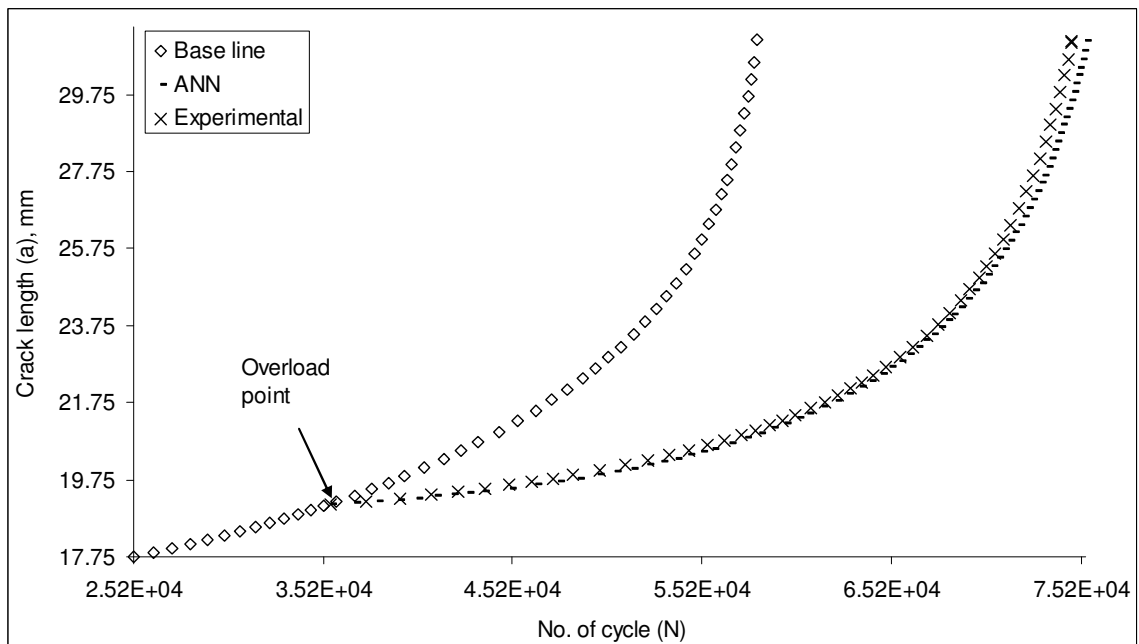


Fig. 6.22 – Predicted (ANN) and experimental number of cycle for $\beta = 54^\circ$ (7020-T7)

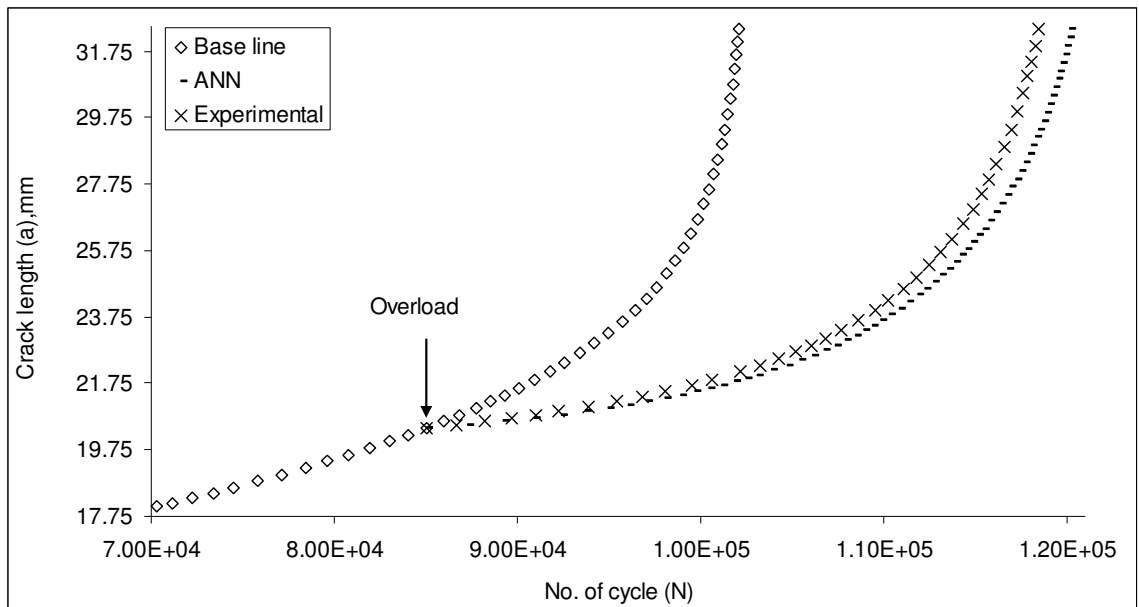


Fig. 6.23 – Predicted (ANN) and experimental number of cycle for $\beta = 54^\circ$ (2024-T3)

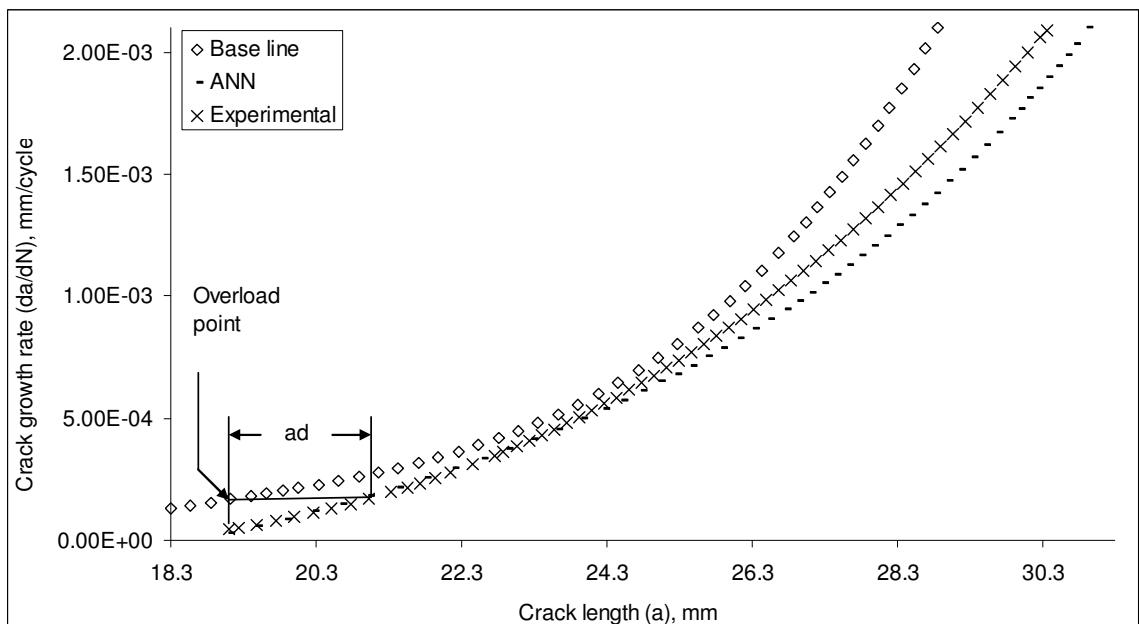


Fig. 6.24 – Predicted (ANN) and experimental retarded crack length (7020-T7)

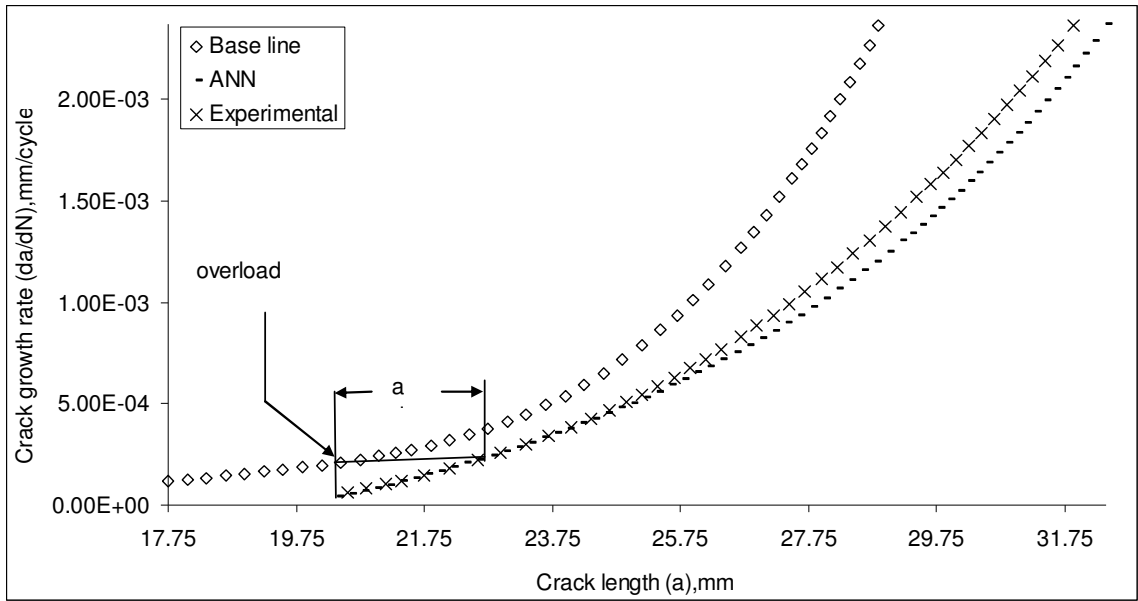


Fig. 6.25 – Predicted (ANN) and experimental retarded crack length (2024-T3)

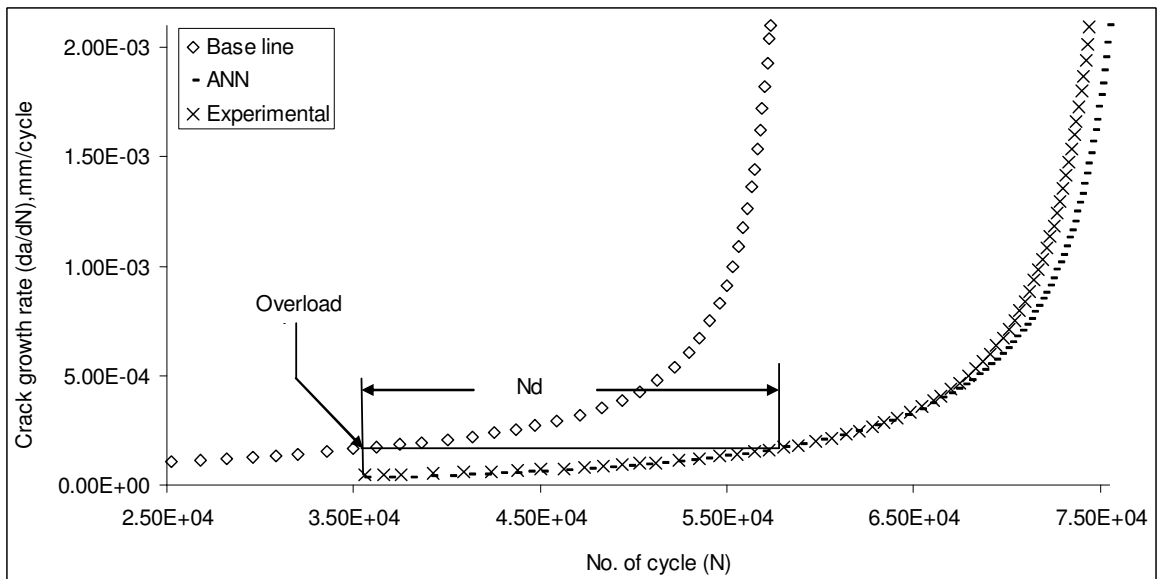


Fig. 6.26 – Predicted (ANN) and experimental delay cycle (7020-T7)

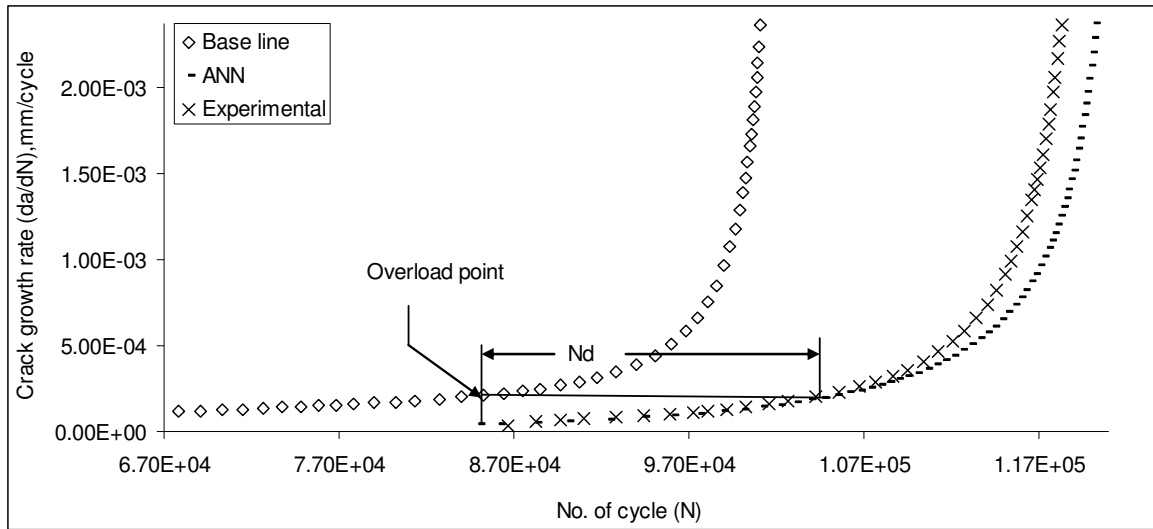


Fig. 6.27 – Predicted (ANN) and experimental delay cycle (2024-T3)

Table 6.6 – Comparison of ANN model results with experimental data

Test sample	a_d^A mm	a_d^E mm	N_d^A K cy.	N_d^E K cy.	N_f^A K cy.	N_f^E K cy.
7020-T7	1.900	1.994	22.547	21.750	75.493	74.778
2024-T3	2.141	2.300	20.791	20.019	120.152	118.48

CHAPTER VII

PREDICTION OF FATIGUE LIFE BY ADAPTIVE NEURO-FUZZY INFERENCE SYSTEM (ANFIS)

7.1 Introduction

A methodology has been developed to predict fatigue crack propagation life under three different loading conditions (as mention in Chapter-III) by adopting adaptive neuro-fuzzy inference system (ANFIS), a novel soft-computing approach, suitable for non-linear, noisy and complex problems like fatigue. It is a novel non-conventional hybrid technique which uses advantages of both ANN and fuzzy logic thereby giving better prediction accuracy than that of ANN. ANFIS model has been formulated for each loading conditions separately and the predicted results have been compared with the experimental data.

7.2 Background

Fuzzy logic methods

Fuzzy logic is a problem solving technique which maps an input space (variables) to an output space. These mappings are performed through linguistic terms of fuzzy *if-then* rules characterized by appropriate membership function in order to achieve optimum outputs, very much close to the target output. One of its advantages is that it has the ability to draw conclusions and generate responses based on imprecise and inconsistent information using simple rules to describe the system behavior rather than analytical equations. It provides a way of catching information by incorporating the qualitative aspects of human experience within its mapping laws. However, it needs expert knowledge in order to define fuzzy rules and also requires relatively long time to fine tune the fuzzy system parameters (parameters of membership functions).

Artificial neural network

Artificial neural networks (ANN) are most effective artificial intelligence system, capable of adapting and learning the system behavior by minimizing the mean-square error (MSE) between the predicted output and targeted output. These are information processing systems consisting of several neurons, which are parallel connected to each other via

synapses. Generally, an ANN has three layers: an input layer, a set of hidden layers (one or more), and an output layer. The information enters at the input layer and then all layers process these signals until they reach the output layer. The learning process is conducted by adopting or modifying the connection weights in response to training data. It is terminated either when the mean square error between the observed data and the ANN outcomes for all elements in the training set has reached a pre-specified threshold or after the completion of a pre-specified number of learning epochs.

ANN has attracted a great deal of attention because of its ability of system identification by which the characteristic features of a system can be extracted from the input output data. However, its ability to perform well is strongly influenced by the weight adaptation algorithm. The knowledge learned by ANN is difficult to understand. Hence, it is a black box that needs to be defined, which is a highly compute-intensive process.

Fuzzy Inference System (FIS)

Fuzzy inference systems also called rule-based systems are capable modeling non-linear complex problems by employing both fuzzy logic and linguistic if-then rules. A simple model of the system is presented in Fig. 7.1. The controller has four main components: the fuzzification interface, inference engine, rule base and defuzzifier. The rule base contains a number of linguistic fuzzy if-then rules provided by experts.

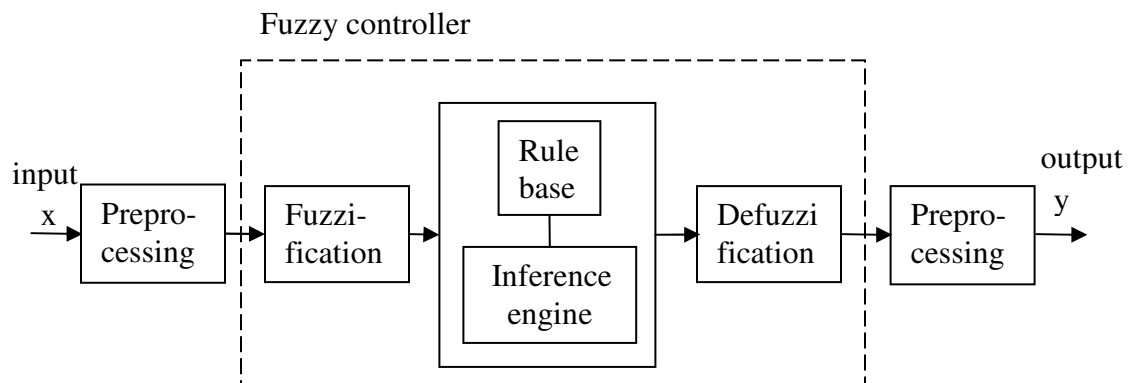


Fig. 7.1 - Fuzzy inference system

The fuzzification interface transforms crisp inputs into corresponding fuzzy memberships in order to activate rules that are in terms of linguistic variables. The inference engine defines mapping from input fuzzy sets into output fuzzy sets. The defuzzifier transforms the fuzzy results into a crisp output through various defuzzification methods including the centroid, maximum, mean of maxima, height and modified height defuzzifier. The most popular defuzzification method is the centroid, which calculates and returns the center of gravity of the aggregated fuzzy sets. One of the important aspects of fuzzy inference system is that the fuzzy rules which are fired in parallel, does not affect its output irrespective of the firing orders.

A fuzzy inference system requires a knowledgeable human operator to first initialize the system parameters and then optimize them to achieve a required degree of accuracy. Manual optimization of parameters is accomplished visually, which is a disadvantage.

Adaptive Neuro-Fuzzy Inference System (ANFIS)

Fuzzy inference system (FIS) faces difficulties in system modeling due to lack of definite criteria for selection of the shape of membership functions, their degree of overlapping and above all optimization of system parameters. Adaptive neuro-fuzzy inference system (ANFIS) which is an integrated system of ANN and FIS utilizes the advantages of both. ANFIS is a class of adaptive networks, whose membership function parameters are tuned (adjusted) using either a back-propagation algorithm or hybrid algorithm based on a combination of back-propagation and least squares estimate (LSE). In the present investigation, type-3 ANFIS [93] topology based on first-order Takagi-Sugeno (TSK) [95] if-then rules has been used. A typical first-order TSK fuzzy inference system with three inputs and one output can be expressed in the following form:

$$\text{IF } x_1 \text{ is } A_j \quad (7.1)$$

$$x_2 \text{ is } B_k \quad (7.2)$$

$$\text{AND } x_3 \text{ is } C_m \quad (7.3)$$

$$\text{THEN } f_i = o_i x_1 + p_i x_2 + q_i x_3 + r_i \quad (7.4)$$

for $j = 1, \dots, S_1$
 $k = 1, \dots, S_2$
 $m = 1, \dots, S_3$
 $i = 1, \dots, S_1 \times S_2 \times S_3$

where A , B , and C are fuzzy sets defined on input variables x_1 , x_2 , and x_3 respectively; S_1 , S_2 , and S_3 are the number of membership functions; f is a linear consequent function defined in terms of input variables; while o , p , q , and r are linear coefficients referred to as consequent parameters of the first-order TSK fuzzy model.

7.3 Model formulation

The proposed ANFIS structure consists of a number of interconnected fixed and adjustable nodes. It corresponds to first-order TSK fuzzy model as shown in Fig. 7.2 below.

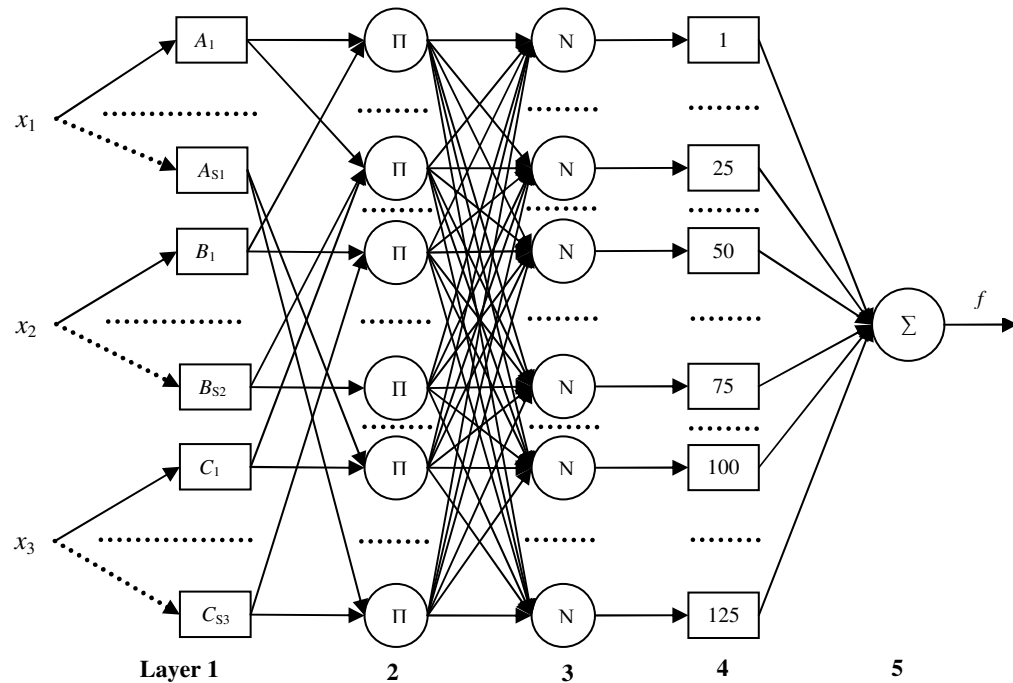


Fig. 7.2 - ANFIS architecture

It is composed of five layers having three inputs and one output. The functions of different layers are as follows:

Layer-1: Every node in this layer is a square node with a particular membership function specifying the degree to which a given input satisfies the quantifier. For three inputs ANFIS model, the output of a given node is given by:

$$O_j^1 = \mu_{A_j}(x_1), \quad j = 1, \dots, S_1 \quad (7.5)$$

$$O_k^1 = \mu_{B_k}(x_2), \quad k = 1, \dots, S_2 \quad (7.6)$$

$$O_m^1 = \mu_{C_m}(x_3), \quad m = 1, \dots, S_3 \quad (7.7)$$

where S_1 , S_2 , and S_3 are universes of discourse of three input variables respectively; x is the input to nodes j , k , and m respectively; A_j , B_k , and C_m are the linguistic labels (small, large etc) associated with the respective node functions; and $\mu_{A_j}(x_1)$, $\mu_{B_k}(x_2)$, $\mu_{C_m}(x_3)$ are membership grade functions. In this layer, the membership function can be any appropriate parameterized membership function such as triangular, Gaussian or bell. Bell membership function has been selected for the present work because, it has the characteristics of smoothness and succinctness, and are extensively applied to the fuzzy sets. It is defined as:

$$\mu_{A_i}(x) = \frac{1}{1 + \left\{ \frac{x - c_i}{a_i} \right\}^{b_i}} \quad (7.8)$$

where a_i , a_i , and a_i are the membership function parameters. Parameters in this layer are referred to as 'premise parameters'.

Layer-2: Every node in this layer is a fixed circle node labeled Π , whose output is the product of all the incoming signals (T-norm operation):

$$O_i^2 = w_i = \mu_{A_j}(x_1) \mu_{B_k} \mu_{C_m} \quad (7.9)$$

The output of a node in the 2nd layer represents the firing strength (degree of fulfillment) of the associated rule. Typical representation of fuzzy rules in a first-order TSK FIS is given as:

$$\text{Rule-1: if } x_1 \text{ is } A_1, x_2 \text{ is } B_1 \text{ and } x_3 \text{ is } C_1 \text{ then } f_1 = o_1 x_1 + p_1 x_2 + q_1 x_3 + r_1 \quad (7.10)$$

Rule-2: if x_1 is A_2 , x_2 is B_2 and x_3 is C_2 then $f_2 = o_2x_1 + p_2x_2 + q_2x_3 + r_2$ (7.11)

Layer-3: Every node in this layer is also a circle node labeled N. The output of i^{th} node is the ratio of the i^{th} rule's firing strength to the sum of all rules' firing strengths:

$$O_i^3 = \bar{w}_i = \frac{w_i}{\sum_{L=1}^{S_1 S_2 S_3} w_L} \quad (7.12)$$

The output is called as 'normalized firing strength'.

Layer-4: Every node i in this layer is a square or adaptive node with a node function:

$$O_i^3 = \bar{w}_i f_i = \bar{w}_i (o_i x_1 + p_i x_2 + q_i x_3 + r_i) \quad (7.13)$$

where \bar{w}_i is the output of layer 3, and $\{o_i, p_i, q_i, r_i\}$ is the parameter set. Parameter in this layer is referred to as the *consequent parameter*.

Layer-5: The single node in this layer is a circle node labeled Σ , which computes the *overall output* as the summation of all incoming signals:

$$O_i^5 = \text{overalloutput} = \sum_i \bar{w}_i f_i = \frac{\sum w_i f_i}{\sum w_i} \quad (7.14)$$

In the proposed ANFIS topology, there are S_1, S_2 and S_3 number of membership functions associated with each of the three inputs respectively. So the input space is partitioned into $(S_1 \times S_2 \times S_3)$ fuzzy subspaces, each of which is governed by fuzzy if-then rules. The premise part of a rule (layer 1) defines a fuzzy sub-space, while the consequent part (layer 4) specifies the output within this sub-space.

The basic learning rule of adaptive network is back-propagation algorithm where the model parameters are updated by a gradient descent optimization technique. However, due to the slowness and tendency to become trapped in local minima its application is limited. A hybrid-learning algorithm, on the other hand is an enhanced version of the back-propagation algorithm. It is applied to adapt the premise and consequent parameters to optimize the network. In the forward pass, functional signals go forward till layer 4 and the consequent parameters are identified by the least square estimate. In the backward pass, the error rates propagate backward and the premise parameters are updated by the gradient descent method. Heuristic rules are used to guarantee fast convergence. The details of the

above technique have been elaborately discussed by Jang [93]. The flow chart of the trained ANFIS model is illustrated in Fig. 7.3.

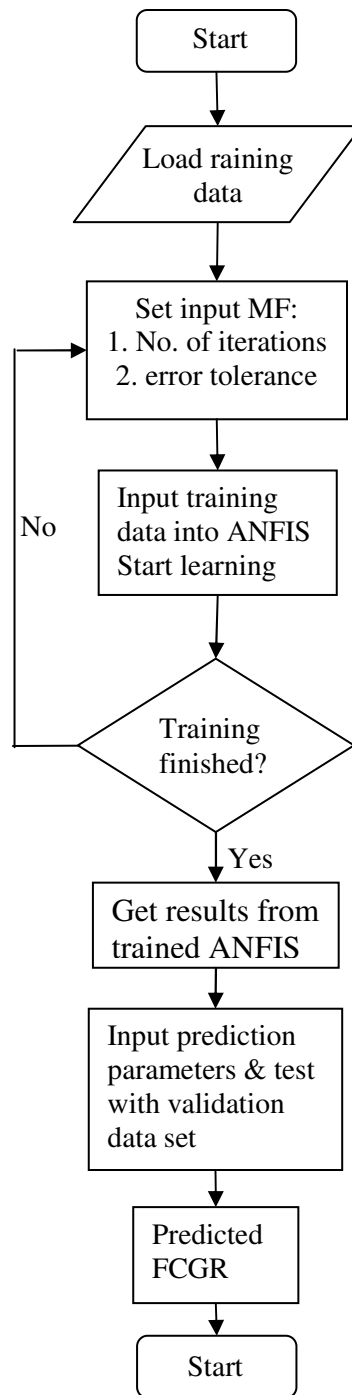


Fig. 7.3 – Flow chart of ANFIS model

The model performance was verified by computing root mean square error (RMSE); coefficient of determination (R^2) and mean percent error (MPE) defined by the following equations:

$$RMSE = \left((1/p) \sum_{i=1}^p |t_i - o_i| \right)^{1/2} \quad (7.15)$$

$$R^2 = 1 - \left(\frac{\sum_{i=1}^p (t_i - o_i)^2}{\sum_{i=1}^p (o_i)^2} \right) \quad (7.16)$$

$$MPE = \frac{1}{p} \sum_{i=1}^p \left(\frac{t_i - o_i}{t_i} \times 100 \right) \quad (7.17)$$

where 't' is the target value, 'o' is the output value, and 'p' is the number of data items.

7.4 Modeling under constant amplitude loading

7.4.1 Application design

It was observed from the tests that fatigue crack propagation life (i.e. number of cycles, N) decreased as load ratio (R) increased. Accordingly, the crack growth rate also varied with respect to different load ratio. The stress intensity factor range (ΔK) and maximum stress intensity factor (K_{\max}) are expected to be the two important controlling crack driving forces [41, 103-107] responsible for these variations. Therefore, in the present case, R , ΔK , and K_{\max} have chosen as the three input parameters for ANFIS structure, whereas crack growth rate (da/dN) as the only output parameter.

Before applying ANFIS model, the pre-processing of experimental data is essential in order to achieve optimum modeling results. Out of six experimental data sets of Chapter III (set-2 of constant amplitude loading results) five sets ($R = 0, 0.2, 0.4, 0.6, 0.8$) were taken as the training sets and one set ($R = 0.5$) was taken as the testing set. The inputs i.e. load ratio, maximum stress intensity factor and stress intensity factor range were normalized in such a way that their maximum values were normalized to unity. The crack growth rate, which constitutes the system output, was also normalized in similar manner.

Referring to Fig. 7.2, layer 1 has 15 (5×3) nodes with 45 parameters. Layers 2, 3 and 4 have 125 (5^3) nodes each with 500 parameters associated in layer 4. The membership functions were chosen to be $5 \times 5 \times 5$ corresponding to the inputs R , ΔK , and K_{\max} respectively. Hence, the total numbers of membership functions (rules) were 125. This choice was based on the fact that R had five distinct values in the experimental data sets.

7.4.2 Model validation

In this research, ANFIS shown in Fig. 7.2 was implemented by using MATLAB 6.5 with Fuzzy Logic Toolbox. The numbers of membership functions (MF) were chosen to be $5 \times 5 \times 5$ corresponding to the inputs R , K_{\max} and ΔK respectively. The $5 \times 5 \times 5 = 125$ fuzzy ‘*if-then*’ rules were constituted in which fuzzy variables were connected by T-norm (fuzzy AND) operators. The adjustment of premise and consequent parameters was made in batch mode based on the hybrid-learning algorithm. The model was trained for 4000 epochs until the given tolerance was achieved. Table 7.1 summarizes all the characteristics of ANFIS network used during training. The performance of the model during training and testing was verified through three statistical indices (Eqs. 7.15 to 7.17) and presented in Table 7.2.

Table 7.1 – Characteristics of the ANFIS network

Type of membership function	Generalized bell
Number of input nodes (n)	3
Number of fuzzy partitions of each variable (p)	5
Total number of membership functions	15
Number of rules (p^n)	125
Total number of nodes	394
Total number of parameters	545
Number of epochs	4000
Step size for parameter adaptation	0.01

Table 7.2 – Performance of ANFIS model

Material	During training	During testing	Computational Time

	RMSE	R^2	MPE	RMSE	R^2	MPE	(Min.)
7020-T7	0.002897	0.99285	0.48546	0.03056	0.92894	0.87986	419
2024-T3	0.001283	0.99987	0.28679	0.01285	0.99783	0.77895	398

The trained ANFIS model was employed to simulate the crack growth rate for load ratio (R) 0.5 in case of both the alloys and the predicted crack growth rates were compared with the experimental data in Figs. 7.4 and 7.5 respectively. The numbers of cycles (fatigue life) were calculated from predicted and experimental results in the excel sheet (Figs. 7.6 and 7.7) as per the following equation:

$$N_j = \frac{a_j - a_i}{da/dN} + N_i \quad (7.18)$$

where, a_i and a_j = crack length in i^{th} step and j^{th} step in ‘mm’ respectively,

N_i and N_j = No. of cycles in i^{th} step and j^{th} step respectively,

i = No. of experimental steps,

and $j = i + 1$

Table 7.3 shows the predicted fatigue lives for both the materials.

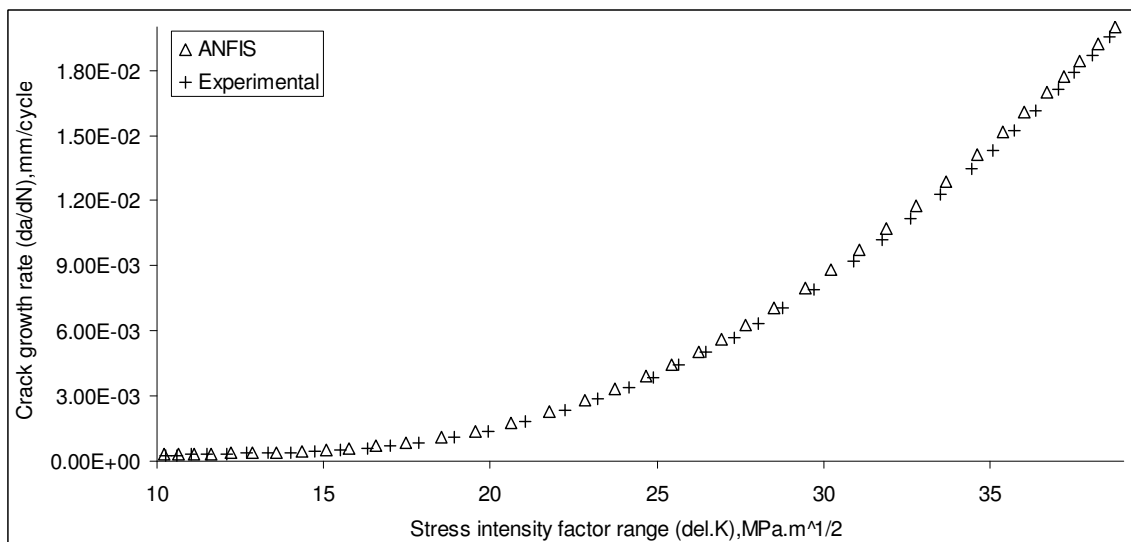


Fig. 7.4 – Predicted (ANFIS) and experimental crack growth rate for $R = 0.5$ (7020-T7)

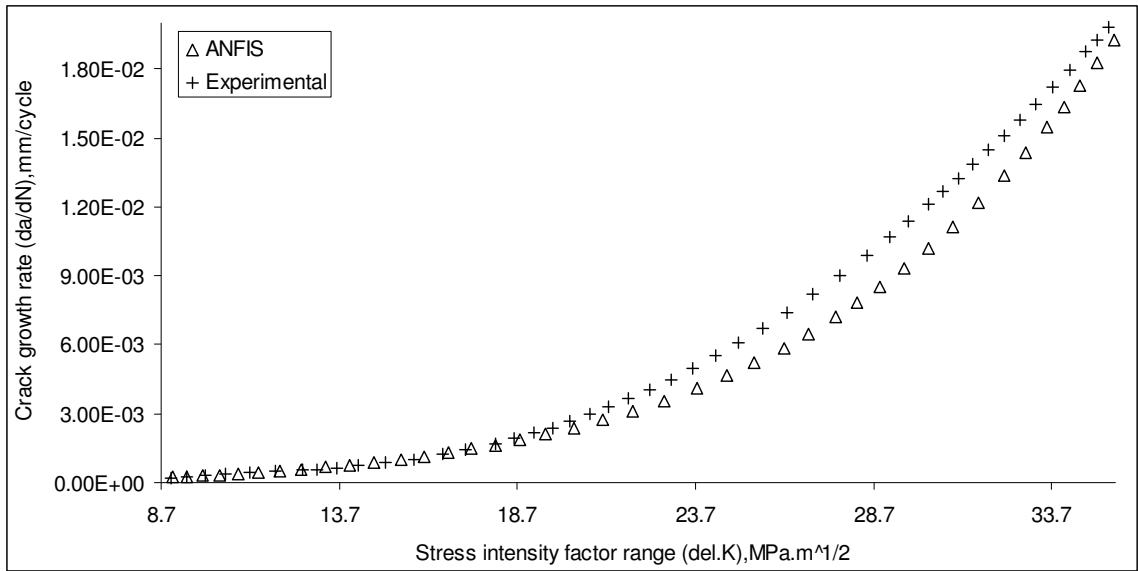


Fig. 7.5 – Predicted (ANFIS) and experimental crack growth rate for $R = 0.5$ (2024-T3)

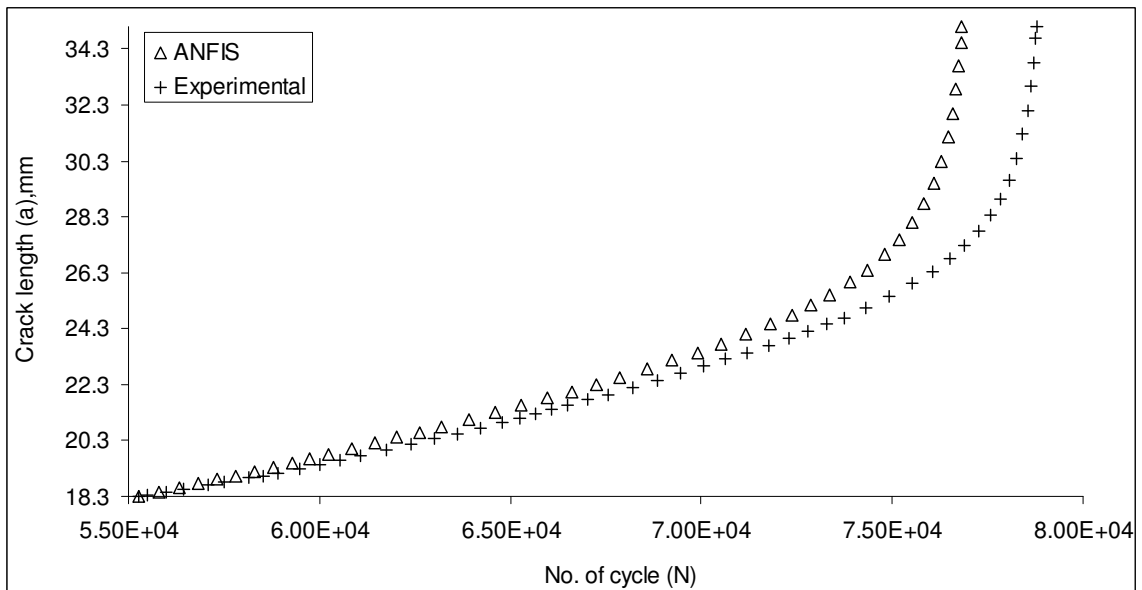


Fig. 7.6 – Predicted (ANFIS) and experimental number of cycle for $R = 0.5$ (7020-T7)

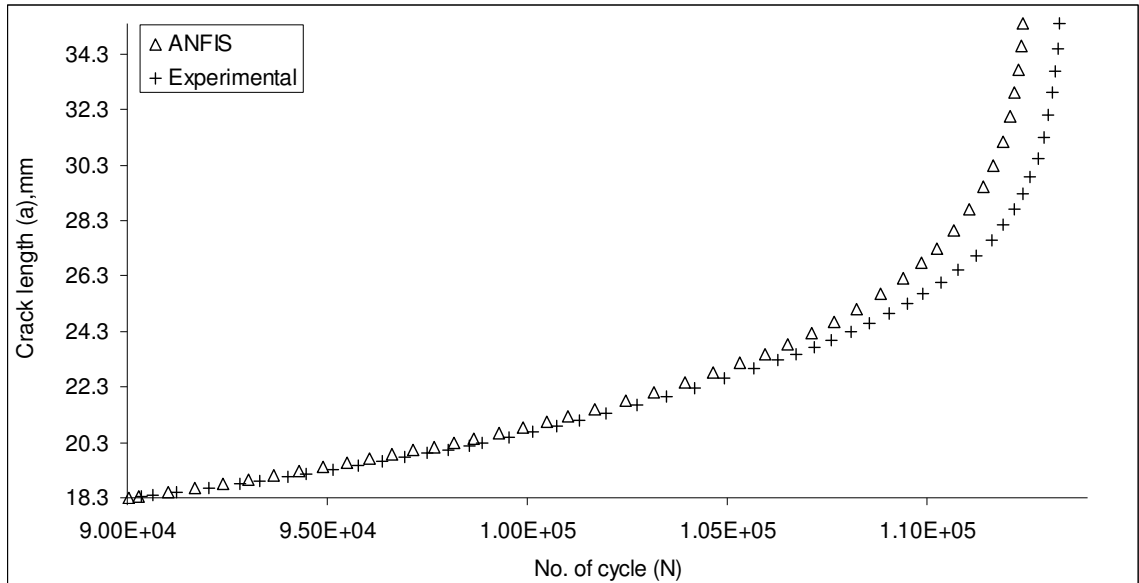


Fig. 7.7 – Predicted (ANFIS) and experimental number of cycle for $R = 0.5$ (2024-T3)

Table 7.3 – Comparison of ANFIS model results with experimental data

Test specimens	N_f^{AN} K cycle	N_f^E K cycle
7020 T7	76.826	78.783
2024 T3	112.391	113.298

7.5 Modeling under Constant amplitude loading interspersed with spike overload in mode-I

7.5.1 Application design

The application of a single tensile overload during fatigue crack propagation can lead to significant retardation of crack growth resulting in an increase in the specimen life time (Fig. 4.16 and 4.17; Chapter-IV). This delaying effect must be taken into account while predicting the residual fatigue crack growth lives of the structures subjected to variable amplitude loading conditions. It depends on the magnitude of overload ratio (R^{ol}). Further, it has been proved that fatigue crack growth rate is governed not only by single

crack driving force ΔK , but, according to ‘Unified Approach’, by the simultaneous action of both ΔK and K_{\max} [41, 104-108]. Therefore, overload ratio (R^{ol}), maximum stress intensity factor (K_{\max}), and stress intensity factor range (ΔK) were considered as linguistic input variables whereas, crack growth rate (da/dN) was taken as output variable for the proposed ANFIS model. Out of six experimental data sets having overload ratios (R^{ol}) 2, 2.25, 2.35, 2.5, 2.6, 2.75 in case of Al 7020 T7, one set ($R_{ol} = 2.35$) was taken as validation set (VS). Similarly, out of six experimental data sets ($R_{ol} = 1.5, 1.75, 2.0, 2.1, 2.25, 2.5$), the set having overload ratio 2.1 was taken as validation set (VS) in case of Al 2024 T3. During training, same parameters were taken (Table 7.1) as that of constant amplitude loading case.

7.5.2 Model validation

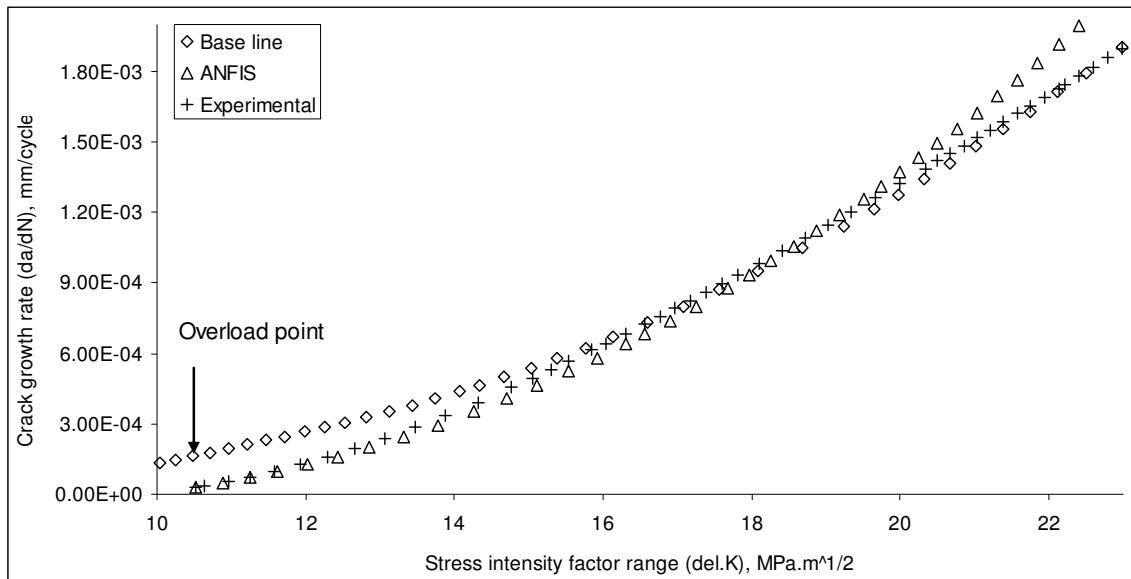
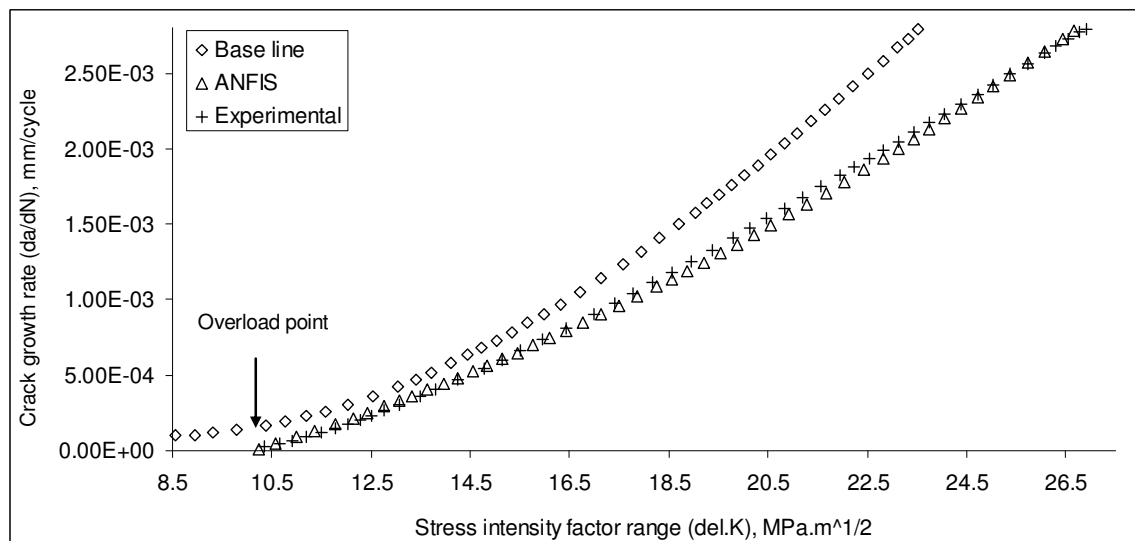
Training and testing were done with Fuzzy Logic Toolbox of MATLAB 6.5 by taking the same parameters as that of constant amplitude loading case (Table 6.1). The performance of the model during training and testing was verified through three statistical indices (Eqs. 7.15 to 7.17) and presented in Table 7.4. The trained ANFIS model was tested for the validation sets and the predicted crack growth rates were compared with the experimental data in Figs. 7.8 and 7.9. The numbers of cycles (fatigue life) were calculated from predicted and experimental results in the excel sheet (Figs. 7.10 and 7.11) as per Eq. 7.18. Figs. 7.12 to 7.15 show the plots of various retardation parameters. The different predicted model results are presented in Table 7.5 along with their percentage variations from the experimental data.

Table 7.4 – Performance of ANFIS model

Material	During training			During testing			Computational Time (Min.)
	RMSE	R^2	MPE	RMSE	R^2	MPE	
7020-T7	0.002643	0.99873	0.348387	0.010879	0.96895	0.86495	355
2024-T3	0.001413	0.99967	0.385620	0.018268	0.93879	0.89697	425

Table 7.5 – Comparison of ANFIS model results with experimental data

Test sample	a_d^{AN} mm	a_d^E mm	% Error in a_d^{AN}	N_d^{AN} K cy.	N_d^E K cy.	% error in N_d^{AN}	N_f^{AN} K cy.	N_f^E K cy.	% error in N_f^{AN}
7020-T7	2.230	2.134	+4.695	31.880	30.509	+4.494	82.388	80.815	+1.946
2024-T3	2.330	2.181	+6.880	40.581	37.599	+7.931	138.307	136.804	+1.099

Fig. 7.8 – Predicted (ANFIS) and experimental crack growth rate, $R^{ol} = 2.35$ (7020-T7)Fig. 7.9 – Predicted (ANFIS) and experimental crack growth rate, $R_{ol} = 2.10$ (2024-T3)

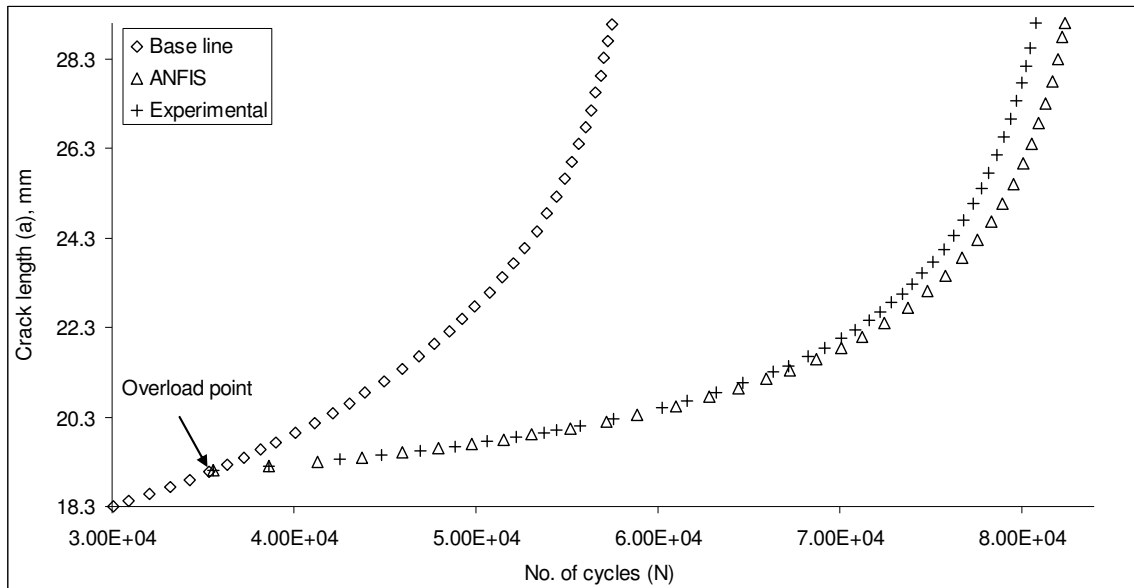


Fig. 7.10 – Predicted (ANFIS) and experimental number of cycle, $R_{o1} = 2.35$ (7020-T7)

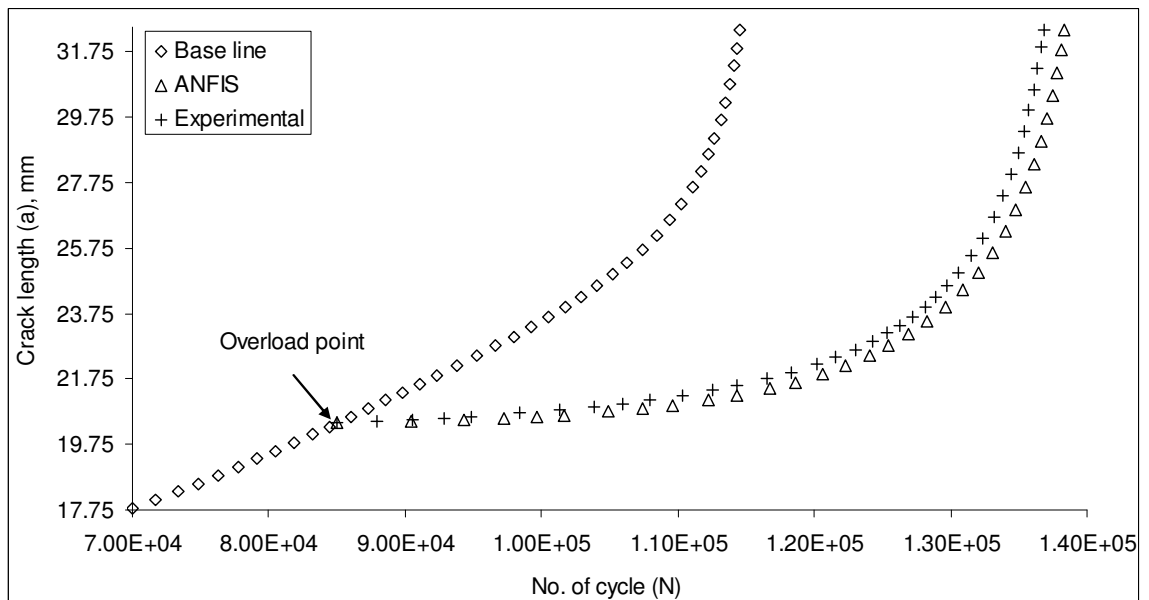


Fig. 7.11 – Predicted (ANFIS) and experimental number of cycle, $R_{o1} = 2.10$ (2024-T3)

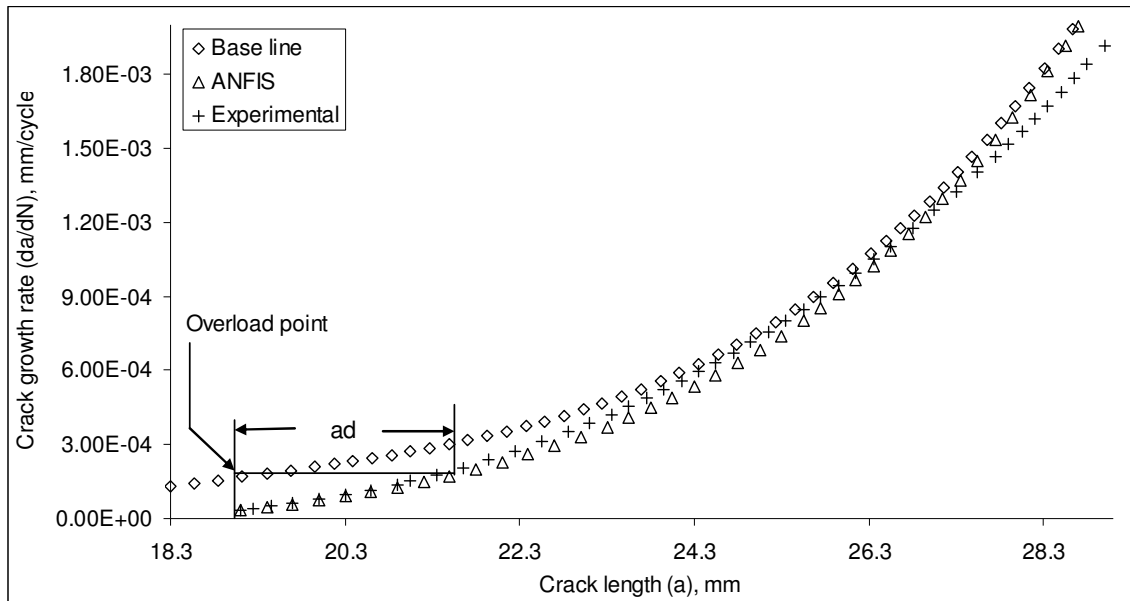


Fig. 7.12 – Predicted (ANFIS) and experimental retarded crack length (7020-T7)

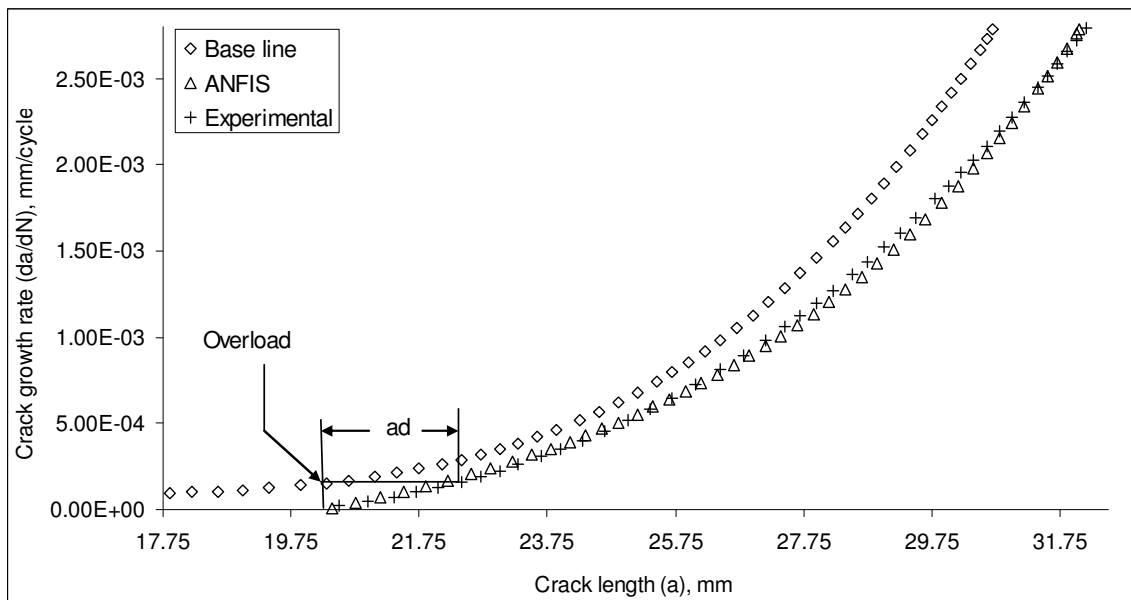


Fig. 7.13 – Predicted (ANFIS) and experimental retarded crack length (2024-T3)

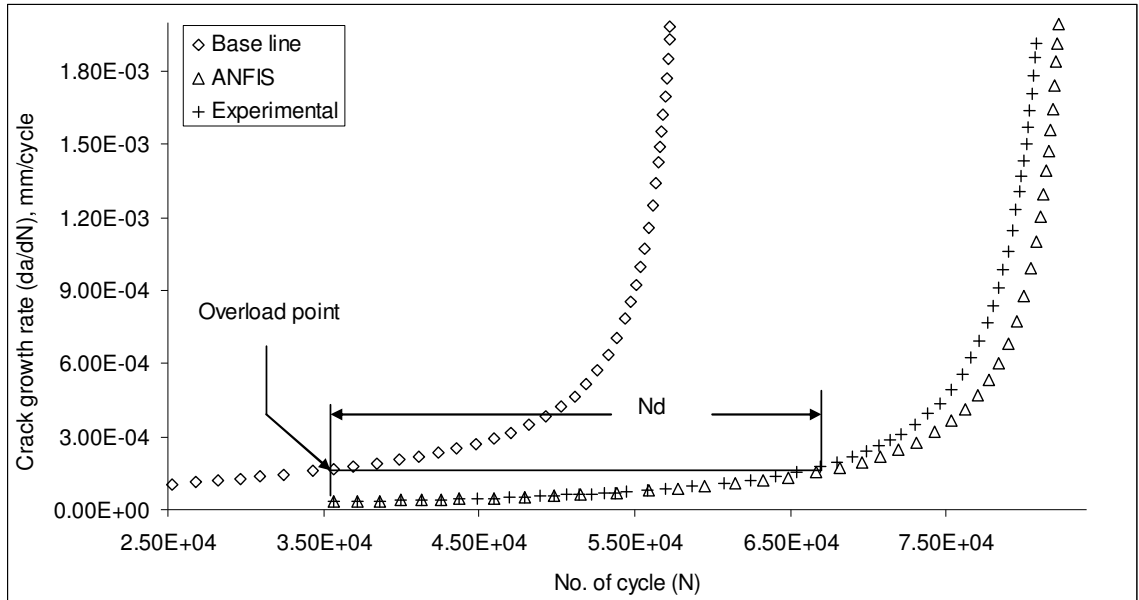


Fig. 7.14 – Predicted (ANFIS) and experimental delay cycle (7020-T7)

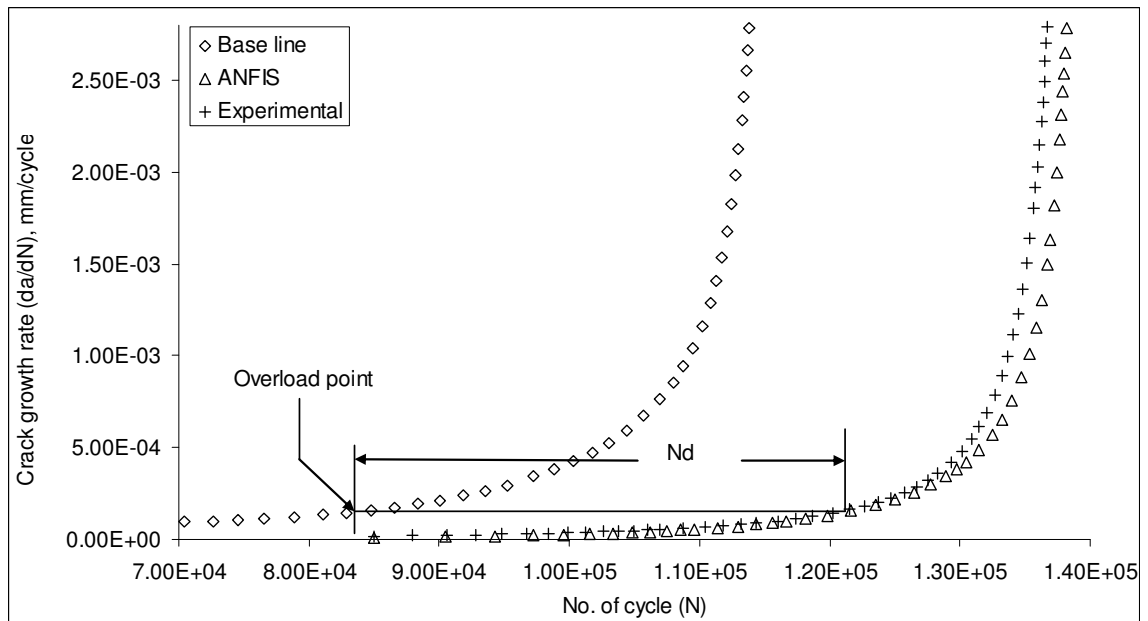


Fig. 7.15 – Predicted (ANFIS) and experimental delay cycle (2024-T3)

7.6 Modeling under constant amplitude loading interspersed with spike overload in mixed mode (I and II)

7.6.1 Application design

It has been verified earlier [2, 58, 59] and also in the present investigation (Figs. 4.26 and 4.27; Section: 4.3.3; Chapter-IV) that a pure Mode-I overload ($\beta=0^\circ$) leads to maximum retardation, while Mode-II overload ($\beta=90^\circ$) has least effect on it. In the intermediate ranges ($\beta = 18^\circ, 36^\circ, 54^\circ, \text{ and } 72^\circ$), the single tensile overload has mixed effect due to the presence of shear stress component. Accordingly, the fatigue crack growth retardation is affected by different angles of overloading leading to variation in residual fatigue life. Therefore, maximum stress intensity factor (K_{\max}) and stress intensity factor range (ΔK) were selected along with overloading angle (β) as three linguistic input variables whereas, crack growth rate (da/dN) was taken as one output variable. A set of linguistic rules formulated, in the “*If-Then*” form were derived from expert observation and experimentation. The model architecture was designed by taking the five overloading angle ($\beta = 0^\circ, 18^\circ, 36^\circ, 72^\circ$ and 90°) fatigue test data as training set (TS) and one data ($\beta = 54^\circ$) as validation set (VS) in case of both the materials. Parameters (Table 7.1) selected during training were also same as that of constant amplitude loading case.

7.6.2 Model validation

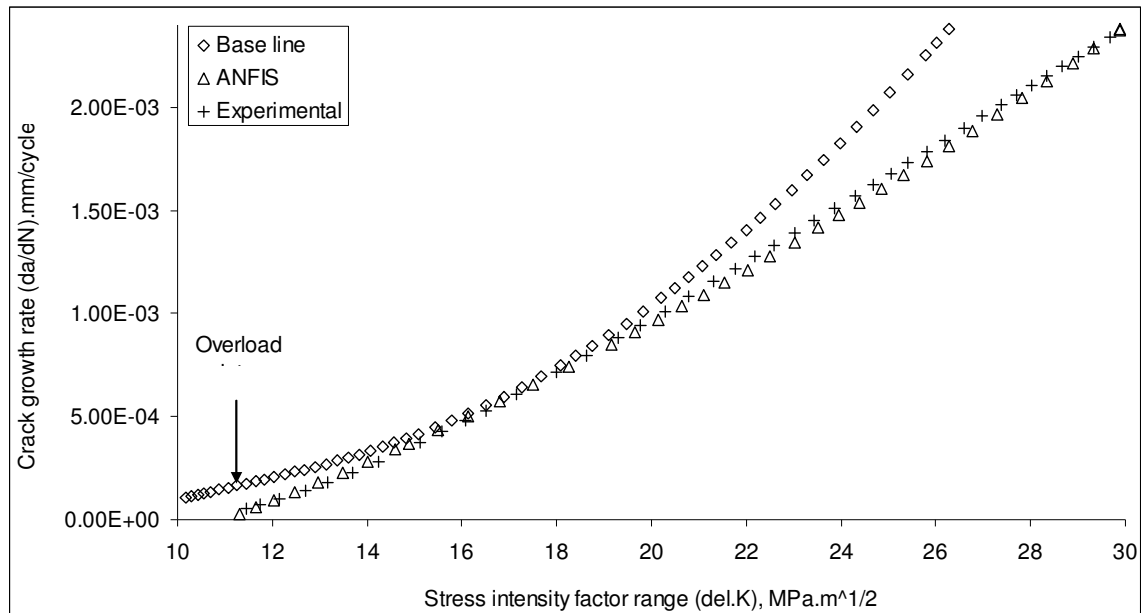
After proper training, the model was tested for overload angle of 54° in both the cases. Table 7.6 shows the performance of the model in terms of three statistical indices both during training and testing. The numbers of cycles were calculated from predicted crack growth rate in a similar manner as that of previous cases. The various model results are compared with the experimental findings both quantitatively and qualitatively as presented in Table 7.7 and also in Figs. 7.16 to 7.23 respectively.

Table 7.6 – Performance of ANFIS model

Material	During training			During testing			Computational Time (Min.)
	RMSE	R^2	MPE	RMSE	R^2	MPE	
7020-T7	0.001643	0.99973	0.388387	0.018899	0.94895	0.89495	395
2024-T3	0.002513	0.99864	0.345620	0.010269	0.96869	0.87694	382

Table 7.7 – Comparison of ANFIS model results with experimental data

Test sample	a_d^{AN} mm	a_d^E mm	% error in a_d^{AN}	N_d^{AN} K cy.	N_d^E K cy.	% error in N_d^{AN}	N_f^{AN} K cy.	N_f^E K cy.	% error in N_f^{AN}
7020-T7	1.880	1.994	-5.717	21.96	21.750	+0.966	75.045	74.778	+0.357
2024-T3	2.150	2.300	-6.522	20.028	20.019	+1.653	119.19	118.48	+0.604

Fig. 7.16 – Predicted (ANFIS) and experimental crack growth rate for $\beta = 54^\circ$ (7020-T7)

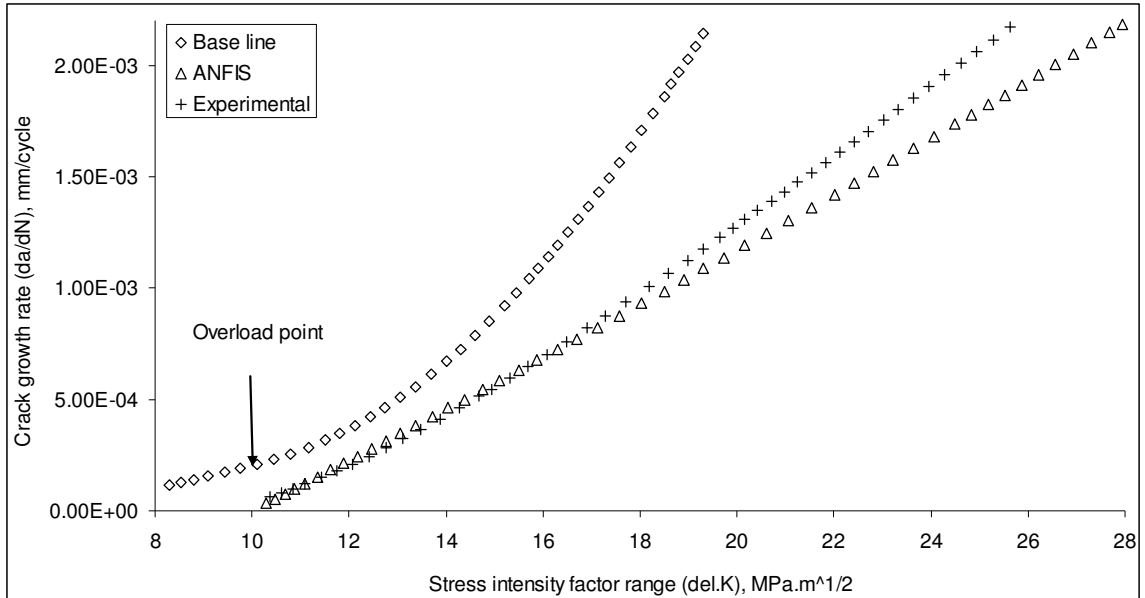


Fig. 7.17 – Predicted (ANFIS) and experimental crack growth rate for $\beta = 54^\circ$ (2024-T3)

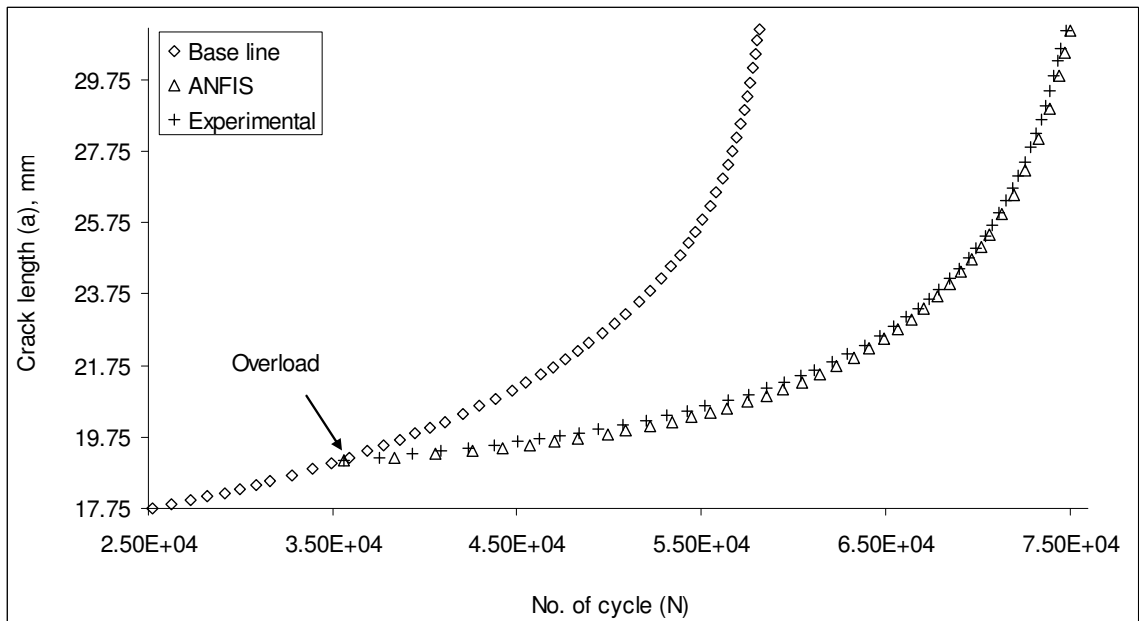


Fig. 7.18 – Predicted (ANFIS) and experimental number of cycle for $\beta = 54^\circ$ (7020-T7)

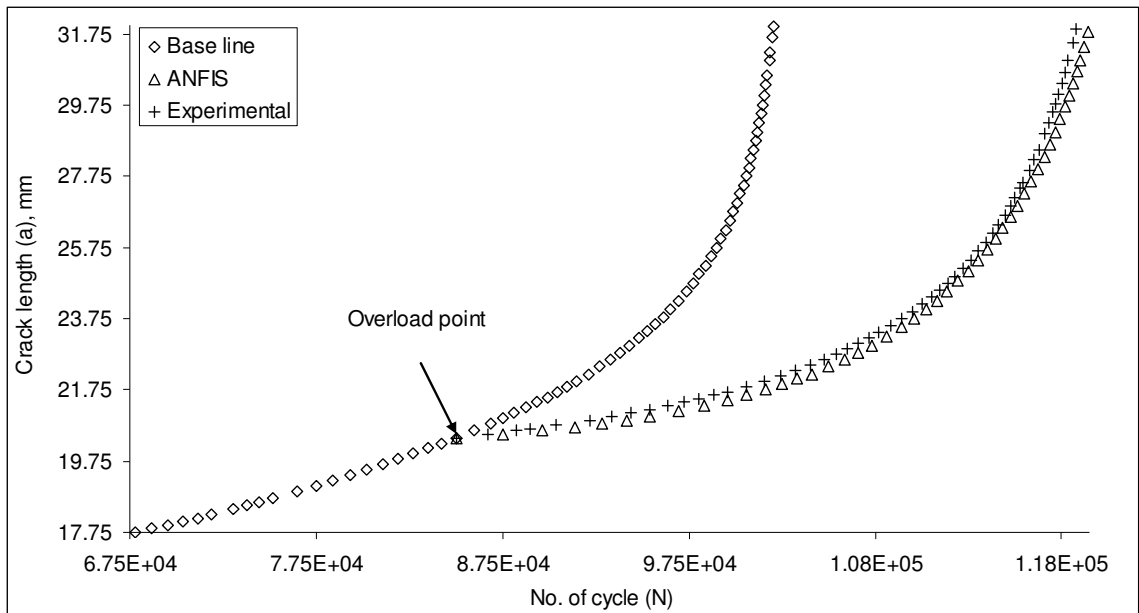


Fig. 7.19 – Predicted (ANFIS) and experimental number of cycle for $\beta = 54^\circ$ (2024-T3)

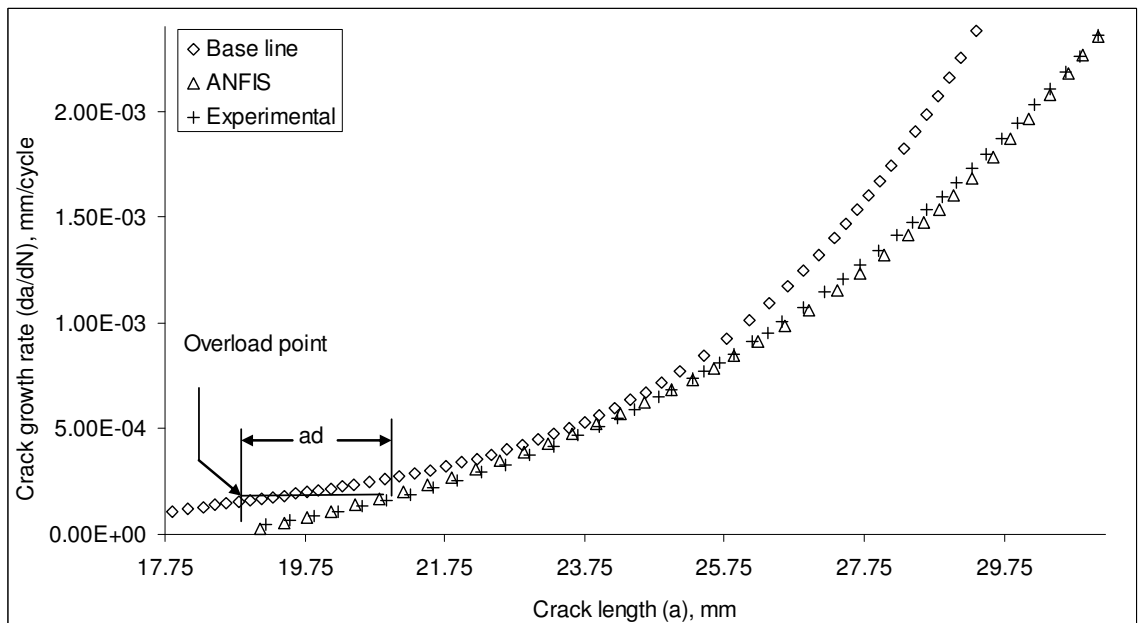


Fig. 7.20 – Predicted (ANFIS) and experimental retarded crack length (7020-T7)

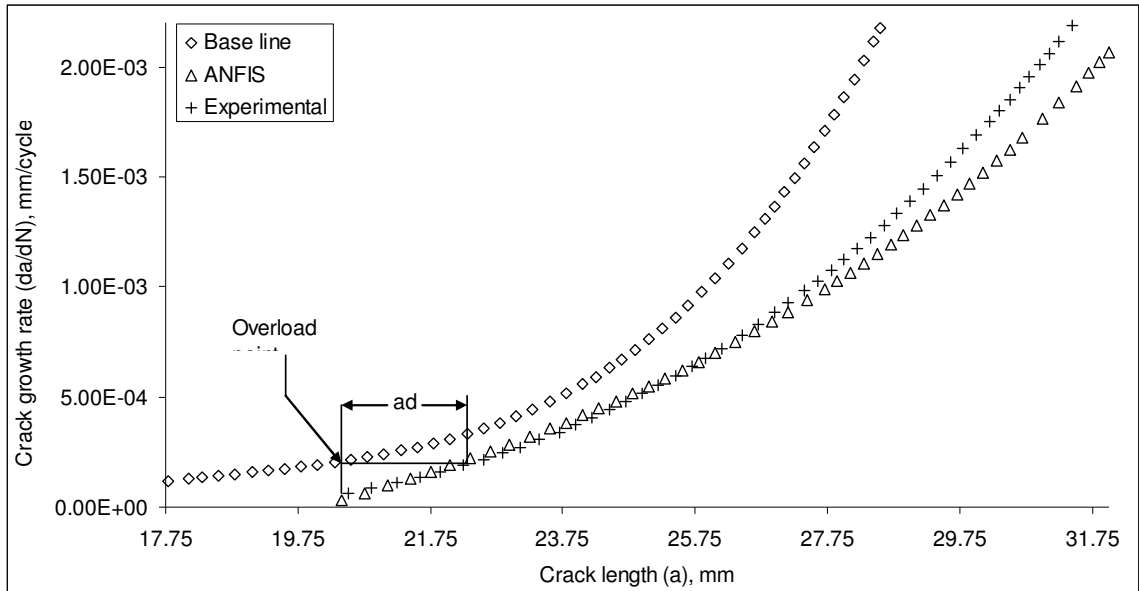


Fig. 7.21 – Predicted (ANFIS) and experimental retarded crack length (2024-T3)

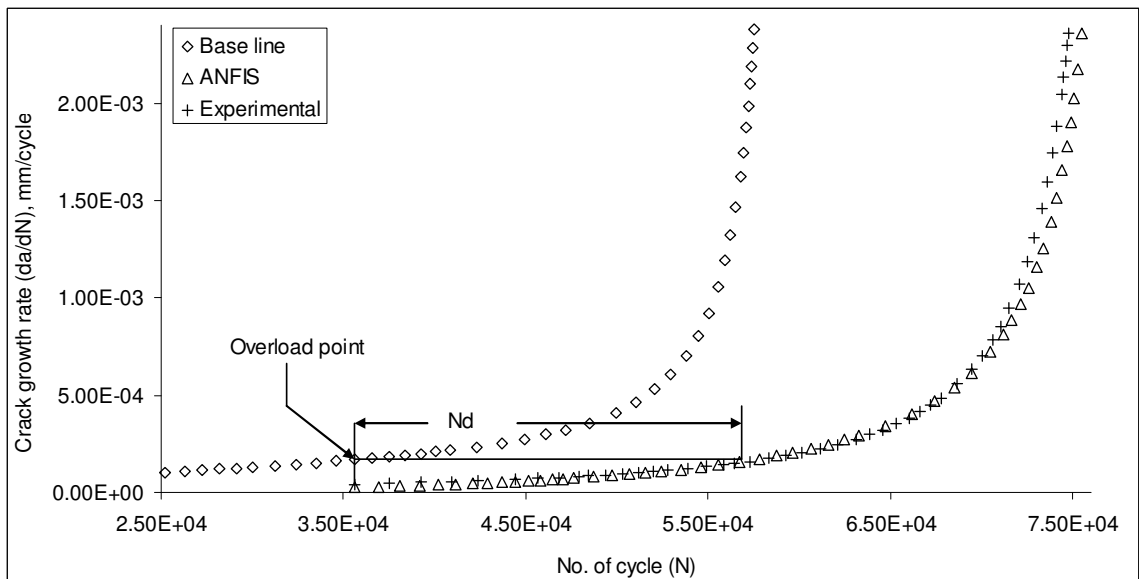


Fig. 7.22 – Predicted (ANFIS) and experimental delay cycle (7020-T7)

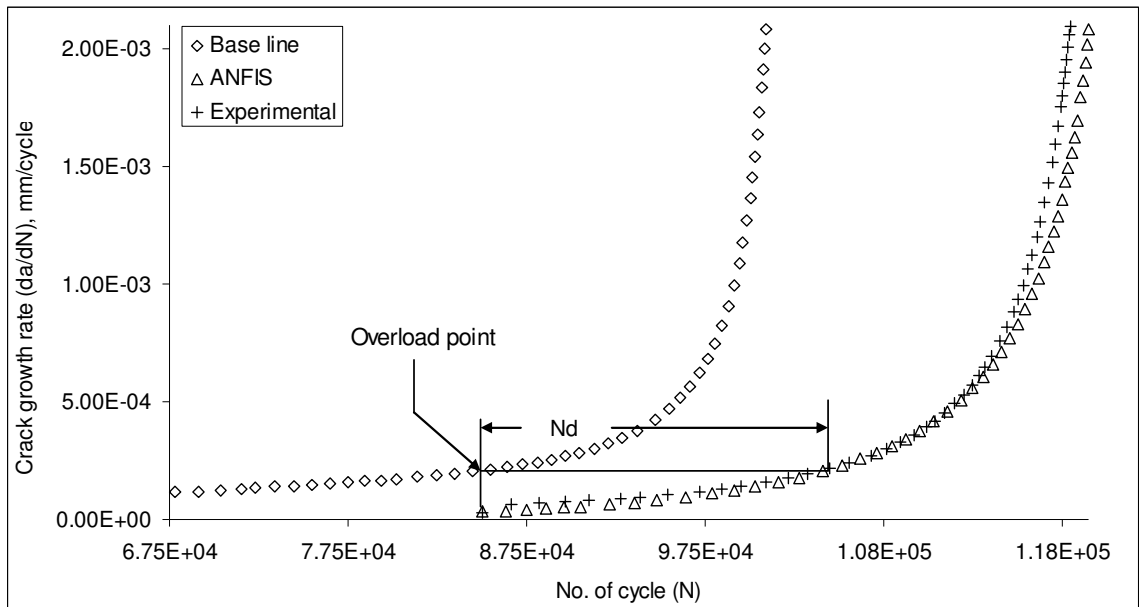


Fig. 7.23 – Predicted (ANFIS) and experimental delay cycle (2024-T3)

CHAPTER VIII

RESULTS AND DISCUSSION

8.1 Introduction

This chapter is devoted to study the performance characteristics of the proposed exponential model. Three evaluation criteria have been adopted to compare its prediction accuracy quantitatively with the two soft-computing methods (i.e. ANN and ANFIS) implemented for life predictions. Finally, a brief discussion has been provided describing the relative merits and limitations of the proposed exponential model with that of soft-computing methods and some of the conventional life prediction models.

8.2 Comparison of predicted and experimental results

In the present investigation, the performances of different fatigue life prediction models are evaluated by comparing the predicted results with the experimental findings by the following criteria:

- Percentage deviation of predicted result from the experimental data i.e.

$$\% \text{Dev} = \frac{\text{Predicted result} - \text{Experimental result}}{\text{Experimental result}} \times 100 \quad (8.1)$$

- Prediction ratio which is defined as the ratio of actual data (i.e. experimental) to predicted result i.e.

$$\text{Prediction ratio, } P_r = \frac{\text{Actual data}}{\text{Predicted result}} \quad (8.2)$$

- Error bands, i.e. the scatter of the predicted life in either side of the experimental life within certain error limits.

8.2.1 Constant amplitude loading

Set-1

As presented in Chapter–III, the constant amplitude fatigue crack growth tests were conducted in two sets for both 7020-T7 and 2024-T3 Al-alloys. In set-1, a fixed load ratio of $R = 0.1$ was maintained whereas in set-2, different load ratios ($R = 0, 0.2, 0.4, 0.5, 0.6$

and 0.8) were maintained to study their effects on crack growth rates. In 1st set, the fatigue life was predicted by applying the exponential model and the predicted results were compared with that of Forman model. It may be mentioned here that the soft-computing techniques are data base dependent and the predictions are confined within training ranges. Hence, there was no scope to apply ANN and ANFIS in case of set-1 as the data base was not enough for the purpose. The percentage deviations and the prediction ratios of the two alloys are presented in Table 8.1. It is observed that the maximum deviation of fatigue life predicted by Forman model is -2% whereas it is -1.3% in case exponential model. The prediction ratio in both the models is approximately 1.0. Heuler and Schuetz [144] suggested that a fatigue life prediction method may be considered adequate if the prediction ratios lie within the range of 0.5 to 2.0. Therefore, the performance of the proposed exponential model may be considered satisfactory and conservative under the given loading condition. The error band scatter of the predicted lives of both the alloys is presented in Figs. 8.1 and 8.2. The figures show that the predictions by the proposed exponential model lie within $\pm 0.025\%$ of experimental life. It under-predicts the life compared to the life predicted by Forman model and hence is a better proposition. The graphical comparisons of predicted lives are presented in Figs. 8.3 and 8.4 for both the materials respectively.

Table 8.1 – Model performances under CAL (R -constant)

Test Specimen	% Dev (N_f^F)	% Dev (N_f^P)	Prediction ratio of Forman model (P_r^F)	Prediction ratio of exponential model (P_r^P)
7020-T7	-1.953	-1.283	1.019	1.008
2024-T3	-0.775	-0.424	1.012	1.004

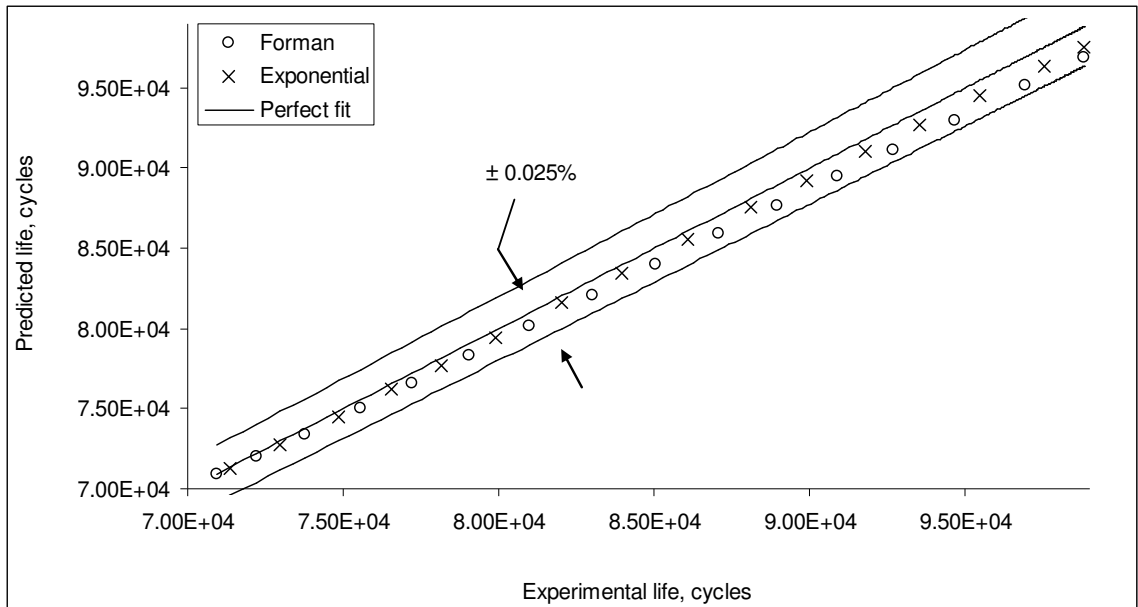


Fig. 8.1 – Error band scatter of predicted lives of 7020-T7 under CAL (R -constant)

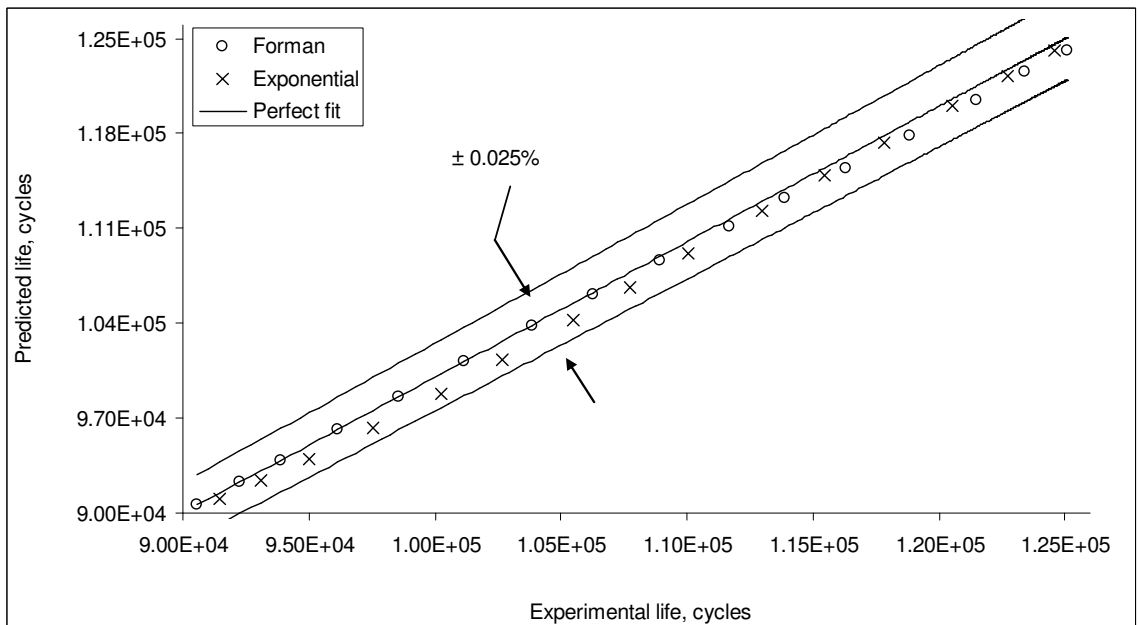


Fig. 8.2 – Error band scatter of predicted lives of 2024-T3 under CAL (R -constant)

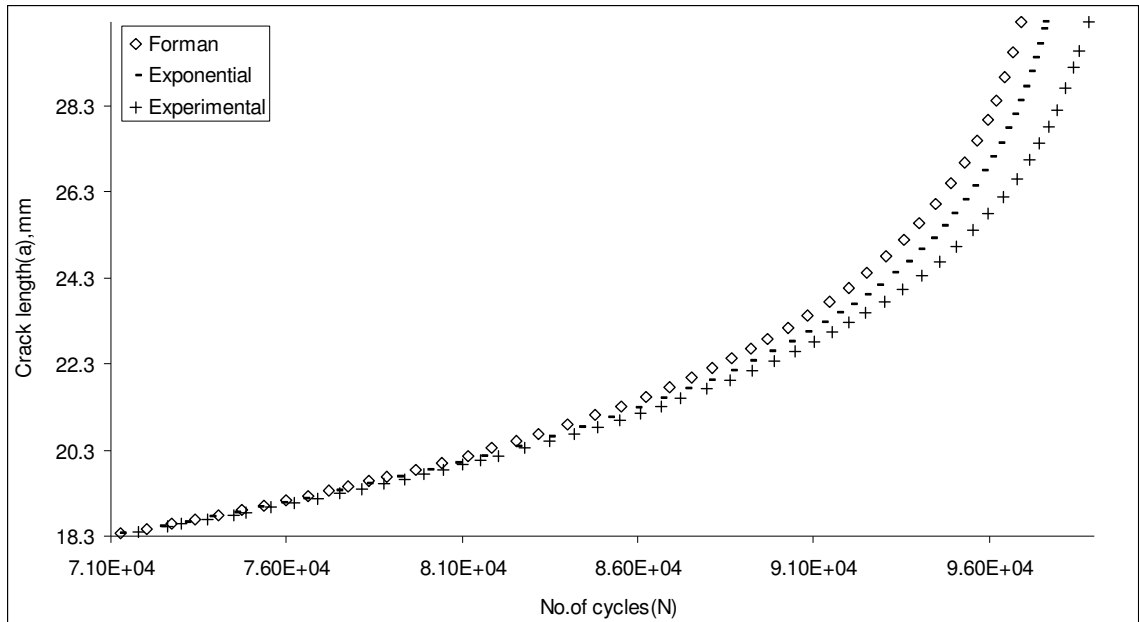


Fig. 8.3 – Superimposed constant amplitude $a-N$ curves of Al 7020-T7 (R -constant)

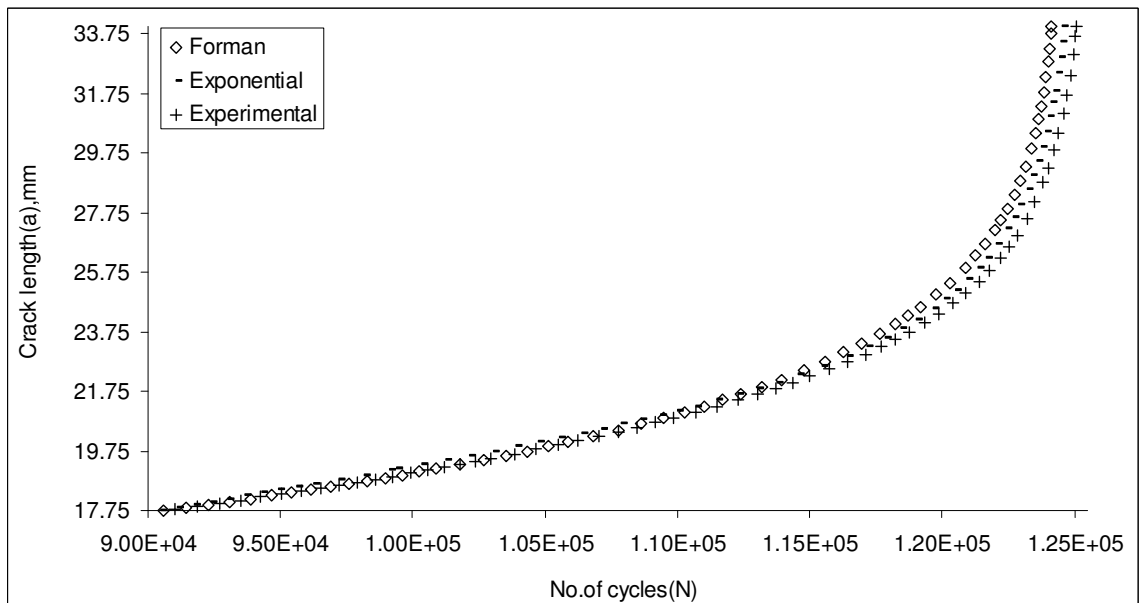


Fig. 8.4 – Superimposed constant amplitude $a-N$ curves of Al 2024-T3 (R -constant)

Set-2

In 2nd set of constant amplitude loading fatigue tests, the results predicted by exponential model were compared with those obtained from ANN and ANFIS. The performance characteristics in terms of percentage deviation and prediction ratio are tabulated in Table 8.2.

It may be observed that the maximum percentage deviations of fatigue lives of exponential, ANN and ANFIS models are -0.7%, -4.4% and -2.5% respectively. The prediction ratios for all the cases are approximately 1.0. It reveals that exponential model gives much better performance in comparison to the other two models in terms of percentage deviation. Comparing the relative performances of ANFIS and ANN, former provides better result than the later. Figs. 8.5 and 8.6 show that the scatter of the predicted lives from all the models are within $\pm 0.05\%$ error band in 7020-T7 alloy and $\pm 0.025\%$ error band in 2024-T3 alloy. Further, predicted lives lie below the experimental data. This indicates that the results are conservative and acceptable. The graphical comparisons of predicted lives are presented in Figs. 8.7 and 8.8 for both the materials respectively.

Table 8.2 – Model performances under CAL (*R*-varying)

Test Specimen	% Dev (N_f^P)	% Dev (N_f^A)	% Dev (N_f^{AN})	Prediction ratio of exponential model (P_r^P)	Prediction ratio of ANN (P_r^A)	Prediction ratio of ANFIS (P_r^{AN})
7020-T7	-0.658	-4.366	-2.484	1.007	1.046	1.025
2024-T3	-0.370	-2.100	-0.801	1.004	1.021	1.008

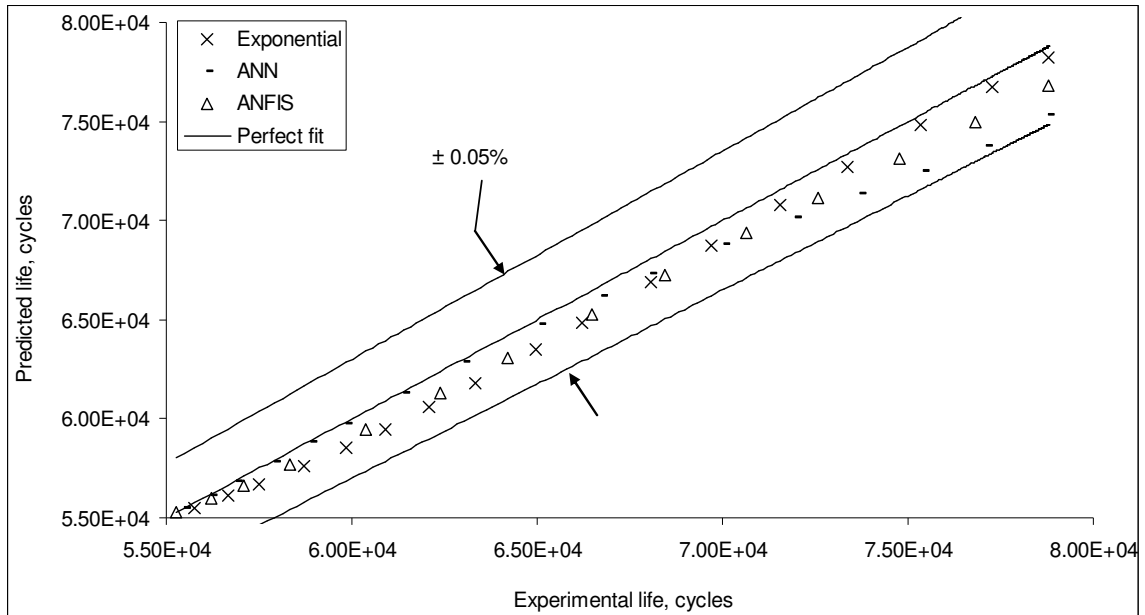


Fig. 8.5 – Error band scatter of predicted lives of 7020-T7 under CAL (R -varying)

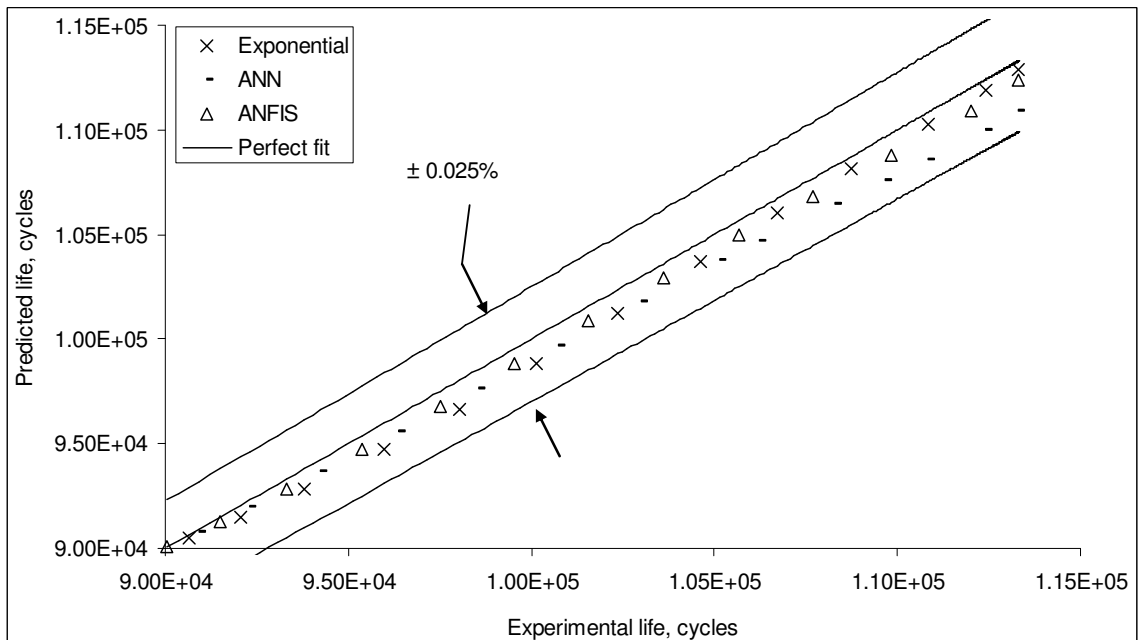


Fig. 8.6 – Error band scatter of predicted lives of 2024-T3 under CAL (R -varying)

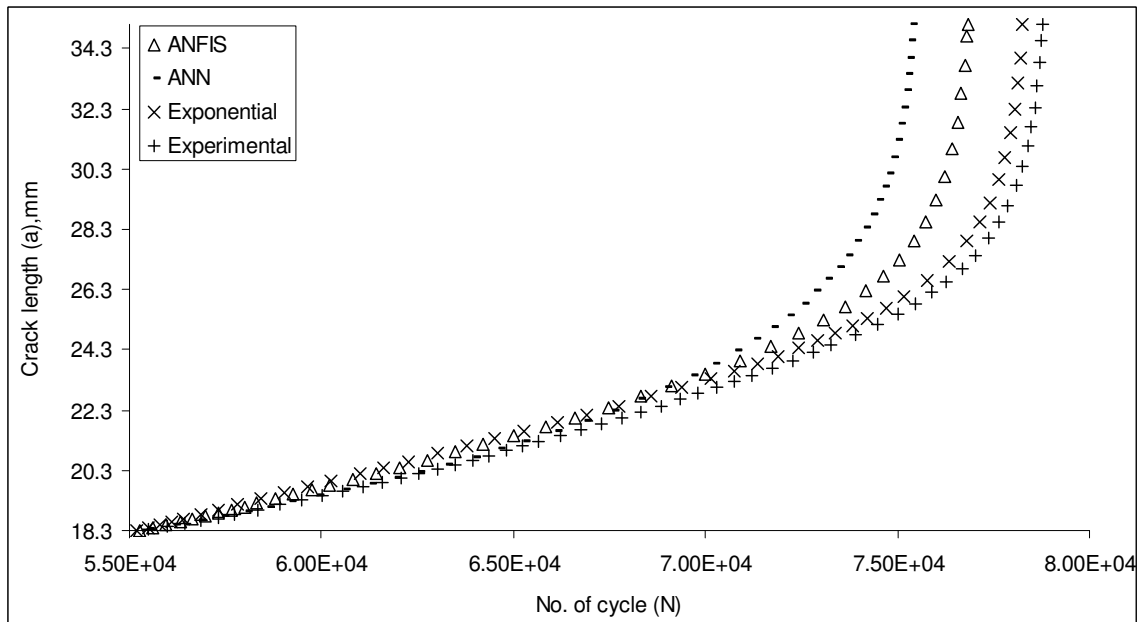


Fig. 8.7 – Superimposed constant amplitude $a-N$ curves of Al 7020-T7 (R -varying)

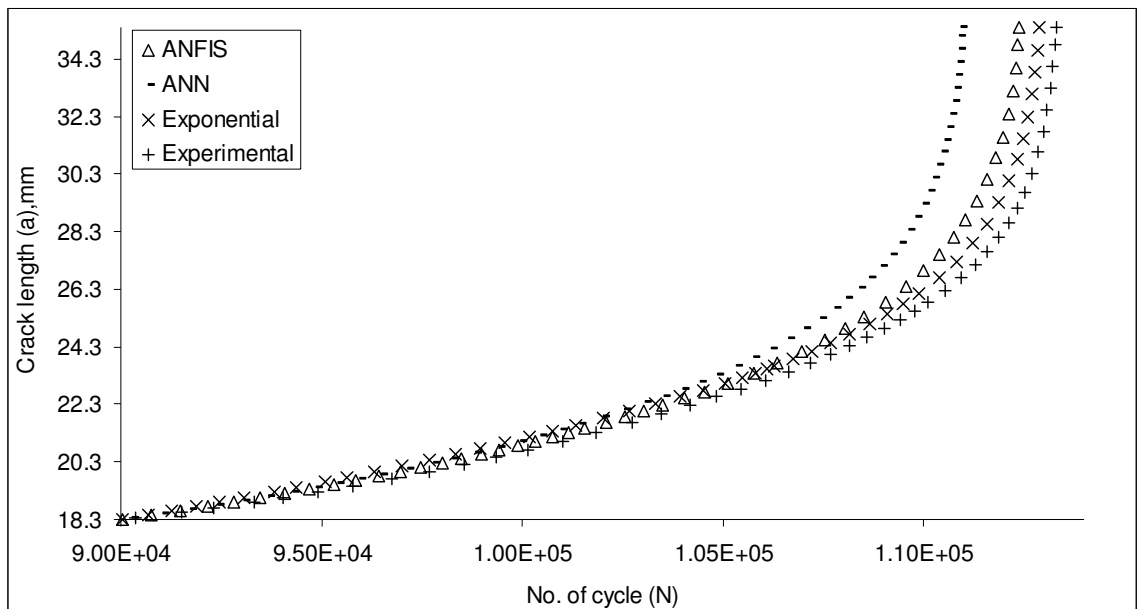


Fig. 8.8 – Superimposed constant amplitude $a-N$ curves of Al 2024-T3 (R -varying)

8.2.2 Constant amplitude loading interspersed with spike overload in mode-I

Since the values of various retardation parameters (a_d , N_d) are equally important, their percentage deviations have been compared with the Wheeler model and presented in Table 8.3. Table 8.4 illustrates the performances of various models in terms of percentage deviations and prediction ratios of post-overload lives for the alloys. Analyzing the performance results of the models, it is observed that the maximum deviations of post-overload fatigue crack propagation life are -1.7%, +3.6% and +2.0% in case of exponential, ANN and ANFIS models respectively and the prediction ratio is approximately 1.0. In this case too the relative performance of exponential model is much better than those obtained by soft-computing techniques. Further, comparing the results of ANN and ANFIS, the predicted results of the later is better than the former one. It is observed that all the model results are within $\pm 0.05\%$ error band in case of Al 7020-T7 alloy (Fig. 8.9), whereas it is $\pm 0.08\%$ in case of Al 2024 T3 alloy (Fig. 8.10). Figs. 8.11 and 8.12 show graphical representation of the predicted fatigue lives under the above load condition.

Table 8.3 – Percentage deviations of retardation Parameters (mode-I overload)

Test sample	% Dev a_d^P	% Dev a_d^A	% Dev a_d^{AN}	% Dev a_d^W	% Dev N_d^P	% Dev N_d^A	% Dev N_d^{AN}	% Dev N_d^W
7020-T7	-1.40	-6.37	+4.70	+3.29	-2.03	+7.09	+4.494	-2.32
2024-T3	-5.50	-8.76	+6.88	+12.4	-2.53	+8.29	+7.931	-8.19

Table 8.4 – Model performances under interspersed mode-I overload

Test Specimen	% Dev (N_f^P)	% Dev (N_f^A)	% Dev (N_f^{AN})	Prediction ratio of exponential model (P_r^P)	Prediction ratio of ANN(P_r^A)	Prediction ratio of ANFIS(P_r^{AN})
7020-T7	-1.68	+3.60	+1.95	1.017	0.965	0.981
2024-T3	-0.77	+1.89	+1.10	1.008	0.981	0.989

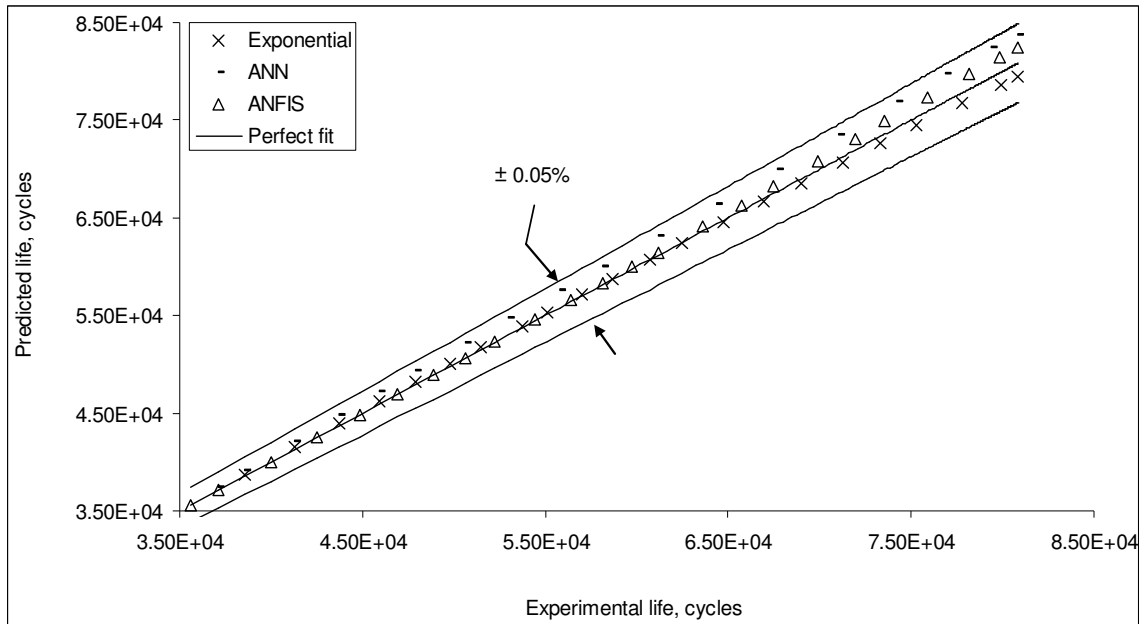


Fig. 8.9 – Error band scatter of predicted lives of 7020-T7 under mode-I overload

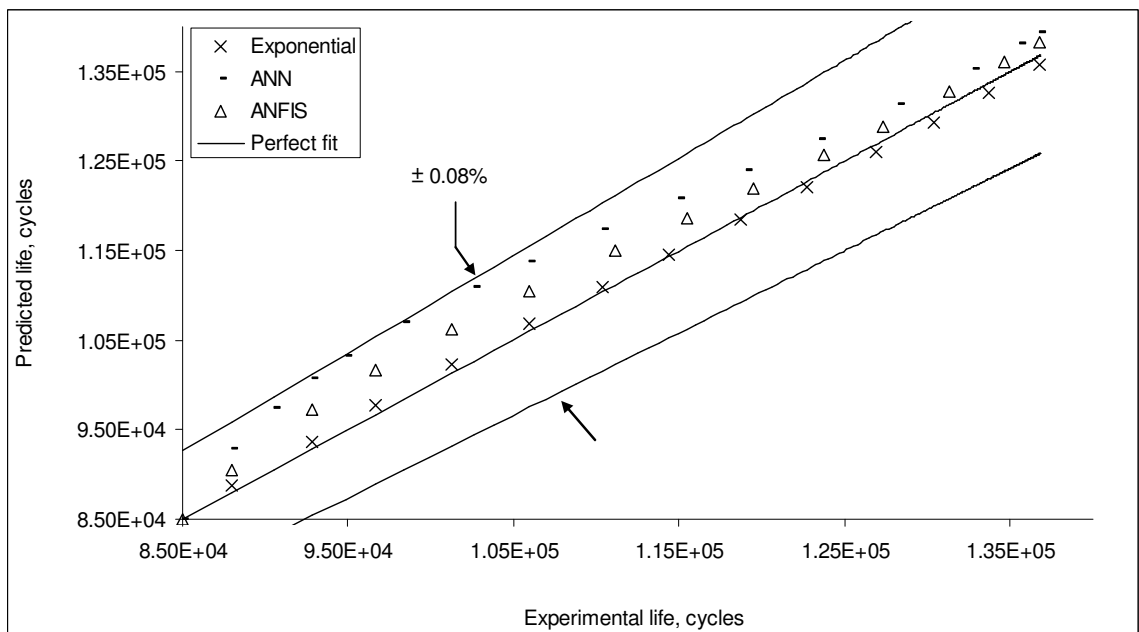


Fig. 8.10 – Error band scatter of predicted lives of 2024-T3 under mode-I overload

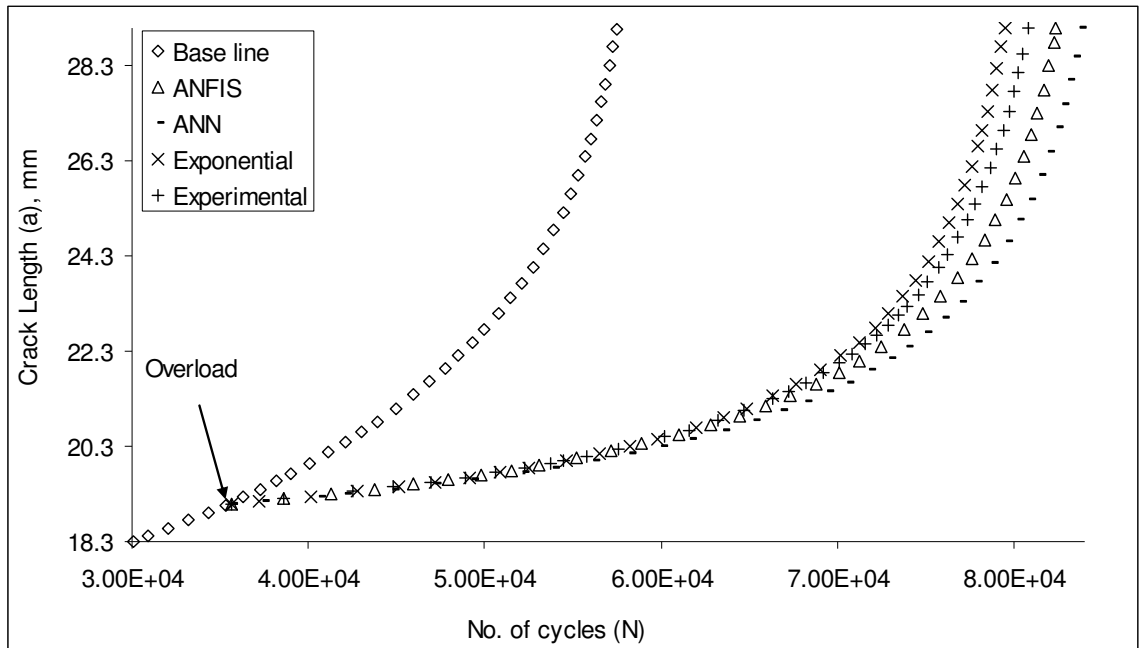


Fig. 8.11 – Superimposed mode-I overload $a - N$ curves of Al 7020-T7

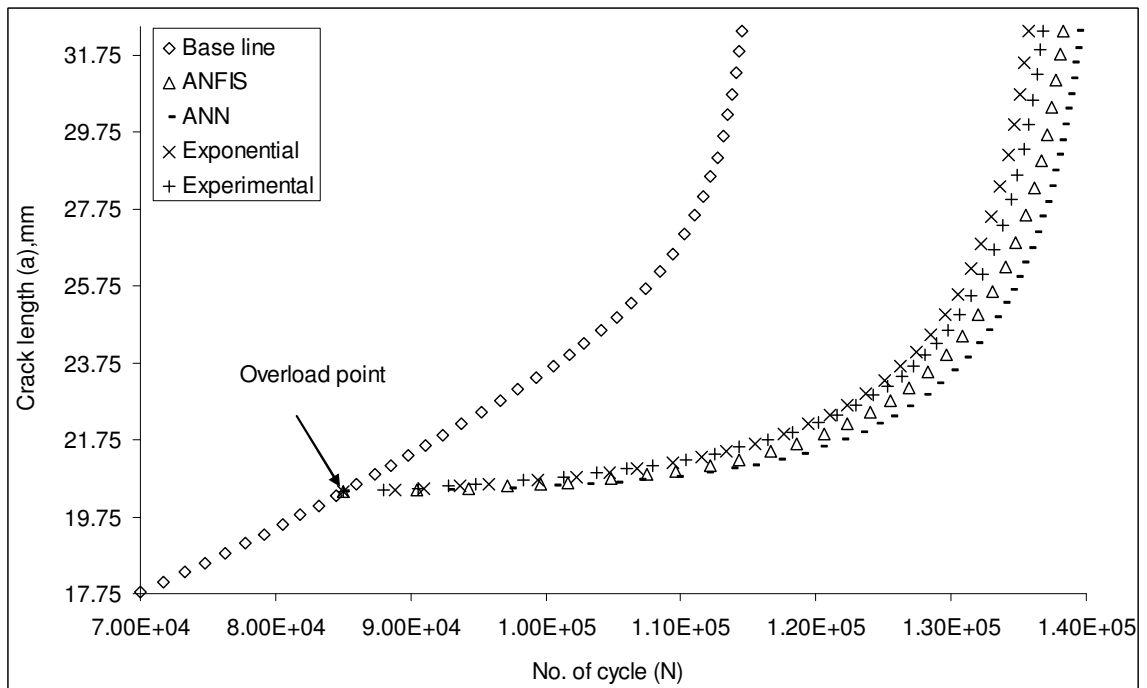


Fig. 8.12 – Superimposed mode-I overload $a - N$ curves of Al 2024-T3

8.2.3 Constant amplitude loading interspersed with spike overload in mixed mode (I and II)

Prediction of fatigue crack propagation life under interspersed mixed mode (I and II) is of particular importance because no such model is available in the literature. Under this loading condition, all the three models are applied to predict the post-overload fatigue crack propagation life alongwith retardation parameters for the alloys. The percentage deviations of retardation parameters of the models are presented in Table 8.5. Table 8.6 shows the performances of the models in terms of post-overload fatigue life.

The post-overload lives are within -0.2% to $+1.5\%$ and the prediction ratio is about 1.0. Hence, the overall performances of all the models are quite satisfactory. As far as relative performance is concerned, the performance of exponential model is better since it under-estimates in all the cases. Analyzing the error band scatter of the predicted model results (Figs. 8.13 and 8.14) it is observed that the results of Al 7020-T7 are within $\pm 0.05\%$ error band while, it is less i.e. $\pm 0.025\%$ for Al 2024-T3. Both the soft-computing methods (ANN and ANFIS) slightly over-predict life whereas exponential model under-predicts life with a better comparative result. The graphical representation of the predicted fatigue lives under the above loading condition for both the alloys are presented in Figure 8.15 and 8.16.

Table 8.5 – Percentage deviations of retardation Parameters (mixed mode overload)

Test sample	% Dev a_d^P	% Dev a_d^A	% Dev a_d^{AN}	% Dev N_d^P	% Dev N_d^A	% Dev N_d^{AN}
7020-T7	-0.80	-4.71	-5.72	-1.195	.664	+0.966
2024-T3	-1.13	-6.91	-6.52	-2.273	3.856	+1.653

Table 8.6 – Model performances under interspersed mixed mode overload

Test sample	% Dev (N_f^P)	% Dev (N_f^A)	% Dev (N_f^{AN})	Prediction ratio, expo. model (P_r^P)	Prediction ratio, ANN (P_r^A)	Prediction ratio, ANFIS (P_r^{AN})
7020-T7	-0.241	+0.956	+0.357	1.0024	0.991	0.996
2024-T3	-0.219	+1.415	+0.604	1.0021	0.986	0.994

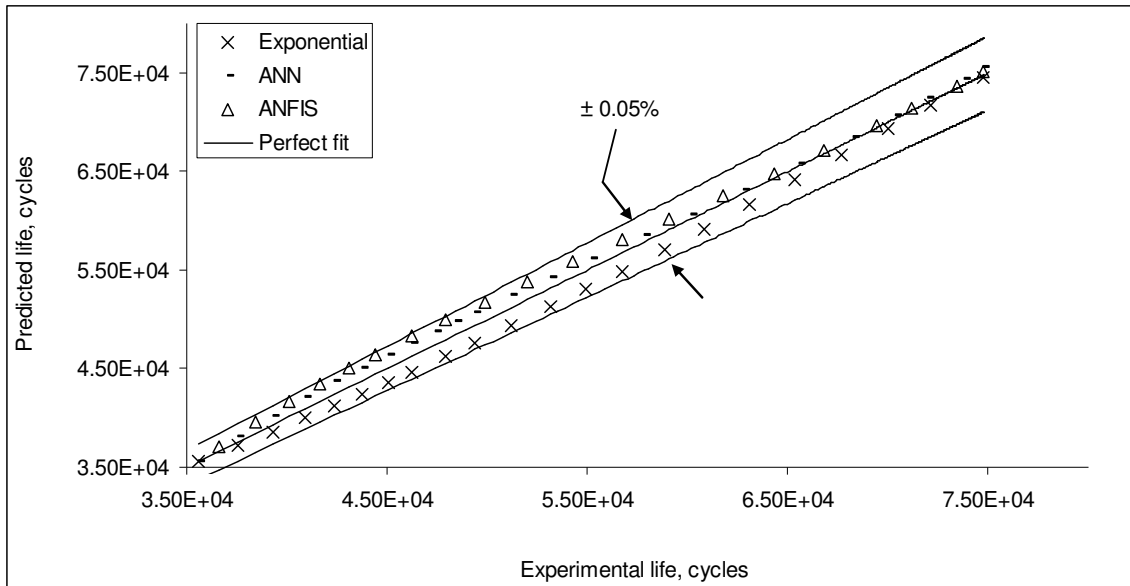


Fig. 8.13 – Error band scatter of predicted lives of 7020-T7 under mixed mode overload

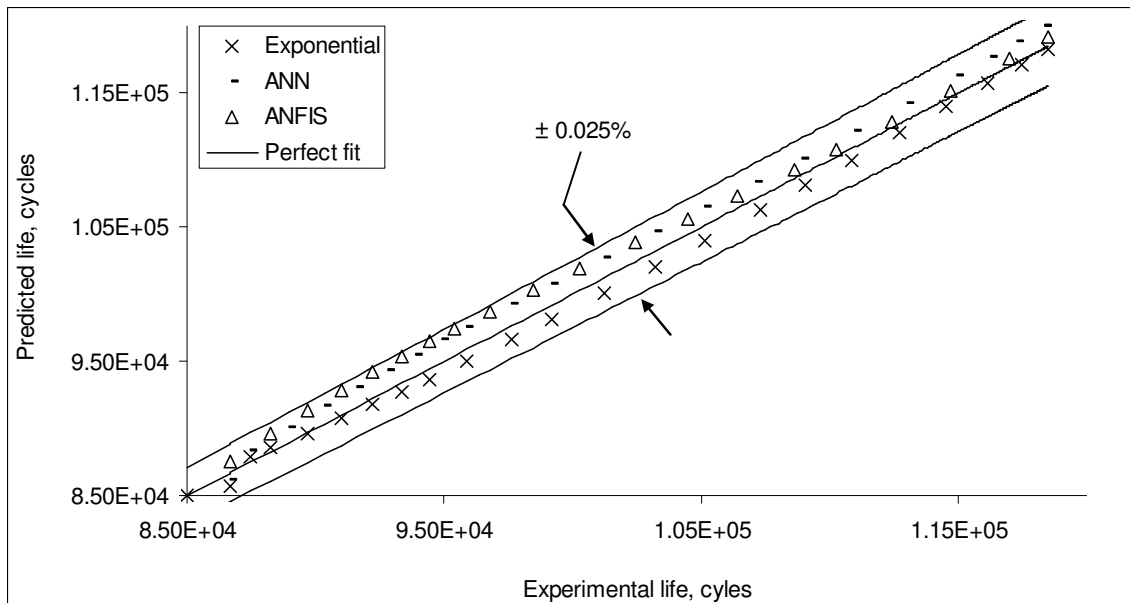


Fig. 8.14 – Error band scatter of predicted lives of 2024-T3 under mixed mode overload

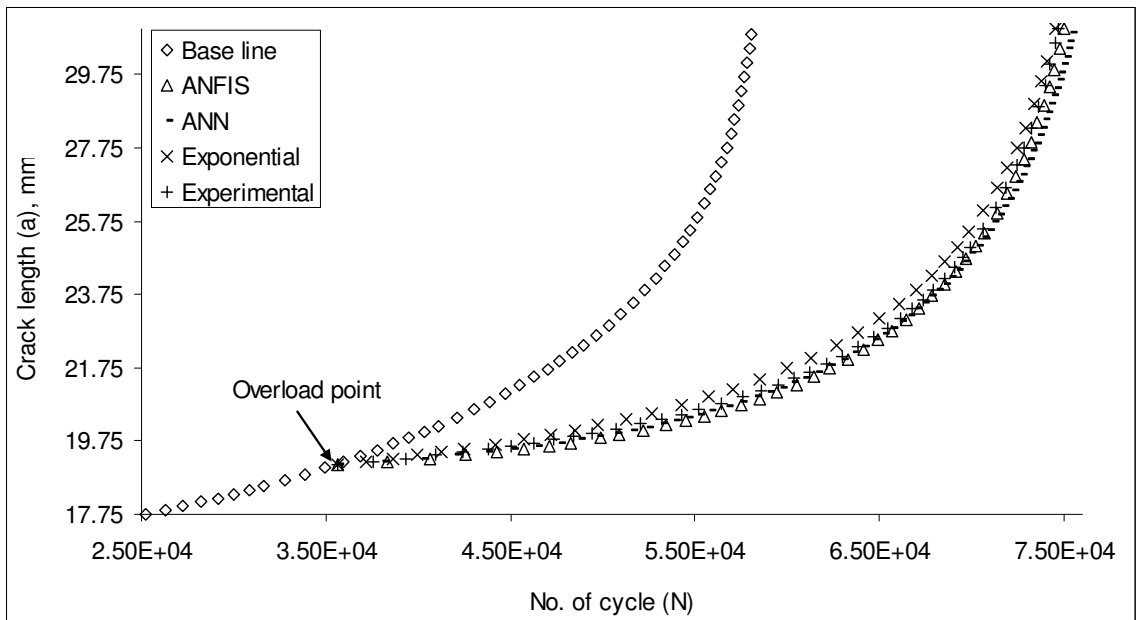


Fig. 8.15 – Superimposed mixed mode (I and II) overload $a - N$ curves of Al 7020-T7

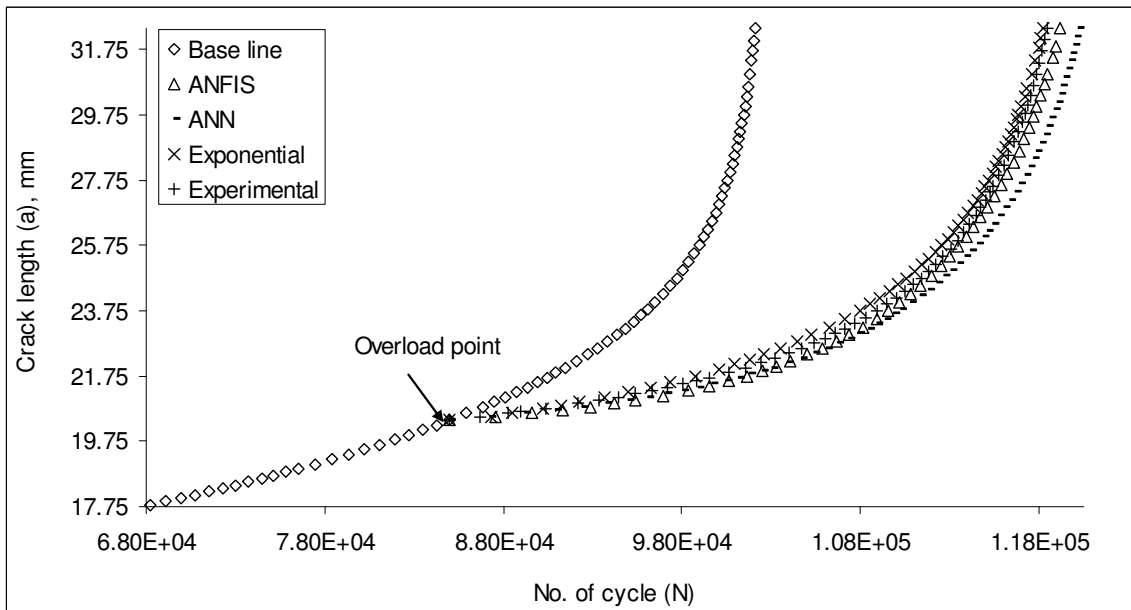


Fig. 8.16 – Superimposed mixed mode (I and II) overload $a - N$ curves of Al 2024-T3

8.3 Discussion

Irrespective of the scatter in the experimental $a-N$ data (Fig. 4.1, Chapter-IV), the growth of sub-critical fatigue crack can be visualized as exponential in nature. The result

of section-4.2 (Chapter-IV) reveals that the experimental crack length vs. number of cycle data can be fitted by an exponential equation of the form $a_j = a_i e^{m_{ij}(N_j - N_i)}$. This facilitates in smoothening the scattered a - N data thereby simplifying the calculation of da/dN . It is also observed that the values of da/dN obtained (Fig. 4.3) from the proposed method reduces scatter in comparison to the incremental polynomial method as per ASTM standard [127]. Further, the above exponential equation has efficiently been used to model and estimate fatigue life under different loading conditions as described in Chapter-V.

In the proposed exponential model, the most important parameter is the exponent of the exponential equation (i.e. specific growth rate m_{ij}). It may be noted that this parameter is not a constant quantity. It varies with number of cycles (and hence crack length) and its variation depends on various crack driving parameters (load history and loading conditions) and material properties. Therefore, it is suitably correlated with two crack driving forces (ΔK and K_{\max}) as per *Unified Approach* and material properties (E and σ_{ys}). Further, these are expressed in non-dimensional forms so that the exponential model equation becomes dimensionally correct.

Till date it is considered that the conventional Paris-Erdogan model is the most fundamental and widely used crack growth model describing fatigue crack propagation in terms of the peak-to-peak range of K in the fatigue cycle. Spagnoli [109] analyzed the Paris-Erdogan law on the basis of both *similarity* methods and *fractal* concepts and presented some experimental evidence of its breakdown of similitude concept. According to his analysis, Paris-like fatigue crack growth law (i.e. based on LEFM parameters) is able to predict crack growth as per similitude concept. But, whenever the crack size is small (for micron-sized crack and for heterogeneous materials), the crack growth rate depends on crack size leading to incomplete self-similarity (non-self similarity) of Paris-Erdogan relation. Based on these facts, Spagnoli proposed a crack-size dependent Paris-Erdogan relation by strengthening the phenomenon of incomplete self-similarity in the fatigue crack growth process. In case of the proposed exponential model, the above fact has been verified by the following analysis.

The fundamental equation of the model is:

$$a_j = a_i e^{m_{ij}(N_j - N_i)} \quad (8.3)$$

Differentiating the above equation the CGR becomes:

$$\frac{da}{dN} = \frac{a_i m_{ij} m'_{ij} (N_j - N_i)}{(1 - e^{m_{ij}(N_j - N_i)})} \quad (8.4)$$

From the differential equation (Eq. 8.4) of proposed exponential model, it can be observed that the equation follows the form proposed by Spagnoli [109] for non-self similar growth. The equation also follows the concept of a fractal crack emphasizing the fact that crack growth rate is crack size dependent as per Frost and Dugdale law.

Further in the Paris-Erdogan model, there is a physical inconsistency when the constants of the crack growth rate equation are randomized as per dimensional analysis point of view [110]. In case of the proposed exponential model (Eqs. 5.5 and 5.8), this type of inconsistency does not arise since the specific growth rate (m_{ij}) is a dimensionless quantity.

Most of the fatigue crack growth models are in the form of differential equations relating crack growth rate and stress intensity factor raised to a power of approximately 3. Hence, any inaccuracy in the value of stress intensity factor is magnified in life calculation. The discrepancies may be even more dramatic for initial cracks loaded near the fatigue threshold limit. The involvement of robust numerical integration scheme also makes the life calculation more complicated particularly for variable amplitude loading [122]. But, in the proposed exponential model any inaccuracy in the values of crack driving forces does not significantly alter the fatigue life as the specific growth rate m_{ij} is related to different crack driving forces raised to a power (highest) of 0.75.

Two soft-computing methods i.e. artificial neural network (ANN) and adaptive neuro-fuzzy inference (ANFIS) techniques have been developed to predict the fatigue lives under the same loading conditions as described in Chapters-VI and VII. The predicted results from the above methods have been quantitatively compared with the proposed exponential model in Chapter-VIII. From the analysis of the predicted results (section 8.2), it can be observed that the proposed exponential model under-predicts the fatigue life while, the two soft-computing methods (ANN and ANFIS) over-estimate it.

CHAPTER IX

CONCLUSIONS AND FUTURE WORK

9.1 Conclusions

In the present work, the fatigue crack growth study was conducted on 7020-T7 and 2024-T3 aluminum alloys. The test programs were performed under three different loading conditions: constant amplitude loading with fixed and variable load ratios, constant amplitude loading interspersed with spike overload in mode-I as well as in mixed-mode (I and II). A new method was suggested to calculate crack growth rate (da/dN) from experimental $a-N$ data. That concept was subsequently utilized to propose a prediction model (i.e. Exponential Model) in order to estimate the residual life under all the three loading conditions. Further, two soft-computing techniques (i.e. ANN and ANFIS) were formulated and applied to predict the fatigue life under same loading conditions. Finally, their predicted results were compared with that of proposed exponential model.

The conclusions drawn from the present work are summarized as follows:

1. An exponential equation of the form $a_j = a_i e^{m_{ij}(N_j - N_i)}$ has been effectively used to smoothen the scattered experimental $a-N$ data which in turn simplifies the calculation of crack growth rate (da/dN) irrespective of loading conditions.
2. Subsequently, to predict fatigue life, the exponent, m_{ij} (specific growth rate) has been judiciously correlated with crack driving parameters ΔK and K_{\max} and material properties K_C (for specific specimen geometry), E , σ_{ys} in the form of dimensionless quantities. The same form of equation can be used for different loading conditions and regimes II and III of crack propagation.
3. The rate equation derived from the exponential model has efficiently been used to estimate fatigue life. It is observed that the proposed exponential model under-predicts the life to an extent $\pm 0.025\%$ which is conservative from reliability point of view. The model also effectively estimates mode-I and mixed-mode (I and II) overload-induced retardation parameters (i.e. a_d and N_d). The differential form of

the equation conforms to dimensional analysis concept showing a dependence of da/dN on a .

4. Soft-computing methods, ANN and ANFIS, can be applied to predict the fatigue life under the given load conditions. In the present investigation, both the methods slightly over-estimate the life.

9.2 Suggested future work

In the course of this study several areas were identified for future investigation.

1. The proposed exponential model may be extended to small fatigue cracks.
2. Soft-computing methods may be used to determine the specific growth rate.
3. The proposed exponential model may be tested on other specimen geometries like MT, CT etc. and also with other materials.
4. Attempts may be made to use the model to predict fatigue life under other load scenarios.

References:

- [1] M. Sander, and H.A. Richard, "Finite element analysis of fatigue crack growth with interspersed mode-I and mixed mode overloads," *Int. J. of Fat.*, vol. 27, pp. 905-913, 2005.
- [2] M. Sander, and H.A. Richard, "Experimental and numerical investigations on the influence of the loading direction on the fatigue crack growth," *Int. J. of Fat.*, vol. 28, pp. 583-591, 2006.
- [3] R. I. Stephens, A. Fatemi, R. R. Stephens, and H. O. Fuchs, "Metal Fatigue in Engineering," 2nd Edition, John Wiley & Sons, Inc., New York, 2001.
- [4] F. A. McClintock, "On the plasticity of the growth of fatigue cracks," In *Fract. of Solids* (eds. D.C. Drucker & J.J. Gilman), New York: Wiley, vol. 20, pp. 65-102, 1963.
- [5] N. E. Frost, "The growth of fatigue cracks," In *Proceedings of the First International Conference on Fracture* (ed. T. Yokobori), Sendai, The Japan Society for Strength and Fracture of Materials, pp. 1433-1459, 1966.
- [6] P. C. Paris, R. J. Bucci, E.T. Wessel, W. G. Clark, and T. R. Mager, "Extensive study of low fatigue crack growth rates in A533 and A508 steels," In *Stress Analysis and Growth of Cracks*, ASTM STP, vol. 513, pp. 141-176, 1972.
- [7] R. A. Schmidt, and P. C. Paris, "Threshold for fatigue crack propagation and the effects of load ratio and frequency," In *Progress in Flaw Growth and Fracture Testing*, ASTM STP, vol. 536, pp. 79-94, 1973.
- [8] K. Sadananda, and P. Shahinian, "Prediction of threshold stress intensity for fatigue crack growth using a dislocation model," *Int. J. of Fract.*, vol. 13, pp. 585-

- 594, 1977.
- [9] C. Laird, "The influence of metallurgical structure on the mechanisms of fatigue crack propagation," In *Fatigue Crack Propagation*, ASTM STP, vol. 415, pp. 131-168, 1967.
- [10] R. W. Lardner, "A dislocation model of fatigue crack growth in metals," *Philosophical Magazine*, vol. 17, pp. 71-82, 1967.
- [11] R. M. N. Pelloux, "Mechanisms of formation ductile fatigue striations," *Transaction of the American society for materials*, vol. 62, pp. 281-285, 1969.
- [12] B. A. Bilby, A. H. Cottrell, and K. H. Swinden, "The spread of plastic yield from a notch," *Proceedings of the Royal Society, London*, vol. A272, pp. 304-314, 1963.
- [13] R. G. Forman, V. E. Kearney, and R. M. Engle, "Numerical analysis of crack propagation in cyclic-loaded structures," *J.I of Basic Engg.*, vol. 89, pp. 459-464, 1967.
- [14] K. Walker, "The effect of stress ratio during crack propagation and fatigue for 2024-T3 and 7075-T6 aluminum," In *Effects of Environment and Complex Load History for Fatigue Life*, ASTM STP, vol. 462, pp. 1-14, 1970.
- [15] J. M. Barsom, "Fatigue crack growth under variable amplitude loading in various bridge steels," In *Fatigue Crack Growth Under Spectrum Loading*, ASTM STP, vol. 595, pp. 217-235, 1976.
- [16] Jr. J. C. Newman, "The merging of fatigue and fracture mechanics concepts: a historical perspective," *Progress in Aerospace Science*, vol. 34, pp. 347-390, 1998.

- [17] O. E. Wheeler, "Spectrum loading and crack growth," *J. of Basic Engg.*, vol. 94, pp. 181-186, 1972.
- [18] J. D. Willenborg, R. M. Engle, and H. A. Wood, "A crack growth retardation model using an effective stress concept," Report AFFEL-TM-71-1- FBR, Dayton (OH), Air Force Flight Dynamics Laboratory, Wright-Patterson Air Force Base, 1971.
- [19] J. L. Rudd, and Jr R. M. Engle, "Crack growth behavior of center-cracked panels under random spectrum loading," In: Chang JB, Hudson CM, editors: *Methods and models for predicting fatigue crack growth under random loading*, ASTM STP, vol. 748, pp. 103-114, 1981.
- [20] J. B. Chang, M. Szamosi, and K.W. Liu, "Random spectrum fatigue crack life predictions with or without considering load interactions," In: Chang J.B, Hudson C.M, editors: *Methods and models for predicting fatigue crack growth under random loading*, ASTM STP, vol. 748, pp. 115-132, 1981.
- [21] D. M. Corbly, and P. F. Packman, "On the influence of single and multiple peak overloads on fatigue crack propagation in 7075-T6511 aluminum," *Engg. Fract. Mech.*, vol. 5, pp. 479-497, 1973.
- [22] F. Taheri, D. Trask, and N. Pegg, "Experimental and analytical investigation of fatigue characteristics of 350WT steel under constant and variable amplitude loadings," *J.of Marine Struct.*, vol. 16, pp. 69-91, 2003.
- [23] J. B. Chang, and C. M. Hudson, "Methods and models for predicting fatigue crack growth under random loading," ASTM STP, vol. 748, 1981.
- [24] J. P. Gallagher, "A generalized development of yield zone models," AFFDL-TM-

- 74-28-FBR, O. H Dayton, 1974.
- [25] J. B. Chang, R. M. Engle, and J. Stolpestad, "Fatigue crack growth behavior and life predictions for 2219-T851 aluminum subjected to variable amplitude loadings," ASTM STP, vol. 743, pp. 3-27, 1981.
- [26] W. S. Johnson, "Multi-parameter yield zone model for predicting spectrum crack growth," ASTM STP, vol. 748, pp. 85-102, 1981.
- [27] B. K. S. Yuen, and F. Taheri, "Proposed modifications to the Wheeler retardation model for multiple overloading fatigue life prediction," Int. J. of Fat., vol. 28, pp.1803-1819, 2006.
- [28] D. S. Dugdale, "Yielding of Steel Sheets Containing Slits," J. of Mech. and Phy. of Solids, vol. 8. pp. 100-108, 1960.
- [29] W. Elber, "The significance of fatigue crack closure. In: Damage tolerance in aircraft structures," ASTM STP, vol. 486, pp. 230-242, 1971.
- [30] C.Y. Kim, and J. H. Song, "Fatigue crack closure and growth behavior under random loading," Engg. Fract. Mech., vol. 49, No. 1, pp. 105-120, 1994.
- [31] J. Dominguez, J. Zapatero, and B. Moreno, "A statistical model for fatigue crack growth under random loads including retardation effects," Engg. Fract. Mech., vol. 62, pp. 351-369, 1999.
- [32] M. Jono, A. Sugeta, and Y. Uematsu, "Fatigue crack growth and crack closure behavior of ti-6al-4v alloy under variable amplitude loadings," In: McClung R.C. and Newman Jr J.C, editors, Advances in fatigue crack closure measurement and analysis, ASTM STP, vol. 1343, West Conshohocken (PA), pp. 265-284, 1999.

- [33] C. F. Lee, "EndoFEM intergrated methodology of fatigue crack propagation with overloaded delay retardation," *The Chinese Journal of Mechanics – Series A*, vol. 19, No. 2, pp. 327-335, 2003.
- [34] P. Ljustell, and F. Nilsson, "Variable amplitude crack growth in notched specimens," *Engg. Fract. Mech.*, vol. 72, pp. 2703-2720, 2005.
- [35] D. Aliaga, A. Davy, and H. Schaff," *Mechanics of Fatigue Crack Closure*," edited by J.C. Newman Jr, pp. 491-504, 1987.
- [36] U. H. Padmadinata, "Investigation of crack closure prediction models for fatigue in aluminum alloy sheet under flight-simulation loading," Ph.D-thesis, Delft, 1990.
- [37] G. Baudin, R. Labourdette, and M. Robert, "In Fatigue crack growth under variable amplitude loading," edited by J. Petit et al., Elsevier Applied Science, London, pp. 292-308, 1988.
- [38] A.U. de Koning, "A simple crack closure model for prediction of fatigue crack growth rates under variable-amplitude loading," In: Roberts Richard, editor. *Fracture mechanics, thirteenth conference, ASTM STP*, vol. 743, pp. 63-85, 1981.
- [39] A. K. Vasudevan, K. Sadananda, N. Louat, "A review of crack closure, fatigue crack threshold and related phenomena," *Mats. Sci. Engg.* Vol. A188, No. 1-2, pp. 1-22, 1994.
- [40] A. K. Vasudevan, K. Sadananda, "Analysis of fatigue crack growth under compression-compression loading," *Int. J. of Fat.*, vol. 23, pp. S365-S374, 2001.

- [41] K. Sadananda, A. K. Vasudevan, R. L. Holtz, and E. U. Lee, "Analysis of overload effects and related phenomenon," *Int. J. of Fat.*, vol. 21, pp. S233–S246, 1999
- [42] J. Quian, and A. Fatemi, "Mixed mode fatigue crack growth: A literature survey," *Engg. Fract. Mech.*, vol. 55, No. 6, pp. 969-90, 1996.
- [43] S. Iida, and A. S. Kobasahi, "Crack propagation in 7075-T6 plates under cyclic tensile and ransverse shear loadings," *J.of Basic Engg. Series*, vol. D91, pp. 764-769, 1969.
- [44] R. Roberts, and J. J. Kibler, "Mode-II fatigue crack propagation," *J.of Basic Engg. Series*, vol. D93, pp. 671-680, 1971.
- [45] K. Tanaka, "Fatigue Crack Propagation from a Crack Inclined to the Cyclic Tensile Axis," *Engg. Fract. Mech.*, vol. 6, pp. 493–507, 1974.
- [46] H.A. Richard, "Role of Fracture Mechanics in Modern Technology," Elsevier Science Publishing, North-Holland, 1987.
- [47] H. A. Richard, "Fracture mechanical predictions for cracks with superimposed normal and shear loading," Dusseldorf: VDI-Verlag, 1985 [in German] (in 10).
- [48] A. B. Patel, and P. K. Pandey, "Fatigue Crack Growth under Mixed-Mode Loading," *Fat. and Fract. of Engg. Mats. and Struct.*, vol. 4, pp. 65–77, 1981.
- [49] D. F. Socie, "Prediction of Fatigue Crack Growth in Notched Members under Variable Amplitude Loading Histories," *Engg. Fract. Mech.* Vol. 9, pp. 849–865, 1977.

- [50] S. C. Reddy, and A. Fatemi, "Small Crack Growth in Multiaxial Fatigue," In *Advances in Fatigue Lifetime Predictive Techniques*, ASTM STP, vol. 1122, pp. 276–298, 1992.
- [51] W. R. Chen, and L. M. Keer, "Fatigue Crack Growth in Mixed-Mode Loading," *J. of Engg. Mat. and Tech.*, vol. 113, pp. 222–227, 1991.
- [52] T. Tamilselvan, K.W. Lo, Y. B. Gong, and M. M. Zhao, "A Model for Mixed-Mode Fatigue," *J. of Testing and Evaluation*, vol. 33, No. 3, pp. 188-196, 2005.
- [53] J. K. Kim, and C. S. Kim, "Fatigue crack growth behavior of rail steel under mode-I and mixed mode loadings," *Mats. Sci. and Engg.*, vol. A338, pp. 191-201, 2002.
- [54] L. P. Borrego, F. V. Antunes, J. M. Costa, and J. M. Ferreira, "Mixed-mode fatigue crack growth behavior in aluminum alloy," *Int. J. of Fat.*, vol. 28, pp. 618-26, 2006.
- [55] K. H. Benrahou, M. Benguediab, M. Belhouari, M. Nait-Abdelaziz, and A. Imad, "Estimation of the plastic zone by finite element method under mixed mode (I & II) loading," *Comput. Mats. Sci.*, vol. 38, pp. 595-601, 2007.
- [56] S. Ma, X. B. Zhang, N. Recho, and J. Li, "The mixed mode investigation of the fatigue crack growth in CTS metallic specimen," *Int. J. of Fat.*, vol. 28, pp. 1780-1790, 2006.
- [57] P. Dahlin, and M. Olsson, "Mode-I fatigue crack growth reduction mechanisms after a single mode-II load cycle," *Engg. Fract. Mech.*, vol. 73, pp. 1833-1848, 2006.
- [58] V. Srinivas, and P. Vasudevan, "Studies of mixed mode crack propagation in D16AT aluminum alloy," *Engg. Fract. Mech.*, vol. 45, No. 4, pp. 415-430, 1993.

- [59] S. B. Biner, "Fatigue crack growth studies under mixed mode loading," *Int.J. of Fat.*, vol. 23, pp. S259-S263, 2001.
- [60] W. S. McCulloch, and W. A. Pitts, "A logical calculus of the ideas immanent in nervous activity," *Bull. Math. Biophysics*, vol. 943, No. 5, pp. 115-133.
- [61] D. Hebb, "The Organisation of Behaviour," Willey, New York, USA, 1949.
- [62] J. J. Hopfeld, "Neural Networks and Physical Systems with Emergent Collective Computational Abilities," *Proc. Natl. Acad. Sci.*, vol. 79, pp. 2554-2558, 1982.
- [63] D. Skapura, "Building neural networks," New York, ACM Press Addison-Wesley Publishing Company, 1996.
- [64] R. J. Schalkoff, "Artificial neural networks," McGraw-Hill, 1997.
- [65] S. Haykin, "Neural networks: a comprehensive foundation," New York, Macmillan, 1994.
- [66] R. Herzallah, and Y. Al-Assaf, "Control of non-linear and time-variant dynamic systems using neural networks," In: *Proceedings of the 4th World Multiconference on Systemics, Cybernetics and Informatics*, Florida, 2000.
- [67] W. Mansoor, H. Al-Nashash, and Y. Al-Assaf, "Image classification using wavelets and neural networks," In: *The 18th IASTED International Conference on Applied Informatics*, Innsbruck, Austria, 2000.
- [68] H. Al-Nashash, Y. Al-Assaf, B. Lvov, and W. Mansoor, "Laser speckle for materials classification utilizing wavelets and neural networks image processing techniques," *J. Mater. Evaluat.*, vol. 59, pp. 1072-1078, 2001.

- [69] C. S. Lee, W. Hwang, H. C. Park, and K. S. Han, "Failure of carbon/epoxy composite tubes under combined axial and torsional loading—1. Experimental results and prediction of biaxial strength by the use of neural networks," *Comp. Sci. Technol.*, vol. 59, pp. 1779–1788, 1999.
- [70] F. Aymerich, and M. Serra, "Prediction of fatigue strength of composite laminates by means of neural networks," *Key. Engg. Mater.*, vol. 144, pp. 231-240, 1998.
- [71] J. A. Lee, D. P. Almond, B. Harris, "The use of neural networks for the prediction of fatigue lives of composite materials," *Comp. Appl. Sci. Manufact., Part A*, vol. 30, pp. 1159-1169, 1999.
- [72] S. Meyer, E. Diegel, "Brückner-Foigt A, Moßsling A. Crack interaction modeling," *Fat. Fract. Engg. Mater. Struct.*, vol. 23, pp. 315–323, 2000.
- [73] P. Artymiak, L. Bukowski, J. Feliks, S. Narberhaus, and H. Zenner, "Determination of S-N curves with the application of artificial neural networks," *Fat. Fract. Engg. Mater. Struct.*, vol. 22, pp. 723–728, 1999.
- [74] T. T. Pleune, O. K. Chopra, "Using artificial neural networks to predict the fatigue life of carbon and low-alloy steels," *Nucl. Engg. Design*, vol. 197, pp. 1–12, 2000.
- [75] V. Venkatesh, H. J. Rack, "A neural network approach to elevated temperature creep-fatigue life prediction," *Int. J. of Fat.*, vol. 21, pp. 225–234, 1999.
- [76] M. E. Haque, K. V. Sudhakar, "Prediction of corrosion-fatigue behavior of DP steel through artificial neural network," *Int. J. of Fat.*, vol. 23, pp. 1-4, 2001.
- [77] Y. Cheng, W. L. Huang, and C.Y. Zhou, "Artificial neural network technology for the data processing of on-line corrosion fatigue crack growth monitoring," *Int. J. of Pres. Ves. and Pip.*, vol. 76, pp. 113–116, 1999.

- [78] R. M. V. Pidaparti, and M. J. Palakal, "Neural Network Approach to Fatigue-Crack- Growth Predictions under Aircraft Spectrum Loadings," *J. of Aircraft*, vol. 32, No. 4, pp. 825-831, 1995.
- [79] J. Y. Kang, and J. H. Song, "Neural network applications in determining the fatigue crack opening load," *Int. J. of Fat.* vol. 20, No. 1, pp. 57-69, 1998.
- [80] K. Genel, "Application of artificial neural network for predicting strain life fatigue properties of steels on the basis of tensile tests," *Int. J. of Fat.* vol. 26, pp. 1027-1035, 2004.
- [81] H. Zenner, and C. Marquardt, "Ermittlung von Bauteilwohlerlinien mittels Ku`nstlicher Neuronaler Netze," *Forschungsbericht FVA und VBFeh*, 2003.
- [82] H. Zenner, L. Bukowski, M. Karkula, and C. Marquardt, "Lifetime prediction with the application of artificial neural networks," 8th International fatigue congress–fatigue, 3-7 June, Stockholm, pp. 2697-2704, 2002.
- [83] C. Marquardt, and H. Zenner, "Lifetime calculation under variable amplitude loading with application of artificial neural networks," *Int. J. of Fat.* vol. 27, pp. 920-927, 2005.
- [84] A. Fotovati, and T. Goswami, "Prediction of elevated temperature fatigue crack growth rates in Ti-6Al-4V alloy – neural network approach," *Mats. Engg. and Design*, vol. 25, pp. 547-554, 2004.
- [85] J. Jia, and J. F. Davalos, "An artificial neural network for the fatigue study of bonded FRP-wood interfaces," *Composite Structures*, vol. 74, pp. 106-114, 2006.
- [86] L. A. Zadeh, "Outline of a new approach to the analysis of complex systems and

- decision processes,” *IEEE Trans. Syst., Man, Cybern.*, vol. SMC-3, pp. 28–44, Jan. 1973.
- [87] S. Barada, and H. Singh, “Generating Optimal Adaptive Fuzzy-Neural Models of Dynamical Systems with Applications to Control” *IEEE Trans. Syst., Man, Cybern. Part-C*, vol. 28, No. 3, pp. 371-391, 1998.
- [88] S. Mitra, and Y. Hayashi, “Neuro-fuzzy rule generation: Survey in soft computing framework,” *IEEE Trans. Neural Netw.*, vol. 11, No.3, pp.748–768, 2000.
- [89] S. N. J. Engin, Kuvulmaz, and V. E. Omurlu, “Fuzzy control of an ANFIS model representing a nonlinear liquid-level system,” *Neural Comput. & Applic.* vol. 13, pp. 202–210, 2004.
- [90] C. T. Lin, and C. Lee, “Neural-network-based fuzzy logic control and decision systems,” *IEEE Trans. Comput.*, Special Issue on Artificial Neural Networks, vol. 40, pp. 1320–1336, Dec. 1991.
- [91] L. X. Wang, and J. Mendel, “ Back-propagation of fuzzy systems as nonlinear dynamic system identifiers,” in *Proc. IEEE Int. Conf. Fuzzy Systems*, San Diego, CA, pp. 1409–1418, 1992.
- [92] F. Zia, and C. Isik, “Neuro-fuzzy control using self-organizing nets,” in *3rd IEEE Int. Conf. Fuzzy Systems*, Orlando, FL, vol. 1, pp. 70–75, 1994.
- [93] J. S. R. Jang, “ANFIS: Adaptive-network-based fuzzy inference system,” *IEEE Transactions on Systems, Man, and Cybernetics*, 23(3), 665–685, 1993.

- [94] J. S. R. Jang, "Structure determination in fuzzy modeling: A fuzzy CART Approach," Proceedings of the third IEEE International conference on Fuzzy Systems, Orlando, Florida, vol. 1, pp. 480–485, 1994.
- [95] T. Takagi, and M. Sugeno, "Fuzzy identification of systems and its applications to modeling and control," IEEE Transactions on Systems, Man, Cybernetics, vol. 15, pp. 116–132, 1985.
- [96] E. B. Rahouyi, J. Hinojosa, and J. Garrigos, "Neuro-fuzzy modeling techniques for microwave components," IEEE Microwave and Wireless Components Letters, vol. 16, No. 2, pp. 72–74, 2006.
- [97] A. Bardossy, and I. Bogardi, "Fuzzy Fatigue Life Prediction", Structure Safety, vol. 6, pp. 25-38, 1989.
- [98] H. Tanka, and S. Uejima, "Linear Regression Analysis With Fuzzy Model", IEEE Transactions on Systems, Man, and Cybernetics, vol. SMC-12, No. 6, pp. 903-907, 11/12 1982.
- [99] S. Naruhito, "Application of Fuzzy set theory to Fatigue Analysis of Bridge Structures", Information Sciences, Vol. 45, pp. 175-184, 1988.
- [100] X. Wu, J. M. Hu, and M. Pecht, "Fuzzy Regression Analysis for Fatigue Crack Growth," TH0334-3/90/0000/0437\$01.00 © 1990 IEEE.
- [101] M. A. Jarrah, Y. Al-assaf, and H. El kadi, "Neuro-Fuzzy Modeling of Fatigue Life Prediction of Unidirectional Glass Fiber/Epoxy Composite Laminates," J. of composite materials, Vol. 36, No. 06, pp. 685-699, 2002.

- [102] A. P. Vassilopoulos, R. Bedi, "Adaptive neuro-fuzzy inference system in modelling fatigue life of multidirectional composite laminates," *Comput. Mats. Sci.*, vol. 43, No. 4, pp. 1086-1093, 2008.
- [103] D. Kujawski, "A new $(\Delta K^+ K_{\max})^{0.5}$ driving force parameter for crack growth in aluminum alloys," *Int. J. of Fat.*, vol. 23, No. 8, pp. 733-740, 2001.
- [104] A. H. Noroozi, G. Glinka, and S. Lambert, "A two parameter driving force for fatigue crack growth analysis," *Int. J. of Fat.*, vol. 27, pp. 1277-1296, 2005.
- [105] S. Dinda, D. Kujawski, "Corelation and prediction of fatigue crack growth for different R-ratios using K_{\max} and ΔK^+ parameters," *Engg. Fract. Mech.*, vol. 71, No. 12, pp. 1779-1790, 2004.
- [106] K. Donald, and P. C. Paris, "An evaluation of ΔK_{eff} estimation procedures on 6060-T6 and 2024-T3 aluminum alloys," *Int. J. of fat.*, vol. 21, pp. S47-S57, 1999.
- [107] D. Kujawski, "A fatigue crack driving force parameter with load ratio effects," *Int. J. of Fat.*, vol. 23, pp. S239-246, 2001.
- [108] P. C. Paris, and F. Erdogan, "A critical analysis of crack propagation laws," *J. of Basic Engg.*, vol. 85, pp. 528-534, 1963.
- [109] A. Spagnoli, "Self-similarity and fractals in the Paris range of fatigue crack growth," *Mech. Mat.*, vol. 37, pp. 519-529, 2005.
- [110] G. Maymon, "The problematic nature of the application of stochastic crack growth models in engineering design," *Engg. Fract. Mech.*, vol. 53, No. 6, pp. 911-916, 1996.

- [111] R. Jones, L. Molent, and S. Pitt, "Similitude and the Paris crack growth law," *Int. J. Fat.*, vol. 30, pp. 1873-1880, 2008.
- [112] S. Pearson, "Initiation of fatigue cracks in commercial aluminum alloys and the subsequent propagation of very short cracks," *Engg. Fract. Mech.*, vol. 7, pp. 235–247, 1975.
- [113] R. A. Pell, P. J. Mazeika, and L. Molent, "The comparison of complex load sequences tested at several stress levels by fractographic examination," *J. Engg. Fail. Anal.*, vol. 12, No. 4, pp. 586–603, 2005.
- [114] R. Jones, L. Molent, S. Pitt, and E. Siores, "Recent developments in fatigue crack growth," In: Gdoutos EE, editor: *Proceedings of the 16th European conference on fracture, failure analysis of nano and engineering materials and structures*, July 3–7, Alexandroupolis, Greece, 2006.
- [115] N. E. Frost, and D. S. Dugdale, "The propagation of fatigue cracks in test specimens," *J. Mech. Phys. Solids.*, vol. 6, pp.92–110, 1958.
- [116] M. J. Caton, J. W. Jones, J. M. Boileau, and J. E. Allison, "The effect of solidification rate on the growth of small fatigue cracks in a cast319-type aluminium alloy," *Metall. Mater. Trans.*, vol. 30A, pp.3055–3068, 1999.
- [117] N. Kawagoishi, Q. Chen, and H. Nisitani, "Significance of the small crack growth law and its practical application," *Metall. Mater. Trans.*, vol. 31A, pp.2005–2023, 2000.
- [118] Y. Murakamia, and K. J. Miller, "What is fatigue damage? A view point from the observation of low cycle fatigue process," *Int. J. of Fat.*, vol. 27, No. 8, pp.991–1005, 2005.

- [119] H. Nisitani, M. Goto, and N. Kawagoishi, "A small-crack growth law and its related phenomena," *Engg. Fract. Mech.*, vol. 41, No. 4, pp.499–513, 1992.
- [120] D. A. Virkler, B. M. Hillberry, and P. K. Goel, "The statistical modeling nature of fatigue crack propagation," *J. Engg. Mat. Technol., ASME*, vol. 101, pp. 148-153, 1979.
- [121] H. Ghonem, and S. Dore, "Experimental study of the constant probability crack growth curves under constant amplitude loading," *Engg. Fract. Mech.*, vol. 27, pp. 1-25, 1987.
- [122] C. Timbrell, R. Chandwani, and G. Cook, "State of The Art in Crack Propagation," Zentech International Limited, <http://www.zentech.co.uk>, 2004.
- [123] A. R. C. Murthy, G. S. Palani, and N. R. Iyer, "State-of-the-art review on fatigue crack growth analysis under variable amplitude loading," *Inst. of Engineers, India, Journal-CV*, vol. 85, pp. 118-129, 2004.
- [124] D. Broek, "The practical use of fracture mechanics," Kluwer, 1988.
- [125] "Standard Test Method for Tension Testing for Metallic Materials," ASTM, E8M-97, 1997.
- [126] G. R. Irwin, NRL Report, pp. 65-98, vol. 21, Nov. 1967.
- [127] "Standard test method for measurement of fatigue crack growth rates," ASTM E647-08, West Conshohocken (PA), American Society for Testing and Materials, 2008.
- [128] W. F. Brown, J. E. Srawley, "Plane strain crack toughness testing of high strength

- metallic materials,” ASTM STP, vol. 410, American Society for Testing and Materials, Philadelphia, USA, p. 1, 1966.
- [129] S. Suresh, “Fatigue of materials,” 1st ed., Cambridge University Press, p. 351, 1992.
- [130] B. Mukherjee, “A note on the analysis of fatigue crack growth data,” *Int. J. Fract.*, vol. 8, pp. 449- 451, 1972.
- [131] R. A. Smith, “The determination of fatigue crack growth rates from experimental data,” *Int. J. Fract.*, vol. 9, pp. 352-355, 1973.
- [132] K. B. Davies, and C. E. Feddersen, “Evaluation of fatigue-crack growth rates by polynomial curve fitting,” *Int. J. Fract.*, vol. 9, pp. 116-118, 1973.
- [133] H. G. Munro, “The determination of fatigue crack growth rates by data smoothing technique,” *Int. J. Fract.*, vol. 9, pp. 366-368, 1973.
- [134] J. Polak, and Z. Knesl, “On the fatigue crack growth rate evaluation from experimental data,” *Int. J. Fract.*, vol. 11, pp. 693-696, 1975.
- [135] D.Y. Wang, “An investigation of initial fatigue quality, design of fatigue and fracture resistant structures,” In: Abelkis P.R, Hudson, C.M., editors, ASTM STP, vol. 761, pp. 191–211, 1982.
- [136] J. Z. Zhang, “A shear band decohesion model for small fatigue cracks growth in an ultra-fine grain aluminium alloy,” *Engg. Fract. Mech.*, vol. 65, pp. 665-681, 2000.
- [137] J. R. Mohanty, B. B. Verma, and P. K. Ray, “Determination of fatigue crack growth rate from experimental data: A new approach,” *Int. J. of Micro-struct. and Mats. Prop.*, Inderscience, Accepted, Ref. No. IJMMP-119/08.

- [138] J. R. Mohanty, B. B. Verma, and P. K. Ray, "Prediction of fatigue crack growth and residual life using an exponential model: Part I (constant amplitude loading)," *Int. J. of Fat.*, Elsevier, vol. 31, pp. 418-424, 2009.
- [139] J. R. Mohanty, B. B. Verma, and P. K. Ray, "Prediction of fatigue crack growth and residual life using an exponential model: Part II (mode-I overload induced retardation)," *Int. J. of Fat.*, Elsevier, vol. 31, pp. 425-432, 2009.
- [140] J. R. Mohanty, B. B. Verma, and P. K. Ray, "Prediction of fatigue life with interspersed mode-I and mixed mode (I & II) overloads by an exponential model: Extensions and Improvements," *Engg. Fract. Mech.*, Elsevier, vol. 76, pp. 454-468, 2009.
- [141] J. R. Mohanty, B. B. Verma, and P. K. Ray, "Evaluation of Overload-induced Fatigue Crack Growth Retardation Parameters using an Exponential Model," *Engg. Fract. Mech.*, Elsevier, vol. 75, pp. 3941-3951, 2008.
- [142] P. K. Ray, P. K. Ray, and B. B. Verma, "A study on spot heating induced fatigue crack growth retardation," *Fat. Fract. Engg. Mat. Struct.*, vol. 28, pp. 579-585, 2005.
- [143] P. J. Werbos, "Backpropagation and neurocontrol: a review and prospectus," *Int. Joint Conf., Neural Netw.*, vol. 1, pp. 209, 1989.
- [144] P. Heuler, and W. Schuetz, "Assessment of concepts for fatigue crack initiation and propagation life prediction," *Z. Werkstofftech.*, vol. 17, pp. 397-405, 1986.

Appendix A

Heat-treatment of Al 7020 aluminum alloy

The 7020 aluminum alloy procured from Hindalco, Renukoot, Maharashtra, India in the as-fabricated condition was subjected to T7 heat-treatment to obtain optimum mechanical properties. It is a two-step aging heat treatment procedure particularly suitable for 7xxx series Al-alloys. It consists of heating at a temperature of 100°C to 120°C for 8 hours followed by aging (over-aging) at a temperature of 145°C to 175°C. It allows the formation of large number of GP zones. These zones transform to the intermediate η' precipitate and finally to the equilibrium η (MgZn₂) phase during over-aging, thereby increasing hardness. To decide the solution treatment temperature, aging temperature, and also aging time the following procedures were followed.

Procedure

1. Total 18 numbers of samples with 10mm×10mm dimension were cut from the plate to prepare three sets of experiments of 6 each.
2. Those sets were given solution treatment at three different temperatures such as 490°C, 510°C and 540°C for 2 hours and water quenched.
3. Three samples (one from each set) were taken and their hardness's were measured in Vicker's hardness testing machine.
4. Rest 5 samples of each set were given 1st step aging at temperatures 110°C for 8 hours in the oven. Then three samples (one from each set) were taken out for hardness measurement and rest of the samples were given 2nd step aging at a temperature of 150°C for 14 hours, 18 hours, 22 hours and 26 hours respectively and their corresponding hardness's were measured at different time intervals.

The noted times and their corresponding hardness's are listed in Table A1 and illustrated in Figs. A1, A2 and A3 respectively. From Table A1 it is observed that set-2 gives the optimum value of hardness which is 132.

Table A1 - Vicker's Hardness of 7020 T7 Al alloy

Test sets	Vicker's Hardness					
	After Quench	After 8-hours at 110°C	After 22 hrs.(8hrs.at 110°C+14hrs.at 150°C)	After 26 hrs.(8hrs.at 110°C +18hrs.at 150°C)	After 30hrs.(8hrs.at 110°C +22hrs.at 150°C)	After 34hrs.(8hrs.at 110°C +26hrs.at 150°C)
Set-1 ($T_{sol}=490^{\circ}$)	81	99	116	119	118	117
Set-2 ($T_{sol}=510^{\circ}$)	81	101	128	131	132	127
Set-3 ($T_{sol}=540^{\circ}$)	81	98	115	121	123	121

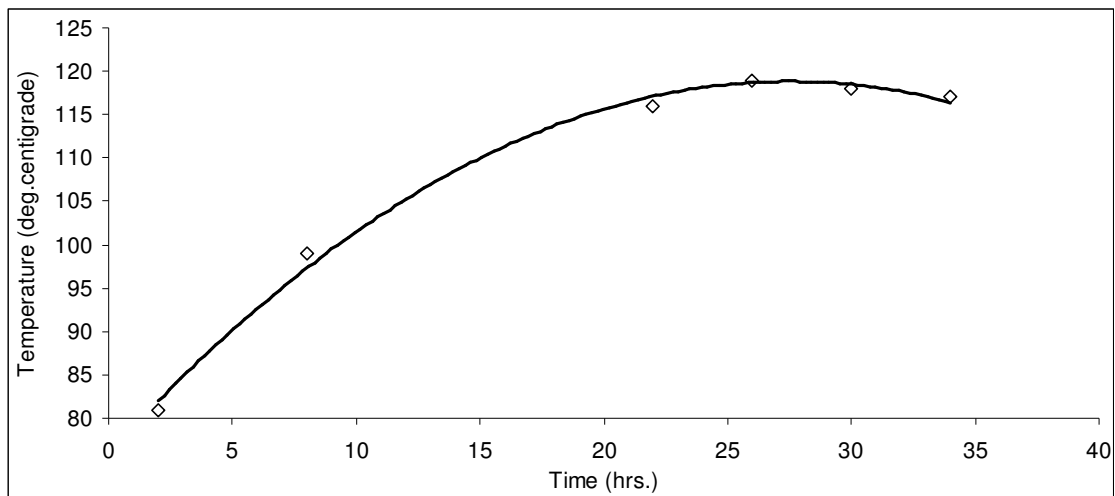


Fig. A1 – Time vs. Temperature plot of set-1

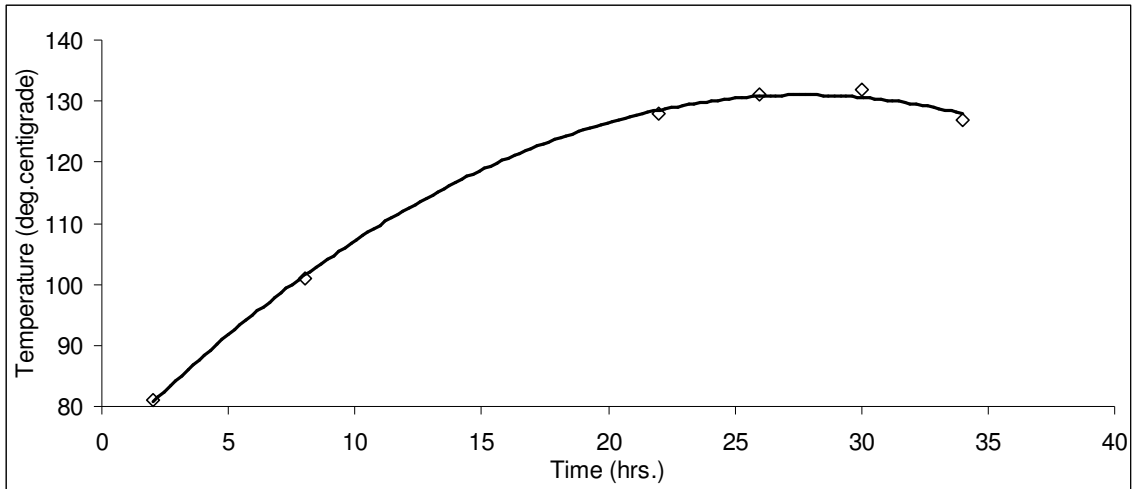


Fig. A2 – Time vs. Temperature plot of set-2

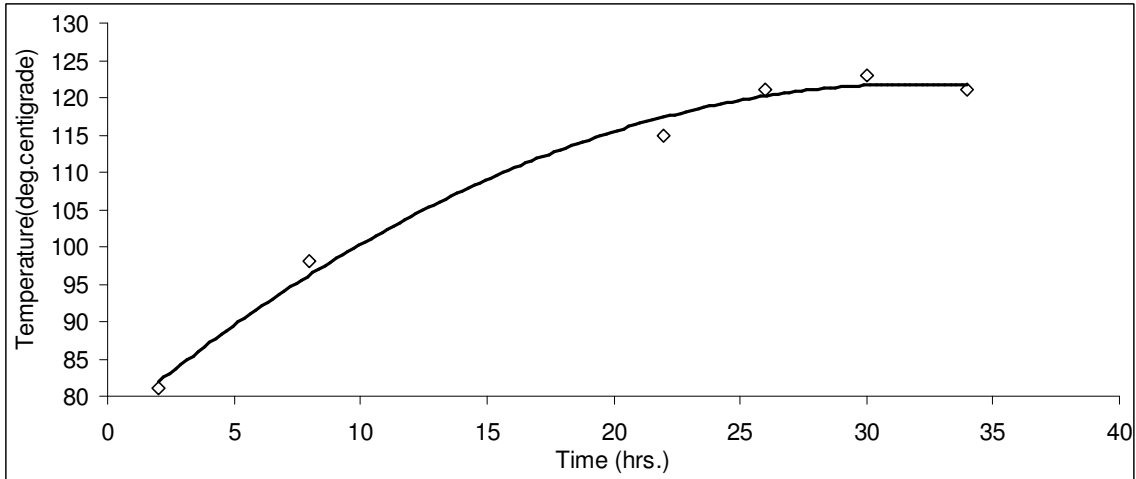


Fig. A3 - Time vs. Temperature plot of set-3

Appendix B

Determination of coefficients for calculation of crack length in DADN software

In order to determine the crack coefficients, six sets of constant amplitude fatigue tests were conducted using single edge notch specimens in *INSTRON 8502* dynamic testing machine at a frequency of 6 Hz. Out of those tests, three tests were used for coefficient calculation and rest three sets were used for validation. General formula used in software for calculation of crack length is:

$$a/w = C_0 + C_1U + C_2U^2 + C_3U^3 + C_4U^4 + \dots \quad (\text{B1})$$

$$\text{where, } U = \frac{1}{\sqrt{(E'\nu B/P)+1}}$$

E' = plane strain modulus = $\frac{E}{1-\eta^2}$, B = specimen thickness, P = load, ν = displacement between measurement points, η = Poisson's ratio, a = crack length and w = specimen width. The coefficients were calculated using MATLAB 7.1 with the following matrix program:

```
>> A' = [.....];
```

```
>> B' = inv(A');
```

```
>> C' = [.....];
```

```
>> D' = C' * B'
```

where, A' is the coefficient matrix from the values; B' is the known matrix i.e. values of a/w ; D' is the unknown matrix and its value will give $C_0, C_1, C_2 \dots$ etc.

Test: 1

The different results of first set of constant amplitude fatigue test are tabulated in Table B1.

Table B1 - Results of constant amplitude fatigue test - 1

Crack length <i>a</i> (mm)	No of cycles <i>N</i>	$E'vB/P$	$U = \frac{1}{\sqrt{(E'vB/P)+1}}$
19.23	47170	3.71	0.3417
20.28	89130	4.221	0.3274
21.43	125500	4.891	0.3114
22.41	148700	5.592	0.2972
23.37	161400	6.272	0.2854
24.24	169400	7.167	0.27195

CALCULATION:

With the above tabulated values, the following sets of simultaneous equations are formulated by using the equation B1.

$$0.3702 = C_0 + C_1 (0.3417) + C_2 (0.1168) + C_3 (0.0399) + C_4 (0.0136) + C_5 (0.00466)$$

$$0.3905 = C_0 + C_1 (0.3274) + C_2 (0.1072) + C_3 (0.0351) + C_4 (0.0115) + C_5 (0.00376)$$

$$0.4126 = C_0 + C_1 (0.3114) + C_2 (0.09697) + C_3 (0.0302) + C_4 (0.0094) + C_5 (0.00293)$$

$$0.4315 = C_0 + C_1 (0.2972) + C_2 (0.0883) + C_3 (0.0263) + C_4 (0.0078) + C_5 (0.00232)$$

$$0.4499 = C_0 + C_1 (0.2854) + C_2 (0.0815) + C_3 (0.0232) + C_4 (0.0066) + C_5 (0.00189)$$

$$0.4667 = C_0 + C_1 (0.27195) + C_2 (0.07396) + C_3 (0.0201) + C_4 (0.0055) + C_5 (0.00149)$$

Solving the above equations with the help of the given program in MATLAB, the first sets of coefficients are obtained as follows:

$$C_0 = 2.762883; C_1 = -16.79367; C_2 = 29.75729; C_3 = 22.77747; C_4 = -48.35849 \text{ and } C_5 = -81.7772$$

Test: 2

Table B2 shows the results of test-2.

Table B2 - Results of constant amplitude fatigue test - 2

Crack length a (mm)	No of cycles N	$E'vB/P$	$U = \frac{1}{\sqrt{(E'vB/P)+1}}$
19.23	48180	3.716	0.34157
20.28	90390	4.243	0.3268
21.43	127100	4.911	0.3109
22.41	149200	5.609	0.2969
23.37	161900	6.326	0.2845
24.24	169400	7.167	0.27195

The coefficients calculated from the 2nd set of experiments using the same procedure are as follows:

$$C_0 = 0.3771; C_1 = 1.3354; C_2 = -0.5490; C_3 = -5.5918; C_4 = -57.3827 \text{ and } C_5 = 130.0125$$

Test: 3

Table B3 shows the results of test-3.

Table B3 - Results of constant amplitude fatigue test - 3

Crack length a (mm)	No of cycles N	$E'vB/P$	$U = \frac{1}{\sqrt{(E'vB/P)+1}}$
19.23	47920	3.703	0.34196
20.28	89890	4.238	0.3269
21.43	126600	4.911	0.3109
22.41	149000	5.598	0.2971
23.37	161600	6.309	0.2848
24.24	169400	7.167	0.27195

The coefficients calculated from the 3rd set of experiments using the same procedure are as follows:

$$C_0 = 0.73762; C_1 = 0.32498; C_2 = -7.91378; C_3 = 4.9771; C_4 = 42.4170 \text{ and } C_5 = -71.18278$$

Validation tests

In validation tests, three constant amplitude fatigue crack growth tests were conducted under same conditions similar to the previous tests. Before the tests, both the surfaces of the specimen were marked at every 1.0 mm interval in order to record the readings by visual (manual reading) method. All the fatigue tests were performed one by one by using the crack coefficients calculated from the previous tests with the help of COD gauge mounted at the edge of the SEN specimen. The few readings (up to six steps) from the machine were recorded and tabulated in Table B4 shown below:

Table B4 - Results of constant amplitude fatigue validation tests

Crack length (a) in mm (manual)	No. of cycles (N)	Crack length (a) in mm (machine for test-1)	Crack length (a) in mm (machine for test-2)	Crack length (a) in mm (machine for test-3)	% Dev (from manual reading for test-1)	% Dev (from manual reading for test-2)	% Dev (from manual reading for test-3)
19.1	51430	20.234	20.012	19.356	0.590	0.480	0.130
20.1	92660	21.825	20.989	20.546	0.860	0.440	0.220
21.1	129300	23.012	21.978	21.234	0.910	0.420	0.600
22.1	150300	23.986	22.864	22.168	0.850	0.350	0.300
23.1	161900	25.213	23.992	23.129	0.920	0.390	0.126
24.1	169525	26.578	24.897	24.157	1.030	0.330	0.237

Analyzing the results presented in Table A4, It was concluded that the coefficients obtained from test-3 were better than the other two. Taking the crack coefficients of test-3, all the fatigue crack propagation fatigue tests were conducted.

CURRICULUM VITAE

Name : **JYOTI RANJAN MOHANTY**

E-mail : guddy95@gmail.com

Date of Birth : 3rd Jan 1966

Nationality : Indian

Permanent Address

AT/PO-Arilo; PO –Sankhatras; DIST- Cuttack; Orissa-753053.

Address for Communication

AT/PO-Arilo; PO –Sankhatras; DIST- Cuttack; Orissa-753053.

Mob: 9437406971

Academic Profile

Exam. passed	Name of Institute/ University	Specialization	Year
B. Sc.	Ravenshaw College, Cuttack.	Chemistry	1984
B. E.	I.G.I.T, Sarang Talcher.	Mechanical Engg.	1989
M. E	R.E.C, Rourkela Sambalpur University.	Machine Design & Analysis	1992
Ph. D.	N.I.T, Rourkela, Deemed University	Fatigue & Fracture Mechanics	Thesis to submitted in May' 2009

Research Publications:

1. International Journal: 12 (Please Refer Page – xxii)
2. National Conference: 03

Experience:

1. In Research: 3 years during Ph. D
2. In Academic: 16 years at O.E.C, BBSR